University College London

Doctoral Thesis

Dual Laser Driven Cavity Cooling of a Levitated Nanosphere to Test Quantum Mechanics, and Other Research

Author:
George A. T. Pender

Supervisor:
Prof. T. S. Monteiro

A thesis submitted in fulfilment of the of the requirements

for the degree of Doctor of Philosophy

in the

Atomic, Molecular, Optical and Positron Physics Group

Department of Physics and Astronomy

September 2016

Declaration of Authorship

I, George Pender, declare that this thesis titled, “Dual Laser Driven Cavity Cooling of a Levitated Nanosphere to Test Quantum Mechanics, and Other Research” and the work presented in it are my own. I confirm that:

- This work was done wholly or mainly while in candidature for a research degree at this University.
- Where any part of this thesis has previously been submitted for a degree or any other qualification at this University or any other institution, this has been clearly stated.
- Where I have consulted the published work of others, this is always clearly attributed.
- Where I have quoted from the work of others, the source is always given. With the exception of such quotations, this thesis is entirely my own work.
- I have acknowledged all main sources of help.
- Where this thesis is based on work done by myself jointly with others, I have made clear exactly what was done by others and what I have contributed myself.

Acknowledgements

Much gratitude is due to my longsuffering and patient Supervisor, Prof. Tania Monteiro. I deeply appreciate her taking me on, and all her support throughout a process which turned out to be a lot longer than originally planned.

Leaders at UCL who helped me, in addition to Tania included: Peter Barker, James Millen, Sougato Bose and Janet Anders as well as Florian Marquartz and Markus Aspelymeyer from the Max Plank Institute for the Science of Light and the Vienna Centre for Quantum Science respectively.

Particular thanks are due to Katy, my loyal and patient wife, without whom I would certainly never have completed this Thesis. For example: At one point I managed to irreparably damage the main disk of the unbacked-up laptop containing 70% of my Thesis, the only record I had being a recently printed copy. This all had to be retyped. Most of this was done by Katy, who spent many days over a period of months, retyping this material (this is also the reason for the document appearing in MS word format rather than the more usual latec). As well as this mammoth assistance, Katy also provided the encouragement and proof reading to finally get me over the line.

Additionally, Katy spend hours with me doing tally charts as I rolled bits of wood and glued together pound coins on various surfaces (over ten thousand rolls in total).

Ten thousand rolls is still very little compared to the millions of rolls simulated by Martin Uhrin's computer simulation wizardry. Martin was a great co-author to work with. Thanks are also due to my former Undergraduate supervisor Alan Walton whose advice was instrumental in getting our paper published by the European Journal of Physics.

I am grateful to my parents, Chales and Helen, as well as numerous school teachers (in particular Andrew Davies, David Harrow and Sarah Gomme) as well as many undergraduate lecturers and supervisors (in particular Alan Walton and Zoran Hazbabaic) for supporting my interest in Science from a young age into my early twenties.

Finally, many thanks to the EPSRC and to three hundred million European taxpayers who funded this work.

Abstract and List of Publications

The first two chapters of the thesis are primarily a review of the work in the field. Chapter 1 focusses on optomechanics broadly and chapter 2 on levitated systems, which are of particular interest due to their thermal isolation from the surroundings. Chapters 3, 4 and 5 consist of my own research, much of which was presented in papers published in 2012* and 2013**.

* Pender, G. A. T., Barker, P.F., Marquardt, F., Millen, J. and Monteiro, T. S. Phys. Rev. A 85 021802 (2012)

** Monteiro, T. S., Millen, J, Pender, G. A. T., Marquardt, F., Chang, D. and Barker, P. F., New J. Phys. 15, 015001 (2013)

Chapter 3 is primarily concerned with determining the conditions for trapping and cooling a dielectric sphere in an optical cavity, with two laser modes. It is found that, by using two symmetric cooling and trapping beams (as opposed to the one-field-trapping-one-field-cooling of Chang *et. al.*) we predict around twenty times greater level of cooling than previously predicted. Typical experimental parameters are presented in section 3.7.

Chapter 4 deals with additional complications and considerations including: beads with a diameter which is a significant proportion of the diving wavelength, the effect of damping, heating and radiometric forces from the background gas, heating by black body radiation and other more realistic assumption. From this I am able to conclude that the dominant source of heating is the background gas and that, despite this heating, ground state cooling would still be possible at realistically low pressure (of less than 10^{-7} mbar). Chapter 5 discusses how we might observe quantum behaviour in this system. In this chapter I am able to determine that quantum behaviour is observable via a heterodyne detection which allows an asymmetry to be observed in the positional power spectrum of the bead (a classically impossible result).

Symbols used in this Thesis

A	Normally the coupling between bead position and cavity (defined equation 3.29).
A	Normally the bead's optical coupling constant but in section 3.1.2 and 3.1.3 just an arbitrary constant.
$\hat{a}^{\dagger}$	Raising ladder operator for the optical field.
$\hat{a}$	Lowering ladder operator for the optical field.
$\tilde{a}$	Fourier Transform of $\hat{a}$
B	Magnetic B-field.
$\boldsymbol{B}$	Magnetic Field Vector
b	Generic Mechanical damping constant
B	In section 3.1.2 and 3.1.3 just an arbitrary constant.
$\hat{b}^{\dagger}$	Normally the raising operator for the mechanical motion but in section 3.1.2 this is the raising operator for the external laser field.
$\hat{b}$	Normally the lowering operator for the mechanical motion.
B_{max}	The maximal value of the magnetic field
b_{signal}	Signal Bandwidth
$\tilde{b}$	Fourier Transform of $\hat{b}$
C	Cavity width definitional parameter.
c	The speed of light in vacuum = 299,792,458 ms^{-1}
D	Electric displacement field. Also $\mathbf{D}$ for vector quantity.
D	Diffusion Constant
$\boldsymbol{D}$	Electric Displacement-field vector often with component *e.g.* $\mathbf{D}_{\perp}$, $\mathbf{D}_{r}$
$\frac{d}{dt}$	Full time derivative
†	Hermitian Conjugate
E	Up to equation 3.28 this is the coupling between laser field and optical cavity. Later it is used for electric field with $\mathbf{E}$ as electric field vector.
E	In section 3.1.2 and 3.1.3 just an arbitrary constant.
$\boldsymbol{E}$	Electric E-field vector often with component *e.g.* $\mathbf{E}_{\parallel}$, $\mathbf{E}_{\theta}$

e	The transcendental number e. The base of the natural logarithm. Given by $\sum_0^\infty \frac{1}{n!}$. Approx: 2.71828182…
$\mathrm{E}_?$	The energy of a particular state "?"
E_G	Gravitational self-energy of a relevant mass difference
F	Force
$f(x)$	Generic function of x
G_1 , G_2	Generic coupling constant, defined in equation 1.8
g_1 , g_2	Coupling constant, defined where used
$\widehat{H}$	Hamiltonian Operator.
$\hbar$	Reduced Planck's Constant = 1.05457×10^{-34} m^2 kg s^{-1}.
$\mathbf{H}$	H field
$\widehat{H}'$	Effective Hamiltonian
$\widehat{H}_{int}$	Interaction Hamiltonian.
H_{rate}	Heating rate
i	The base of irrational numbers = $+\sqrt{-1}$
$I(r)$	Beam intensity as a function of radius within beam
k	Wave vector. Also k_1 and k_2, referring to fields 1 and 2 respectively.
k_B	Boltzman's Constant = 1.38064853 x 10^{-23} JK^{-1}
k_{sp}	Spring Constant
l	a length scale
L	Cavity length
m	Mass (normally bead mass)
n	The excitation state of the cavity of interest OR the occupancy of the mechanical degree of freedom.
$\widehat{\mathrm{N}}$	Stochastic noise operator.
n	Refractive Index
$\bar{\mathrm{n}}$	The mean occupancy of the mechanical degree of freedom.
$\bar{n}$	Average phonon occupancy of mechanical mode
$\hat{O}$	General Operator.
p	Dipole moment. Also $\mathbf{p}$ for dipole moment vector.
$\hat{p}$	Momentum operator (*x*-direction)
$\boldsymbol{p}$	Dipole moment vector
$\mathrm{p}_{\mathrm{photon}}$	Photon momentum

P	Power
P_{cas}	Casimir Pressure
P_L	The laser power (also P_1 and P_2 for individual laser powers).
P_{cool}	Cooling power in Watts.
P_{min}	Minimum detectable pressure
Q	Quality factor
q	Bead hollowness parameter
R	Sphere Radius
R_{sc}	Photon Scattering Rate
r , θ , ϕ	Standard spherical polar co-ordinates
S_{xx}	*x*-power spectrum of bead motion within cavity
t	Time.
T_0	Temperature of vacuum chamber and gas.
T_{bead}	Temperature of bead surface.
U	System energy.
u	System energy density.
V_{cav}	Cavity Volume.
V_{sphere}	Sphere volume =$\frac{4}{3}\pi R^3$
w	Cavity diameter.
$\hat{x}$	Position Operator, lengthways position along the cavity.
$\hat{x}$	*x*-position operator
x_0	The equilibrium value of *x*.
x_0	The average value of $\hat{x}$, the equilibrium axial bead position.
$\dot{x}$	*x*-velocity
$\ddot{x}$	*x*-acceleration
α	Either bead polarisability or the averaged value of $\hat{a}$.
α_1 , α_2	The average value of $\hat{a}_1$, $\hat{a}_2$.
γ	Gas Damping Rate
$\Gamma_{\uparrow}$	$\Gamma_{0\to1}$. *i.e.* rate of transition from ground to first excited state.
$\Gamma_{\downarrow}$	$\Gamma_{1\to0}$. *i.e.* rate of transition from first excited state to ground state.
$\Gamma_{a\to b}$	Rate of transition from state a to b.
Γ_{cool}	Cooling rate.
Γ_M	Rate of mechanical damping.
Γ_{osc}	Oscillation decay rate

Γ_{op}	Optical heating or cooling (negative for cooling)
Γ_{opt}	Rate of optical damping.
$\delta(\ )$	Dirac Delta Function
Δ_1	The optical detuning of field 1 = $\omega_{L1} - \omega_{c1}$
Δ_1^x	The adjusted optical detuning of field 1 = $\Delta_1 + \frac{A}{\hbar}\cos k_2 x_0$
Δ_2	The optical detuning of field 2 = $\omega_{L2} - \omega_{c2}$
Δ_2^x	The adjusted optical detuning of field 2 = $\Delta_2 + \frac{A}{\hbar}\cos(k_2 x_0 - \phi)$
ϵ_0	Permittivity of free space = 8.85419×10^{-12} C^2 m^{-3} kg^{-1} s^2.
ϵ_r	Relative Permittivity.
κ	The loss rate of photons from the cavity.
λ	Laser wavelength (virtually always 1064 nm)
$\bar{v}$	The mean gas particle speed
μ_0	Permeability of free space = $4\pi \times 10^{-7}$ m kg s^{-2} A^{-2}
π	The transcendental number, Pi. The ratio of the circumference to the diameter of a circle. Given by $4\sum_0^\infty \frac{(-1)^n}{2n+1}$. Approx: 3.14159…
ρ	Density.
σ_{SB}	Stefan-Boltzmann Constant = 5.670367(1) x 10^{-8} $Wm^{-2}K^{-4}$
τ	Characteristic timescale (often with subscript)
ϕ	Phase difference between the two fields within the cavity.
Φ	Electric potential (voltage).
$\boldsymbol{\Phi}_{ext}$, $\boldsymbol{\Phi}_{int}$	Electric potential (external and internal to the sphere)
ϕ_{bead}	Bead diameter = 2R
χ	Complex number relating two quantities, defined where used.
$\|\psi\rangle$	Wavefunction state vector
ω	Angular Frequency
ω_c	The angular frequency of the unmodified optical cavity.
ω_L	The angular frequency of the driving laser field.

Contents

1 Introduction to Optomechanics

The primary motivation of this research was to determine how it would be possible to test quantum theory in a larger system than it had previously been tested in (at the beginning of the period of research).

Once fully quantum mechanical behaviour has been observed in this system, it could be used as a quantum laboratory to study positional superpositions or decoherence.

The main area of research in this thesis is cavity optomechanics with a trapped dielectric particle. This is in some ways similar to the field of trapped ion physics, which developed earlier and led to the creation of Bose Einstein condensates and fermi-gasses in the 1990s.

In addition to the testing of quantum theory further research in this area could be used to test models of gravitational collapse perhaps leading, ultimately, to a full theory of quantum gravity.

The cooling of optomechanical systems into the quantum regime also allows, potentially, for very sensitive force detection which has a variety of possible applications.

This introductory chapter starts by outlining the earliest developments of Optomechanics, going on to discuss the variety of optomechanical systems and the phenomena that these systems allow us to observe. It includes a discussion of optomechanical cooling, as well as sensitive force detection and some of the most state-of-the-art research in non-levitated cavity Optomechanics, such as Optomechanically Induced Transparency and non-linear optomechanical systems.

1.1 Optical Forces

1.1.1 Optical forces from the Seventeenth Century to 1970.

Radiation pressure of light was first hypothesised by Kepler in 1619 to explain why comet tails deviate from the comet's trajectory,[1] pointing away from the Sun (although the true explanation for this may be as much due to ionised solar wind as to pressure from electro-magnetic radiation). In 1862 Maxwell realised that light carried momentum (with a ratio

of energy to momentum equal to the speed of light).[2] This was a consequence of the four fundamental equations of electromagnetism and was proven experimentally in the early Twentieth Century.[3,4,5,6] In 1909 Einstein was able to invoke the corpuscular nature of light (suggested from his work on the Photoelectric effect)[7] to derive the statistical fluctuations in this light pressure and also to show that it would give rise to frictional forces in some circumstances.[8]

1.1.2 Optical tweezers.

During the 1970s various researchers managed to trap small particles in optical tweezer arrangements.[9,10] By the late 1980s researchers had also managed to trap groups of atoms,[11] and even individual atoms,[12] in optical tweezer arrangements.

There are two approaches to understanding the action of optical tweezers:

1) A "Field" approach: A polarisable particle achieves a lower energy by seeking the high field intensity area.

2) A "Ray" approach: Whenever a refractive particle moves away from the middle of the trapping beam it bends light even further in this direction. The net Newton's third law force on this particle is restorative (however it is generally easier to calculate the magnitude to the force using the first method, due to multiple internal reflections and refractions).

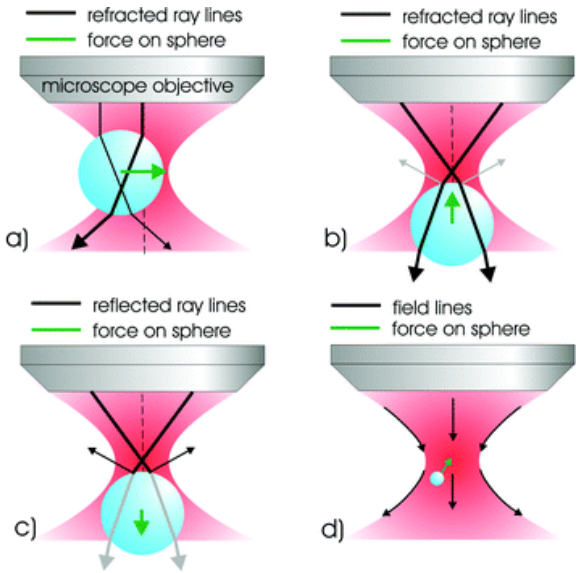

Figure 1.1. Schematic ray diagram explanation for optical tweezer effect.[13]

1.2 Optical Cavities

The behaviour of reflective cavities was well studied in the late Nineteenth Century, especially by Charles Fabry and Alfred Perot.[14] They studied both optical cavities formed by a pair of mirrors, and also etalons formed from a slab of dielectric material. Their work showed that interferometers such as these can be used as wavelength filters, with 100 percent transmittance for slab thicknesses at odd-quarter-multiples of an internal wavelength (*e.g.* a quarter-wave plate).

Cavities can also be used to stabilise and enhance an optical field. This was essential in the development of lasers in the 1960s.[15]

The combination of an optical cavity, or similar optical system, interacting with a mechanical motion comprises the field of cavity optomechanics. As with the original Fabry-Perot Etalon the use of the cavity both enhances the build-up of the internal electromagnetic oscillation and acts as a wavelength filter.

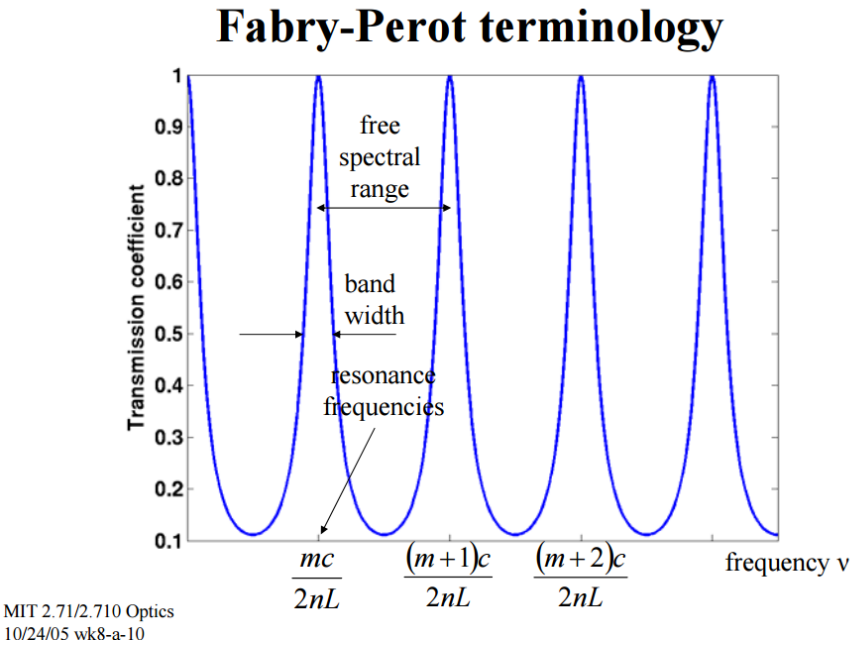

Figure 1.2. Diagram of etalon transmittance as a function of frequency.[16] The transmittance of a cavity is given by: $T = \frac{(1-R)^2}{1-2Rcos\frac{4\pi mL}{\lambda}+R^2}$ where R is the intrinsic reflectance of one end mirror alone, m is the mode of excitation, L is the cavity length and λ is the laser wavelength.

1.3 Optomechanical Systems

There are a wide variety of systems studied in optomechanics. They vary in size over perhaps thirteen orders of magnitude in length (from kilometre scale LIGO down to atomic scale) and perhaps twenty-one orders of magnitude in mass.

The system studied in this thesis will be an optically trapped dielectric sphere suspended in an optical cavity. However, to illustrate the breadth of the field, it will be instructive to look at a few, quite different, optomechanical systems (see Figure 1.3).

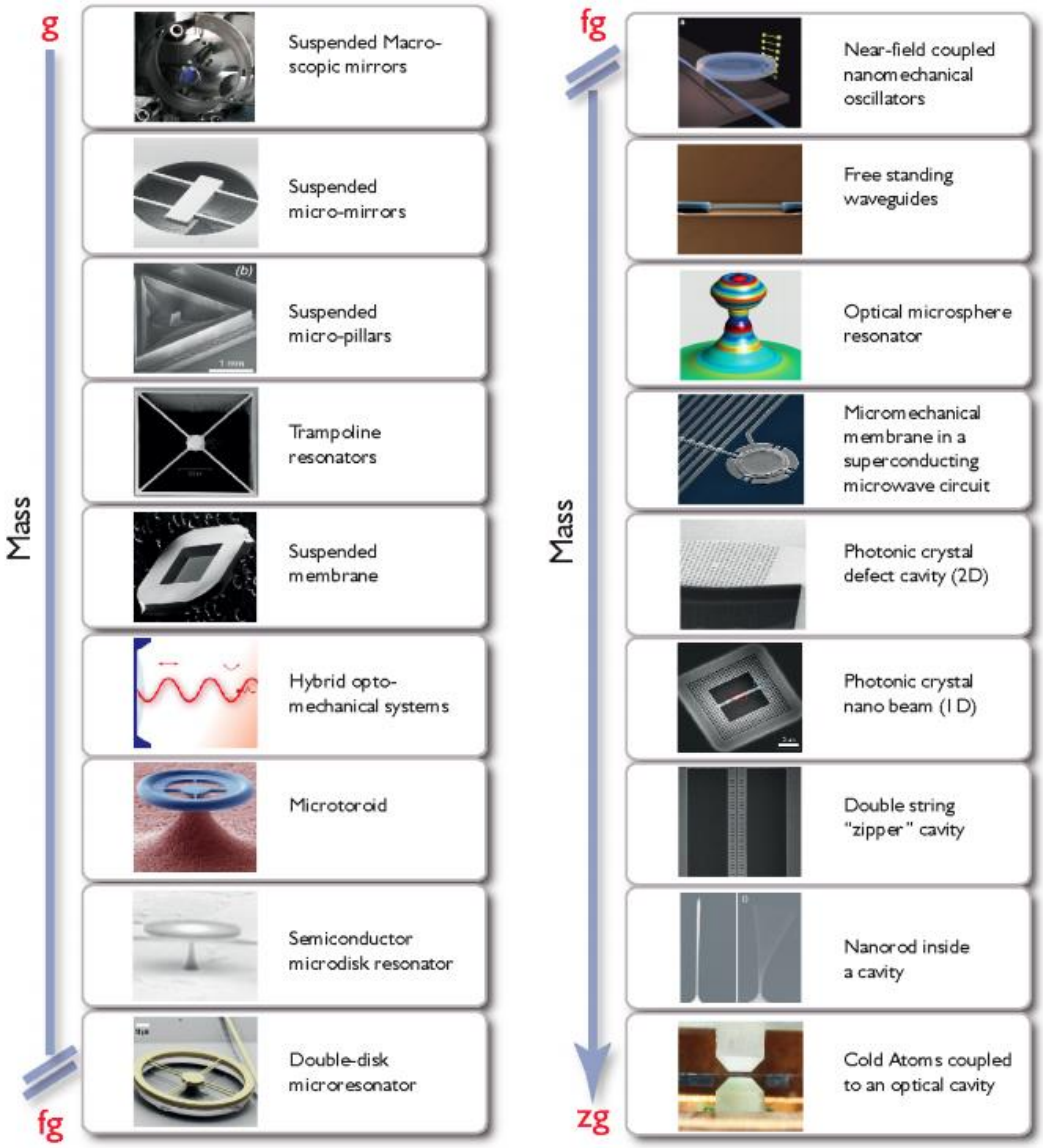

Figure 7 A gallery illustrating the variety of optomechanical devices, arranged according to mass. Pictures courtesy (from top left, down): N. Mavalvala, M. Aspelmeyer, A. Heidmann, D. Bouwmeester, J. Harris, P. Treutlein, T. J. Kippenberg, I. Favero, M. Lipson, T. J. Kippenberg/E. Weig/J. Kotthaus, H. Tang, K. Vahala/T. Carmon, J. Teufel/K. Lehnert, I. Robert, O. Painter, O. Painter, I. Favero/E. Weig/K. Karrai, D. Stamper-Kurn

Figure 1.3. Figure from Aspelmeyer *et al.*[17] showing the variety of commonly studied optomechanical systems, with mechanical oscillators covering twenty-one orders of magnitude in mass.

1.3.1 Micro-toroids (*i.e.* a micron scale torus)

Micro-toroids fabricated in Silica (see Figure 1.4) are high quality-factor oscillators that support optical modes via whispering gallery modes:[18] modes that consists of total internal reflections around the perimeter of the toroid, with resonances for wavelengths that are an integer factor of the circumference). These modes couple to the mechanical vibration; *i.e.* the toroid rings like a cymbal.

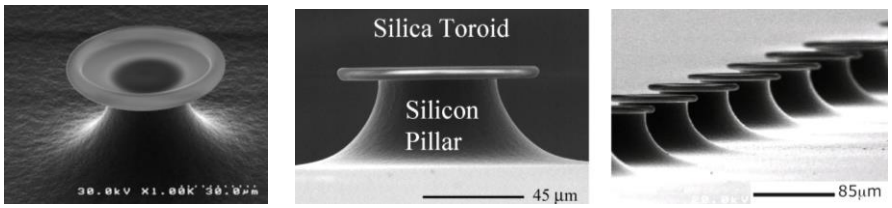

Figure 1.4. SEM images showing Micro-toroidal array,[19] together with their 3D structure and scale.

The direct excitation in the optical mode is often done by an obliquely aligned laser or tapered, tangential, optical fibre,[20] and what can be done for toroids can also be done (with some extra complications) for microspheres.[21]

1.3.2 Laser Interferometer Gravitational Wave Observatory (LIGO)

The largest length scale optomechanical experiment is probably the LIGO.

Figure 1.5. One of the many kilometre long LIGO arms.[22]

The aim of LIGO is to directly observe gravitational waves that have previously only been indirectly detected. For example, it is known from the Nobel prize winning work of Hulse

and Taylor that binary pulsars lose rotational energy in a way that is consistent with the emission of gravitational waves. [23] This is akin to determining that a diesel heater is working by noticing the depletion of the fuel. However, it is natural to want to make the determination more directly. LIGO attempts to directly observe gravitational waves by observing the spatial distortions as a wave passes through our planet.

The operation of LIGO requires a thorough understanding of the interaction between light and the suspended mirrors, the effect of the light on the dynamics of the mirrors, the action of a gravitational distortions on the mirror positions, and the effect that this, in turn, has on the light field, as well as the direct effects of gravitational distortion on the laser beam in each of its polarisations.[24]

In February 2016, gravitational waves emitted from the merging of two black holes, each of around thirty Solar Masses, at a distance from the Sun of 1.5 billion light years, were directly detected by LIGO.[25] This result certainly competes with the discovery of the Higgs' boson as the most impressive experimental physics result since the turn of the Century.

1.3.3 Other Optomechanical Systems

Other mechanical systems include micromechanical cantilevers (*i.e.* Atomic Force Microscope (AFM) cantilevers),[26,27,28,29] nanobeams,[30,31] and a Microwave frequency drum[32] coupled to quantum bits or Rydberg atoms (*i.e.* nearly ionised atoms / atoms with high principle quantum number).[33] There are also membrane systems which behave a little bit like two AFM-type systems sharing the same mechanical oscillator,[34,35] as well as, in principle, hybrid systems of all of all the above.

Instead of optical driving we can use a radio frequency[36] or microwave circuit.[29,37] With a microwave circuit a single electron in a superconducting circuit can be coupled to the microwave resonator via a Josephson Junction.[38] Alternatively, the cavity can be replaced by an atom or an ensemble of atoms,[39,37] as can the suspended particle, which can even be replaced by a virus.[40]

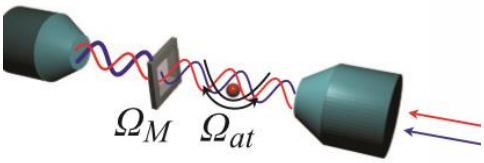

Figure 1.6. A membrane and bead/atom system.[41]

As well as superconducting microwave circuits[29] and ultra-cold atoms[42] we can use Bose-Einstein Condensates (BECs).[43] Indeed, the creation of the first BECs relied on optomechanical methods as it was important to be able to trap atoms[44] and molecules[45] in an optical field, and to cool them using techniques such as Sisyphus cooling and the optical molasses[46] (Doppler cooling with red detuned light) before going on to use evaporation cooling at the final stage.

One system which has received increased prominence since the bulk of this thesis was written is the Fibre Fabry-Perot (FFP) cavity where the ordinary Gaussian (TE00) mode of one cavity is coupled to a different mode (*e.g.* HE11) of another cavity via a metallic filament (or fibre).[47]

1.4 Cooling

In order to use optomechanical systems to test quantum mechanics it is essential to be able to cool these systems into the quantum regime, *i.e.* close to the mechanical ground state. [48] A key goal within the field is to cool oscillators to their ground state and then to verify that they have achieved this energy.[49]

The first verified mechanical damping via an optical force was done by Braginsky *et al.* with an optical cavity one wall of which was a high frequency oscillator, similar to modern Atomic Force Microscope (AFM) Cantilever experiments. [50,51] Damping of Brownian motion of an oscillator (*i.e.* optically cooling an oscillator below the background temperature of the gas with which it is in thermal contact) was done by a number of different groups in various different systems.[52]

Of particular interest is the cooling of mechanical modes to their quantum ground state in mesoscopic systems.[53] Shortly after I embarked on this PhD, several groups around the world achieved this,[54,55] see Figure 1.7 for an indication of this progression.

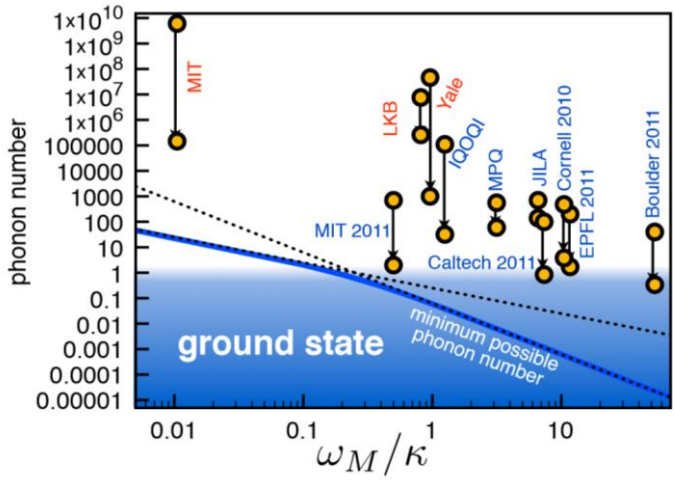

Figure 1.7. Graph showing progression to the quantum ground state.[17]

One difficulty in achieving ground state cooling is isolating the system from the thermal environment (*e.g.* lab, walls of vacuum chamber *etc.*). Much of this thesis will explore the possibility of removing such thermal contact by use of an optically suspended bead, but an alternative has been to use a photonic silicon nano-beam (see Figure 1.8). The quantum ground state has been achieved in this system[53] as well as with a nano-resonator coupled to a microwave optical cavity.[56]

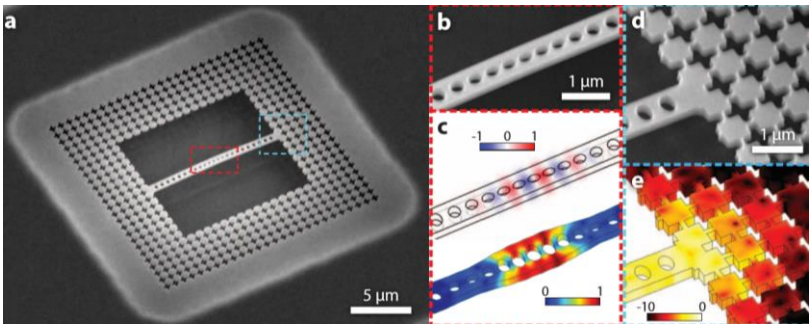

Figure 1.8. Silicon nano-beam structure: One of the first mesoscopic systems to be cooled to the ground state. The detailed substructure of the silicon, as shown, allows the beam to be thermally isolated from its environment by shielding it from vibrational phonons from its background environment (*i.e.* whatever the chip is affixed to). The beam itself is then used in conjunction with a laser cavity and cooled in the same way as an AFM system.[53]

1.5 Qualitative Theoretical Discussion of Cooling via Optical Detuning in the AFM Cantilever System

Perhaps the most well studied optomechanical system, and one of the earliest to be considered, is the cavity with a fixed mirror at one end and a mirror attached to an AFM cantilever at the other end (see Figure 1.9).

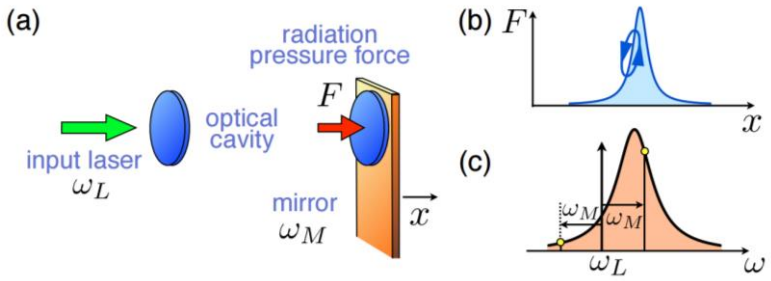

Figure 1.9. Schematic of AFM cantilever system, the archetypal optomechanical system. Image from Marquardt *et al.*[47]

We see that the mirror is pushed out of equilibrium by the radiation pressure of light circulating in the cavity while the movement of the mirror alters the length of the cavity, shifting its resonant frequency.

Both this, and all the systems in section 1.3, have something in common which is that a mechanical motion interacts with an optical degree of freedom (normally via a light pressure force or equivalent) and the position (sometimes velocity) of the mechanical degree of freedom alters the resonant frequency of the optical oscillator (*e.g.* cavity).

Crucially, in most of these systems, the occupancy of the optical excitation is not purely dependent on the positon of the mechanical oscillator but rather on an integral of the position over a period of time (typical characteristic times would be the cavity ring down rate). Alternatively, there might be a direct velocity dependent force (as per ordinary dashpot damping). Without a force that correlates with velocity, cooling of the system is impossible, and so we are unlikely to be able to observe quantum phenomena.

Whether we get heating or cooling depends on the detuning of the driving laser field with respect to the cavity. The wavelength of the driving laser can be either longer or shorter (redder or bluer) than the length of the cavity with cantilever at equilibrium (*i.e.* at the

centre of its oscillation). We find that if the laser is of longer wavelength than the cavity (red detuning) then the energy of oscillation of the cantilever is reduced (the cantilever is cooled) by the laser field. Inversely if the laser is blue detuned we get heating.

If we imagine a cavity with an AFM cantilever at one end (as per Figure 1.9) then there are three ways in which we can qualitatively predict whether this gives rise to cooling or heating of the AFM oscillation: a broadly classical picture, broadly quantum picture and a relativistic picture. See Appendix 9.1 for more details.

These qualitative considerations show us that we get cooling for red detuning and heating for blue detuning. We also find that, for maximal cooling, we need a good match between the detuning, the cavity decay rate and the mechanical frequency of the mechanical oscillation.

1.6 Cavity Sideband Cooling

By the beginning of this decade a number of groups had proposed cavity sideband cooling schemes to take a levitated nano-particle down to its ground state.[57,58,59,39] Passive cavity cooling has been realised but not yet to the ground state.[60,61] In particular Kiesel *et al.*[60] were able use cavity cooling but were unable to reduce pressure bellow the radiometric threshold of around 4 mbar. This meant they got to an excitation temperature of sixty or seventy Kelvin. If they can get past the radiometric threshold and get the pressure down to around 10^{-7} mbar then they believe they can achieve ground state cooling (although their work has not identified the radiometric threshold “as such” as being the major difficulty).

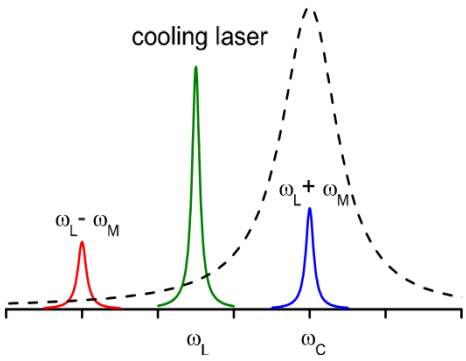

Figure 1.10. Cavity cooling principle: The cooling transmission curve peaks at the laser driving plus one mechanical frequency. This means that the cavity is at its most receptive for anti-stokes cooling whereby the photon energy is upshifted from the incident frequency, thereby cooling the mechanical motion.

This leads to cooling (in the absence of background gas interactions, and for negative detuning) to an equilibrium phonon number of:[62]

$$\bar{n} = -\frac{4(\omega_M + \Delta')^2 + \kappa^2}{16\omega_M \Delta'} \tag{1.1}$$

Whereby the modified detuning, Δ', is given by:

$$\Delta' = \Delta \quad + 2g^2|\alpha|^2 \tag{1.2}$$

And the equilibrium photon number, α, is given by:

$$\alpha = \frac{2iE/\hbar}{2i\Delta' - \kappa} \tag{1.3}$$

And the effective Hamiltonian of the system is:

$$\hat{H}' = \hbar\omega_M \hat{b}^\dagger \hat{b} - \hbar\Delta \hat{a}^\dagger \hat{a} + E\left(\hat{a}^\dagger + \hat{a}\right) + \hbar g \hat{a}^\dagger \hat{a}\left(\hat{b}^\dagger + \hat{b}\right) \tag{1.4}$$

In the case of optimal detuning, $\Delta' = -\omega_M$, we get:

$$\bar{n} = -\frac{\kappa^2}{16\omega_M \Delta'} \leq 1 \tag{1.5}$$

1.7 Motivations and Applications

There are many motivations for cooling an oscillator to its quantum ground state. Three main motivations given by Aspelmeyer *et al.* are: [17]

(a) In order to make fundamental tests of quantum theory into larger mass and length scale systems.

(b) Parametric amplification of small forces, in other words to understand and to detect small oscillatory forces and to understand how to ensure that forces are sufficiently damped so as to be undetectable.

(c) Various applications in quantum information processing.

Some of these applications include making optical atomic clocks, precision measurements of the gravitational field (as discussed in section 1.3.2), various applications in computing such as optomechanical devices coupled to silicon photonics, and simulations of quantum many-body physics problems. [63,64]

There is also a possibility of using this kind of system for very sensitive oscillatory force detection, as well as using an understanding of these systems to determine what kinds of forces are inherently undetectable.

1.7.1 The Lower Limit of Detectable Sound Pressure

There is formula for the minimum detectable force,[65] detectable by either a classical or quantum oscillator of given properties. This is found by noting the level of force which will lead to displacements of less than the thermal noise, and will therefore be virtually undetectable.

We find that the quantum limit on the sensitivity of an oscillating force is given by:

$$F_{min-rms\ (quantum\ limit)} \approx \sqrt{\frac{\hbar k_{sp} b_{signal}}{Q}} = \omega_0 \sqrt{\frac{\hbar m b_{signal}}{Q}} \tag{1.6}$$

where Q is the oscillator Quality Factor, b_{signal} is the signal bandwidth, and k_{sp} is the spring constant of the oscillator. A derivation of this formula is included in Appendix 9.2.

This means that in order to detect low-amplitude vibrational forces one needs to have a high-quality factor oscillator with a low spring constant, with the right frequency and bandwidth to match the signal. This is, therefore, a strict limit on what can be detected.

One application for this would be sound proofing a room such that no one outside the room would be able to detect speech from inside the room, even if they have the most sensitive possible devices to listen with (*i.e.* devices with quantum limited sensitivity).

To determine this, we need to know what the sound wave's pressure amplitude would have to be attenuated to. Clearly, we can see that increasing the size of any receiving microphone would be helpful in detection. Doubling the collecting area would double the force for a given pressure, and while it would also increase the mass of the oscillator (up to doubling it) this would (by equation 1.6) increase the minimum detectable force by less than it would increase the actual force received. Of course, there would be some limit to the amount that a receiving plate could be increased in size, and it would be reasonable to assume that when the receiving area got larger than a square wavelength, it would be no longer helpful to increase its size.

Consequently, we end up with minimum detectable R.M.S. pressure of:

$$P_{min-rms\ (quantum\ limit)} \sim \frac{\omega^2}{c}\sqrt{\frac{\hbar \rho b_{signal}}{Q}} \tag{1.7}$$

Where the usual symbols stand for angular frequency, wave speed, quality factor, signal bandwidth *etc.* and ρ is the minimum area density material out of which a microphone plate could be made.

If we are to make the most absurdly sensitive estimate for a potential microphone we might imagine a plate made of graphene ($\rho = 0.77$ mg m^{-3}), a signal bandwidth and wave frequency of a few hundred Hertz (actually it would be much higher) and the quality factor of the best available oscillators might be 10^9. (Of course, the bandwidth could not be that narrow while having such a large quality factor.)

Given this extreme estimate for sensitivity the smallest detectable oscillating pressure would be of order 10^{-20} Pa. If you can be sure than any listening device is limited by thermal noise at room temperature, then the smallest detectable pressure would be of order 10^{-15} Pa.

The lower limit on human hearing is about 2×10^{-5} Pa, this is about the sound of a mosquito flapping its wings at a distance of a few metres, and it is also the point that is traditionally defined as zero on the volume decibel scale. Normal speech at about a metre's distance is around 60 decibels (an R.M.S. pressure of one thousand times greater than the mosquito, or 2×10^{-2} Pa).

This means that, to be certain that a room has been sound proofed to beyond detectable levels, one needs sound-attenuating material of six times the depth required to reduce speech to inaudible levels. The depth factor of six is reduced to four and a half if one wishes the sound proofing to be only good enough to withstand thermally noisy detectors at room temperature.

To reduce sound from 60 dB to quantum undetectable levels (-300 dB) requires approximately 15 cm of butyl rubber or 10 m of glass, according to attenuation constants given by Kayle and Layby.[66]

Although "six times thicker than required to reduce to inaudible" may be a good guideline, this doesn't take into account attenuation at boundaries of materials, rather than through materials. A thicker slab of material will, generally, still have the same number of interfaces. What one really needs is a structure that gives six times the exponential attenuation constant of the material that is able to reduce sound to inaudible levels. This may mean six times as many layers of sound proofing, rather than one layer of six times the width.

1.8 Phenomena

Finally, it is worth mentioning some phenomena that either occur persistently within the field, or that have attracted particular interest in the community.

1.8.1 Avoided crossings and hybridisation

When two modes of a coupled system (classical or quantum) might naively be expected to have the same or very similar frequencies we often find that these modes hybridise to give one higher and one lower energy/frequency mode. This is familiar in many areas of physics and even theoretical chemistry (for example the hybridisation of atomic orbitals to give bonding and anti-bonding orbitals) and, generally, the closer in energy the original energy

levels are (and the stronger the coupling) the more their energies will shift. The new states can generally be modelled as linear combinations of the states being hybridised. On an energy level diagram these states will often look like they have moved towards each other and then turned away, hence the other name which is often given, an "avoided crossing".

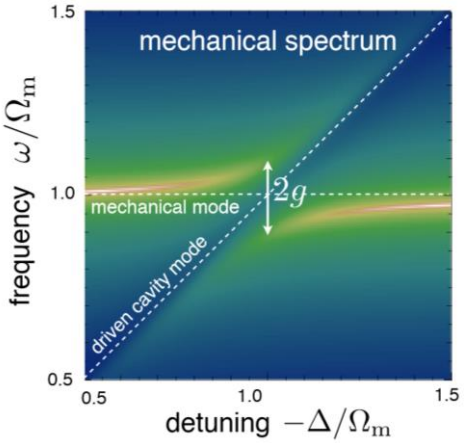

Figure 1.11. Typical mechanical frequency spectrum.[17] When the optical detuning approaches the mechanical frequency we see an avoided crossing between the frequency of the two modes. Rather than having one optical and one mechanical mode at this point we see hybridisation between the two.

Hybridisation between optical and mechanical modes is considered to be of particular interest. This is perhaps because we expect optical modes to be much higher in frequency than mechanical modes. However, often the underlying frequency of the optical mode is not of chief importance but rather it is the detuning between the optical excitation and, for example, the cavity frequency, that is important. This can be much lower in frequency and, as such, has the capacity to be of similar size to a mechanical vibration frequency.

In general, when we have an interaction Hamiltonian, $\widehat{H}_{int}$, which would not affect the energy of the pure mechanical or optical states, ψ_{opt}, ψ_{mech} (*i.e.* $\langle\psi_{opt}|\widehat{H}_{int}|\psi_{opt}\rangle = \langle\psi_{mech}|\widehat{H}_{int}|\psi_{mech}\rangle = 0$), we get energy splitting $g = |\langle\psi_{opt}|\widehat{H}_{int}|\psi_{opt}\rangle|$ so the energies of the hybridised modes are $E_0 \pm g$, where E_0 is the energy of the (degenerate) unhybridised energy levels.

There is also interest in hybrid systems with two different mechanical modes coupled to an optical mode.[67]

1.8.2 Optomechanically Induced Transparency (OMIT).

Optomechanically Induced Transparency (OMIT) is the optomechanical analogue of Electromagnetically Induced Transparency[68] and has attracted much interest recently with one of its earliest proposals receiving over 400 citations.[69]

In Electromagnetically Induced Transparency we have a bulk medium, often an array of non-mutually interacting three-level atomic systems, that become transparent when an external oscillating electric field is applied. In OMIT we have an optomechanical system which becomes transmitting when a secondary laser field is allowed to interact with the mechanical mode.

Weis *et al.* outline a variety of potential applications for this, mostly concerning computer science and the development of optically mutable microchips.[69]

Specifically OMIT occurs where the optical cavity is driven by both a strong and a weak field, often called the "control" and "probe" field, respectively. The strong field maintains trapping at a frequency, ω_M, while the weak field is red detuned by ω_M.

The mechanical sideband of the strong field interferes destructively with the probe field resulting in a window of transparency in the cavity transmission at the frequency of the weaker field (see Figure 1.11 and 1.12).

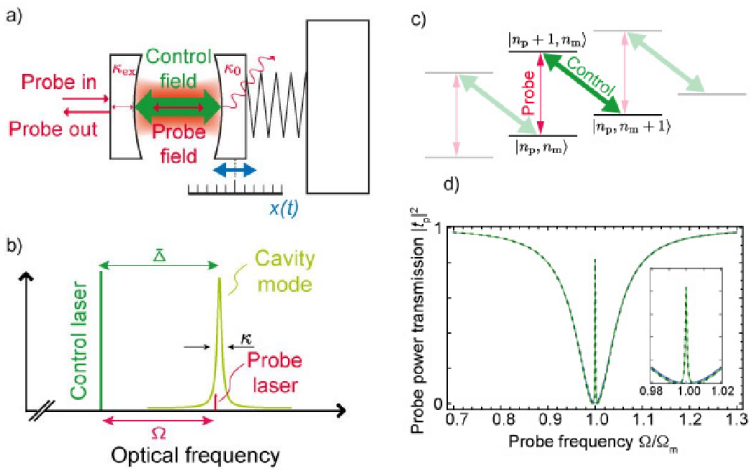

Figure 1.12. Probe field is detuned from cavity resonance by one mechanical frequency. This gives rise to the iconic OMIT signature, a needle sharp increase in transmission in an otherwise broad optical resonance curve.[68]

Since the characteristic width of the window is the mechanical damping of the system, and since the loss rate of the cavity is much greater than the mechanical damping ($\kappa \gg \Gamma_M$) the distinctive phenomenon of OMIT is a very sharp dip in the much broader cavity resonance.

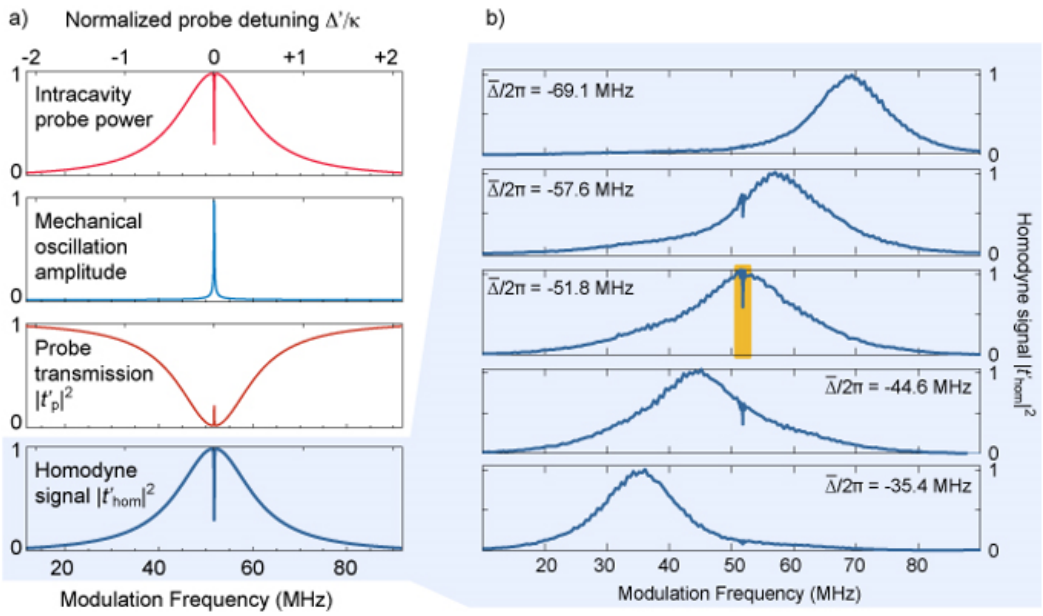

FIG. 3: Observation of OMIT. a) Theoretically expected intracavity probe power $|A^-|^2$, oscillation amplitude X, probe power transmission $|t_p|^2$ and the homodyne signal $|t_{hom}|^2$ as a function of the modulation frequency $\Omega/2\pi$ (top to bottom panels). The first two panels have additionally been normalized to unity. When the two-photon resonance condition is met, the mechanical oscillator is excited $\Delta' = 0$, giving rise to destructive interference of excitation pathways for an intracavity probe field. The probe transmission therefore exhibits an inverted dip, which can be easily identified in the homodyne signal. b) Experimentally observed normalized homodyne traces when the probe frequency is scanned by sweeping the phase modulator frequency Ω for different values of control beam detuning $\bar{\Delta}$. While the center of the response of the bare optical cavity shifts correspondingly, the sharp dip characteristic of OMIT occurs always for $\Delta' = 0$. The power of the control beam sent to the cavity is 0.5 mW in these measurements and the He-3 buffer gas has a pressure of 155 mbar at a temperature of 3.8 K. The middle panel shows the operating conditions where the control beam is tuned to the lower motional sideband $\bar{\Delta} \approx -\Omega_m = -2\pi \cdot 51.8$ MHz. The region around the central dip (orange background) is studied in more detail in a dedicated experimental series (cf. figure 4).

Figure 1.13. Right: Experimental omit curves for various control field frequencies. Left: The archetypical, needle-sharp transparency corresponding to the linewidth of the mechanical oscillator (theoretical).[68]

As the relative strength of the weaker field is increased, OMIT merges into the mode-splitting regime and we see ordinary hybridisation between optical and mechanical modes.

There is a growing interest in non-linear OMIT,[70,71] but so far this has not been detected experimentally.

1.8.3 Non-Linear Optomechanics

Of particular importance is light-matter coupling of the form:

$$(\hat{a} + \hat{a}^\dagger)(G_1\hat{x} + G_2\hat{x}^2) \tag{1.8}$$

Where we can tune the relative size of G_1 and G_2.

While we will often use linearised equations of motion (*i.e.* taking $G_2 = 0$) the existence of a non-linear coupling (especially a tuneable non-linear coupling, where the relative strength of G_1 and G_2 could be under the control of experimenters) would open up new possibilities in quantum mechanics.

In particular, having coupling of the form $(\hat{a} + \hat{a}^\dagger)\hat{x}^2$ is helpful in the realisation of Quantum Non-Demolition measurement (QND)[72] even though neither $\hat{x}^2$ nor $\hat{x}$ actually commutes with the Hamiltonian.

$$[\hat{x}^2, \hat{p}^2] = 2[\hat{x}, \hat{p}](\hat{x}\hat{p} + \hat{p}\hat{x}) = 2i\hbar(\hat{x}\hat{p} + \hat{p}\hat{x}) \tag{1.9}$$

$$[\hat{x}, \hat{p}^2] = 2[\hat{x}, \hat{p}]\hat{p} = 2i\hbar\hat{p} \tag{1.10}$$

QND would allow for preparation of non-classical states and may lead to non-linear OMIT. However, as yet, theoretical interest in non-linear OMIT has not been matched by experimental progress. [68]

Non-linearities can arise in two different ways. One is through a genuinely separate mechanism (such as an optical potential), but this requires strong one-photon coupling. The other possibility is to have couplings of the general form $(\hat{a} + \hat{a}^\dagger)f(\hat{x})$ where the gradient and curvature of $f(\hat{x})$ are independently tuneable.

The earliest non-linear optomechanical systems to be studied were, perhaps, membrane-in-the-middle systems[73] (see Figure 1.13 and also 1.14) and the strength of these nonlinearity effects can be tuned independent of the mechanical frequency, and are not simply due to anharmonics in the optical potential.[74]

These membrane-in-the-middle systems, like the nano-bead system that forms the focus of most of this thesis, see quadratic coupling arise naturally from the induced-dipole forces of the system's interaction with the cavity standing wave.

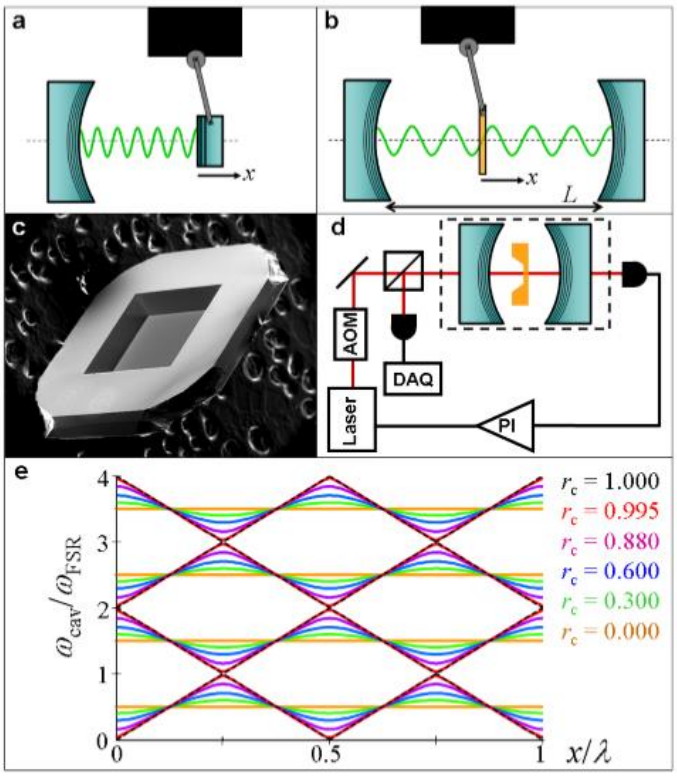

Figure 1.14. (a) Ordinary AFM type optomechanical setup. (b) Membrane-in-the-middle type experiment. (c) Electron microscope image of membrane-in-the-middle chip. This membrane is 1mm square, 50mm thick and made of SiN. (d) Experimental schematic. Vacuum chamber (dotted line) is pumped down to 10^{-9} atmospheres. Electronics includes elements to switch the laser on and off as well as to phase lock the laser to the cavity. (e) Mode hybridisation and avoided crossings in this system. This shows the cavity frequencies as a function of membrane position with the reflectance of the membrane shown by colour.[75]

1.8.4 *x*-Sideband Asymmetry

One of the signatures of low quantum number mechanical excitation is *x*-sideband asymmetry.

Classically, *x*-sideband asymmetry is clearly impossible. If *x* is a mere real number its Fourier transform would be symmetric in the real part, anti-symmetric in the imaginary part, and therefore it would have a symmetric power spectrum. However, the lower sideband corresponds to interaction with the optical field to lose a phonon while the upper sideband shows an interaction to gain a phonon.

As we near the ground state, it becomes impossible for the mechanical oscillator to give up a photon and so the lower sideband becomes repressed.

If we think in terms of mechanical ladder operators, then:

$$\dot{\hat{b}} = \left(-i\omega_M - \frac{\Gamma_M}{2}\right)\hat{b} + \sqrt{\Gamma_M}\hat{b}_{in} \tag{1.11}$$

And taking the Fourier transform we get:

$$\tilde{b}(\omega) = \frac{-\sqrt{\Gamma_M}}{i(\omega-\omega_M)-\frac{\Gamma_M}{2}}\tilde{b}_{in} \tag{1.12}$$

$$\tilde{b}(\omega) + \tilde{b}^{\dagger}(\omega) = \frac{\sqrt{\Gamma_M}}{i(\omega_M-\omega)+\frac{\Gamma_M}{2}}\tilde{b}_{in} + \frac{\sqrt{\Gamma_M}}{i(\omega_M+\omega)+\frac{\Gamma_M}{2}}\tilde{b}_{in}^{\dagger} \tag{1.13}$$

$$\left[\tilde{b}(\omega) + \tilde{b}^{\dagger}(\omega)\right].\left[\tilde{b}(-\omega) + \tilde{b}^{\dagger}(-\omega)\right] = \Gamma_M\left(\frac{\tilde{b}_{in}^{\dagger}\tilde{b}_{in}}{(\omega_M+\omega)^2+\frac{\Gamma_M^2}{4}} + \frac{\tilde{b}_{in}\tilde{b}_{in}^{\dagger}}{(\omega_M-\omega)^2+\frac{\Gamma_M^2}{4}}\right) \tag{1.14}$$

Since $\tilde{b}_{in}\tilde{b}_{in}^{\dagger} \propto (\bar{n}+1)$ while $\tilde{b}_{in}^{\dagger}\tilde{b}_{in} \propto \bar{n}$ we find that the *x* power spectrum is symmetric in the classical regime but starts to become asymmetric as $\bar{n} \longrightarrow 1$ as shown in figure 1.15. Note: $\bar{n}$ is the phononic occupancy of the cooled oscillator.

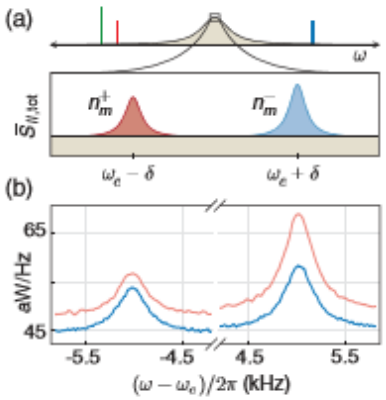

Figure 1.15. Theoretical and experimentally observed sideband asymmetry in a membrane-in-the-middle system.[76] This result was initially controversial, and was challenged by the Kippenberg group,[77] but it now seems to have met with general acceptance. For further sideband observations see Weinstein *et al.*[78]

This obviously cannot be measured by using a camera to plot the position, both because the camera would not be sensitive enough and because it would only ever give a real number trace for the position (in fact these two reasons are linked). However, the spectrum can be directly measured via homodyne detection.[79,53]

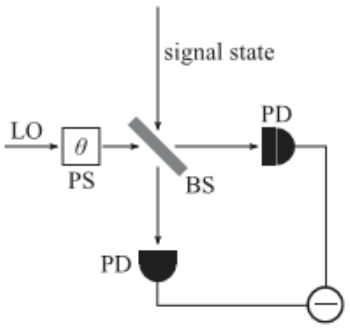

Figure 1.16. Homodyne detection, where the signal output is interfered with the input beam. Diagram from Kawakubo et al.[80] PD = Photodetector, BS = Beam Splitter.

Sideband asymmetry has also been observed in phononically shielded nano-beam structures.[76]

1.8.5 Other Phenomena

These kinds of optomechanical systems can be used to perform experiments with squeezed states (particularly squeezed states of light)[81,82] and entanglement, particularly entanglement of an optical mode with a mechanical mode.[83,84] (See Appendix 1 sections 7.3 and 7.4 for a basic discussion of squeezing and entanglement respectively.)

Another important phenomenon is light transduction: the conversion of optical excitations into mechanical excitations, and visa versa, on a quantum level (*i.e.* on the level of single photons or single phonons). This was realised in 2011,[85] whilst efficient bi-directional conversion between microwave frequencies and optical light was achieved in 2014.[86]

Being able to convert between mechanical, electronic and optical excitations is of particular advantage in information and communication technology because mechanical and electronic methods are generally better for the stable storage of data, whilst optical methods are generally better transmission (the "communications" side of ICT) due to speed of transmission, and the potential for high carrier frequencies.

For the same reasons a future quantum network[87] would benefit from similar processes that operate on a quantum level.[85]

1.9 Chapter Conclusions

While the mechanical interaction of light has been discussed and studied for nearly five centuries the field of optomechanics did not really exist as such until the discovery of optical tweezers in the 1980s. There are a plethora (see Figure 1.3) of optomechanical systems which couple an optical degree of freedom to a mechanical degree of freedom and, in many cases, in such a way that a quantum treatment of the system may be necessary to describe its behaviour in certain circumstances.

The natural question is whether these systems can be used to test quantum theory and, in order to do this, it is normally essential to cool the system into a state where the mechanical degree of freedom has, on average, a small number of quanta of mechanical vibrations. Cooling has been observed in a number of different mechanical systems, including a number of systems involving an optical cavity.

There are a number of ways to understand the cooling, but the essential requirement is to have a force that is not merely position dependent but, perhaps, which depends upon the retarded position of the mechanical system.

Cooling is most effective when there is a strong match between the detuning of the optical excitation and the position of the mechanical sideband of the oscillator to be cooled, in a good cavity.

As well as the prospect of testing fundamental quantum theory cavity optomechanical systems open up technological applications in both sensing and information processing.

There is a wide variety of phenomenological study in the field including: avoided crossings, hybridisation, entanglement, non-linear optomechanics, OMIT and other important optomechanical phenomena.

2 Levitated Systems

This second introductory chapter outlines developments in levitated optomechanics, discusses the motivation for levitated systems and other work that has been done in this field. It discusses the particle loss problem, active and passive cooling schemes and other applications of levitated cooling systems.

2.1 Introduction to Levitated Systems

The previous chapter covered a variety of optomechanical systems, but this thesis is primarily concerned with levitated optomechanical systems, and in particular the system of two laser modes and a single suspended glass bead.

Levitated systems have the particular advantage that they are easier to thermally isolate from their surroundings than systems with a physical support, although the nano-photonic beam system covered section 1.4 did claim to achieve isolation from thermal phonons due to a specially designed geometry.[54]

Before trying to cool the centre of mass motion of a glass bead, Doppler cooling (or the optical molasses technique) had been used to cool both atoms[88] and molecules[89] to ~10^{-6} Kelvin. This has been crucial in the formation of Mott Insulators,[90] Bose-Einstein Condensates,[91,92] and Fermi Gasses (gasses with a pressure deriving almost exclusively from electron degeneracy pressure).[93] Finally, the use of optical potentials has a number of many-body physics applications, especially when optical forces give rise to a lattice potential (see Figure 2.1).

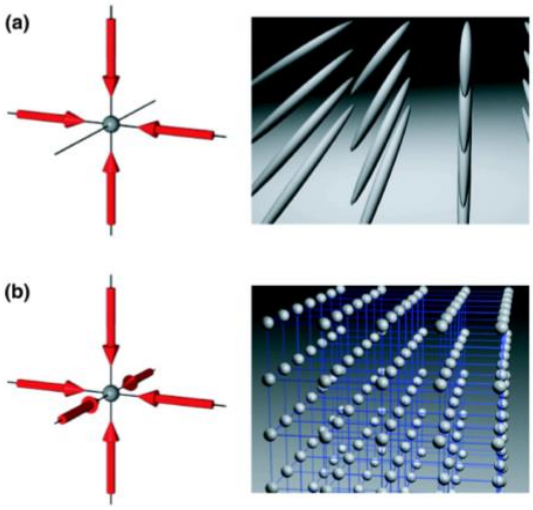

Figure 2.1. Optical lattice potentials with two minima per wavelength (with (a) two-dimensional and (b) three-dimensional trapping). These allow many body interactions between objects trapped at the various local minima.[63]

2.2 Cooling of polarisable particles

While Doppler cooling is useful, not every species has an appropriate electronic transition. Consequently, cavity cooling (which only requires that the atom or molecule has some polarisability) opens up optical cooling to a far wider range of particles.[94] Alternatively, one can think of this as being a cavity resonance with transitions of the energy of the cavity, equivalent to the atomic transitions in Doppler cooling.

Cavity cooling of atoms,[95] ions,[96] and groups of atoms[97] was achieved in the early Twenty-First century. Recent work has seen cooling rates steadily improve; we now see cooling (in three dimentions) from 200 to 10 microkelvin within 100 ms.[98]

Various schemes for cooling mesoscopic, levitated oscillators were proposed in 2009. Barker *et al.* proposed optical trap cooling with gravity assistance (see Figure 2.2),[99] Chang *et al.* put forward a two-cavity scheme with one field trapping, the other cooling,[59] and Romero-Isart *et al.* suggested a vivid scheme involving the trapping of a virus.[39]

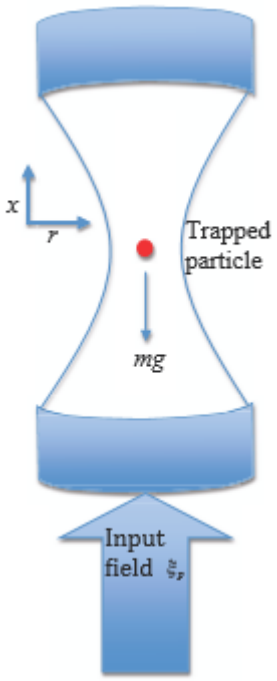

Figure 2.2. Schematic showing a trapping scheme for a single trapped particle (*e.g.* a small glass bead) trapped by an optical field with displacement from the point of maximum field intensity as a result of gravity. Cooling timescales on the order of 10^{-5} seconds are achievable and ground state cooling could be achieved on the order a few seconds, up to a hundred or so seconds, were the vacuum sufficiently strong. [99,100]

Barker's cooling profile (Figure 2.2) shows clearly that, as expected, we get cooling for red detuning (Figure 2.3 showing a typical cooling trace) and heating for blue detuning with (in both cases) an optimal detuning for heating/cooling. This figure also shows that the cooling or heating effect is stronger the more the bead is pulled from the optical potential's minimum. Since gravity is only so strong this is a severe limitation of simply using gravity to displace from the equilibrium of the trapping field.

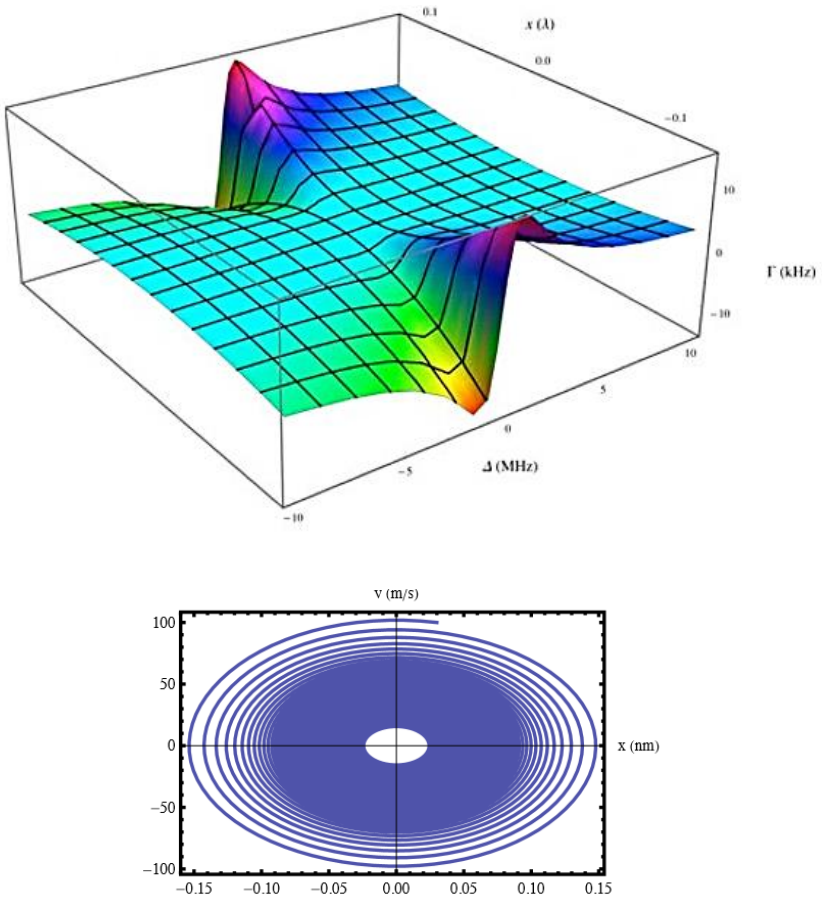

Figure 2.3.

Top: Cooling rate (*Γ*, vertical axis) as a function of detuning frequency (*Δ*, bottom axis) and oscillation amplitude (*x*, top axis). Barker *et al.*[99]

Bottom: Simulation data showing an *x*-phase-space trace for the gravity setup.[99] Position on the vertical axis and velocity on the horizontal axis. We can see that initial damping is very good with significant energy loss over even one cycle.

The gravity set-up is, however, severely limited by the strength of Earth's gravity and is, therefore, an ineffective apparatus with which to attempt ground state cooling which needs to be achieved over significantly less than a minute if it is to be achieved at all.

The Chang *et al.* set-up is very similar to that studied in the bulk of this thesis and has two laser modes: One (strong) trapping field and another (weaker) cooling field, offset by a quarter of a wavelength (see Figure 2.4).

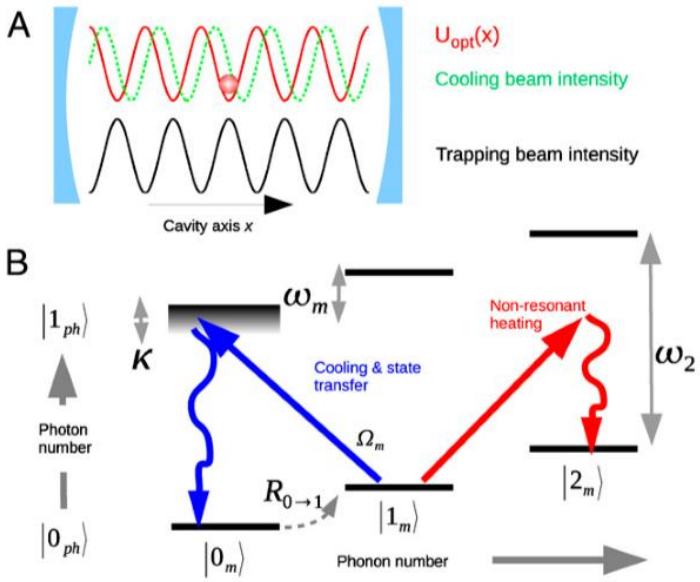

Figure 2.4. Chang scheme, with a cooling and trapping lasers. By using red detuned light for the cooling beam, the shift to lower phonon numbers is on resonance. In these cavity schemes the energy levels that, in Doppler cooling, are given by internal electronic or magnetic excitations of atomic species, are now given by the cavity photon number and mechanical phonon number combination.[57]

Meanwhile Singh *et al.*[100] suggested simply replacing the AFM cantilever from the traditional cavity-AFM set up, with an optically supported mirror (see Figure 2.5).

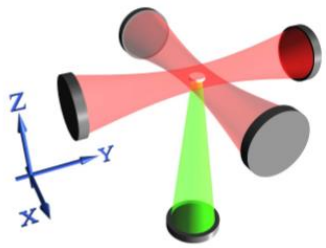

Figure 2.5. The red beams in this profile are elliptical in profile in order to provide stronger trapping. This would be a rather difficult experiment to perform but it is closest to the traditional AFM with cavity set-up that levitated systems reach.[101]

All these schemes require high vacuum conditions, and the presence of background gas is the primary source of reduction in oscillatory quality factor and decoherence. In general, with these systems gas in the chamber is the main barrier to observing quantum phenomena.

2.3 Particle Loss

During the early part of this decade, several groups attempted to cool levitated beads of between a hundred and a thousand nano-metres diameter. Cooling itself has been very effective and well-demonstrated since at least 2013. [59](See Figure 2.6 for picture of typical bead/cavity set up.)

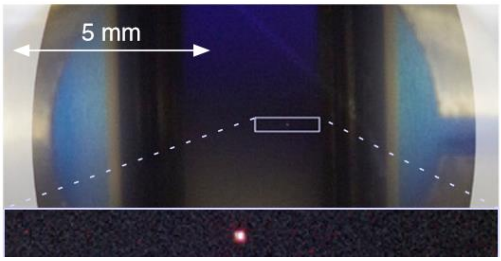

Figure 2.6. The first levitated bead system in which cooling was demonstrated.[59]

However, it was not possible to reach the quantum regimes because of strong gas interaction in the 1 mbar pressure region. Generally, there has been a difficulty in keeping the bead trapped once the gas pressure falls to a few millibars.[110,102] Nonetheless it has been shown many times that cooling occurs and that stronger laser powers can lead to strong cooling (see Figure 2.7).

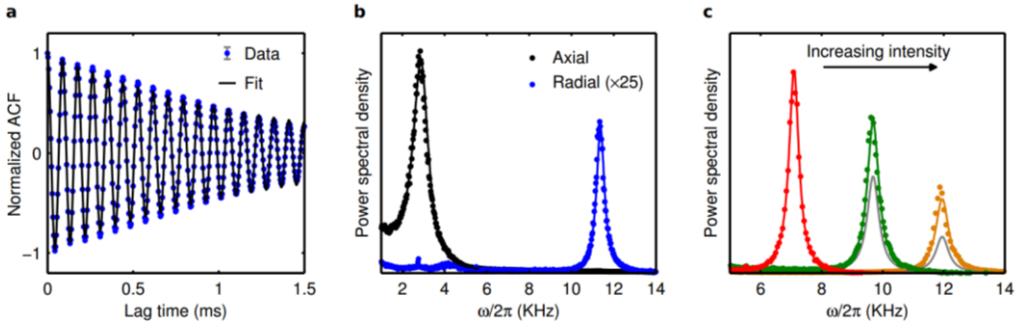

Figure 2.7. Left: Position trace showing optical cooling over time (technically the radial autocorrelation function which strips out the effect of further stochastic heating). Middle: Power spectrum for Axial and Radial trapping in steady state. Right: As laser power is increased the peak position increases and the area of the spectrum decreases. This corresponds to increasing trapping and increased cooling respectively.[115]

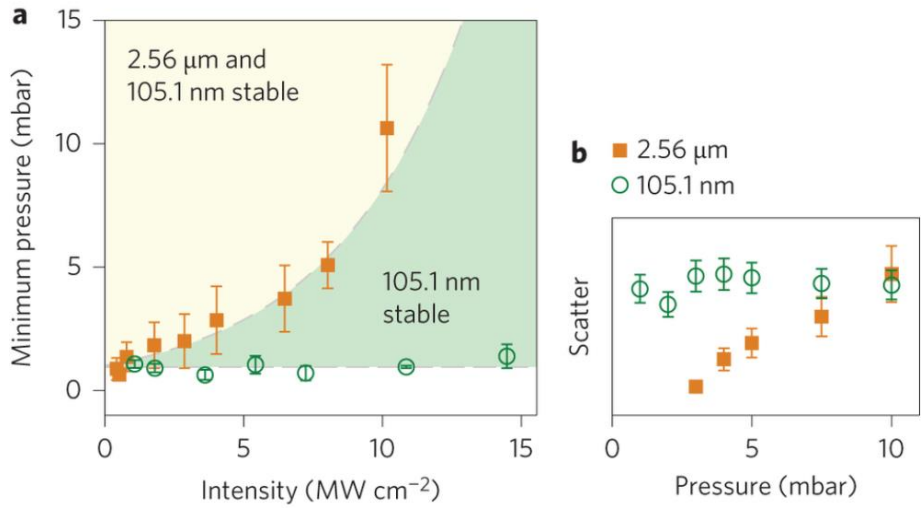

Figure 2.8. Graph Showing minimum achievable pressure as a function of trapping laser intensity for two sizes of bead.[115] Beads are lost (either melting or simply falling out) from the cavity, below the pressure shown, for a given laser intensity.

It is worth taking a moment to explain the trends in Figure 2.8. The rate of laser heating of a mostly transparent bead is proportional to its volume (not area, as would be the case with an opaque bead), while the rate of loss of heat from the bead is proportional to the product of its area and the background gas pressure (so long as the background gas remains the dominant source of surface cooling for the bead). This being the case the overall temperature of the bead increases in line with the product of bead diameter, laser intensity and the inverse of gas pressure. This means that larger beads (including the larger beads form Figure 2.8) eventually melt but smaller beads will not melt as easily.

For low laser intensities, and large beads (orange points), the minimum attainable pressure is proportional to laser intensity. At higher laser intensities the linear relationship breaks down but the general positive relationship remains.

The smaller beads are lost from the cavity as a result of radiometric forces, rather than melting. These are larger for larger temperature gradients within the bead. Increased laser intensity does increase the temperature differences within the bead, but it also increases the size of the overall trapping potential (in both cases it is reasonable to assume a linear relationship with laser intensity). As a result, the radiometric forces (which grow as the pressure drops until the point that there is a good match between bead diameter and mean free gas path, whereupon they start to fall again) dislodge the bead at a pressure which is independent of laser intensity. I would expect that, were it possible to keep the bead trapped (perhaps actively) as the pressure is dropped a further order of magnitude, then

the bead may become trappable once again. However, for this to work, it must also be the case that the bead will not melt, even in the absence of gas cooling, *i.e.* thermal radiation cooling must be sufficient to maintain the bead's temperature at less than its melting point.

Because of radiometric forces we have not seen passive cooling of levitated beads in this regime, only active cooling via an ion trap or similar.[103]

The cooling of un-trapped particles, transitioning through the cavity, has also been demonstrated at very high vacuum, but the limited transition time means that this does not provide a good quantum laboratory. [104]

2.4 Active vs. Passive Cooling

2.4.1 Feedback Cooling

If we can measure the instantaneous velocity of an optically trapped particle we can cool its motion by applying a force which is negatively correlated to the particle's centre of mass motion. For example:

$$\boldsymbol{F}_{cool} = -m\Gamma_{cool}\frac{d\boldsymbol{x}}{dt} \tag{2.1}$$

With this linear feedback cooling the Langevin equation of motion is:

$$\left(\frac{d^2}{dt^2} + \left(\gamma_{gas} + \Gamma_{cool}\right)\frac{d}{dt} + \boldsymbol{\Omega}^2.\right)\boldsymbol{x} = \boldsymbol{\zeta}(t)\sqrt{\frac{2k_B T\gamma_{gas}}{m}} \tag{2.2}$$

Where $\boldsymbol{\Omega}^2 = \begin{pmatrix} \omega_x^2 \\ \omega_y^2 \\ \omega_z^2 \end{pmatrix}$ and $\boldsymbol{\zeta}(t)$ is a stochastic term with the following properties:

$$\zeta_i(t_1)\zeta_i(t_2) = \delta(t_1 - t_2)$$

(no summation convention)

The fact that γ_{gas} appears as both a cooling and a driving term in equation 2.2 is due to the fluctuation dissipation theorem. Effectively γ_{gas} drives an exponential approach of the Bead's centre-of-mass temperature toward the temperature of the gas, however the optical cooling will counteract this leading to a cooled temperature, T_{cool}, of:

$$T_{cool} = \frac{T_{cool}\,\gamma_{gas}}{\gamma_{gas} + \Gamma_{cool}} \tag{2.3}$$

Meanwhile the *x*-power spectrum, S_{xx}, is given by:[114]

$$S_{xx}(\omega) = \frac{2k_B T_{cool}}{m} \frac{\gamma_{gas} + \Gamma_{cool}}{\left(\omega_M^2 - \omega^2\right)^2 + \left(\gamma_{gas} + \Gamma_{cool}\right)^2 \omega^2} \tag{2.4}$$

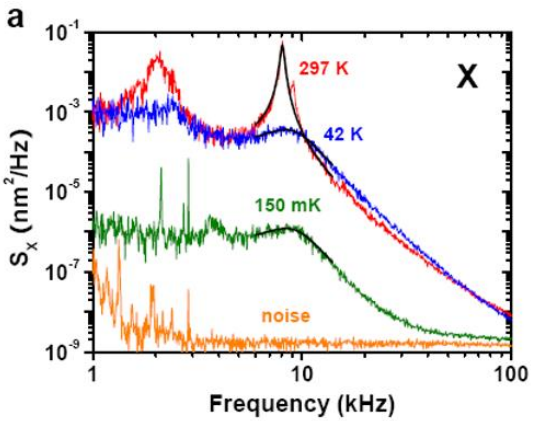

Figure 2.9. Power spectrum for a trapped 3 micron glass sphere along x axis as it is cooled. Red is the intrinsic spectrum with no cooling, the blue curve is with feedback cooling. Both curves are at 637 Pa of pressure (0.06 Bar). The green curve is at a much lower pressure of 5.2 mPa while the orange curve shows the noise spectrum of the cavity in the absence of any trapped bead. This corresponds to around 3.4 million phonons.[105]

Li *et al.* have been able to reduce the energy of a trapped particle to around 3400 phonons in some cases.[105] However, because of the difficulties of cavity cooling and particle loss, early progress did not involve passive cavity cooling but rather active (feedback) cooling obtaining sub-Kelvin[105] and milli-Kelvin[106] temperatures.

A particular example of feedback cooling is the low temperatures achieved by Frimmer *et al*.[107] This set up also involved two coherently coupled modes, although it has not, at the current time, been used to reach the ground state.

2.4.2 Cavity Sideband Cooling

However, feedback cooling is unlikely to take a quantum laboratory usefully to the ground state, as is relies on detailed observation of the particle, which may become increasingly difficult at low energies and, in any case, is likely to cause a disturbance in its state. [127]

Feedback cooling should therefore be thought of as a mechanism for pre-cooling and, in particular, getting past the radiometric threshold, but only passive cooling techniques (such as sideband-resolved cavity cooling) indisputably offer the final energy withdrawal that can take a system like this to the quantum ground state. [127] Section 1.6 gave more detail on cavity sideband cooling.

While most of the work discussed in this Thesis involves just one spatial dimension of analysis, work by Bhattcharya, Vamivkas and Barker[108] suggests cooling in all three Cartesian directions, which serves to reduce the importance of any coupling between oscillation modes.

2.5 UCL Hybrid Trap

In 2015, Millen *et al.* overcame the mbar threshold using a Paul Trap inside an optical cavity.[102] This allowed for trapping and cooling for up to 0.3 seconds in high vacuum and there have been further substantial improvements in both cavity finesse and light-matter coupling since then.

A key result is that the particle displacement is now able to strongly modulate the cavity frequency, *i.e.* we can detect the bead's oscillation spectrum via the output laser field, rather than direct imaging, and it has been possible, combining with a heterodyne detection scheme, to decompose the optical coupling into a linear and a non-linear part.

Furthermore, the strength of the nonlinearity effect is independent of the mechanical frequency and is not simply due to anharmonicities in the optical potential, allowing for thorough investigation of non-linear dynamics.[109]

For stationary state coupling, the nonlinear coupling is overpowered by the linear coupling.[110]

The ~30Hz cooling of Millen *et al.*[102] was enhanced to ~2 kHz allowing for permanent trapping at a cold temperature in the hybrid trap by Froncesca *et al.*.[111] This corresponds to a cooling of just a few hundred phonons, well into the sub-milli-Kelvin range.

2.6 Motivation for cooling of levitated polarisable particles in UHV.

At the ultra-low pressures of modern vacuum chambers (*e.g.* 10^{-9} mbar) oscillators cooled to near the quantum limit would allow for previously unprecedented tests of quantum theory at large scale. For example, it allows the possibility of massive superposition states, which, in turn, allow for the testing of proposed mechanisms of wavefunction collapse and decoherence of those states. One example of these is the Penrose theory of gravitational decoherence, which states that a superposition, or entangled state, will lose its entanglement over a timescale of order, $\tau_{penrose}$:[112,113]

$$\tau_{penrose} = \frac{\hbar}{E_G} \tag{2.5}$$

Where E_G is the gravitational self-energy of the difference between the mass distribution of the two entangled states.

This would mean that a superposition of distinct position states for a proton might persist for 10^{16} seconds before decohering due to gravitational interaction, while a superposition state of a 100 nm bead would definitely not last for more than a day (still a long for such a macroscopic state to persist, although obviously external buffeting – *i.e.* observations, will reduce this time in both instances).

The Penrose model of gravitational collapse is innately attractive because it provides an answer to the measurement paradox in quantum mechanics.[111, 114, 115]

There are, however, alternative models of decoherence, such as the continuous spontaneous localisation model of Stephen Adler, which predicts a Brownian type heating as a result of quantum fluctuations[116] as well as other models of wavefunction collapse derived from the incompleteness of Quantum Theory.[117,102 ,118]

Optomechanical systems may soon be able to determine which, if either, of these two models is correct.[119] For example, the Adler model predicts an extra diffusion constant, for a large trapped glass bead proportional to one over the bead radius to the power 4 or to the power 6.[118] The Penrose model, on the other hand, because the decoherence rate is proportional to the gravitational self-energy, suggests a diffusion constant proportional to the inverse square of R (see equations 1.7 to 1.9 – R is the radius of the bead while r_c

is a parameter which emerges from the Adler model, *m* is the mass of the bead and ω is the angular frequency of trapping).

$$D_{Adler}(R \ll r_c) \propto \frac{\hbar m}{\omega R^6} \tag{2.6}$$

$$D_{Adler}(R \gg r_c) \propto \frac{\hbar m}{\omega R^4} \tag{2.7}$$

$$D_{Penrose} \propto \frac{\hbar m}{\omega R^2} \tag{2.8}$$

These are not the only two models attempting to answer the measurement problem with reference to a new mechanism of decoherence and, indeed, Penrose's hypothesis is not the only proposal to suggest that gravity has an important role to play in this.[120]

To test any of these models more massive (*i.e.* mesoscopic) quantum laboratories are self-evidently essential.

Our suggestions for how to cool levitated particles, have been the subject of theoretical papers published as part of this PhD programme.[121,122] These papers are explored further in Chapters 3, 4 and 5.

There have also been various experimental papers cooling levitated systems, both active and passive. Li *et al.* used laser-cooled micro-gyroscopes,[123] while others have used more traditional cavity / levitated bead apparatus. [124,125,59]

2.7 Sensing of weak forces

The use of hybrid traps (because of the isolation from the environment) has presented opportunities to perform more sensitive force measurements, approaching the force limit of equation 1.6 better than ever before.[126,127] Such hugely increased force sensitivity may allow for measurement of the very weak Casimir force.[128]

The Casimir pressure on two conductors a small distance l apart is (see estimate of Casimir Force and derivation Appendix 7.5):

$$P_{cas} = \frac{-\pi^2 \hbar c}{240 l^4} \tag{2.1}$$

More recently Nie *et al.*[129] have proposed a scheme for using the Casimir interaction to generate optomechanical entanglement between two cavity suspended nano-spheres.

2.8 Chapter Conclusions

There are two main levitated optomechanical systems. The first is the levitated atom which has particular quantum transitions which are used to aid in its manipulation. These systems have been used to produce BECs, slowing light, Sisyphus cooling and a number of other experiments very famous even beyond the scientific community. The second is the levitated dielectric particle in an optical cavity, which forms the basis of study for the next three chapters.

Levitated systems have the particular advantage that, at low air pressure, they are highly thermally isolated from the surrounding system. This means it may be possible to cool them to a quantum ground state of their oscillatory degree of freedom and also means that de-coherence due to thermal noise is reduced.

There is an observed problem that, as pressure drops, some particles are lost and I believe this is due to radiometric forces of the kind I go on to outline in section 4.2.2.

Amongst levitated systems which set out to cool an excitation both actively cooled and passively cooled systems exist, although it is doubtful whether purely active cooling can be used to study quantum behaviour, since it relies on constant observation of the particle under consideration.

These systems also have potential technological application. As well as the applications which are common to almost all quantum systems hybrid levitated systems have the potential to give us increased sensitivity in the measurement of small forces.

3 Cavity System with Two Laser Fields and one Dielectric Bead.

This chapter mainly outlines work from our 2012 paper "Optomechanical cooling of levitated spheres with doubly-resonant fields" by G A T Pender, P F Barker, Florian Marquardt, James Millen, and T S Monteiro. This showed an order of magnitude improvement on the cooling scheme of Derek Chang et al.'s laser trapping-laser cooling scheme.[59] *This was achieved by abandoning the idea of one cooling field and one trapping field and allowing both fields to do both roles. The dynamics of this new paradigm are examined and calculations made showing the cooling in certain special cases and showing that ground state cooling may be practicable in a very good vacuum.*

3.1 Introduction

3.1.1 The System

The main system studied in this PhD thesis is a doubly-driven optical cavity. This system consists of two mirrors with very high reflectance (99% or more) facing each other to form an optical cavity of perhaps a centimetre or more in length, L. The laser being used would typically be the Neodymium-doped Yttrium Garnet laser (Nd : $Y_3Al_5O_{12}$) normally known as an Nd : YAG laser. This is a 1064 nm laser in which narrowband tuning is possible over a range of around 4 nm. A CO_2 laser can probably achieve the same frequency.

Within this cavity it is possible to suspend a glass bead (a transparent glass sphere) of radius 10-100 nm.

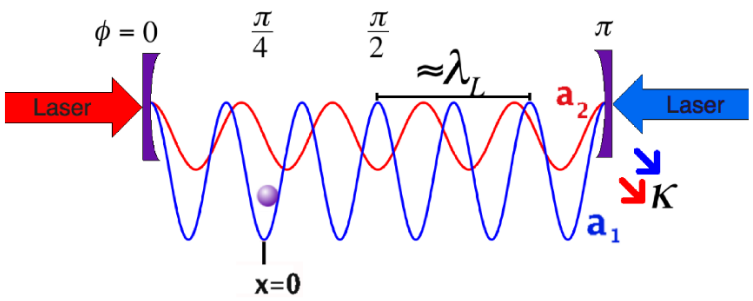

Figure 3.1. Schematic set-up: A levitated nano-sphere is suspended in an optical cavity by two optical modes. We will later show that this system behaves as a damped harmonic oscillator

3.1.2 Building up the Hamiltonian – The empty, driven Cavity

The Hamiltonian for a closed cavity is given by:

$$\hat{H} = \hbar\hat{a}^{\dagger}\hat{a} \tag{3.1}$$

In other words, the energy of the system is just given by the energy of the photons in the cavity.

An open cavity driven by a laser is initially best thought of as being a closed, two-cavity system, with coupling between the two cavities *i.e.* the cavity of the driving laser and the cavity of interest. Our basis for forming the Hamiltonian will therefore be the eigenstates $\hat{b}^{\dagger}$ / $\hat{b}$ and $\hat{a}^{\dagger}$ / $\hat{a}$. These are, respectively, the creation / annihilation operators for the laser cavity and the cavity of interest, hereafter simply called the cavity. The ladder operators for the system as a whole are then superpositions of these operators, making the new Hamiltonian:

$$\hat{H} = \left(A\hat{a}^{\dagger} + B\hat{b}^{\dagger}\right)\left(A^{*}\hat{a} + B^{*}\hat{b}\right) \tag{3.2}$$

Assuming that the laser is only weakly coupled to the system (*i.e.* the decay rate of the cavity is much lower than the frequency of the laser, $\frac{\kappa}{\omega_c} \ll 1$) then the eigenstates of the system would approach the separate states.

So as $\frac{\kappa}{\omega_c} \to 0$, $|A|^2 \to \hbar\omega_c$ and $|B|^2 \to 0$.

Discarding the smallest term (quadratic in B), we get:

$$\hat{H}_{TOT} = |A|^2\hat{a}^{\dagger}\hat{a} + AB^{*}\hat{a}^{\dagger}\hat{b} + A^{*}B\hat{b}^{\dagger}\hat{a} \tag{3.3}$$

It is reasonable to assume that the driving capacity is a purely classical oscillatory force, and so we can replace $\hat{b}$ with a phased oscillation, a simple number. The value of $|A|^2$ is equal to the energy per photon in the cavity and we can assume without loss of generality that *AB** (which we will now call *E*) is real and positive. So equation 3.3 becomes:

$$\hat{H} = \hbar\omega_c\hat{a}^{\dagger}\hat{a} + Ee^{-i\omega_L t}\hat{a}^{\dagger} + Ee^{i\omega_L t}\hat{a} \tag{3.4}$$

3.1.3 The Value of *E*

To complete the construction of the Hamiltonian for an empty cavity we must find the value of E in terms of physical parameters. This will clearly be linked, in some way, to system parameters such as the power of the laser and the cavity rate of decay.

One way to do this is to carry out a transformation of the Hamiltonian to remove the explicit time-dependence.

The fifth postulate of quantum mechanics gives the relationship between the Hamiltonian and the time derivative operator when applied to the system wavefunction:

$$\hat{H}|\psi\rangle - i\hbar\frac{d}{dt}|\psi\rangle = 0 \tag{3.5}$$

We are now going to pre-multiply equation 3.5 by a prefactor at the frequency of the driving laser field, $e^{i\omega_L\hat{a}^\dagger\hat{a}t}$, and substitute in the expression for $\hat{H}$ from equation 3.4.

$$e^{i\omega_L\hat{a}^\dagger\hat{a}t}\left(\hbar\omega_c\hat{a}^\dagger\hat{a} + Ee^{-i\omega_L t}\hat{a}^\dagger + Ee^{i\omega_L t}\hat{a} - i\hbar\frac{d}{dt}\right)|\psi\rangle = 0 \tag{3.6}$$

It is worth taking a moment to consider the important commutation relations. Equation 3.7 comes from the definition of ladder operators while equations 3.8 to 3.17 follow logically from 3.7 and from the knowledge that any function can be written as a Taylor expansion:

$$[\hat{a}^\dagger\hat{a}] = 1 \tag{3.7}$$

$$\hat{a}(\hat{a}^\dagger\hat{a}) = (\hat{a}^\dagger\hat{a} + 1)\hat{a} \tag{3.8}$$

$$\hat{a}^\dagger(\hat{a}^\dagger\hat{a}) = (\hat{a}^\dagger\hat{a} - 1)\hat{a}^\dagger \tag{3.9}$$

$$\hat{a}(\hat{a}^\dagger\hat{a})^n = (\hat{a}^\dagger\hat{a} + 1)^n\hat{a} \tag{3.10}$$

$$\hat{a}^\dagger(\hat{a}^\dagger\hat{a})^n = (\hat{a}^\dagger\hat{a} - 1)^n\hat{a}^\dagger \tag{3.11}$$

$$(\hat{a}^\dagger\hat{a})^n\hat{a} = \hat{a}(\hat{a}^\dagger\hat{a} - 1)^n \tag{3.12}$$

$$(\hat{a}^\dagger\hat{a})^n\hat{a}^\dagger = \hat{a}^\dagger(\hat{a}^\dagger\hat{a} + 1)^n \tag{3.13}$$

$$\Big(f(\hat{a}^\dagger\hat{a})\Big)\hat{a} = \hat{a}\Big(f(\hat{a}^\dagger\hat{a} - 1)\Big) \tag{3.14}$$

$$\left(f(\hat{a}^\dagger\hat{a})\right)\hat{a}^\dagger = \hat{a}^\dagger\left(f(\hat{a}^\dagger\hat{a}+1)\right) \tag{3.15}$$

$$\hat{a}\left(f(\hat{a}^\dagger\hat{a})\right) = \left(f(\hat{a}^\dagger\hat{a}+1)\right)\hat{a} \tag{3.16}$$

$$\hat{a}^\dagger\left(f(\hat{a}^\dagger\hat{a})\right) = \left(f(\hat{a}^\dagger\hat{a}-1)\right)\hat{a}^\dagger \tag{3.17}$$

Equation 3.6 thus becomes:

$$\left(\hbar(\omega_c-\omega_L)\hat{a}^\dagger\hat{a} + E\hat{a}^\dagger + E\hat{a} - i\hbar\frac{d}{dt}\right)e^{i\omega_L\hat{a}^\dagger\hat{a}t}\left|\psi\right\rangle = 0 \tag{3.18}$$

The rotating exponential outside the bracket can be thought of as simply modifying the basic states of the wavefunction. In this way the entire time dependence can be buried in the wavefunction, leaving an effective Hamiltonian, $\widehat{H}'$.

$$\widehat{H}' = \hbar(\omega_c-\omega_L)\hat{a}^\dagger\hat{a} + E(\hat{a}^\dagger+\hat{a}) \tag{3.19}$$

Ehrenfest's theorem relates the time evolution of the expectation value of an observable to the commutator of that observable's operator with the Hamiltonian as follows:

$$\frac{d}{dt}\langle\hat{O}\rangle = \frac{i}{\hbar}\langle[\widehat{H},\hat{O}]\rangle + \langle\frac{\delta\hat{O}}{\delta t}\rangle \tag{3.20}$$

Applying equation 3.20 to $\hat{a}$, $\hat{a}^\dagger$, and $\hat{a}^\dagger\hat{a}$ will not quite give us the full-time evolution of these observables because Hamiltonian 3.19, derived from Hamiltonian 3.4, includes nothing about the rate of decay of the cavity. These terms have to be added in by hand (as is typical across all of optomechanics) and are shown in the following equations in blue:

$$\frac{d}{dt}\langle\hat{a}\rangle = -i(\omega_c-\omega_L)\langle\hat{a}\rangle - \frac{iE}{\hbar} - \frac{\kappa}{2}\langle\hat{a}\rangle \tag{3.21}$$

$$\frac{d}{dt}\langle\hat{a}^\dagger\rangle = i(\omega_c-\omega_L)\langle\hat{a}\rangle + \frac{iE}{\hbar} - \frac{\kappa}{2}\langle\hat{a}^\dagger\rangle \tag{3.22}$$

$$\frac{d}{dt}\langle\hat{a}^\dagger\hat{a}\rangle = \frac{i}{\hbar}(\langle\hat{a}\rangle - \langle\hat{a}^\dagger\rangle) - \kappa\langle\hat{a}^\dagger\hat{a}\rangle \tag{3.23}$$

In the steady state we therefore find that in the classical limit:

$$\langle \hat{a} \rangle = \frac{E/\hbar}{\left((\omega_c - \omega_L) + i\frac{\kappa}{2}\right)} \tag{3.24}$$

$$\langle \hat{a}^\dagger \rangle = \frac{E/\hbar}{\left((\omega_c - \omega_L) - i\frac{\kappa}{2}\right)} \tag{3.25}$$

$$\langle \hat{a}^\dagger \hat{a} \rangle = \frac{E^2/\hbar^2}{(\omega_c - \omega_L)^2 + \frac{\kappa^2}{4}} \tag{3.26}$$

Logically we know that, when driven on resonance, the mean occupancy of the cavity, $\langle \hat{a}^\dagger \hat{a} \rangle$, is given by $\frac{P_L}{\hbar \omega_c \kappa}$.

This means that:

$$E = \sqrt{\frac{\hbar P_L \kappa}{4\omega_c}} \tag{3.27}$$

Meaning the overall Hamiltonian for an empty cavity is:

$$\widehat{H} = \hbar\omega_c \hat{a}^\dagger \hat{a} + \sqrt{\frac{\hbar P_L \kappa}{4\omega_c}} \left(e^{-i\omega_L t}\hat{a}^\dagger + e^{i\omega_L t}\hat{a}\right) \tag{3.28}$$

3.1.4 Adding a bead into the Hamiltonian

The one-dimensional Hamiltonian of a cavity with a bead (with centre of mass position $\hat{x}$, along the line of the cavity) is as follows:

$$\widehat{H} = \hbar\omega_c \hat{a}^\dagger \hat{a} + \sqrt{\frac{\hbar P_L \kappa}{4\omega_c}} \left(e^{-i\omega_L t}\hat{a}^\dagger + e^{i\omega_L t}\hat{a}\right) - A\cos^2(k\hat{x})\hat{a}^\dagger \hat{a} + \frac{\hat{p}^2}{2m} \tag{3.29}$$

A bead modifies the energy of the system because the electric field induces a dipole and that dipole aligns with the inducing field. A bead also gives us the standard term for the kinetic energy of the bead.

3.1.5 Two ways to think about the energy shift

There are two ways to think about the energy shift brought about by the optical trapping of an optically polarisable bead in this system.

The first way is to consider that the polarisable bead (which we will assume is small compared to the cavity diameter – typically 100 nm as compared to 50 μm) presents an induced dipole that sits in the electric field of the cavity, lowering the overall energy of the system.

The second is that the bead modifies the permittivity of the cavity, lowering the energy of photons in the cavity (effectively the cavity length, as measured in wavelengths).

We will also need to define a diameter for the cavity and, consequently, a cavity volume. We will assume that the radial intensity of the beam is Gaussian:

$$I(r) = I(0)exp\left(\frac{-Cr^2}{w^2}\right) \tag{3.30}$$

Where *w* is the cavity diameter. We will therefore say the volume of the cavity is given by:

$$V_{cav} = \frac{\pi w^2 L}{4} \tag{3.31}$$

There are a number of different ways to define the diameter of the cavity. The following table shows various standard ways of referring to the width as well as the corresponding value of C.

If ***w*** **is a standard diameter**	**Value of *C***
Full 1/*e* width	4
D86	4
FWHM	4 ln2
Full 1/e^2 width	8
D4σ	8
Half 1/e width (*i.e.* 1/e radius)	1

Table 3.1. Table of values of C. Generally, we use $C = 1$. The Full 1/*e*, full width at half-maximum (FWHM) and Full 1/e^2 are, respectively, the full width at which the beam intensity declines by a factor of *e*, 2 and e^2. The D86 width is the diameter of the circle containing 86% of the intensity while the D4σ width is four times the horizontal standard deviation of the beam intensity.

3.1.6 A dipole bead

A fixed dipole aligned with a fixed electric field gives an energy of –*pE* where *E* is the electric field strength a *p* is the dipole moment. This can be calculated by considering a fixed dipole being rotated from perpendicular to parallel relative to the external field. However, it is well-known that an induced dipole only exhibits half this energy. This can be shown by considering a polarisable rod (which starts without a dipole) being rotated in a similar way.

$$U_{shift} = -\frac{1}{2}\boldsymbol{p}.\boldsymbol{E} = -\frac{1}{2}\alpha E^2 \tag{3.32}$$

Where α is the bead's polarisability.

Exactly which electric field to use is not immediately clear. Clearly, we want to use the electric field seen by the bead, and not at any other position in the cavity. Since the bead does not have any particular magnetic properties the energy shift will depend on the time averaged square of the electric field.

So the E^2 in equation 3.32 refers to **half** the square of the maximal electric field seen by the bead (we assume the bead is much smaller in length than both the wavelength of the laser and the physical diameter of the cavity beam).

In sections 3.1.8 and 3.1.9 we will derive the equations for the bead polarizability and the maximum electric field (which will be given in equations 3.45 and 3.51).

This leads to a form for U_{shift} of:

$$U_{shift} = -\frac{1}{2}\left(3\epsilon_0 \frac{\epsilon_r - 1}{\epsilon_r + 2} V_{sphere}\right)\frac{1}{2}\frac{C\hbar\omega_c \hat{a}^\dagger \hat{a}}{\epsilon_0 V_{cav}} cos^2(kx) \tag{3.33}$$

$$= -\frac{3C}{4}\frac{\epsilon_r - 1}{\epsilon_r + 2}\frac{V_{sphere}}{V_{cav}}\hbar\omega_c \hat{a}^\dagger \hat{a} cos^2(kx) \tag{3.34}$$

3.1.7 Modified Permittivity Method

Firstly, we will assume that any shift in the frequency of the cavity as a result of the bead will be small compared to the frequency of the cavity itself. We will also, as previously, assume that the bead is small compared to both the wavelength of the cavity and the cavity diameter.

We will need to know the proportion of the total square-of-electric-field-weighted cavity volume that is occupied by the bead.

This is given by the following expression:

$$\frac{E_0^2 V_{sphere} cos^2(kx)}{\int E_0^2 cos^2(kx) exp\left(\frac{-Cr^2}{w^2}\right) dV} = \frac{V_{sphere} cos^2(kx)}{\left(\frac{L}{2}\right)\left(\frac{\pi w^2}{C}\right)} \tag{3.35}$$

$$= \frac{2C}{4}\frac{V_{sphere}}{V_{cav}} cos^2(kx)$$

The energy of a field with a modified dielectric constant (*i.e.* a new refractive index) given by the product of 3.35 with the previous energy and the refractive index of the bead:

$$U = U_{shift} + U_{prev} = -(\hbar\omega_c \hat{a}^\dagger \hat{a})\frac{1}{\sqrt{\epsilon_r}}\frac{2C}{4}\frac{V_{sphere}}{V_{cav}} cos^2(kx) \tag{3.36}$$

The $\epsilon_r^{\frac{-1}{2}}$ factor being a proxy for the bead's refractive index. However, this expression is only valid for small refractive index. We know that the general form must follow the form for the polarisability of a glass sphere.

So, in order to extend this to higher permittivities we will have make the substitution $\left(\frac{1}{\sqrt{\epsilon_r}} - 1\right) \rightarrow -\frac{3}{2}\frac{\epsilon_r - 1}{\epsilon_r + 2}$.

This means the value of *A* is given by:

$$A = \frac{3C}{4}\frac{\epsilon_r - 1}{\epsilon_r + 2}\frac{V_{sphere}}{V_{cav}}\hbar\omega_c \tag{3.37}$$

Which is the same as in equation 3.34. The expression given by Chang et al.[130] is:

$$A_{Chang} = \frac{3}{4}\frac{\epsilon_r - 1}{\epsilon_r + 2}\frac{V_{sphere}}{V_{cav}}\hbar\omega_c \tag{3.38}$$

This implies that Chang takes a value of $C = 1$. We will use the Chang formula for A extensively, as this is the standard expression used by others.

3.1.8 Polarisability of a bead

By the uniqueness theorem of electrostatics, if we find an electric potential that replicates $\nabla . \mathbf{D} = \rho_{Free} = 0$, both inside and outside the sphere, then this will give us the correct field.

So we know that the component of **E** parallel to the surface of the sphere $(\mathbf{E}_{\parallel})$ is continuous as we cross from one side of the sphere to the other, as is the component of **D** perpendicular to the surface of the sphere $(\mathbf{D}_{\perp})$.

The standard ansatz is that the field outside the sphere can be considered as the sum of a uniform field, E_0, added to the dipole field of a dipole with polarisability, α, located at the centre of the sphere (at r = 0) while the internal field is a uniform field that matches the boundary conditions.

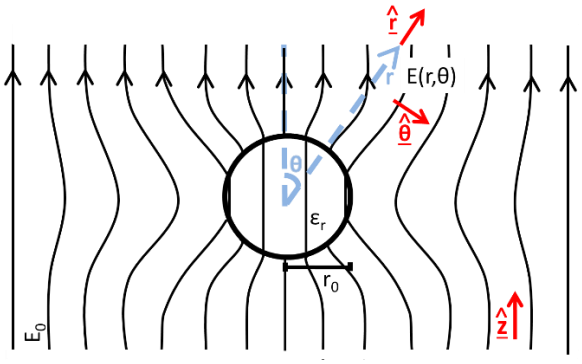

Figure 3.2. Diagram showing the Electric Field (the E-field) caused by a bead in a uniform external electric field.

This would give us external and internal potentials, Φ_{ext} and Φ_{int}, of (in spherical polars r, θ, ϕ):

$$\Phi_{ext} = E_0\left(\frac{\alpha}{4\pi\epsilon_0 r^3} - 1\right) r\cos\theta \tag{3.39}$$

$$\Phi_{int} = E_0\left(\frac{\alpha}{4\pi\epsilon_0 r_0^3} - 1\right) r\cos\theta \tag{3.40}$$

The electric field is then given by:

$$\boldsymbol{E_{ext}} = E_0\left(\frac{\alpha}{2\pi\epsilon_0 r^3} + 1\right)\cos\theta\hat{\boldsymbol{r}} + E_0\left(\frac{\alpha}{4\pi\epsilon_0 r^3} - 1\right)\sin\theta\hat{\boldsymbol{\theta}} \tag{3.41}$$

$$\boldsymbol{E_{int}} = E_0\left(\frac{\alpha}{4\pi\epsilon_0 r_0^3} - 1\right)\hat{\boldsymbol{z}} \tag{3.42}$$

We can see therefore that the boundary condition on $\mathbf{E}_{\parallel}$ $(= \mathbf{E_\theta})$ is met.

We also know that $\mathbf{D} = \epsilon_r\epsilon_0\mathbf{E}$.

So, the boundary condition on $\mathbf{D}_{\perp}(= \mathbf{D_r})$ is met if and only if:

$$E_0\epsilon_0\left(\frac{\alpha}{2\pi\epsilon_0 r_0^3} + 1\right)\cos\theta = -E_0\epsilon_0\epsilon_r\left(\frac{\alpha}{4\pi\epsilon_0 r_0^3} - 1\right)\cos\theta \tag{3.43}$$

$$\left(\frac{\alpha}{2\pi\epsilon_0 r_0^3} + 1\right) = -\epsilon_r\left(\frac{\alpha}{4\pi\epsilon_0 r_0^3} - 1\right) \tag{3.44}$$

$$\alpha = 4\pi\epsilon_0 r_0^3\frac{\epsilon_r - 1}{\epsilon_r + 2} = 3\epsilon_0\frac{\epsilon_r - 1}{\epsilon_r + 2}V_{sphere} \tag{3.45}$$

So equation 3.45 gives us the polarisability of a dielectric sphere. As a sanity check we can see that this is plausible, as, for $\epsilon_r \approx 1$, for any geometry, we would get $\alpha \approx (\epsilon_r - 1)\epsilon_0 V$. So the limiting behaviour for equation 3.45 is correct for weak dielectrics.

3.1.9 Maximum Electric Field Strength as a function of cavity occupancy

The energy density, u, of a cavity supporting a standing wave is given, at the moment of maximum electric field, by:

$$u = \frac{1}{2}\epsilon_0 E_{max}^2 cos^2(kx) exp\left(\frac{-Cr^2}{w^2}\right) \tag{3.46}$$

The full expression for the energy being:

$$u = \left(\frac{1}{2}\epsilon_0 E_{max}^2 cos^2(kx) sin^2(\omega t) + \frac{1}{2\mu_0} B_{max}^2 sin^2(kx) cos^2(\omega t)\right) exp\left(\frac{-Cr^2}{w^2}\right) \tag{3.47}$$

Integrating over the full volume of the cavity of length L (and knowing from standard electromagnetic theory that $\epsilon_0 E_{max}^2 = \frac{B_{max}^2}{\mu_0}$) to get the total energy, U, gives:

$$U = \frac{1}{2}\epsilon_0 E_{max}^2 \left(\frac{L}{2}\right)\left(\frac{\pi w^2}{C}\right)\left(sin^2(\omega t) + cos^2(\omega t)\right) \tag{3.48}$$

$$U = \frac{\pi}{4C}\epsilon_0 E_{max}^2 L w^2 \tag{3.49}$$

$$U = \frac{1}{C}\epsilon_0 E_{max}^2 V_{cav} \tag{3.50}$$

We also know that $U = \hbar\omega_c \hat{a}^\dagger \hat{a}$ so:

$$E_{max} = \sqrt{\frac{C\hbar\omega_c \hat{a}^\dagger \hat{a}}{\epsilon_0 V_{cav}}} \tag{3.51}$$

3.1.10 Two Modes

The main system we are studying is a two-mode system. Two laser modes, very close in frequency, will be used, and with some level of detuning in the driving. This detuning will normally be much less than the frequency gap between individual modes of the cavity.

$$\widehat{H} = \hbar\omega_c\left(\hat{a}_1^\dagger\hat{a}_1 + \hat{a}_2^\dagger\hat{a}_2\right) + \sqrt{\frac{\hbar P_1\kappa}{4\omega_c}}\left(e^{-i\omega_1 t}\hat{a}_1^\dagger + e^{i\omega_1 t}\hat{a}_1\right) + \sqrt{\frac{\hbar P_2\kappa}{4\omega_c}}\left(e^{-i\omega_2 t}\hat{a}_2^\dagger + e^{i\omega_2 t}\hat{a}_2\right) - Acos^2(k\hat{x})\hat{a}_1^\dagger\hat{a}_1 - Acos^2(k\hat{x} - \phi)\hat{a}_2^\dagger\hat{a}_2 + \frac{\hat{p}^2}{2m} \tag{3.52}$$

This is the Hamiltonian presented by Chang *et al.* in their 2010 publication.[59]

3.2 Cooling of Levitated spheres with a doubly-resonant field.

3.2.1 Rotating Wave Approximation

In section 3.1.3 we pre-multiplied a more limited Hamiltonian by $e^{i\omega_L\hat{a}^\dagger\hat{a}t}$ in a process known as the "rotating wave approximation". This time we will pre-multiply Hamiltonian 3.53 by $e^{i\omega_L\hat{a}_1^\dagger\hat{a}_1}e^{i\omega_L\hat{a}_2^\dagger\hat{a}_2}$ to, once again, remove the explicit time dependence of the Hamiltonian. This is desirable because the quickly oscillating terms will later average out making the problem more analytically tractable.

$$\widehat{H}' = \sqrt{\frac{\hbar P_1\kappa}{4\omega_c}}\left(\hat{a}_1^\dagger + \hat{a}_1\right) - \left(\hbar\Delta_1 + Acos^2(k_1\hat{x})\right)\hat{a}_1^\dagger\hat{a}_1 + \sqrt{\frac{\hbar P_2\kappa}{4\omega_c}}\left(\hat{a}_2^\dagger + \hat{a}_2\right) - \left(\hbar\delta\Delta_2 + Acos^2(k_2\hat{x} - \phi)\right)\hat{a}_2^\dagger\hat{a}_2 + \frac{\hat{p}^2}{2m} \tag{3.53}$$

Where $\Delta_1 = \omega_{L1} - \omega_{c1}$ and $\Delta_2 = \omega_{L2} - \omega_{c2}$ *i.e.* $\Delta_{1,2}$ refers to the detuning between the driving frequency and the frequency of the mode of the cavity that is being driven by that

laser. The easiest way to do this is to use modes that are very close in frequency, for example the n = 10,000 and the n = 10,002 modes of the cavity. If we do this, then the position of the bead along the cavity will tell us the phase relationship between the two beads (see Fig 3.1). We are mainly interested in $\phi = \pi/4$ *i.e.* the point at which the maximum of one laser field falls halfway between the maximum and the zero of the other field.

3.2.2 Equations of Motion – expectation values

We now apply the usual process of replacing operators with the expectation values and applying Ehrenfest's theorem (equation 3.20) to Hamiltonian 3.53. If we do this, we get the following equations for the bulk of motion of the system:

$$\ddot{\hat{x}} = -\frac{A}{m}\left(k_1|\hat{a}_1|^2 sin(2k_1\hat{x}) + k_2|\hat{a}_2|^2 sin(2k_2\hat{x} - 2\phi)\right) \tag{3.54}$$

$$\dot{\hat{a}}_1 = -i\sqrt{\frac{P_1\kappa}{4\hbar\omega_c}} + i\Delta_1\hat{a}_1 + \frac{iA}{\hbar}\hat{a}_1 cos^2(k_1\hat{x}) - \frac{\kappa}{2}\hat{a}_1 \tag{3.55}$$

$$\dot{\hat{a}}_2 = -i\sqrt{\frac{P_2\kappa}{4\hbar\omega_c}} + i\Delta_2\hat{a}_2 + \frac{iA}{\hbar}\hat{a}_2 cos^2(k_2\hat{x} - \phi) - \frac{\kappa}{2}\hat{a}_2 \tag{3.56}$$

In section 3.6 we see that the cooling is strongest when $\phi = \pi/4$.

3.2.3 Equilibrium

We will now use equations 3.54, 3.55 and 3.56 to find the equilibrium position, and to analyse the dynamics of the deviation from that equilibrium, by linearising these equations about that equilibrium. Because we are now dealing in expected outcomes these equations are no longer really quantum equations, but are classical. The equilibrium coordinates are:

$$\alpha_1 = \frac{i\sqrt{\frac{P_1\kappa}{4\hbar\omega_c}}}{i\Delta_1 + i\frac{A}{\hbar}cos^2(k_1x_0) - \frac{\kappa}{2}} \tag{3.57}$$

$$\alpha_2 = \frac{i\sqrt{\frac{P_2\kappa}{4\hbar\omega_c}}}{i\Delta_2 + i\frac{A}{\hbar}cos^2(k_2x_0 - \phi) - \frac{\kappa}{2}} \tag{3.58}$$

$$\frac{|\alpha_2|^2}{|\alpha_1|^2} = \frac{-sin(2k_1x_0)}{sin(2k_2x_0 - 2\phi)} \tag{3.59}$$

$$= -cos(2\phi) + sin(2\phi)tan\left(2kx_0 - 2\phi - \frac{\pi}{2}\right)\ if\ k_1 \approx k_2 = k \tag{3.60}$$

Equations 3.57, 3.58 and 3.59 can be solved numerically by an iteration, such as the Newton Raphson Method or simple direct iteration using the above equations. The simplest (though not the most quickly convergent) way to form the iteration is to simply set $x_0 = 0$ and then to iteratively set the values of $|\alpha_1|^2$, $|\alpha_2|^2$ and x_0. For $\phi = \pi/4$ and $k_1 \approx k_2$ this leaves:

$$|\alpha_1|^2 \to \frac{P_1\kappa/\hbar\omega_c}{\kappa^2 + 4\left(\Delta_1 + \frac{A}{2\hbar} + \frac{Acos2kx_0}{2\hbar}\right)^2} \tag{3.61}$$

$$|\alpha_2|^2 \to \frac{P_2\kappa/\hbar\omega_c}{\kappa^2 + 4\left(\Delta_2 + \frac{A}{2\hbar} + \frac{Asin2kx_0}{2\hbar}\right)^2} \tag{3.62}$$

$$x_0 \to \frac{1}{2k}arctan\frac{|\alpha_2|^2}{|\alpha_1|^2} \tag{3.63}$$

Once the value of x_0 has converged, the precise values of α_1 and α_2 can be found using 3.57 and 3.58.

3.2.4 Linearised equations of motion

Having found the equilibrium positions, we can then linearise the equations (3.54, 3.55 and 3.56) about that equilibrium *i.e.* $x \to x_0 + x$ and $a_i \to \alpha_i + a_i$.

$$\ddot{x} = -\omega_M^2 \hat{x} - g_1 sin2k_1x_0 - g_2 sin(2k_2x_0 - 2\phi) \tag{3.64}$$

where $\omega_M^2(\Delta_1, \Delta_2) = \frac{2A}{m}\left(k_1^2|\alpha_1|^2 cos2k_1x_0 + k_2^2|\alpha_2|^2 cos(2k_2x_0 - 2\phi)\right)$

and $g_i = \frac{Ak_i}{m}\left(\alpha_i^* a_i + \alpha_i a_i^\dagger\right)$

$$\dot{a}_1 = i\Delta_1^x a_1 - \frac{iAk_1}{\hbar}\alpha_1 x sin2k_1x_0 - \frac{\kappa}{2}a_1 \tag{3.65}$$

where $\Delta_1^x = \Delta_1 + \frac{A}{\hbar}cos^2 k_1x_0$

$$\dot{a}_2 = i\Delta_2^x a_2 - \frac{iAk_2}{\hbar}\alpha_2 x sin(2k_2x_0 - 2\phi) - \frac{\kappa}{2}a_2 \tag{3.66}$$

where $\Delta_2^x = \Delta_2 + \frac{A}{\hbar}cos^2(k_2x_0 - \phi)$

This means that the system behaves as a harmonic oscillator with a frequency and equilibrium position that depends on the two detunings, as well as the occupancy of the two cavities (set by the power of each of the two lasers).

The acceleration (equation 3.64) also has other terms which either drive or damp this primary oscillation depending on the phase relation between these terms and that of the primary oscillation.

As per section 1.5, we expect to find that, for light that is red-detuned relative to the shifted cavity frequency, we get damping (or cooling) of this oscillation, while for light that is blue-detuned, we expect to drive oscillations that increase the amplitude (heating).

We expect this cooling to be maximal for detuning of one mechanical frequency less than the shifted cavity frequency. Under these circumstances the absorption of a red detuned photon, coupled with the emission of a photon at the shifted cavity frequency, can be facilitated by the mechanical mode giving up one quanta of excitation (see Figure 3.3).

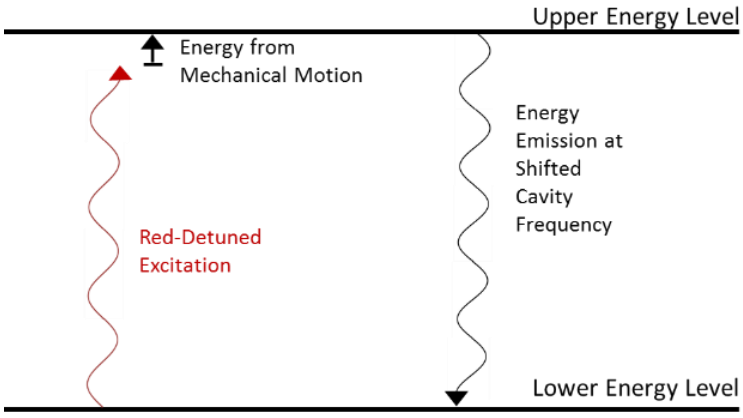

Figure 3.3. Diagram showing adjacent energy levels of cavity excitation. When red detuned light is used the mechanical oscillation can provide the extra energy required to excite the cavity. This means that the energy of the mechanical oscillator falls, *i.e.* red detuning will lead to mechanical damping.

3.2.5 Classical Cooling rate

To get cooling we need a force in the opposite direction to the velocity of the oscillator, $P_{cool} = -m\ddot{x}\dot{x}$. We will imagine there is a mechanical damping Γ_M (*i.e.* a term in $\ddot{x}$ equal to $-\Gamma_M\dot{x}$). We will let $x = x_+e^{i\omega t} + x_-e^{-i\omega t}$ and $a_{1,2} = a_{1,2_+}e^{i\omega t} + a_{1,2_-}e^{-i\omega t}$. Note that, because x is real, $x_+ = x_-^*$. We find from equation 3.64 and 3.66 that:

$$-\omega^2 x_\pm = \mp i\omega\Gamma_M x_\pm - \omega_M^2 x_\pm - \frac{Ak_1}{m}\left(\alpha_1 a_{1\pm}^* + \alpha_1^* a_{1\pm}\right) sin\, 2k_1x_0 - \frac{Ak_2}{m}\left(\alpha_2 a_{2\pm}^* + \alpha_2^* a_{2\pm}\right) sin(2k_2x_0 - 2\phi) \tag{3.67}$$

$$\pm i\omega a_1 = i\Delta_1^x a_{1\pm} - \frac{iAk_1}{\hbar}\alpha_1 x_\pm\, sin\, 2k_1x_0 - \frac{\kappa}{2}a_{1\pm} \tag{3.68}$$

$$\pm i\omega a_2 = i\Delta_2^x a_{2\pm} - \frac{iAk_2}{\hbar}\alpha_2 x_\pm\, sin(2k_1x_0 - 2\phi) - \frac{\kappa}{2}a_{2\pm} \tag{3.69}$$

We then want to find the complex relationship between $a_{1,2\pm}$ and $x_\pm$. So we invent an object $\chi_1(\omega)$, such that $a_{1,2\pm} = \chi_{1,2}(\pm\omega)x_\pm$.

$$\chi_1(\omega) = \frac{Ak_1\alpha_1}{\hbar}\frac{sin\,2k_1x_0}{\Delta_1^x - \omega + \frac{i\kappa}{2}} \tag{3.70}$$

$$\chi_2(\omega) = \frac{Ak_2\alpha_2}{\hbar}\frac{sin(2k_2x_0 - 2\phi)}{\Delta_2^x - \omega + \frac{i\kappa}{2}} \tag{3.71}$$

We can now see that the imaginary terms from equation 3.67 contribute to damping the oscillations, just as a mechanical damping would.

$$\begin{aligned}\Gamma_{Op} = Im\left(\frac{Ak_1}{m\omega}\left(\alpha_1\chi_1^*(-\omega) + \alpha_1^*\chi_1(\omega)\right)sin\,2k_1x_0\right) \\ + Im\left(\frac{Ak_2}{m\omega}\left(\alpha_2\chi_2^*(-\omega)\right.\right. \\ \left.\left. + \alpha_2^*\chi_2(\omega)\right)sin(2k_2x_0 - 2\phi)\right)\end{aligned} \tag{3.72}$$

$$\begin{aligned}\Gamma_{Op} = \frac{A^2k_1^2\kappa}{2m\hbar\omega}|\alpha_1|^2 sin^2 2k_1x_0\left(\frac{1}{(\Delta_1^x + \omega)^2 + \frac{\kappa^2}{4}} - \frac{1}{(\Delta_1^x - \omega)^2 + \frac{\kappa^2}{4}}\right) \\ + \frac{A^2k_2^2\kappa}{2m\hbar\omega}|\alpha_2|^2 sin^2(2k_2x_0 - 2\phi)\left(\frac{1}{(\Delta_2^x + \omega)^2 + \frac{\kappa^2}{4}}\right. \\ \left. - \frac{1}{(\Delta_2^x - \omega)^2 + \frac{\kappa^2}{4}}\right)\end{aligned} \tag{3.73}$$

The real parts of these damping terms also give rise to a reduction in the frequency of the oscillations. However, this reduction is small for an underdamped system, so it will be reasonable to assume $\omega = \omega_M$ from 3.64. Similarly, it will be reasonable to assume $k_1 \approx k_2$.

We are interested in seeing cooling down to the ground state of this oscillator and, for this, we will need to consider a quantum calculation for the cooling.

First, however, it will be useful to look at the structure of the cooling rate in more detail. Figure 3.4 shows the cooling is greatest for the doubly resonant detuning (*i.e.* (ii) in the Figure) where both laser fields are red-detuned by the amount of the mechanical frequency of the bead's oscillation.

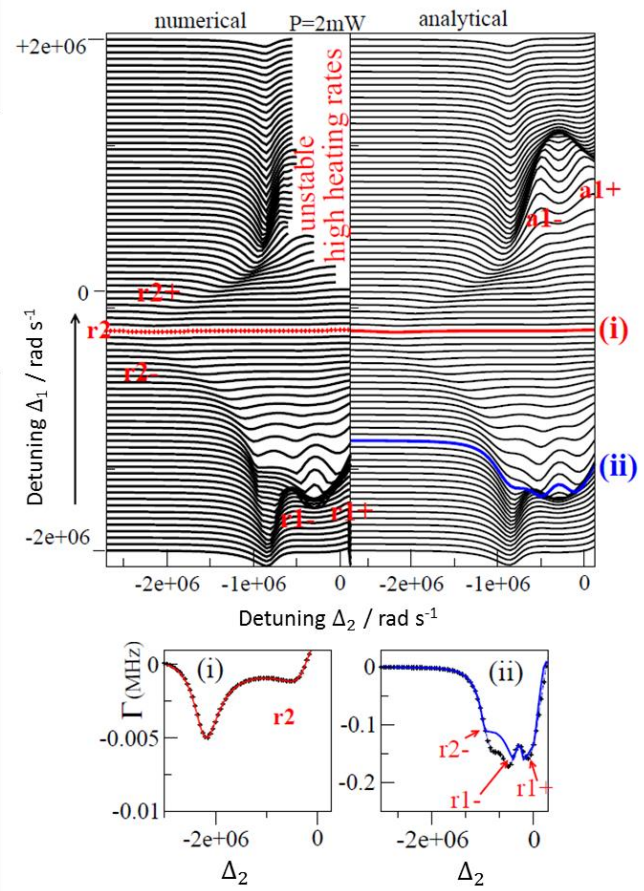

Figure 3.4. The curves show cooling for P_1 = 2 mW, P_2 = 0.5 mW, $\kappa = \frac{2A}{\hbar} = 6 \times 10^5$ Hz, λ = 1064 nm, with a phase difference between the two curves of $\phi = \frac{\pi}{4}$. This corresponds to a bead diameter of 100 nm and a laser diameter of 25 µm.

Upper right panel shows cooling rates as derived in this section. Upper left panel shows cooling rates as derived from numerical simulation propagating equations 3.64, 3.65 and 3.66. These equations show clear agreement with one another demonstrating that the approximations involved in linearization is valid for these parameters. The curves correspond to different values of Δ_1 between +2 x 10^6 *rad* s^{-1} to -2 x 10^6 *rad* s^{-1}.

The lower panels show the two cooling curves picked out in red and blue in the upper panels, again with good agreement between analytic (dotted line) and numeric (solid coloured line) predictions. The red trace shows the best cooling that can be obtained from singly resonant cooling where one field (field one) simply traps the bead while the weaker field is concerned with cooling. For this trace $\Delta_1^x = 0$ *i.e.* $\Delta_1 = -\frac{A}{\hbar} cos^2 k_1 x_0$.

As we can see, if both fields are used to simultaneously trap and cool (lower right panel), then cooling is up to twenty times greater than can be achieved if only the weaker field cools (lower left panel).

Finally, we see various energy level splittings, or resonances, where, for example, there is cooling at an adjusted cavity detuning of plus or minus the mechanical frequency. So we get r2+ and r2- which are cooling resonances of field 2. We get r1+ and r1- which are cooling resonances of field 1 and a1+ and a1- which are heating resonances of field 1. This information is also shown in the upper left panel of figure 3.6 later.

3.2.6 Cooling Rate General – Fermi's Golden Rule

There is a general expression from perturbation theory for the cooling rate of a system weakly coupled to a large reservoir (or bath).

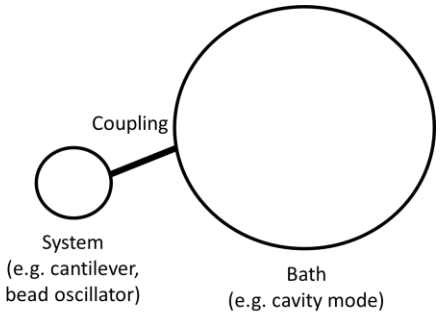

Figure 3.5. Perturbation Theory for bath coupled with system.

In this case the system is the bead oscillator and the "bath" is the laser cavity.

We will assume that the coupling between the system and the bath is "weak". In other words, any cooling or heating rate is small compared to the mechanical frequency of the trapping.

We will also assume that this coupling enters the Hamiltonian in the following, linear, fashion:

$$\widehat{H}' = -\hat{x}\hat{F} \tag{3.74}$$

Where $\hat{x}$ is a variable associated with the system and $\hat{F}$ is a variable associated with the bath. In the example we have here we will use the scaled position of the bead (relative to its equilibrium position) and the scaled ladder operators of the laser field (relative to the equilibrium field).

This could work with any kind of system. $\hat{x}$ could be the z-position of an electron in an atom with $\hat{F}$ being the force it feels from an external electric field (so long as that field was relatively weak compared to the field from the nucleus, and so long as that field only depends on the changes in the field and not on the position of the electron). Or $\hat{x}$ could be the angular position of a child on a swing while $\hat{F}$ could be the torque provided to the swing by an older sibling, so long as that torque was only dependent on time, and not on the position or velocity of the swing.

We are interested in the transition rate of a system from state i_s to f_s.

Fermi's Golden Rule is given by equation 3.75 for a continuous distribution of energy states with a density of states at the final energy of $\rho(E_f)$. The rule becomes 3.76 for a discrete transition between individual energy levels i_s and f_s with $E_{i_s} - E_{f_s} = \hbar\omega_0$.

$$\Gamma_{i\to f} = \frac{2\pi}{\hbar}\left|\langle f|\hat{H}|i\rangle\right|^2 \rho(E_f) \tag{3.75}$$

$$\Gamma_{i\to f} = \frac{2\pi}{\hbar}\left|\langle f|\hat{H}|i\rangle\right|^2 \delta(E_f - E_i) \tag{3.76}$$

The delta function shows that the overall energy of the bath plus system must be conserved, and the density of states is such that the energy range covering the final state contains one state, *i.e.* that final state.

The bra-ket in equation 3.76 can be split into separate system and bath parts to give a transition rate.

Note that the terms of the Hamiltonian that only include variables in system/bath will give no contribution in equation 3.75 (assuming we are using a mutually orthogonal basis set for bath and system).

If we are only interested in the transition between states of the system, and are uninterested in the system's effect on the bath, then we can sum over all states of the bath to find the transition rate from i_s to f_s as follows:

$$\Gamma_{i_s\to f_s} = \frac{2\pi}{\hbar}|\langle f_s|\hat{x}|i_s\rangle|^2 \sum_{f_b}\left|\langle f_b|\hat{F}|i_b\rangle\right|^2 \delta(E_{f_s} - E_{i_s} + E_{f_b} - E_{i_b}) \tag{3.77}$$

To correctly calculate the transition rate, the algebrisation of this delta function must be done with care.

We want a delta function such that $\int_{-\infty}^{\infty}\delta(E)dE = 1$. This can be achieved by using $\delta(E) = \frac{1}{2\pi\hbar}\int dte^{iEt/h}$. Furthermore, we can replace the sum from equation 3.77 with an integral over all energies to give:

$$\Gamma_{i_s\to f_s} = \frac{1}{\hbar^2}|\langle f_s|\hat{x}|i_s\rangle|^2 \int \sum_{f_b}\left|\langle f_b|\hat{F}|i_b\rangle\right|^2 exp\left(\frac{-E_{i_b}t}{\hbar}\right)exp\left(\frac{E_{f_b}t}{\hbar}\right)e^{-i\omega_0 t}dt \tag{3.78}$$

Now we note that:

$$\sum_{f_b}\left|\langle f_b|\hat{F}|i_b\rangle\right|^2 \; exp\left(\frac{-E_{i_b}t}{\hbar}\right)exp\left(\frac{E_{f_b}t}{\hbar}\right)$$

$$= \sum_{f_b}\left|\langle f_b|\hat{F}|i_b\rangle\right|^2 \left\langle i_b\middle|exp\left(\frac{-E_{i_b}t}{\hbar}\right)\hat{F}exp\left(\frac{E_{f_b}t}{\hbar}\right)\middle|f_b\right\rangle \tag{3.79}$$

$$= \langle\hat{F}(0)\hat{F}(t)\rangle \tag{3.80}$$

So equation 3.78 becomes:

$$\Gamma_{i_s\to f_s} = \frac{1}{\hbar^2}|\langle f_s|\hat{x}|i_s\rangle|^2 \int \sum_{f_b}\langle\hat{F}(0)\hat{F}(t)\rangle\, e^{-i\omega_0 t}dt \tag{3.81}$$

It is also worth noting the reverse rate of transition (which is got by switching the sign of ω).

$$\Gamma_{f_s\to i_s} = \frac{1}{\hbar^2}|\langle f_s|\hat{x}|i_s\rangle|^2 \int \sum_{f_b}\langle\hat{F}(0)\hat{F}(t)\rangle\, e^{i\omega_0 t}dt \tag{3.82}$$

For harmonic oscillator, if $\hat{x}$ is a position, $|\langle n+1|\hat{x}|n\rangle|^2 = (n+1)|\langle 1|\hat{x}|0\rangle|^2$ so:

$$\Gamma_{n\to n-1} = (n)\Gamma_{1\to 0} \tag{3.83}$$

$$\Gamma_{n\to n+1} = (n+1)\Gamma_{0\to 1} \tag{3.84}$$

However, there is not, in general, any particular relationship between $\Gamma_{1\to 0}$ and $\Gamma_{0\to 1}$. I will also sometimes use the notation $\Gamma_{0\to 1} \equiv \Gamma_{\uparrow}$ and $\Gamma_{1\to 0} \equiv \Gamma_{\downarrow}$.

3.2.7 Cooling Rate General – Net Cooling Rate

The net cooling rate is given by the net rate of loss of energy in the system, divided by the total energy in the system (equation 3.85). At high energies this tends to a limiting value (the classical cooling rate) but at lower energies it is reduced, as might be expected. The energy of the system will approach a limiting phonon number, $\bar{n}$ (equation 3.86) where the net cooling rate reaches zero.

$$\Gamma_{cool} = \frac{n\Gamma_{\downarrow} - (n+1)\Gamma_{\uparrow}}{n} \tag{3.85}$$

$$\bar{n} = \frac{\Gamma_{\uparrow}}{\Gamma_{\downarrow} - \Gamma_{\uparrow}} \tag{3.86}$$

$$\Gamma_{cool\ as\ n\to\infty} = \Gamma_{\downarrow} - \Gamma_{\uparrow} \tag{3.87}$$

3.2.8 Cooling in our system

Hamiltonian 3.54 contains a number of terms, but the only terms that include both bath and oscillator variables are as follows:

$$\hat{H}_{int} = A\hat{a}_1^{\dagger}\hat{a}_1 cos^2 k_1\hat{x} + A\hat{a}_2^{\dagger}\hat{a}_2 cos^2(k_2\hat{x} - \phi) \tag{3.88}$$

If we expand about equilibrium and keep only terms $O(\hat{x}, \hat{a}_{1,2})$ we will get the dominant contribution to the cooling.

$$\begin{aligned}\hat{H}_{cool} = &-Ak_1\hat{x}\left(\alpha_1\hat{a}_1^{\dagger} + \alpha_1^{*}\hat{a}_1\right) sin\, 2k_1x_0 \\ &- Ak_2\hat{x}\left(\alpha_2\hat{a}_2^{\dagger} + \alpha_2^{*}\hat{a}_2\right) sin(2k_1x_0 - 2\phi)\end{aligned} \tag{3.89}$$

Perturbation theory (*i.e.* applying equation 3.85 to the first of the two terms from equation 3.89) gives:

$$\begin{aligned}\Gamma_{n\to n-1}^{term\ 1} = \frac{A^2k_1^2 sin^2 2k_1x_0}{\hbar^2}\frac{n\hbar}{2m\omega_M}|\alpha_1|^2\int_{-\infty}^{\infty}\big(\langle\hat{a}_1^{\dagger}(0)\hat{a}_1(t)\rangle \\ + \langle\hat{a}_1(0)\hat{a}_1^{\dagger}(t)\rangle\big)e^{i\omega_M t}\,dt\end{aligned} \tag{3.90}$$

We need to calculate $\int\langle\hat{a}_1^{\dagger}(0)\hat{a}_1(t)\rangle\, e^{i\omega_0 t}dt$

In calculating the evolution of $\hat{a}(t)$ we ignore the interaction with the bead (because this is perturbation theory) so:

$$\dot{\hat{a}}_1 = i\Delta_1^x \hat{a}_1 - \frac{\kappa}{2}\hat{a}_1 + \widehat{N}(t) \tag{3.91}$$

Where $\widehat{N}(t)$ is a stochastic noise term.

$$\hat{a}_1(t) = \left(\hat{a}(0) + \int_{t'=0}^{t} \widehat{N}(t') e^{-i\Delta_1^x t'} e^{\frac{\kappa|t'|}{2}} dt'\right) e^{i\Delta_1^x t} e^{\frac{-\kappa|t|}{2}} \tag{3.92}$$

Because $\widehat{N}(t)$ is random and stochastic we get:

$$\langle \hat{a}_1^\dagger(0)\hat{a}_1(t)\rangle = \langle \hat{a}_1^\dagger(0)\hat{a}_1(0)\rangle e^{i\Delta_1^x t} e^{\frac{-\kappa|t|}{2}} \tag{3.93}$$

$$\langle \hat{a}_1(0)\hat{a}_1^\dagger(t)\rangle = \langle \hat{a}_1(0)\hat{a}_1^\dagger(0)\rangle e^{-i\Delta_1^x t} e^{\frac{-\kappa|t|}{2}} \tag{3.94}$$

$$\Gamma_{n\to n-1}^{term\ 1} = \frac{A^2 k_1^2 n|\alpha_1|^2 sin^2 2k_1 x_0}{2m\hbar\omega_M}\kappa\left(\frac{\langle \hat{a}_1^\dagger(0)\hat{a}_1(0)\rangle}{(\Delta_1^x + \omega_M)^2 + \frac{\kappa^2}{4}} + \frac{\langle \hat{a}_1(0)\hat{a}_1^\dagger(0)\rangle}{(\Delta_1^x - \omega_M)^2 + \frac{\kappa^2}{4}}\right) \tag{3.95}$$

Now we know that $\hat{a}_1\hat{a}_1^\dagger - \hat{a}_1^\dagger\hat{a}_1 = 1$. At the same time, because the average photon number, $|\alpha_1|^2$, has been factored out, $\langle \hat{a}_1^\dagger\hat{a}_1\rangle = 0$. So $\langle \hat{a}_1\hat{a}_1^\dagger\rangle = 1$.

$$\Gamma_{n\to n-1} = \frac{A^2\kappa n}{2m\hbar\omega_M}\left(\frac{|\alpha_1|^2 k_1^2 sin^2 2k_1 x_0}{(\Delta_1^x + \omega_M)^2 + \frac{\kappa^2}{4}} + \frac{|\alpha_2|^2 k_2^2 sin^2(2k_2 x_0 - 2\phi)}{(\Delta_2^x + \omega_M)^2 + \frac{\kappa^2}{4}}\right) \tag{3.96}$$

Which is as we calculated classically (see equation 3.73) and Figure 3.6.

3.2.9 N-bar

Having determined Γ_{cool} in this way allows us to calculate the average occupancy, $\bar{n}$, of the harmonic oscillator that is the optically trapped bead. This is given by the following equation (derived from equation 3.86):

$$\bar{n} = \frac{S_1(\omega_M) + S_2(\omega_M)}{S_1(-\omega_M) + S_2(-\omega_M) - S_1(\omega_M) - S_2(\omega_M)}$$

$$S_1(\omega) = \frac{|\alpha_1|^2 k_1^2 sin^2 2k_1 x_0}{\left(\Delta_1^x - \omega\right)^2 + \frac{\kappa^2}{4}} \quad ; \quad S_2(\omega) = \frac{|\alpha_2|^2 k_2^2 sin^2 (2k_2 x_0 - 2\phi)}{\left(\Delta_2^x - \omega\right)^2 + \frac{\kappa^2}{4}} \tag{3.97}$$

3.3 The relative merits of single versus double resonance cooling

In single resonance cooling one field is resonant with the cavity and traps the bead in a harmonic trap. The other field is detuned by one mechanical frequency from the cavity and acts to cool this new mechanical degree of freedom. In double resonance cooling both fields are detuned providing both the trapping and the cooling. Figure 3.4 already shows that the double resonance cooling can give us an order of magnitude stronger cooling than single resonance cooling.

This analysis has not yet considered other sources of heating (*e.g.* photon scattering or background gas collisions, which will be considered in Chapter 4.

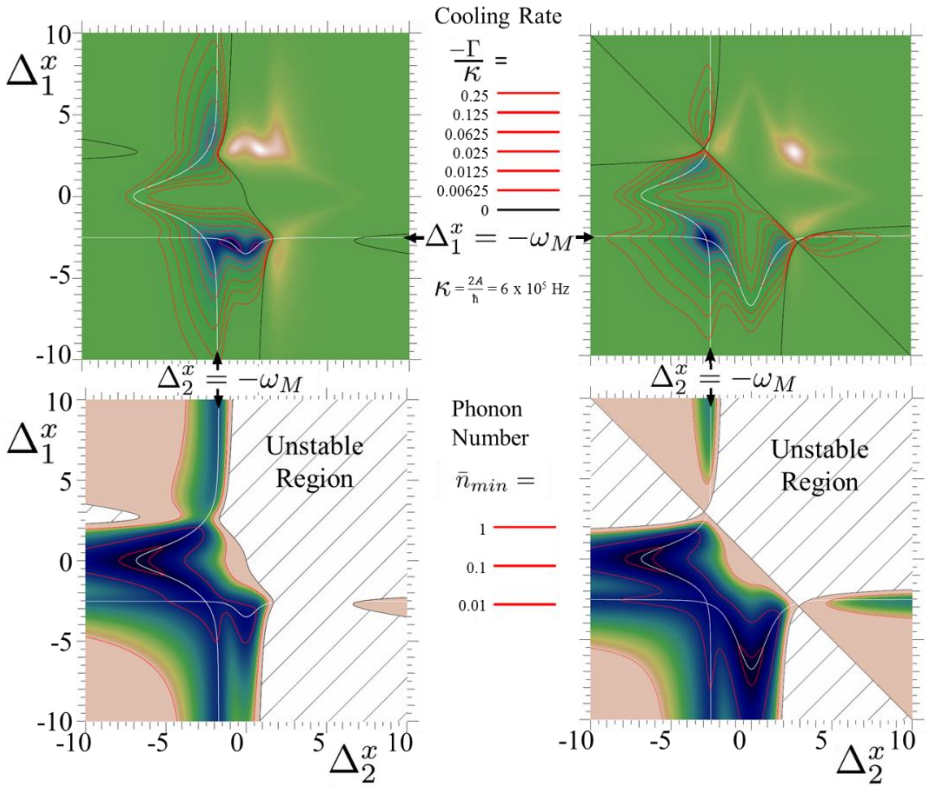

Figure 3.6. Upper Panels: Rate of cooling (blue) and heating (pink to white) for field strength ratio of a half (left) and one (right). The strongest cooling regime occurs roughly for symmetric cooling/trapping where both fields are red-detuned by roughly the mechanical frequency. The darkest blue areas correspond to r2- and r1- from Figure 3.4 with matching heating for Δ_1^x, 2>0.

The upper left hand panel shows almost exactly equivalent information to Figure 3.4, the white lines indicate the single resonances r1 and r2 where detuning is matched to the mechanical frequency.

Note that while the cooling is maximal for $\Delta_1^x = \Delta_2^x = -2.72\frac{A}{\hbar}$, the smallest phonon numbers occur at the single resonances. This is because the cooling rate depends only on the difference between the heating and the cooling terms, whereas the average phonon number depends on the ratio of those terms as well as on the mechanical frequency (which is larger for the single resonance case).

All detunings are shifted detunings, and they are shown in units of $A/\hbar$.

3.4 r2, Single Field Cooling

An expression for the single-field cooling (where a strong field traps and a weaker field cools) can be obtained from equation 3.73 (for $\phi = \pi/4$ and $k_1 \approx k_2$, as ever). Γ_{SR} is obtained by setting $\Delta_1^x = 0$, $\Delta_1^x = -\omega_M$. With expressions for $\alpha_{1,2}$ coming from equations 3.61, 3.62 and ω_M is given by 3.64.

Because the field that is resonant with the cavity is the more powerful field, we can assume that $\tan kx_0 \approx kx_0$, $\cos 2kx_0 \approx 1$ and $|a_1| \gg |a_2|$. At higher powers we can also assume that the mechanical frequency is greater than the loss rate from the cavity which allows us to make approximations like $\omega_M^2 = \frac{2Ak^2P_1}{m\kappa\hbar\omega_c}$.

$$\Gamma_{SR} = \frac{2A^2k^2\kappa}{m\hbar\omega_M}|a_2|^2 cos^2 2kx_0 \left(\frac{1}{\kappa^2} - \frac{1}{16\omega_M^2 + \kappa^2}\right) \tag{3.98}$$

$$\approx \frac{2A^2k^2P_2}{m\hbar\omega_c}\frac{1}{\omega_M}\frac{1}{\kappa^2 + 4\omega_M^2} \tag{3.99}$$

$$\lim_{P_1 \to \infty, P_1 \gg P_2} \Gamma_{SR} \approx \frac{P_2}{k}\sqrt{\frac{Am\omega_c\kappa^3}{32\hbar P_1^3}} \tag{3.100}$$

Equation 3.100 shows us that single resonance cooling has a problem whereby if we just increase the power of both fields the cooling rate will actually start to get worse as ω_M grows beyond κ while the maximum cooling, for a given field ratio, is for a power such that $\omega_M = \frac{\kappa}{2}$.

As we can see in Figure 3.7 this mean that the cooling rate for single field cooling peaks for a relatively low laser power and then falls away, unlike double resonance cooling which continues to grow as laser power increases.

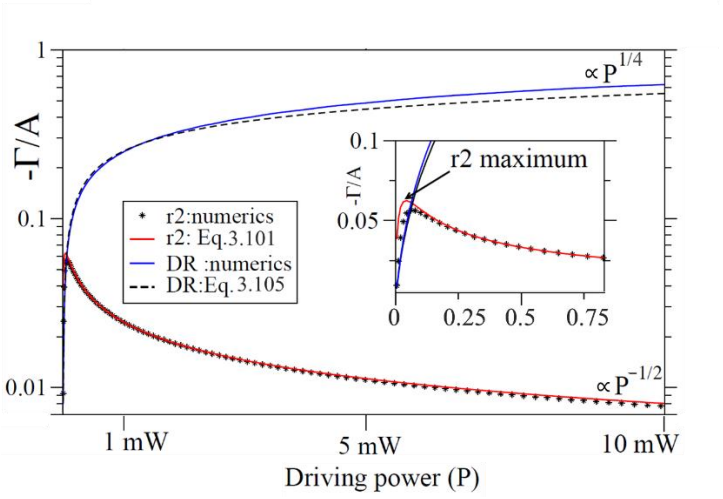

Figure 3.7. Graph showing that as field strength increases, the relative advantage of double resonance cooling increases relative to single resonance cooling. As we can see, for strong fields the cooling is nearly two orders of magnitude better with double resonance cooling. In this diagram, $P_2 = \frac{1}{4}P_1$.

3.5 Double Resonance Cooling

As illustrated in Figure 3.4 r2- and r1- never actually cross, they undergo an avoided crossing.

The double-field cooling rates for the region of closes approach can be estimated from equation 3.73 by assuming that the two resonances actually cross *i.e.* by assuming that $-\omega_M(\Delta_1, \Delta_2) \approx \Delta_1^x \approx \Delta_2^x$.

I will examine two cases of double resonance cooling that are analytically tractable. The first is where P_2 is sufficiently less than P_1 such that we can still assume $\sin kx_0 \approx \tan kx_0 \approx kx_0$, $\cos 2kx_0 = 1$ *etc.* and the second is where $P_1 = P_2$.

In the former case we can assume $\omega_M^4 = \frac{Ak^2\kappa P_1}{2m\hbar\omega_c}$ and so we have:

$$\Gamma_{DR} = \frac{2A^2k^2\kappa}{m\hbar\omega_M}(|\alpha_2|^2 cos^2 2kx_0 + |\alpha_1|^2 sin^2 2kx_0)\left(\frac{1}{\kappa^2} - \frac{1}{16\omega_M^2 + \kappa^2}\right) \tag{3.101}$$

$$\Gamma_{DR,P_1 \gg P_2} \approx P_2\left(\frac{8A^5k^5}{m^5\hbar^5\omega_c^5\kappa^2P_1^3}\right)^{\frac{1}{4}} \tag{3.102}$$

In the case of symmetric double resonance cooling we can use the symmetry of the problem to be more exact and say that $\omega_M = \sqrt{\frac{-\kappa^2}{8} + \sqrt{\frac{\kappa^4}{64} + \frac{Ak^2 P_\kappa}{\sqrt{2}\hbar m \omega_c}}}$.

$$\Gamma_{DR,P_1=P_2=P} = \frac{2A^2k^2\kappa^2 P}{\hbar^2 m\omega_c}\frac{1}{\omega_M}\left(\frac{1}{\kappa^2} - \frac{1}{16\omega_M^2 + \kappa^2}\right)\left(\frac{1}{\kappa^2 + 4\omega_M^2}\right) \tag{3.103}$$

$$\lim_{P\to\infty} \Gamma_{DR,P_1=P_2=P} = \left(\frac{\sqrt{2}A^5k^2\kappa^2 P}{8m\hbar^5\omega_c\kappa^3}\right)^{\frac{1}{4}} \tag{3.104}$$

3.6 Phase difference between the two modes

Figure 3.8 shows that the cooling is reasonably insensitive to the phase difference between the two modes under a variation of about 30% from $\phi = \pi/4$.

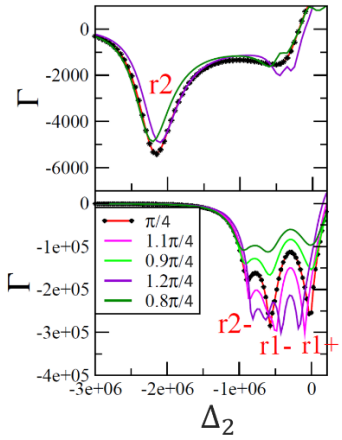

Figure 3.8. Shows the cooling as a function of detuning for the single resonance (upper) and double resonance (lower) cooling, in the strong cooling regime with $P_1 =$ 2mW and $P_2 = 0.5$ mW. Different curves show different phase differences ϕ between the two fields. As we can see, although $\phi = \pi/4$ gives optimal cooling the cooling is not terribly sensitive to variation in phase about this equilibrium.

3.7 Typical Experimental Parameters

If we want to use this system to study quantum effects, then it will be useful to have a set of typical parameters for near ground state cooling. One set of parameters is as follows:

$$L = 9.4 \text{ mm}$$

$$\lambda = 1064 \text{ nm}$$

$$\omega_C = 1.772 \times 10^{15} \text{ rad s}^{-1}$$

$$k_1 \approx k_2 \approx 5.9 \times 10^6 \text{ m}^{-1}$$

$$\epsilon_r = 2$$

$$\phi_{bead} = 200 \text{ nm}$$

$$\phi_{cavity} = 2w = 50 \text{ µm}$$

$$\kappa = 6 \times 10^5 \text{ Hz}$$

$$\rho_{glass} = 4{,}500 \text{ kg m}^{-3}$$

$$m_{bead} \approx 1.4 \times 10^{-17} \text{ kg}$$

$$n \approx 18{,}000$$

$$P_1 = P_2 = 4 \text{ mW}$$

$$\frac{A}{\hbar} = \frac{3}{4}\frac{V_{sphere}}{V_{cavity}}\frac{\epsilon_r - 1}{\epsilon_r + 2}\omega_C = 3.6 \times 10^5 \text{ s}^{-1}$$

$$\Delta_1 = \Delta_2 = -1.07 \times 10^6 \text{ s}^{-1}$$

$$\omega_M = 9 \times 10^5 \text{ s}^{-1}$$

$$\Gamma_{opt} = 2.9 \times 10^5$$

$$\bar{n}_{min} = 0.016$$

(3.105)

Using the above parameters, it will be possible to achieve a very good rate of cooling and, in the absence of external heating, additional complications and considerations, it will be possible to cool to the ground state.

4 Additional Complications and Considerations.

This Chapter extends the work of the previous Chapter into new regimes. The problem is considered in situations where previous approximations are no longer valid, including where the bead is an appreciable fraction of wavelength. Consideration is made of various thermal effects from the background gas including an approximation of the pressure for peak radiometric force. Again, further analysis is made of the dynamics in special cases.

4.1 A bead with diameter similar to the laser's wavelength

4.1.1 Introduction

In Chapter 3 we always assumed that the bead was small with respect to the wavelength of the driving laser ($r_{bead} \ll \lambda$). A larger bead is an advantage because it means stronger coupling between the bead and the laser field. However, a larger bead presents a difficulty in analysis as the whole of the bead is no longer located at the point of maximum field intensity. So the assumption of dipole coupling from 3.1.8 breaks down.

4.1.2 A simple model for larger beads

The simplest way to model larger beads is to modify our equation for the coupling, *A*, based on the assumption that the bead sees the volume-weighted square of the average beam intensity *i.e.* the volume-weighted averaged squared electric field. This will definitely be correct for bead refractive indices close to one. In general, however, it will be an approximation with the true value depending on the exact geometry of the resultant field. The validity of the approximation will also depend on the bead diameter being small compared to the beam waist.

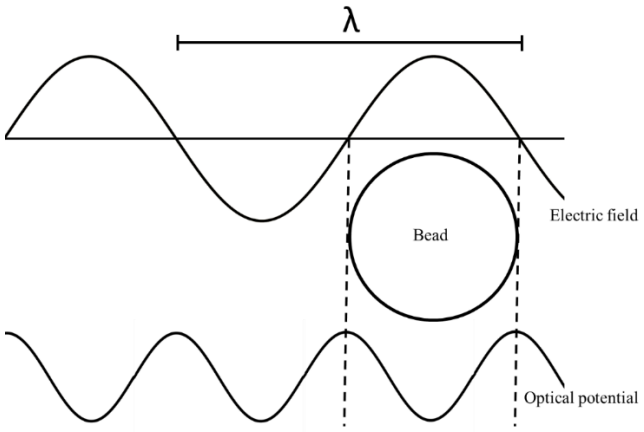

Figure 4.1. Diagram showing a bead of half a wavelength's diameter (we will later find that this bead size presents a local maximum for *A* (actually an approximation to the local maximum for *A*, under the volume-weighted averaged squared electric field model).

The volume-weighted average squared electric field $\langle E^2 \rangle$, can be calculated as follows:

$$\frac{4}{3}\pi R^3 \langle E^2 \rangle = \int E^2(x,r)\, dV \tag{4.1}$$

$$\frac{4}{3}\pi R^3 \langle E^2 \rangle = E_{max}^2 \int_{x=x_0-R}^{x_0+R} \int_{r=0}^{\sqrt{R^2-(x-x_0)^2}} cos^2 kx\, 2\pi r\, dr\, dx \tag{4.2}$$

$$\frac{\langle E^2 \rangle}{E_{max}^2} = \frac{3}{4R^3} \int_{x=x_0-R}^{x_0+R} (R^2 - (x-x_0)^2) \left(\frac{1}{2} cos\, 2kx + \frac{1}{2}\right) dx \tag{4.3}$$

$$\frac{\langle E^2 \rangle}{E_{max}^2} = \frac{3}{8R^3} \int_{u=-R}^{+R} (R^2 - u^2)\big(cos\big(2k(u+x_0)\big) + 1\big)\, du \tag{4.4}$$

$$\frac{\langle E^2 \rangle}{E_{max}^2} = \frac{1}{2} + \frac{3sin2kR - 6(kR)cos2kR}{16(kR)^3} cos2kx_0 \tag{4.5}$$

$$\frac{\langle E^2 \rangle}{E_{max}^2} = \frac{1}{2} + \frac{3\sqrt{1+(2kR)^2}}{(2kR)^3} sin\left(2kR - sin^{-1}\left(\frac{2kR}{\sqrt{1+(2kR)^2}}\right)\right)\left(cos^2 kx_0 - \frac{1}{2}\right) \tag{4.6}$$

As we would hope, equations 4.5 and 4.6 tend to one as kR and kx_0 tend to zero. Additionally, the prefactor to the cos-squared term in equation 4.6 also tends to unity as kR tends to zero.

The prefactor to $cos^2 kx_0$ in equation 4.6 gives us a modifying factor on the effective value of *A*, for larger spheres. The other terms are just small additive changes in the energy per photon in the cavity *i.e.* an effectively very slightly different cavity length. For the radial dynamics these extra terms are important, however they can be largely ignored when calculating the axial dynamics of the bead, as they just slightly alter the baseline of the detuning of the cavity.

So the effective value of *A* for larger beads, which here we call A_R, is given by:

$$A_R = \frac{3\sqrt{1+(2kR)^2}}{(2kR)^3} sin\left(2kR - sin^{-1}\left(\frac{2kR}{\sqrt{1+(2kR)^2}}\right)\right) A_0 \tag{4.7}$$

Where A_0 is given by equation 3.38.

When $A_R = 0$ this would mean that the bead would not see any axial field and so would travel freely along the length of the laser cavity, although it would still remain trapped radially. When A_R goes negative this would mean that the bead goes from being high field seeking to low field seeking.

4.1.3 Oscillation Frequencies

The general formula for the axial and radial frequency of oscillation for beads that are small compared to both the cavity diameter and the wavelength of the bead (ω_{x0} and ω_{r0} respectively) are given as follows:

$$\omega_{x0} = k\sqrt{\frac{A\hat{a}^\dagger\hat{a}}{m}} \tag{4.8}$$

$$\omega_{r0} = \frac{1}{w}\sqrt{\frac{2CA\hat{a}^\dagger\hat{a}}{m}} \tag{4.9}$$

Where *C* is the constant given in the table from section 3.1.5, based on the precise definition of the cavity width, *w* (assuming the simplest Gaussian profile for the radial dependence of the cavity intensity). Note for a given material composition, and for small beads, the value of *A* scales with *m* and, as such, these frequencies are independent of the

size of the bead (so long as the bead is still at least an order of magnitude smaller than one wavelength).

Also, since the cavity width tends to be nearly an order of magnitude larger than the wavelength of the laser, we expect ω_r to be smaller than ω_x.

For beads that are large, as compared to the laser wavelength, but still small compared to the cavity width ($w \gg R \sim \lambda$), these frequencies are reduced to:

$$\omega_{xR} = \omega_{x0}\sqrt{\left|\frac{3\sqrt{1+(2kR)^2}}{(2kR)^3}\,sin\left(2kR - sin^{-1}\left(\frac{2kR}{\sqrt{1+(2kR)^2}}\right)\right)\right|} \tag{4.10}$$

$$\omega_{rR} = \omega_{r0}\sqrt{\frac{1}{2}+\frac{1}{2}\left|\frac{3\sqrt{1+(2kR)^2}}{(2kR)^3}\,sin\left(2kR - sin^{-1}\left(\frac{2kR}{\sqrt{1+(2kR)^2}}\right)\right)\right|} \tag{4.11}$$

4.1.4 Limitations of this model

There are a number of ways in which this model will give only an approximation to the correct frequencies.

Firstly, there are zero-point fluctuations in both *x* and *r* positions, such that the field seen is actually reduced from that assumed above. This will slightly reduce both the frequencies above.

Secondly, in so far as the bead is an appreciable fraction of the cavity diameter, the effective field seen by the bead, near the centre of the cavity, is actually reduced further. This, again, will slightly reduce both frequencies of oscillation.

Thirdly, there is an inherent approximation in the Volume Weighted Average Field Intensity method. Actually, it is required that we recalculate the full electric field under this new dielectric perturbation. This approximation is more severe the higher the refractive index of the bead.

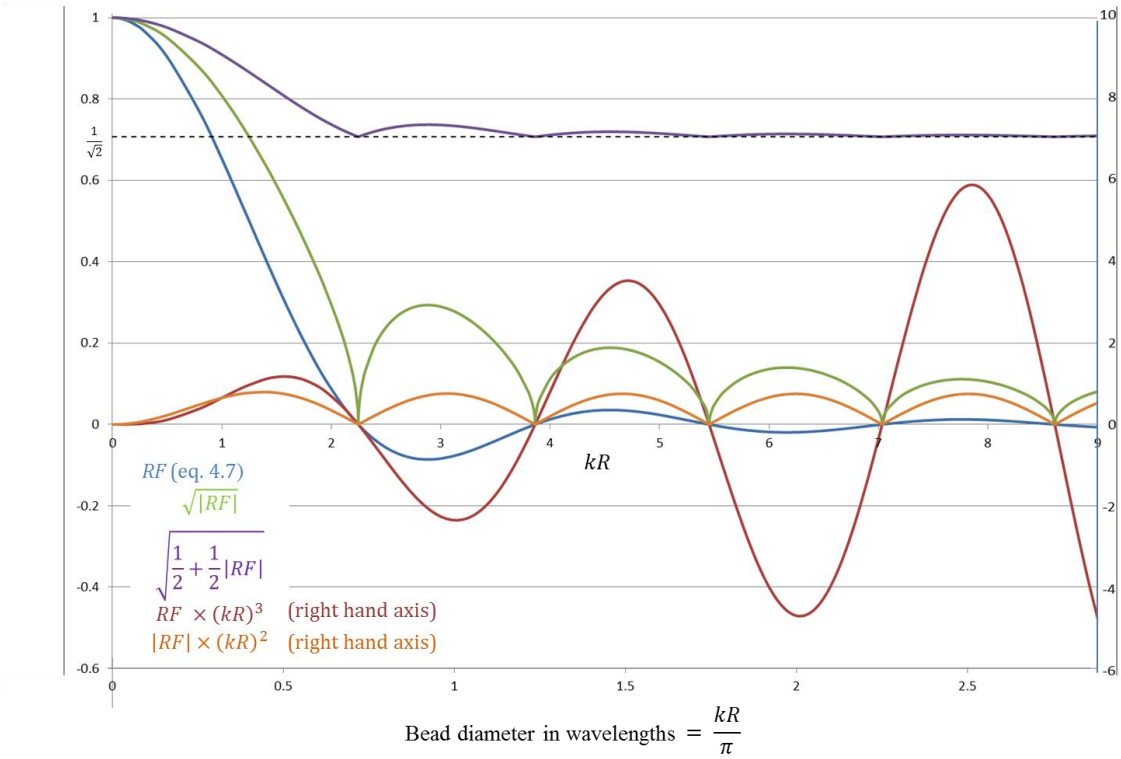

Figure 4.2. Graph showing how bead couplings and oscillation frequencies vary with bead size.

The blue line shows the reduction factor (RF) from equation 4.7, a negative reduction factor means that the bead becomes low field seeking instead of high field seeking.

The red line shows the reduction factor multiplied by the cube of the bead radius. This shows the functional form of how the value of *A* varies with bead diameter.

The green line shows the square root of the absolute value of the reduction factor. This shows the functional form of how the axial frequency of oscillation varies as the radius increases. See equation 4.10.

The orange line shows the functional form of A/R which, we will see, is a relevant statistic when considering an attempt to cool the system to close to the ground state in the face of an external heat source of constant power. The first and most important maximum of this line occurs for a bead diameter of 0.44λ.

Finally, the purple line shows how the radial frequency of oscillation changes with bead size, relative to that of a small bead. See equation 4.11. Both frequency curves are shown relative to 1 for a small bead, though, of course, a small bead will normally have a much higher axial frequency of oscillation than its radial oscillation frequency.

There are some particular points of interest that are worth picking out. The extrema of A, according to this model, occur for bead diameters that take integer multiples of $\lambda/2$. The zeroes of the axial frequencies (ω_x – green line) occur nearly half way between these extrema, tending to the midpoint for the largest beads. So the first zero is at 0.715 λ, the second at 1.23 λ, the third at 1.74 λ tending towards all the odd, quarter multiples of λ.

4.1.5 Real Data

James Millen and others in the group carried out an experiment measuring both the axial and radial trapping frequency of beads in a laser standing wave.[110] The laser standing wave field used our typical 1064 nm laser and the beads had a range of diameters from 50 to over 1 µm *i.e.* up to a whole wavelength.

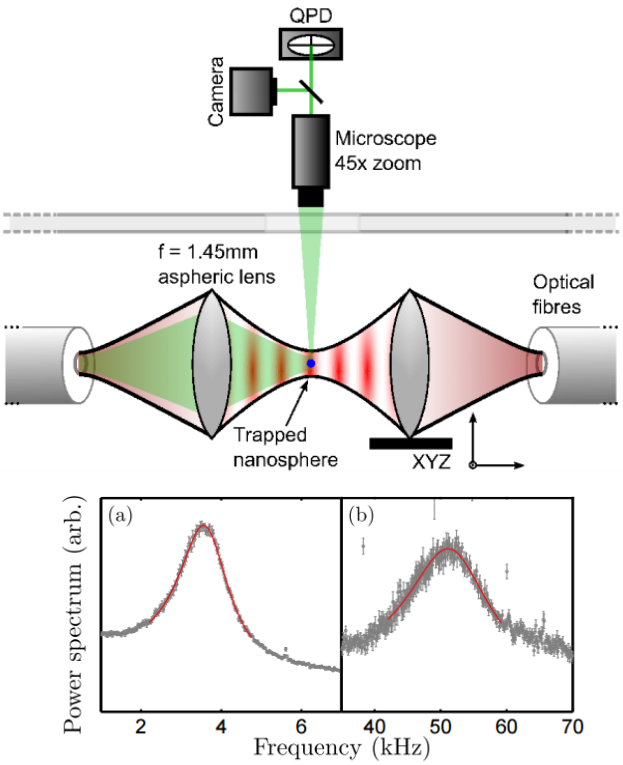

Figure 4.3. Experimental power spectra at 5 (mbar PI: James Millen) calculated from direct measurement of the position of a trapped 200 nm bead. Position of the peak tells us the trapping frequency while the area of the peak would tell us the trapped energy. (a) is for radial frequency measurement while (b) is for the axial motion.

The glass used had a refractive index of 1.5 and a density of 2,100 kg m^{-3}.

Rather than using a reflective optical cavity this experiment was done with two, phase locked, counter propagating lasers of, in one instance, 37.5 mW each and in the other instance 150 mW each (P_L = 37.5 mW, 150 mW).

Assuming that there is no effective optical cavity (in other words each photon from a laser passes along the cavity and is then lost) then the formula for $A\hat{a}^\dagger\hat{a}$ transforms as follows:

$$\frac{\hbar\omega_c\hat{a}^\dagger\hat{a}}{V_{cav}} \rightarrow \frac{2P_L}{\pi w^2 c} \tag{4.12}$$

So:

$$A_{Chang}\hat{a}^\dagger\hat{a} = \frac{3}{4}\frac{\epsilon_r - 1}{\epsilon_r + 2}\frac{V_{sphere}}{V_{cav}}\hbar\omega_c\hat{a}^\dagger\hat{a} \rightarrow \frac{3}{2\pi}\frac{P_L}{w^2 c}\frac{\epsilon_r - 1}{\epsilon_r + 2}V_{sphere} \tag{4.13}$$

For small beads (and taking $C = 1$) we expect the radial frequency to be $\omega_{r0} = \frac{1}{w^2}\sqrt{\frac{3P_L}{\pi c\rho_{glass}}\frac{\epsilon_r-1}{\epsilon_r+2}}$ and the axial frequency should be $\omega_{x0} = \frac{k}{w}\sqrt{\frac{3P_L}{2\pi c\rho_{glass}}\frac{\epsilon_r-1}{\epsilon_r+2}}$.

Under this VWASF model we expect that for beads much longer than a wavelength the radial frequency to tend to $\omega_{rR|_{\lambda \ll R \ll w}} \rightarrow \frac{1}{w^2}\sqrt{\frac{3P_L}{2\pi c\rho_{glass}}\frac{\epsilon_r-1}{\epsilon_r+2}}$ while the axial frequency tends to zero.

Figures 4.3 and 4.4 show some of the early experimental results (from James Millen and Peter Barker). The green line is that VWSAF approximation from section 4.1.2.

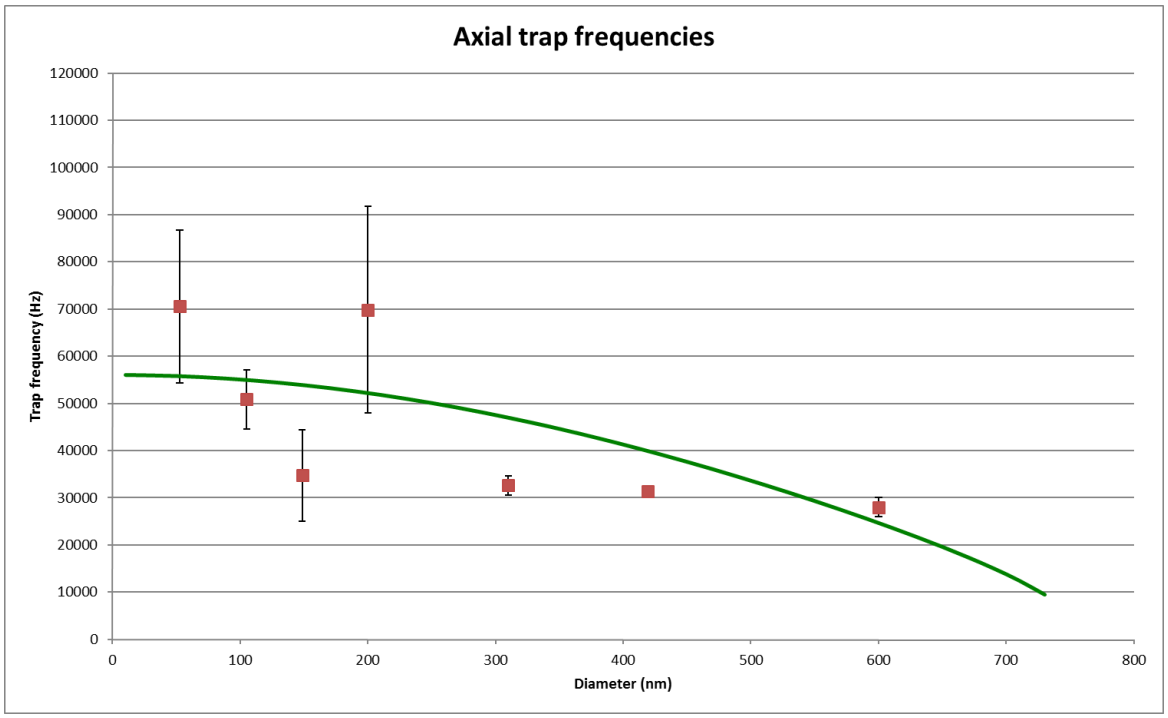

Figure 4.4. Graph showing axial frequency of oscillation of a number of beads. Experimental results by James Millen and Peter Barker, as compared to theoretical line showing the VWASF approximation. These results were taken without an optical cavity, with two counter propagating, 1064 nm laser beams, each of 37.5 mW power. The radius of the laser beam was 2 µm. The glass beads had density 2,100 kg m^{-3} and refractive index 2, *i.e.* $\epsilon_r = 4$).

Frequencies are in oscillations per second *i.e.* $f = \frac{\omega_x}{2\pi}$.

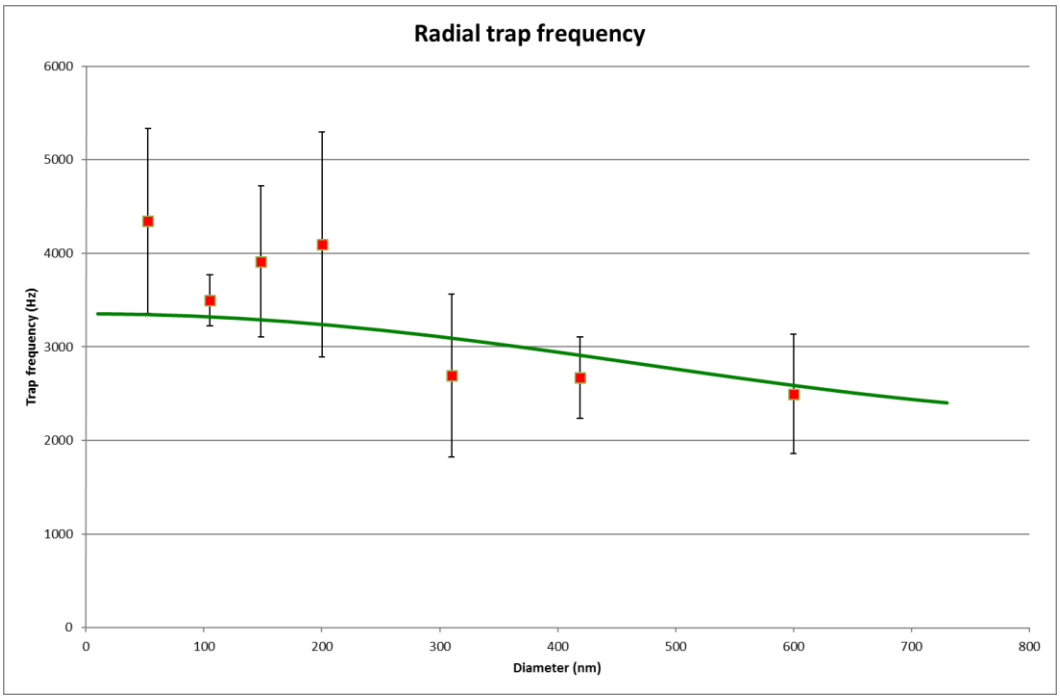

Figure 4.5. Graph showing radial frequency of oscillation, experimental data and VWASF theoretical prediction. Parameters as per graph 4.3.

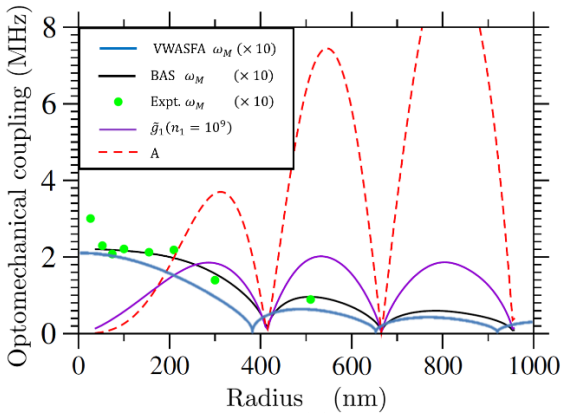

Figure 4.6. Further experimental results (by James Millen and Peter Barker) from our paper[110] as compared against two theoretical models. The black line is from the (more accurate) theory of Barton, Alexander and Shaub (BAS)[131], whereas the blue line is the VWASFA from 4.10. Again, there is no real optical cavity, just a pair of counter-propagating laser beams. The laser is focussed down to a waist, which was initially unknown (beyond knowing that is was of order a few microns). However, from the ratio of the axial to radial oscillation frequencies, for small beads, we can calculate that, in this case, the diameter is 1.34 microns. $w = \frac{\sqrt{2}}{k}\frac{\omega_{x0}}{\omega_{r0}} = 0.67\mu m$. This time each trapping laser has a power of 150 mW, while the remaining parameters are as per graph 4.3.

If you are interested in cooling to the ground state, against some fairly fixed power of external heating, *H*, it is important to have strong cooling but also to have a large value of ω_M.

In such a circumstances the average phonon occupancy, $\bar{n}$, is given by:

$$\bar{n} = \frac{H}{\hbar \omega_M \Gamma_{cool}} \tag{4.14}$$

So the relative factor would be:

$$\omega_M \Gamma_{cool} \rightarrow \sqrt{\frac{A^3 k^2 P}{2\sqrt{2} m \hbar^6 \omega_c \kappa}} \qquad as\ P \rightarrow \infty \tag{4.15}$$

This is why we showed the orange line from graph 4.2 or the purple line from graph 4.5.

So we do not wish to simply boost *A* but rather the ratio of the cube of *A* to the mass of the bead. Since the local maxima of *A* with respect to *R* grows with R^3 (and the mass of the bead also, obviously grows with R^3) the later maxima of *A* do not help us. Furthermore, larger beads may present other difficulties (*e.g.* the heating from other sources may be larger for larger beads).

If we assume that the laser wavelength is always going to be 1064 nm then the best diameter for a bead, to maximise the chance of reaching ground state cooling, is around 600 nm (if we take the accurate formula for the reduction factor in *A*) or 470 nm if we use the VWASF approximation.

4.1.6 Direct calculation of the Axial frequency for $\lambda \ll R > w$

At one point I thought it might be possible to calculate the value of *A* directly using a ray-diagram approach.

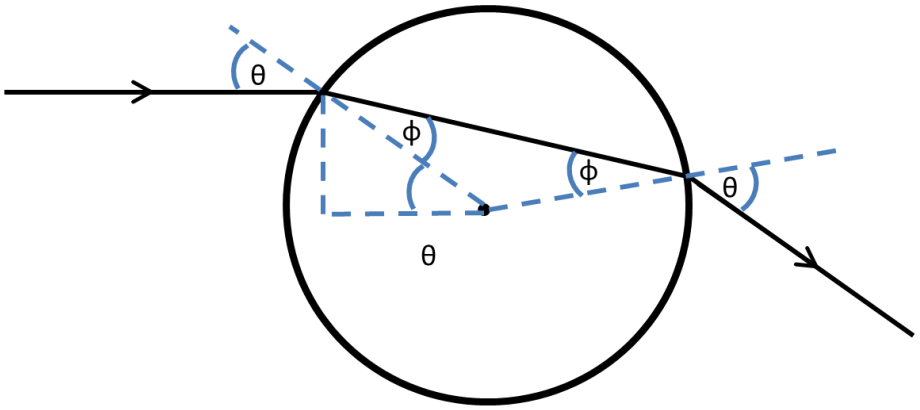

Deflection angle = 2 θ – 2 ϕ

Figure 4.7. Photon path through a bead of radius *R* and refractive index *n*. We have assumed that the photon beam is incident with the bead at distance *r* above the centre of the profile of the bead as looked at along the laser cavity. The beam-bead incidence angle is θ and the internal angle of refraction is ϕ. We have assumed (without loss of generality) that the incident, internally propagating, and exiting beam are in the same plane. The overall angular deviation of the beam from passing through the bead is *D(h, R)*. *D(h, R)* = 2θ - 2ϕ. It will be helpful later if we note now that for $n > \sqrt{2}$ it is possible to bend some of the light through an obtuse angle.

This actually gives a huge over-estimate of the force, perhaps because the reflected beam partially counteracts the force exerted by the refracted beam.

To calculate the force on the bead in this way we first consider the force from a single photon, or beam of photons, passing through the bead and being refracted out of the cavity.

Initially we will assume that the photon path (both in and out of the bead – of refractive index *n*) and the direction in which we are resolving the force (*i.e.* up) are co-planar.

We can see by considering the geometry of the problem, and by invoking Snell's Law that:

$$D(r,R) = 2sin^{-1}\left(\frac{r}{R}\right) - 2sin^{-1}\left(\frac{r}{nR}\right) \tag{4.16}$$

$$sin\,D = \frac{2r}{R}\sqrt{1-\frac{r^2}{R^2}}\left(1-\frac{2r^2}{n^2R^2}\right) - \frac{2r}{nR}\sqrt{1-\frac{r^2}{n^2R^2}}\left(1-\frac{2r^2}{R^2}\right) \tag{4.17}$$

To obtain equation 4.17 from equation 4.16 we have used double angle trigonometric identities. It will be useful to have *sin D* as this will help us to resolve the change of momentum of light passing through the bead, and hence the force on the bead.

The impulse upwards on the bead is equal to the change in momentum downwards of the light passing through the bead. With a little algebra we can determine the small force upwards on the bead as a result of radiation of intensity, *I*, over a small area $rdrd\psi$ of the bead profile.

$$dF(r,\psi,R) = \frac{-2I}{c} r\,drd\psi\,cos\,\psi\,\frac{2r}{R}\left(\sqrt{1-\frac{r^2}{R^2}}\left(1-\frac{2r^2}{n^2R^2}\right) - \frac{1}{n}\sqrt{1-\frac{r^2}{n^2R^2}}\left(1-\frac{2r^2}{R^2}\right)\right) \tag{4.18}$$

The leading "2" is because this equation is for a pair of counter-propagating laser beams.

So, in the unlikely event that the beam was very narrow (*i.e.* $w \ll R$ while still maintaining $w \gg \lambda$) and focussed at (x_0, h_0) we can replace $I\,dxdh \rightarrow P_L$ to give:

$$F_x(r_0,\psi_0,R) = \frac{-2P_L}{c}cos\,\psi\,\frac{2r_0}{R}\left(\sqrt{1-\frac{r_0^2}{R^2}}\left(1-\frac{2r_0^2}{n^2R^2}\right) - \frac{1}{n}\sqrt{1-\frac{r_0^2}{n^2R^2}}\left(1-\frac{2r_0^2}{R^2}\right)\right) \tag{4.19}$$

However, this is not the result we are likely to be interested in. If we assume a beam in the TE10 mode with an *r*-separation of r_0 we use $I = I_0 exp\left(\frac{-C\left(r^2+r_0^2-2rr_0cos\,\psi\right)}{w^2}\right)$ with $I_0 = \frac{CP_L}{\pi w^2}$.

The general form for $w, R \gg \lambda$ with any ratio of *w* to *R* for a beam in the TE10 mode is given by:

$$F = \frac{-2CP_L}{\pi c w^2} \int_{r=0}^{R} \int_{\phi=0}^{2\pi} exp\left(\frac{-C(r^2 + r_0^2 - 2rr_0 cos\,\psi)}{w^2}\right) \cos\psi \frac{2r}{R} \left(\sqrt{1 - \frac{r^2}{R^2}} \left(1 - \frac{2r^2}{n^2 R^2}\right) - \frac{1}{n} \sqrt{1 - \frac{r^2}{n^2 R^2}} \left(1 - \frac{2r^2}{R^2}\right) \right) r\, dr d\psi \tag{4.20}$$

The general equation can be simplified substantially by considering the case of most interest to us, which is where $w \gg R \gg \lambda$. In that case we can make the approximation:

$$\int_{\phi=0}^{2\pi} exp\left(\frac{-C(r^2 + r_0^2 - 2rr_0 cos\,\psi)}{w^2}\right) cos\,\psi \; d\psi \approx exp\left(\frac{-Cr^2}{w^2}\right) \int_{\phi=0}^{2\pi} \left(1 + \frac{2Crr_0 cos\,\psi}{w^2} + O(r_0^2)\right) cos\,\psi \; d\psi = \frac{2\pi C r_0}{w^2} exp\left(\frac{-Cr^2}{w^2}\right) \tag{4.21}$$

Making the approximation that $w \gg R$ (*i.e.* $\exp\left(\frac{-CR^2u^2}{w^2}\right) \approx 1$) and then substituting $u = \frac{r}{R}$ into equation 4.20 gives:

$$F = \frac{-8C^2 P_L R^3 r_0}{c w^4} \int_{0=0}^{1} u^3 \left(\sqrt{1 - u^2} \left(1 - \frac{2u^2}{n^2}\right) - \frac{1}{n} \sqrt{1 - \frac{u^2}{n^2}} (1 - 2u^2) \right) du \tag{4.22}$$

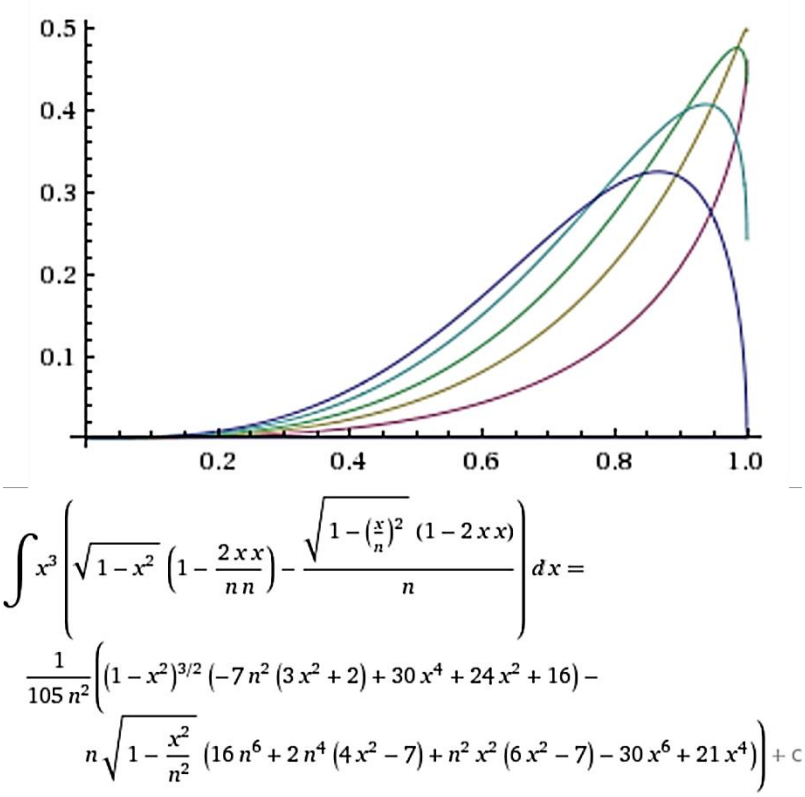

Figure 4.8. Top: Graph of the unitless integrand from equation 4.22 plotted against *u*. Values of *n* shown, in colours from red to blue, are *n* = 1.2, 1.5, 2.0, 4.0 and for $n \to \infty$ respectively. Bottom: The indefinite integral computed by "Wolfram Alpha"

The use of a computerised indefinite integral (Figure 4.8) yields:

$$F = \frac{-8C^2 P_L R^3 r_0}{cw^4}\left(\frac{2n^5(8n^2-7)+2(7n^2-8)-(n^2-1)^{\frac{3}{2}}(16n^4+10n+9)}{105n^2}\right) \tag{4.23}$$

Which means that the frequency of oscillation for small oscillations perpendicular to the laser propagation is:

$$\omega_r = \frac{C}{w^2}\sqrt{\frac{6P_L}{\pi c \rho_{glass}}}\left(\frac{2n^5(8n^2-7)+2(7n^2-8)-(n^2-1)^{\frac{3}{2}}(16n^4+10n+9)}{105n^2}\right)^{\frac{1}{2}} \tag{4.24}$$

This frequency is found to be far too high and this is because of an over-estimate of the force. We have not taken into account the fact that much of the ray gets reflected both externally and internally in accordance with the Fresnel reflection/transmission coefficients.

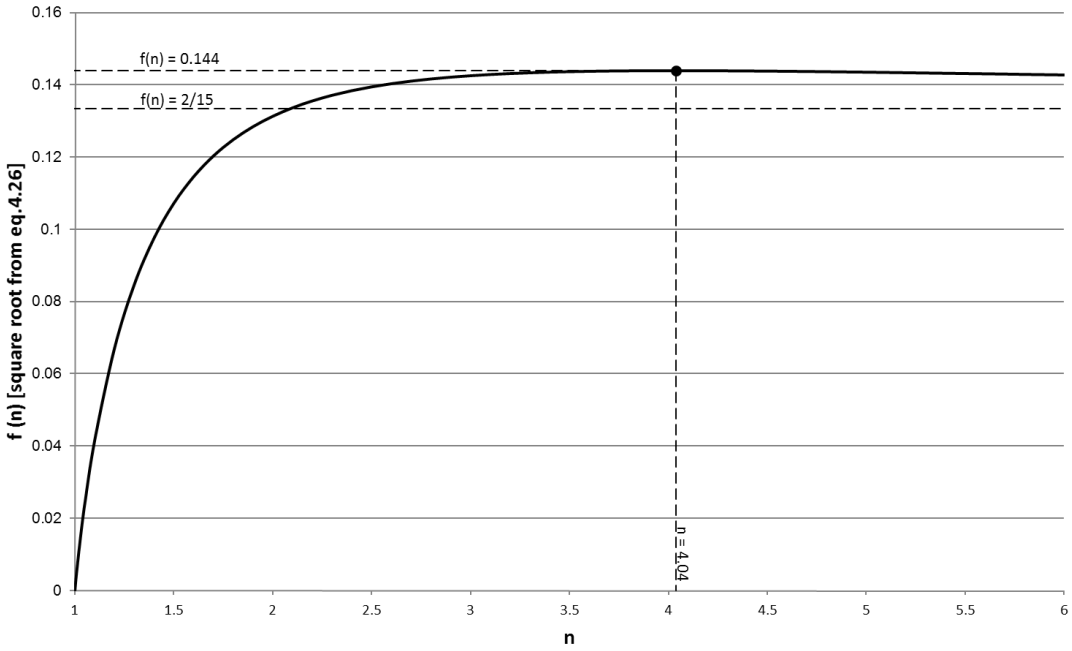

Figure 4.9. The first thing to notice about this graph is that the force rises very quickly with *n*. According to this model the force does not grow significantly after about *n*=2 (where it moves to within 90% of its maximum value). The second thing to notice is that for *n* > 4.0375 so much of the light is bent through an obtuse angle (see Figure 4.7) that the force on the bead actually starts to decrease, although it approaches a limiting value of 92.6% of this maximum force. However, this is all somewhat moot given that real materials rarely exhibit *n* > 4.

4.2 Other sources of heating

We are interested in reaching the ground state of the centre of mass motion of the bead in the optical trap.

The main impediment to achieving ground state cooling is the background gas that heats the bead by a variety of mechanisms. The most important is simple Brownian heating. There is also heating by radiometric forces from the background gas.

At very low pressures we must consider heating as a result of the recoil from photons emitted by the sphere's thermal (or black/grey-body) emission.

Finally, there are a variety of other, more minor, heating and damping effects such as the stochastic variation in the mode occupancy, the recoil from scattered photons from the laser field and, perhaps, even the off-spherical geometry of the bead.

4.2.1 Brownian damping (and heating) by background gas

On the average the forces on a stationary sphere, from collisions with the background gas, should cancel out. However, because a moving sphere sees more (and more energetic) collisions with its front than its rear, it will experience a damping force (*i.e.* air resistance). As well as this, the stochastic nature of these collisions are such that they also impart some thermal energy to the centre of mass motion of the sphere.

Here we derive the magnitude of these forces:

The rate, R_{col}, at which a gas of average speed $\bar{v}$ and number density *n* collides with a stationary sphere of radius R, is the same as the rate at which a sphere of velocity $\bar{v}$ would collide with stationary gas. This rate is thus:

$$R_{col} = \pi R^2 n \bar{v} \qquad OR \qquad \tau_{col} = \frac{1}{\pi R^2 n \bar{v}} \tag{4.25}$$

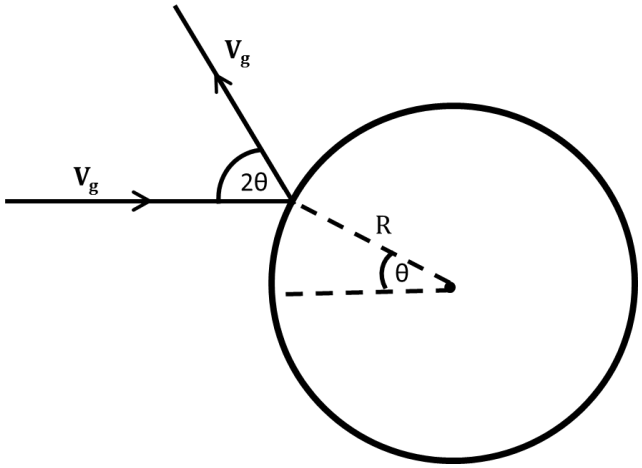

Figure 4.10. The momentum kick from a gas molecule, felt by an initially stationary bead, in the direction of travel of the original direction of travel of the gas molecule, is given by equation 4.25. Equation 4.26 shows that, on average, this is just the momentum of the incident gas molecule.

Assuming the sphere is very much heavier than the gas particle the horizontal momentum "kick" (Δp_h) imparted by the collision is given by:

$$\Delta p_h = m_g v_g (1 + cos\, 2\theta) \tag{4.26}$$

The average horizontal momentum "kick" is therefore:

$$\langle \Delta p_h \rangle = \frac{\int_{\theta=0}^{\pi/2} \Delta p_h dA}{\int_{\theta=0}^{\pi/2} dA} \tag{4.27}$$

$$= m_g v_g \frac{\int_{\theta=0}^{\pi/2} (1 + cos\, 2\theta)(2\pi R\, sin\, \theta)(Rd\theta)(cos\, \theta)}{\int_{\theta=0}^{\pi/2} (2\pi R\, sin\, \theta)(Rd\theta)(cos\, \theta)} = m_g v_g$$

So the average momentum kick for a stationary sphere, in the direction of travel of an incident gas particle, is simply the initial momentum of that incident gas particle.

However, we are not mainly interested in the kick received by a stationary glass sphere, but rather we are interested in the kick received by a sphere that is moving relative to the bulk motion of the background gas.

Consider such a collision in two frames of reference (see Figure 4.10). The first is the stationary frame of the bulk of the background gas (also the stationary form of the apparatus, the lasers, the lab *etc.*). The second is the stationary form of the glass sphere (*i.e.* the view of the collision from a video camera moving with the sphere).

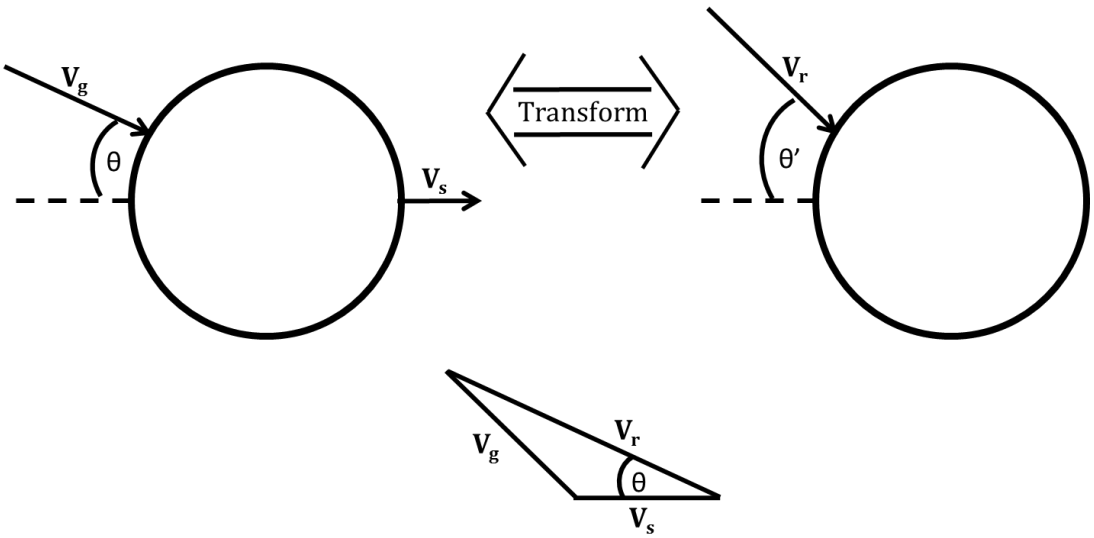

Figure 4.11. It will be useful to consider the incident velocity of the gas both in the lab frame (left) and in the rest frame of the bead (right) (v_g and v_r) and to consider that

the magnitude of these velocities are related to the velocity of the sphere via the cosine rule. We can assume without loss of generality that the sphere is travelling in the horizontal direction in the lab frame (we will call the magnitude of this velocity v_s). We can then consider two angles *i.e.* the angle between the velocity of the gas and the horizontal in both the lab and the stationary frame. By considering the x and y components of the molecule's velocity we can write down the relationship between these angles, as given by equation 4.28.

We can then consider the angle that the incoming molecule makes (in each frame) with the direction of travel of the glass sphere (as observed in the lab frame) – see Figure 4.11 and equation 4.28.

$$sin\,\theta' = \frac{v_g\,sin\,\theta}{\sqrt{v_g^2 + v_s^2 - 2v_g v_s\,cos\,\theta}} \tag{4.28}$$

Pulling together what we know from equations 4.27 and 4.28 we can determine that the average impulse (*i.e.* "kick") imparted by a collision from a gas molecule, from a particular direction, θ, to the direction of travel of the bead is given by:

$$\begin{aligned} Impulse\left(\theta, v_g, v_s\right) &= m_g v_r\,cos\,\theta' \\ &= m_g\sqrt{v_g^2 + v_s^2 - 2v_g v_s\,cos\,\theta}\,\sqrt{1 - \frac{v_g^2 sin^2\theta}{v_g^2 + v_s^2 - 2v_g v_s\,cos\,\theta}} \\ &= m_g\sqrt{v_r^2 - v_g^2 sin^2\theta} \end{aligned} \tag{4.29}$$

All that is left in order to determine the average damping force felt by the bead is to know the rate of bombardment by gas particles from various values of theta, θ.

$$\begin{aligned} dR_{col} &= \pi R^2 n v_r \frac{2\pi\,sin\,\theta\,d\theta}{4\pi} \\ &= \pi R^2 n\sqrt{v_g^2 + v_s^2 - 2v_g v_s\,cos\,\theta}\,\frac{sin\,\theta}{2}\,d\theta \end{aligned} \tag{4.30}$$

Finally, we wish to find the average force on the sphere, which means integrating the product of equations 4.29 and 4.30 over the range of theta (from 0 to π).

$$\langle F\rangle = \int_{\theta=0}^{\pi} Impulse\ (\theta, v_g, v_s) dR_{col} \tag{4.31}$$

$$\langle F\rangle = \frac{\pi R^2 n m_g v_s v_g}{2} \int_{\theta=0}^{\pi} \frac{v_r(\theta)}{v_s} sin\,\theta \sqrt{\frac{v_r(\theta)^2}{v_g^2} - sin^2\theta}\, d\theta \tag{4.32}$$

If we assume that the gas is, on average, moving much faster than the sphere, then we can replace $\frac{v_r}{v_s}$ with $\frac{v_g}{v_s}\left(1 - \frac{v_s}{v_g}\cos\theta + O\left(\frac{v_s^2}{v_g^2}\right)\right)$:

Under this approximation equation 4.32 becomes:

$$\begin{aligned}
\langle F\rangle &\approx \frac{\pi R^2 n m_g v_s v_g}{2} \int_{\theta=0}^{\pi} \left(\frac{v_g}{v_s} - \cos\theta\right) \sin\theta \sqrt{1 - 2\frac{v_s}{v_g}\cos\theta - sin^2\theta}\, d\theta \\
&= \frac{\pi R^2 n m_g v_s v_g}{2} \int_{\theta=0}^{\pi} \left(\frac{v_g}{v_s} - \cos\theta\right) \sin\theta\cos\theta \sqrt{1 - 2\frac{v_s}{v_g\cos\theta}}\, d\theta \\
&\approx \frac{\pi R^2 n m_g v_s v_g}{2} \int_{\theta=0}^{\pi} \frac{v_g}{v_s} \sin\theta\cos\theta - \sin\theta\, cos^2\theta - \sin\theta\, d\theta \\
&= \frac{-\pi R^2 n m_g v_s v_g}{2} \int_{\theta=0}^{\pi} \sin\theta\, cos^2\theta + \sin\theta\, d\theta = \frac{-4\pi R^2 n m_g v_s v_g}{3}
\end{aligned} \tag{4.33}$$

Equation 4.33 gives the force for a gas of uniform velocity. To get the average force we simply average over the velocity distribution. So:

$$\langle \boldsymbol{F}\rangle . \hat{\boldsymbol{v}}_{\boldsymbol{s}} = \frac{-4\pi R^2 n m_g v_s \bar{v}_g}{3} \tag{4.34}$$

Chang *et al.*[125] quote this result as being:

$$\langle \boldsymbol{F}\rangle . \hat{\boldsymbol{v}}_{\boldsymbol{s}} = -m_g v_s \frac{8P_{gas}}{\pi \rho_{gas} v_{g-rms}} \tag{4.35}$$

Equations 4.34 and 4.35 can be shown to be equivalent by recalling that for a thermal gas, $v_{rms} = \sqrt{\frac{3\pi}{8}}\bar{v}$.

So, in conclusion, when we consider the gas damping on the momentum of a sphere the effect of background gas is:

$$\frac{d\langle \mathbf{p}\rangle}{dt} = -\frac{\gamma_g}{2}\mathbf{p} \qquad \text{Where} \qquad \frac{\gamma_g}{2} = \frac{4}{3}\pi R^2 n \bar{v}_g \frac{m_g}{m_s} \tag{4.36}$$

The fluctuation dissipation theorem states that the energy loss (or gain) of the bead due to interaction with the background gas will be:

$$\frac{d\langle E\rangle}{dt} = -\gamma_g\left(E - k_B T_g\right) \tag{4.37}$$

Which gives both the rate of cooling of an energetic sphere, due to the background gas and, perhaps more importantly, the rate of heating of the trapped-sphere-oscillator, from the background gas.

It will also be useful to write γ_g in terms of the molecular mass and sphere density (m_g and ρ_{glass} respectively) as well as gas pressure and temperature (P_g and T_g):

$$\gamma_g = 4\sqrt{\frac{2}{3\pi}}\frac{P_g}{\rho_{glass} R}\sqrt{\frac{m_g}{K T_g}} \tag{4.38}$$

$2R$	P_g	$\frac{1}{R_{col}}$	$\frac{1}{\gamma_g}$	$\frac{\hbar\omega_M}{k_B T_g}$	$\frac{\hbar\omega_M}{\gamma_g k_B T_g}$
100 nm	10^{-10} Torr	146 ms	14.5 days	2.7×10^{-8}	0.04 s
200 nm	10^{-10} Torr	36 ms	29 days	2.7×10^{-8}	0.07 s
600 nm	10^{-10} Torr	4.06 ms	87 days	2.0×10^{-8}	0.15 s
100 nm	760 Torr	1.9×10^{-14} s	0.17 μs	2.7×10^{-8}	4.5×10^{-15} s
200 nm	760 Torr	4.8×10^{-15} s	0.34 μs	2.7×10^{-8}	8.9×10^{-15} s
600 nm	760 Torr	5.3×10^{-16} s	0.99 μs	2.0×10^{-8}	2.0×10^{-14} s

Table 4.1. Table showing important timescales for gas heating for various bead diameters (column 1) and pressures (column 2). Column 3 shows the average time between hits from background gas – this is the smallest timescale associated with the gas-bead interaction and, over times less than this, the bead gas can be assumed to have no effects at all. Over times larger than this the gas may give rise to decoherence of the quantum state of the oscillator, even if there is no significant heating of the oscillator.

Column 4 shows the long thermal timescale of the oscillator – the timescale over which the background gas would, if unchecked by a cooling mechanism, raise the temperature of the oscillator to the temperature of the background gas. As you can see this timescale can be so long as to be unimportant in high vacuum.

Column 5 shows the size of the quantum energy scale of the oscillator in units of the thermal energy scale. As described in section 4.1.3, this is constant for small beads, but it starts to drop off for larger beads. Column 6 shows the quantum thermal timescale – the time over which the gas might heat the bead from its ground to its first excited state. As we can see, for this to be of order seconds requires a very strong vacuum. The other parameters used to calculate the values in this table are taken to be typical parameters of:

m_g = 4.8 x 10^{-26} kg – just a little more than the mass of a Nitrogen molecules

ρ_{glass} = 2,100 kg m^{-3} – the density of beads used by James Millen

T_g = 300 K – room temperature.

Table 4.1 shows that we need to have good vacuums in order to make observations of the ground state behaviour, and that we need to have even better vacuums if we are worried

about decoherence of any coherent quantum state of this oscillation. What vacuum is required depends, to some extent, on the relevant timescale of any observation we make, but vacuums close to 10^{-10} Torr may be needed. Vacuums of this rarefication have been achievable for a long time[132], and the best laboratory vacuums are around 10^{-15} Torr[133].

To keep the oscillator in ground state requires that the optical cooling timescale be smaller than the gas heating timescale.

4.2.2 Radiometric force by the background gas

Figure 4.12. A picture of a standard Crookes' Radiometer consisting of freely turning vanes (one side silvered and one side matt black) balanced on a needle in an evacuated chamber. Crookes' original idea was that the radiometer would be driven by differential photonic pressure as light was reflected from the silver side but absorbed by the dark side. This is why he called his radiometer a "light mill". However, this would have caused the vanes to move such that the dark side led while the silver side followed.

Crookes actually found that the radiometer moved in the opposite direction. This is because of the radiometric force, whereby gas hitting the black (and therefore hotter) side would recoil more quickly that the gas hitting the (colder) reflective side. The net force from this is much more considerable than the force of photon pressure on the vanes.

There is an optimum pressure of the gas that will depend on the dimensions of the vanes of the radiometer, but radiometers are often made with gas pressure of 0.01 to 0.1 Torr. At pressures of 10^{-5} to 10^{-4} Torr it is possible, if the fulcrum friction is sufficiently low, to see the radiometer spin the other way[134], due to the photon pressure on the vanes, as Crookes originally intended.

Radiometric gas-pressure forces can occur when two sides of the same body have a different temperature. The gas on the hot side of the object expands on contact with the object, pushing it away from the hot side. The most well-known example is that of Crookes' Radiometer (see Figure 4.12). However, the force only acts if there is a significant temperature change over less than the mean free path of the gas. Otherwise the hotter side will see a gas with a lower number density, and the pressure of the gas on each side of the body will equalise.

We wish to calculate the order of magnitude of radiometric forces on certain sizes of object, under certain vapour pressures and temperature differences.

In order to do this, we will need to know the mean-free path, l_μ, of a gas particle of radius, σ_g, within a gas of number density, n.

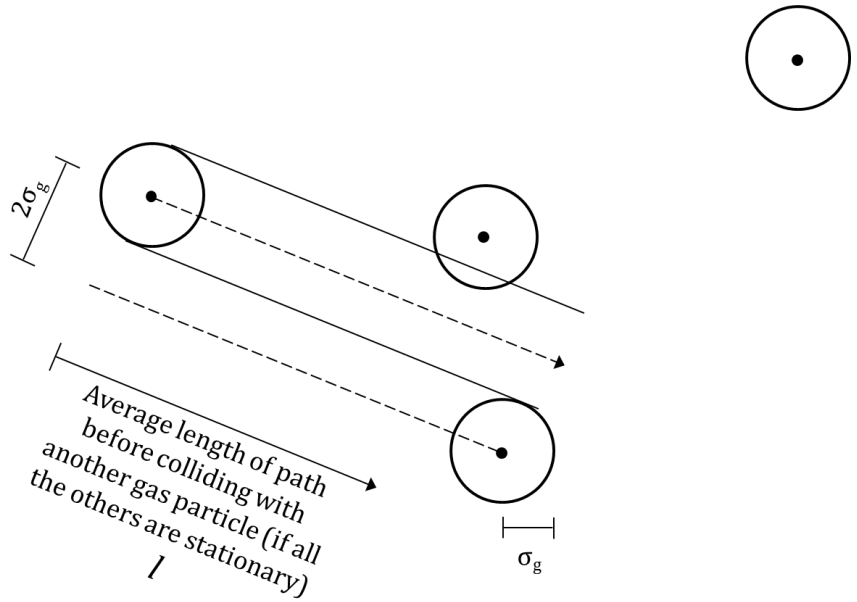

Figure 4.13. The mean free path of a spherical gas molecule travelling through a field of similar (but stationary) molecules would be such that $4\pi\sigma_g^2 l = \frac{1}{n}$. However, in reality, the other molecules are moving, which increases the average relative speed of molecules by a factor of $\sqrt{2}$. So $l_\mu = \frac{1}{4\pi\sqrt{2}\sigma_g^2 n}$.

So the mean-free path, l_μ,is given by (Figure 4.13):

$$l_\mu = \frac{1}{4\pi\sqrt{2}\sigma_g^2 n} \tag{4.39}$$

Imagine we have a small slab of width Δx and area, A (Figure 4.14). Let the top side have temperature T_1 and the bottom side have temperature T_2. The flux of particles hitting each side is the well-known result:

$$Flux = \frac{1}{4} n\bar{v} = \frac{1}{4} n \sqrt{\frac{8k_B T_g}{\pi m_g}} \tag{4.40}$$

Where T_g is the temperature of the gas.

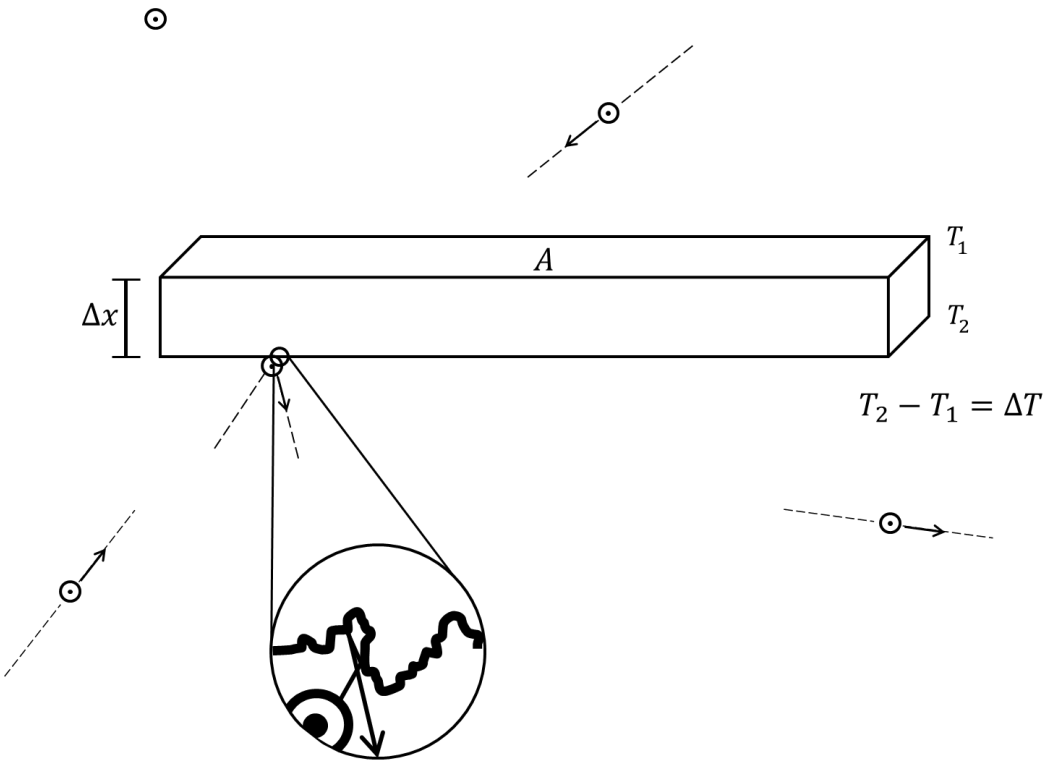

Figure 4.14. A slab of area, A with the bottom hotter than the top (T_2 > T_1) and thickness Δx. Such a slab will experience an upward radiometric force. However, this force will only be significant for a slab thinner than the mean-free path within the gas.

However, the idea that the temperature of the gas would be the same on both sides of the slab is only valid as long as the scale of the slab is smaller than the mean-free path of particles within the gas (*e.g.* $\Delta x < l_\mu$).

When the gas hits the matt surface of the top or bottom of the slab it thermalizes with the surface and recoils from that side with an average perpendicular velocity of:

$$v_{x-rms} = \sqrt{\frac{k_B T_{1,2}}{m_g}} \qquad OR \qquad \bar{v}_x = \sqrt{\frac{8k_B T_{1,2}}{3\pi m_g}} \tag{4.41}$$

This means that the net (upward) force on this small slab is:

$$\begin{aligned} F_{net} &= \frac{1}{4} n \sqrt{\frac{8k_B T_g}{\pi m_g}} A m_g \sqrt{\frac{8k_B}{3\pi m_g}} \left(\sqrt{T_2} - \sqrt{T_1}\right) \\ &= \frac{2nAk_B}{\pi\sqrt{3}} \sqrt{T_g} \left(\sqrt{T_2} - \sqrt{T_1}\right) \end{aligned} \tag{4.42}$$

The sign of this force simply tells us that the force on the body acts upwards if the top is colder than the bottom. If we assume that the difference in the temperature is relatively small compared to their average, and that the average temperature is the temperature of the gas in proximity to the slab, we can replace $T_1 \to T_g - \frac{1}{2}\Delta T$ and $T_2 \to T_g + \frac{1}{2}\Delta T$. Then the upward force on the cold-topped slab becomes:

$$F_{net|\Delta x, \sqrt{A} \ll l_\mu} \approx \frac{nAk_B}{\pi\sqrt{3}} \Delta T \tag{4.43}$$

But this is only for slabs of small width and small area *i.e.* where the length scales of the slab are small compared to the gas particle mean-free path. For slabs of larger area (but still small width) the force only acts on an area near to the perimeter of the slab, within about one mean-free path of the edge. So for a square slab:

$$F_{net|\Delta x \ll l_\mu \ll \sqrt{A}} \approx \frac{4nk_B l_\mu \sqrt{A}}{\pi\sqrt{3}} \Delta T \tag{4.44}$$

For a thicker slab the relevant temperature difference is no longer between the sides but rather the temperature difference between the surface of the slab and the temperature approximately one mean-free path from the side of the slab, along its width. This temperature difference is $\frac{l_\mu \Delta \mathrm{T}}{\Delta x}$.

$$F_{net|\Delta x,\sqrt{A}\gg l_\mu} \approx \frac{4nk_B l_\mu^2 \sqrt{A}}{\pi\sqrt{3}} \frac{\Delta T}{\Delta x} \tag{4.45}$$

The numerical pre-factors (in equations 4.45 and 4.46) should not be taken too seriously due to the inherent uncertainty in the approximations we have been making.

We will model a bead as being like a small cube, with opposite faces of different temperatures:

$$F_{radiometric|R\ll l_\mu} \approx nR^2 k_B \Delta R = P_g R^2 \frac{\Delta T}{T_g} \tag{4.46}$$

$$F_{radiometric|R\gg l_\mu} \approx nl_\mu^2 k_B \Delta R = \frac{k_B \Delta T}{32\pi^2 \sigma_g^4 n} = \frac{k_B^2 T_g \Delta T}{32\pi^2 \sigma_g^4 P_g} \tag{4.47}$$

So the peak radiometric force is given by:

$$F_{radiometric|MAX} \approx \frac{k_B R \Delta T}{4\pi\sigma_g^4} \tag{4.48}$$

It might be reasonable to assume that the bead could achieve a side to side temperature difference that varied by as much as fifty degrees across the bead's length. This is the roughest of rough estimates, and it could be that this temperature difference increased (something less than linearly) with the radius of the bead.

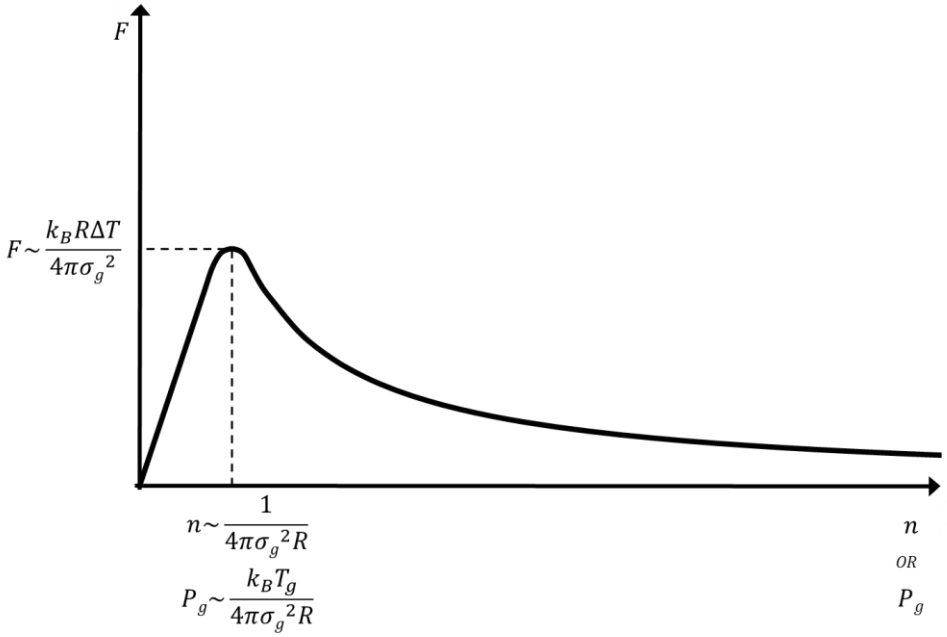

Figure 4.15. Sketch of the radiometric forces on a bead against number density (or pressure). Right of the peak $l_\mu < R$.

A reasonable approximation for σ_g would be the length of an N_2 bond, which is about one Angstrom (0.1 nm).

This means that for the smallest beads (say *R* = 50 nm) the peak radiometric force should not exceed 10^{-11} N. For the largest beads (say *R* = 300 nm) this force may be an order of magnitude larger, at 10^{-10} N. This would occur for a pressure of around 50 Torr for the smallest beads, and around 10 Torr for the largest beads *i.e.* the gas rarefaction where the mean-free path is similar to bead radius.

The maximum trapping force in the *x*-direction is $\omega_M^2 m_s \lambda \sim 10^{-11}$ N or, in the radial direction it could be as little as $\frac{\omega_M^2 m_s \lambda^2}{w} \sim 10^{-12}$ N (this is assuming the other parameters are as shown in section 3.7).

Radiometric forces in the radial direction may present a particular problem for two reasons. The first is simply that the confining forces are less strong in this direction. The less obvious reason is because if the bead moves in this direction then this will exacerbate the cross-bead temperature gradient that drives these radiometric forces, and the direction of such forces (with the hottest part of the bead being towards the middle of the laser cavity) will be to push the bead further from the centre of the laser cavity.

A larger bead can help matters slightly, as, although the maximum radiometric force grows proportionately to the radius of the bead, the confining force from the laser cavity grows with the cube of the radius of the bead (at least for $R < \frac{\lambda}{3}$).

Were we to pick a bead of diameter 600 nm, instead of 200 nm, this would improve any radiometric difficulties by an order of magnitude. If we used a slimmer cavity diameter (say 5 µm instead of 50 µm), this might give us another order of magnitude of improvement. Finally, although increasing the laser power will increase the temperature within the bead, it would also strengthen the confinement of the bead (so increasing the power from 4 mW to 40 mW might also give us another order of magnitude of improvement).

With these improvements it might be possible to passively cool through the radiometric threshold (although it is equally possible that we have underestimated the temperature difference by an order of magnitude – which would bring radiometric problems back into play).

All in all, although it may just be possible, with finely tuned parameters, to cool through the radiometric threshold at ~ 10 Torr, it might be necessary to have some kind of active negative feedback (for example the UCL ion trap) to confine the bead until we reach lower temperatures. Miller, Fonseca, Mavrogordatos, Monteiro and Barker have implemented a scheme of active trapping in an ion trap (Paul trap) to overcome the radiometric forces[135]. It might be possible later to turn off this active trapping once we pass the threshold pressure.

The radiometric force therefore presents a technical hurdle to be overcome as the gas pressure is decreased from atmospheric pressure down to the very low pressures at which we might hope to make quantum observations. However, at these very low pressures, the radiometric forces do not present a significant problem, because at pressures lower than 10-50 Torr, the radiometric forces drop in proportion to the pressure.

We do not anticipate radiometric forces being a problem near to the ground state for the simple reason that we would not attempt to cool the ground state until we had reduced the gas pressure to well below the radiometric threshold.

4.2.3 Heating by black body radiation (stochastic)

It has been suggested that the recoil from the thermal emission from the bead might cause some increase in the bead's centre of mass momentum.

The power of the black body spectrum coming off the black sphere (If it did radiate as a black body) would be $4\pi R^2\sigma_{SB}T_s^4$. However, we are not interested in this but rather in the (much smaller) power of heating of the centre of mass motion of the sphere as a result of the recoil from the emission of thermal radiation. Later we will perform an integration over the black body spectrum in order to determine this exactly, but for now we will make the ruthless approximation that all the photons coming off the bead are of energy k_BT_s. This result will give a good approximation to the order of magnitude of the recoil power.

Under this approximation the number of photons radiated in time, Δt, is $\frac{4\pi R^2\sigma_{SB}T_s^4}{k_BT_s}$ and each photon provides an impulse of $\frac{k_BT_s}{c}$ to the sphere.

An N-step random walk in three dimensions gives rise to an average displacement of $\sqrt{\frac{8}{3\pi}}\sqrt{N}$ times the step size.

Similarly, the average momentum imparted to the bead from the photons emitted in Δt seconds is:

$$\Delta p = \sqrt{\frac{8}{3\pi}}\sqrt{\frac{4\pi R^2\sigma_{SB}T_s^4\Delta t}{k_BT_s}}\frac{k_BT}{c} \tag{4.49}$$

So the energy gain by the bead is:

$$\Delta E = \frac{(\Delta p)^2}{2m_s} = \frac{4}{3\pi m_s}\frac{4\pi R^2\sigma_{SB}T_s^4}{k_BT_s}\frac{k_B^2T_s^2}{c^2}\Delta t \tag{4.50}$$

$$P_{recoil} = \frac{\Delta E}{\Delta t}\frac{4}{3\pi}\frac{k_BT_s}{m_sc^2}(4\pi R^2\sigma_{SB}T_s^4) \tag{4.51}$$

This does not depend hugely on the spectrum of the radiation as everything in the bracket can just be replaced with the total power of emission.

In this derivation we have assumed that all photons emitted by the black body spectrum of this bead have the same momentum $\frac{k_B T_s}{c}$ and energy $k_B T_s$ but we will now take a moment to fix the numerical pre-factor.

We have found from the above that the power of heating via recoil from black body radiation is proportional to the square of this photon momentum, multiplied by the numerical rate of photon emission.

However, really it is proportional to the integral of the square of photon momentum multiplied by the rate of photon emission at that momentum, over all photon momenta *i.e.* the amount of energy gained by the bead's centre of mass motion in a given time is proportional to the sum of the squares of all photon momenta (p_{photon}) emitted in that time.

$$\frac{\sum_{All\ Photons}\left(p_{photon}\right)^2}{4\pi R^2 \sigma_{SB} T_4^s \Delta t} = \frac{\int_{\lambda=0}^{\infty}\left(\frac{h}{\lambda}\right)^2 P_\lambda \frac{\lambda}{hc}\, d\lambda}{\int_{\lambda=0}^{\infty} P_\lambda\, d\lambda} \sim \frac{k_B T_s}{c^2} \tag{4.52}$$

Where h is the unreduced Planck's constant and $P_\lambda\, d\lambda$ is the power of emission between wavelengths of λ and $\lambda + d\lambda$. The functional form of P_λ is well-known as:

$$P_\lambda \propto \frac{1}{\lambda^5\left(exp\left(\frac{hc}{\lambda k_B T}\right) - 1\right)} \tag{4.53}$$

And so equation 4.53 becomes:

$$\frac{\int_{\lambda=0}^{\infty} P_\lambda \frac{h}{\lambda c}\, d\lambda}{\int_{\lambda=0}^{\infty} P_\lambda\, d\lambda} = \frac{h}{c}\frac{\int_{\lambda=0}^{\infty} \frac{1}{\lambda^6\left(exp\left(\frac{hc}{\lambda k_B T}\right) - 1\right)}\, d\lambda}{\int_{\lambda=0}^{\infty} \frac{1}{\lambda^5\left(exp\left(\frac{hc}{\lambda k_B T}\right) - 1\right)} d\lambda} \tag{4.54}$$

$$= \frac{k_B T}{c^2}\frac{\int_{u=0}^{\infty} \frac{1}{u^6\left(exp\left(\frac{1}{u}\right) - 1\right)}\, du}{\int_{u=0}^{\infty} \frac{1}{u^5\left(exp\left(\frac{1}{u}\right) - 1\right)} du} \tag{4.55}$$

The integrals on the top and bottom of 4.55 turn out to be $24\zeta(5)$ and $\pi^4/15$ respectively, where $\zeta(s)$ is the Riemann zeta function *i.e.* $\zeta(5) = \sum_{n=1}^{\infty} \frac{1}{n^5} = 1.036928 \ldots$ So:

$$\frac{\int_{u=0}^{\infty} \frac{1}{u^6\left(exp\left(\frac{1}{u}\right)-1\right)}\,du}{\int_{u=0}^{\infty} \frac{1}{u^5\left(exp\left(\frac{1}{u}\right)-1\right)}\,du} = \frac{360\zeta(5)}{\pi^4} = 3.832229 \ldots \tag{4.56}$$

Which means that our estimate in 4.51 was actually an underestimate by a factor of just under four.

We should probably not take the prefactor too seriously as the size of this will be a function of the greyness of the body (if anything actually this prefactor might be smaller than shown in 4.56).

Going back to the general form of equation 4.51 we can see that the recoil power equation contains a ratio between the energy of a single photon leaving the sphere and the sphere's entire nuclear annihilation energy. The nuclear annihilation energy of a small sphere will be of order Joules, while the thermal energy of photons emitted is of order tenths of an Electron Volt, so the ratio between these energy scales is 10^{-20}.

The fluctuation-dissipation theorem tells us that this heating would not continue without limit, in fact the power we have calculated would only be the power of heating if the oscillation temperature had reached zero. Rather, the effect of black-body radiation would be to draw the bead's oscillation temperature towards the bead's surface temperature. The idea that we could have black-body recoil damping (when the oscillation temperature was higher than the surface temperature – not a likely part of our parameter space but conceptually possible) may seem counter-intuitive and provides an interesting thought experiment in relativity.

From the Lab frame the forward travelling photons would seem to be slightly blue-shifted, while the backwards travelling photons would seem to be slightly red-shifted. This would lead to more momentum in the forward photons relative to the backwards photons, and hence, a damping force on the bead.

From the frame of the bead however, it is not clear where the damping force would come as the outgoing radiation would be emitted isotropically. However, in-coming thermal

photos hitting the bead would see a Doppler shift, and in the event that the bead's surface was in thermal equilibrium with, say, the surface of the vacuum chamber, the decelerating force on the bead from this would be identical to that seen in the Lab frame. So all observers would agree that the bead was experiencing a damping force, but the people in the Lab frame would say it was caused by the Doppler shift of the emission from the bead's surface while an observer travelling with the bead would argue that is was caused by the fact that the light hitting the "front" of the bead was bluer (*i.e.* more powerful) that the light hitting the rear of the bead. In fact, he would say that the surface ahead of him was hotter than the surface behind him.

Getting back to the mechanics of the oscillation damping it is useful to notice the similarity of the functional forms of the damping as a result of background gas, and the black-body radiation.

We also have to take into account that a transparent glass sphere is very much not a black body. The emissivity (or greyness) is likely to be, at most, about ten percent.

Equation 4.38 gave the damping rate γ_g such that the maximal heating power as a result of background gas is $\gamma_g k_B T_{gas}$:

$$\gamma_g = 4\sqrt{\frac{2}{3\pi}}\frac{1}{\rho_{glass} R}P_{gas}\sqrt{\frac{m_g}{KT_g}} \tag{4.57}$$

Similarly, we can find a damping rate γ_{BB} such that the maximal heating power as a result of black-body recoil is $\gamma_{BB} k_B T_{bead}$:

$$\gamma_{BB} = \frac{1440\zeta(5)}{\pi^5}\frac{1}{\rho_{glass} R}\frac{\sigma_{SB} T_{bead}^4}{c^2} \tag{4.58}$$

This means that the behaviour of the bead is as if there are two separate, and mutually non-interactive gasses in the vacuum chamber. As well as the real gas of temperature T_{gas} and pressure P_{gas} we have a virtual gas (made up of virtual particles of the same effective mass as the real gas particles *i.e.* just over 28 Daltons) of temperature T_{bead} and effective pressure P_{eff}, where P_{eff} is given by:

$$P_{eff} = 360\zeta(5)\sqrt{\frac{3}{2\pi^5}}\frac{\sigma_{SB}T_{bead}^4}{c^2}\sqrt{\frac{k_B T_{gas}}{m_{gas}}} \tag{4.59}$$

$$= \left(\frac{\varepsilon_{mis}}{0.1}\right)\left(\frac{T_{bead}}{300\,Kelvin}\right)^4\left(\frac{T_{gas}}{300\,Kelvin}\right)^{1/2} \; 4.039\,x\,10^{-13}\,Pascals \tag{4.60}$$

4.039 x 10^{-13} Pascals = 4.039 x 10^{-15} mbar = 3.029 x 10^{-15} mmHg. (4.61)

Where ε_{mis} is the emissivity of the surface.

So if the bead is the same temperature as the background gas then we can capture the dynamics by simply adding a very small amount (4 x 10^{-15} mbar) to the gas pressure.

If the bead is hotter than the background gas, then we have something a little more complicated whereby the damping rate is higher (going with the fourth power of temperature) but also the temperature that it damps towards is larger.

So the heating at cold temperatures would be proportional to the bead temperature to the power of 5 (4 for the increase in the heating rate pressure plus one for the fact that the power of heating is proportional to the heating rate times the temperature difference between the two reservoirs).

Most glass would melt at temperatures between 1700 and 1900 Kelvin. At 1900 Kelvin the heating from the black-boy spectrum would start to dominate over the gas pressure at about 4 x 10^{-10} mbar *i.e.* four orders of magnitude higher than for a 300 Kelvin bead.

We see in experiments that the bead does not normally melt, and furthermore, in a cavity with laser power 4mW and cavity diameter 25 μm even a perfectly black bead would only be able to reach a maximum temperature 2500 Kelvin. $T_{Max-BB} = \left(\frac{P_L}{\pi\phi_{bead}^2\sigma_{SB}}\right)^{1/4}$

At 2000 Kelvin, a 200 nm diameter spherical black-body radiates at 10^{-7} Watts, which means the power of recoil heating from black-body radiation cannot be more than about 10^{-27} to 10^{-28} Watts.

This would mean that the recoil heating would be adding one phonon (*i.e.* $\hbar\omega_M$) of energy every second or so (or even lesser power, for larger beads).

This compares to an optical cooling which, when well-tuned, can cut the energy of the oscillator by one e^{th} every 10^{-5} seconds. This recoil heating effect is therefore not particularly relevant.

4.2.4 Heating by black-body radiation (non-homogeneity)

When we examined the heating of the oscillator by buffeted by the gas (in sections 4.2.1 and 4.2.2) we found that there were general stochastic heating effects and also effects as a result of differences in temperature.

Similarly, with photon recoil from black-body radiation, the power can be increased considerably if we consider that some parts of the bead may be hotter (or blacker – *i.e.* of higher relative emissivity) than others.

In other words, rather than considering a stochastic force (as per section 4.2.3), there may be a directional force of the bead, due to differential albedo.

This would be akin to the force that gave rise to the Pioneer anomaly[136]. Pioneers 10 and 11 were unmanned space craft which, as they travelled away from the Sun, seemed to be slowing down slightly more than Newtonian gravity, solar wind, and other calculated phenomena could account for. For a long time, it was hypothesised that this might be a result of some non-Newtonian gravitational interaction, a deviation from the inverse-square law of gravity, or similar. However, the solution turned out to be that the pattern of high and low albedo areas of the craft led to systematically different overall levels of black-body radiation in different directions, and consequently, an additional deceleration for the craft.[137]

The most extreme potential for differential levels of thermal radiation within the bead would be if some large proportion of the bead was radiating like a black body while the other did not radiate at all. It is very unclear that even this would produce a problem as, with the bead being in thermal equilibrium with its surroundings, it would be hard to set up an averaged net force as a result of radiation pressure. Even with a dark spot on the surface of the bead that spot would also radiate through the bead and out the other side. Furthermore, the bead would be spinning, which would be likely to average out any net force (although not necessarily the thermal effects of such a force).

As an absolute upper limit to the size of any such force we could imagine that, say, a tenth of the total thermal radiation that could come from a black body of that size and temperature was emitted definitely in one direction (while all other radiation from the bead gave rise to self-cancelling forces).

Under such circumstances the bead experiences a force of:

$$F = \frac{1}{10}\frac{4\pi R^2 \sigma_{SB} T_s^4}{c} \tag{4.62}$$

If $T_s = 1000\ K$ and $R = 100\ nm$ this force $\sim 10^{-18}$ N.

The first thing to say is that Radiometric Forces from section 4.2.2 would dominate this force (and they would act broadly in the same direction *i.e.* a net force on the hotter side of the bead) down to about 10^{-8} Torr.

This leads to a couple of orders of magnitude of pressure where these forces may become relevant (at least a little more relevant than a force we have already dismissed as irrelevant). However, these forces could be mitigated substantially by the factors discussed earlier in this section *e.g.* by using a glass bead that was reasonably transparent and homogeneous, which does not radiate as a black body and which does not radiate one tenth of its thermal energy in a directed beam (which is what we have assumed here), or which achieves a temperature of only 500 K instead of 1000 K (giving a factor of 16 less in the way of radiation power).

This section shows us that it is important to make sure that our bead is reasonably transparent and homogeneous but, if we do that, the recoil forces from the bead's thermal emissions are not going to be an important source of heating.

4.2.5 Stochastic heating based on laser occupancy variation

The laser modes in our trapping mechanism have an occupancy of $\left|\alpha_{1,2}\right|^2 \pm \sqrt{\left|\alpha_{1,2}\right|^2}$. In other words, there is a stochastic variation in the photon occupancy that obeys Poisson statistics. This variation over time leads to a variable force exerted on the bead and therefore a heating of the bead.

To calculate the magnitude of this heating we will first consider the most basic optomechanical system of a driven cavity with a Hookean oscillator at one end (see diagram 4.15).

Such a system will have mean photon occupancy $|\alpha|^2$. If we were to suddenly put an extra N photons into the cavity the number would be $N + |\alpha|^2$.

This number would decay exponentially as:

$$N(t) = N(0)exp(-\kappa t) \tag{4.63}$$

In equation 4.60 $N(0)$ could be positive or negative. These extra photons would give rise to an extra force of:

Figure 4.16. One of the most basic optomechanical systems. A laser cavity of length L, with a mirrored mass on spring oscillator at one end. Spring constant k_{sp}, mass m, equilibrium displacement x_{eq}.

$$F = m\ddot{x} = k_{sp}\left(\frac{x_{eq}N(0)}{|\alpha|^2}\right)e^{-\kappa t} \tag{4.64}$$

$$\dot{x} = \left(\frac{k_{sp}x_{eq}N(0)}{|\alpha|^2}\right)^2 \int_{t=0}^{\infty} e^{-\kappa t}(1 - e^{-\kappa t})\,dt = \frac{1}{2m}\left(\frac{k_{sp}x_{eq}N(0)}{|\alpha|^2\kappa^2}\right)^2 \tag{4.65}$$

Equation 4.64 tells us how much energy the oscillator will gain as a result of an extra "hit" of $N(0)$ photons in the cavity. We will now consider a small increment of time, Δt. In this time the number of photons leaving the cavity is: $\kappa|\alpha|^2\Delta t \pm \sqrt{\kappa|\alpha|^2\Delta t}$. In other words, the losses obey Poisson statistics. Of course, because the photons going into the cavity obey the same statistics the net number entering or leaving is $0 \pm \sqrt{2}\sqrt{\kappa|\alpha|^2\Delta t}$.

This variation will lead to an extra heating of the oscillator as given by equation 4.64 with $N(0)^2 = 2\kappa|\alpha|^2\Delta t$:

$$H_{rate} = \frac{\Delta E}{\Delta t} = \frac{k_{sp}^2 x_{eq}^2}{m\kappa|\alpha|^2} \tag{4.66}$$

This extra heating rate (equation 4.66) is for a simple mass on spring system. H_{rate} is independent of Δt (which is as it should be because Δt was an arbitrarily picked short time period).

For our system $k_{sp}x_{eq}$is the force supplied by the trapping field (say field 1) while $|\alpha|^2$ is the occupancy of the other field. However, we also have a variation in field 1 that effectively means we have a spring constant that also varies stochastically. We find that, for $|\alpha_1| \gg |\alpha_2|$ these two terms are exactly equal, leading to:

$$H_{rate} \to \frac{A^2 k_1^2 |\alpha_2|^2}{2\kappa m} \tag{4.67}$$

For the symmetric cooling regime ($\alpha_1 = \alpha_2 = \alpha$, $k_1 \approx k_2 = k$) we find:

$$H_{rate} \to \frac{A^2 k^2 \, |\alpha|^2}{2\kappa m} \tag{4.68}$$

The optical cooling power when the bead oscillator is in the ground state is $\Gamma\hbar\omega_M$, at other times the optical cooling rate is even greater. From equation 3.102 we see that $\Gamma\hbar\omega_M \approx \frac{2\sqrt{2}A^2k^2\,|\alpha|^2}{m\kappa}$. This means that:

$$\frac{H_{rate-DR,P_1=P_2}}{\Gamma_{DR,P_1=P_2}\hbar\omega_M} = \frac{1}{4\sqrt{2}} \approx 0.18 \tag{4.69}$$

Equation 4.68 means that this stochastic heating is rarely significant and that even as we approach the ground state it is not particularly significant as, by that stage, the optical heating associated with the cooling mechanism will still just about be dominant over stochastic cooling. So, we do not have to worry about this mechanism of heating.

4.2.6 Rayleigh Scattering

Any polarisable particle scatters incident radiation and that scattering cross-section is proportional to the fourth power of the frequency of the incident radiation. This is a result that famously explains blue skies and red sunsets.

We are not only interested in small particles, but also in particles of larger size, such as the 600 nm diameter sphere. So it will be useful to recap this derivation considering, as we do, what effects we might need to take into account for larger spheres.

The standard derivation proceeds as follows:

Consider a small polarisable particle, such as our glass sphere, with polarisability α. The induced dipole moment in such a sphere, p, is αE, where E is the electric field in which it sits. This means that the square of the second time-derivative of the dipole moment is given by:

$$\ddot{p}^2 = \omega^4 \alpha^2 E^2 \tag{4.70}$$

This is important because of the well-known result that an oscillating Hertzian dipole emits with a power:

$$P_{Hertzian} = \frac{\mu_0 \langle \ddot{p} \rangle}{6\pi c} \tag{4.71}$$

For small spheres the polarisability, α, will be as per equation 3.45. Giving a Rayleigh Scattering Power of:

$$P_{Rayleigh} = \frac{3\mu_0 \omega^4 \epsilon_0^2 \langle E^2 \rangle}{2\pi c} \left(\frac{\epsilon_r - 1}{\epsilon_r + 2} \right)^2 V_{sphere}^2 \tag{4.72}$$

For larger spheres the effective polarisability will be reduced from this. Exactly how much it will be reduced by is difficult to say without further calculation. The bead may start to radiate as a quadrupole (which would mean a much-reduced power from a simple dipole) or the effective polarisability may be reduced in a way similar to that calculated in section 4.1. It is fair to say that for a 600 nm diameter bead the radiated power might be as much as 50 % smaller than that given by equation 4.72.

The incident, average, Poynting vector, in free space, is $\langle \mathbf{E} \wedge \mathbf{H} \rangle = \frac{\langle E^2 \rangle}{\mu_0 c}$ which means the ordinary Rayleigh cross-section (in free space) is:

$$\sigma_R = \frac{P_{Rayleigh}}{\langle \boldsymbol{E} \wedge \boldsymbol{H} \rangle} = \frac{3k^4}{2\pi}\left(\frac{\epsilon_r - 1}{\epsilon_r + 2}\right)^2 V_{sphere}^2 \sim \frac{4\phi_{bead}^6}{\lambda^4} \tag{4.73}$$

However, for a standing wave the effective cross-section is dependent on whether we are at a node or an anti-node of the Electric Field. At a node there is no cross-section (to first order) while at an anti-node the cross-section is doubled from that given by equation 4.73. In our case the equilibrium position of the bead is dependent on the relative strength of the two fields. In general, we will be closer to a node of the stronger field, than to an anti-node, so this will give rise to an increase in this cross-section of up a factor 2. However, this depends on the detunings and relative powers of the two fields. Furthermore, we are not particularly interested in small factors like 2 when estimating the overall effect of Rayleigh Scattering, so we will press on and calculate the rough power with this ordinary measure of cross-section.

The power of the scattering is thus:

$$P_{Sc} \approx \frac{\sigma_R}{\pi w^2}(P_1 + P_2) = \frac{3k^4}{2\pi^2 w^2}\left(\frac{\epsilon_r - 1}{\epsilon_r + 2}\right)^2 V_{sphere}^2 (P_1 + P_2) \tag{4.74}$$

$$\sim \frac{\phi_{bead}^6}{\lambda^4 w^2}(P_1 + P_2)$$

Or, alternatively, the rate of photon scattering (R_{Sc}) will be:

$$R_{Sc} \sim \frac{\phi_{bead}^6}{\lambda^4 w^2}\frac{P_1 + P_2}{\hbar \omega_c} \tag{4.75}$$

The increase in the centre of mass kinetic energy as a result of a single photon being scattered would be of the order $\frac{\hbar^2 k^2}{2m_s}$, which means the scattering power would be of the order:

$$\frac{d\, KE_{bead}}{dt} \approx Rate_{Sc}\frac{\hbar^2 k^2}{2m_s} \sim \frac{6\hbar\phi_{bead}^3}{\lambda^5 w^2 \rho_{glass} c}(P_1 + P_2) \tag{4.76}$$

For a bead diameter of 100 nm, a glass density of 2100 kg m^{-3} and a cavity diameter of 5 μm this gives a heating power of the thermal motion of the sphere of 10^{-25} times the combined laser power, or $\sim 10^{-27}$ Watts of heating (assuming laser power of tens of milliwatts). Again, this is negligible and therefore does not warrant further investigation.

The referees have pointed out that, were the gas pressure low enough, this heating power would eventually dominate over the heating from the background gas. An estimate of when this occurs can be made by equating 4.76 with equation 4.38 (times K_BT).

This gives us a pressure at which the two heating mechanisms become comparable of $\sim \frac{\hbar \phi_{bead}^4 (P_1+P_2)}{\lambda^5 w^2 c \sqrt{k_B T_g m_g}}$. For the typical experimental parameters given in 3.105 this gives a pressure of 10^{-10} to 10^{-9} Pa = 10^{-12} to 10^{-11} mbar. This is for a 200nm bead (note the sensitivity of this pressure to bead diameter). Later (see figure 4.17) I analyse the cooling down to a pressure of 10^{-9} mbar (on the basis that we find pressures lower than this give results which are not fundamentally different to this pressure, and that other heating mechancism, such as the black body heating, provide an effective pressure emulates this kind of pressure). So I am happy to neglect the Rayleigh heating for the pressures I am considering.

It is, however, useful to note that if we were to go further in estimating the heating of the centre of mass motion of the sphere it would be useful to consider the angular distribution of the force exerted by this scattering.

The angular distribution of scattering from a Hertzian dipole is:

$$P(\theta, \phi) = \frac{3}{8\pi} sin^2\,\theta\; d\Omega = \frac{3}{8\pi} sin^2\,\theta\; (sin\,\theta\;\; d\theta\; d\phi) \tag{4.77}$$

While the angular distribution of the scattered radiation is always in line with the cavity direction.

Consequently, a high proportion of the effect (of the negligibly small recoil heating power) will affect the degree of freedom in which we have the most interest, namely the centre of mass motion along the length of the cavity, which I have generally referred to as the *x*-direction.

4.2.7 Will the bead melt or vaporise?

Glass melts at between 1700 and 2000 Kelvin and may boil from around 2500 K. A glass bead, in a vacuum, with as high an absorption coefficient for the incident radiation as it has an emissivity (*i.e.* a grey body, or black body) will reach a temperature of T_{bead}:

$$T_{bead} = \left(T_0^4 + \frac{P_L}{4\pi\sigma_{SB}w^2}\right)^{\frac{1}{4}} \tag{4.78}$$

Where T_0 is the background temperature, P_L , is the combined power of the lasers, w is the cavity radius and σ_{SB} is Stefan Boltzmann's constant.

Taking $P_L = 2$ mW, $w = 25$ μm and $\sigma_{SB} = \frac{\pi^2 k_B^4}{60\hbar^3 c^2} = 5.67 \times 10^{-8}$ W m^{-2} K^{-4} gives a bead temperature of 1450 K. So, for these parameters, the bead would remain solid.

However, the bead's temperature will, according to this formula, depend on the parameters in question. For example, doubling the laser power flux will cause a 20 percent (three hundred degree) jump in temperature. Consequently, melting is a distinct possibility. A bead that melts does not immediately become a problem, as the centre of mass dynamics may well be unaffected. However, a bead that starts to boil is a problem, and some care will need to be taken to mitigate against this.

Order of magnitude calculations suggest that, at the working pressures we are interested in, radiative cooling will dominate over conductive cooling via the background gas.

4.3 Recap

In section 4.2 we have covered four main external heating mechanisms (Stochastic forcing by the background gas, Heating from Black body radiation recoil, Stochastic heating based on laser occupancy, Rayleigh Scattering recoil heating).

We have found that heating via the background gas is normally the largest of these mechanisms, and also that the black body radiation heating has the capacity to raise the effective gas pressure as well.

Now we will examine the feasibility of reaching the ground state in spite of this heating.

4.4 Cooling with external thermal effects

We now wish to know whether and in what circumstances we are able to reach the ground state, given the thermal effects we have seen up till now.

First, we will assume that the dominant external heating mechanism is that of the background gas.

In section 3.2.8 and 3.2.9 we saw how to calculate the equilibrium phonon number in the absence of external heating.

In particular, equations 3.86 and 3.87 (now 4.79 and 4.80) gave us:

$$\bar{n} = \frac{\Gamma_{\uparrow}}{\Gamma_{\downarrow} - \Gamma_{\uparrow}} \tag{4.79}$$

$$\Gamma_{cool-classical} = \Gamma_{\downarrow} - \Gamma_{\uparrow} \tag{4.80}$$

Where $\Gamma_{\uparrow}$ and $\Gamma_{\downarrow}$ are $\Gamma_{0\to1}$ and $\Gamma_{1\to0}$ respectively.

The interaction with the background gas is a similar heating/cooling process to the optical cooling. In the event that the background gas interaction was to utterly dominate over the optical heating/cooling interaction we would find that, analogous to 4.79, the background gas could cause a heating from (and cooling to) the ground state that we could denote as $R_{\uparrow}$ (and $R_{\downarrow}$). We would then find that:

$$\bar{n}_{thermal} = \frac{R_{\uparrow}}{R_{\downarrow} - R_{\uparrow}} \tag{4.81}$$

$$\gamma_{g-classical} = R_{\downarrow} - R_{\uparrow} \tag{4.82}$$

From equations 4.79 and 4.80 we can determine that $R_{\uparrow} = \gamma_g \bar{n}_{thermal}$ and we also know that $\bar{n}_{thermal} = \frac{k_B T_g}{\hbar \omega_M}$.

When we have background gas cooling that neither dominates, nor is dominated by, the optical cooling (*i.e.* in the general case) we see:

$$\bar{n}_{TOT} = \frac{\Gamma_{\uparrow} + R_{\uparrow}}{\Gamma_{\downarrow} + R_{\downarrow} - \Gamma_{\uparrow} - R_{\uparrow}} = \frac{\frac{k_B T_g}{\hbar \omega_M}\gamma_g + \Gamma_{\uparrow}}{\Gamma_{cool} + \gamma_g} = \frac{\frac{k_B T_g}{\hbar \omega_M}\gamma_g + \Gamma_{cool}\bar{n}_{opt}}{\Gamma_{cool} + \gamma_g} \tag{4.83}$$

Where $\bar{n}_{opt}$ is as per equation 3.97, Γ_{cool} is as per equation 3.96, γ_g is from equation 4.38 and ω_M is from equation 3.64

We have already (in chapter 3) done a detailed study of the feasibility of ground-state cooling in the absence of interaction with the background gas. Figure 4.17 shows that, as pressure is raised from zero the background gas initially has very little effect and only starts to be felt at 10^{-9} mbar. At pressures above 10^{-8} mbar we see the temperature and phonon number increasing in proportion to the background gas pressure. This is because the temperature is a weighted average of the gas temperature (300 K) and the hypothecated temperature in the absence of gas (as per equation 4.83). At pressures towards 10^{-7} mbar (the bottom of Figure 4.17) the former weighting factor is much smaller than the latter and is proportional to the gas pressure.

Turning to Figure 4.18, and looking at the optical heating region, we start to see a distinction between the unstable region (where optical heating is sufficient to entirely overcome gas damping) and the rest of the heating region (solid grey) where the bead centre of mass motion energy is contained as some temperature greater than that of the background gas.

Across this entire range of these pressures, we see a temperature and phonon number increasing in proportion to the pressure (in the cooling region).

Figure 4.19 shows how the unstable region shrinks and ultimately disappears at around 30 mbar. The temperatures start to approach room temperature as the effect of the gas starts to dominate over the optical cooling.

In the final diagram of figure 4.19, at just over a tenth of an atmosphere of pressure, we see that the temperature is fairly flat and, to a good approximation, the average phonon number plot simply looks like a plot of the inverse of the mechanical frequency, with little difference between the “heating” and the “cooling” domains.

Finally, figure 4.20 shows the average number of mechanical photons against detuning for a slightly different set of mechanical frequencies, from our paper.[121]

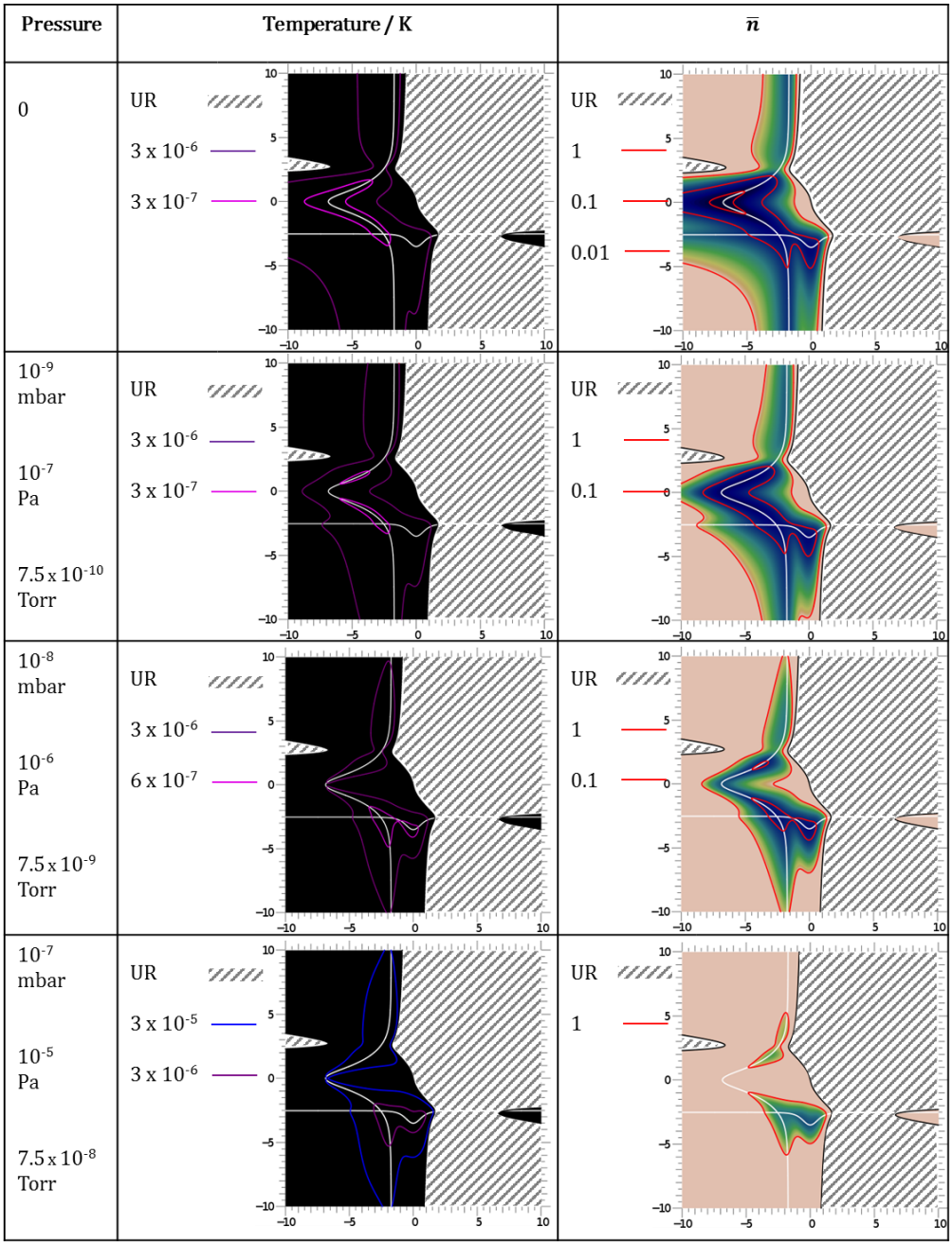

Figure 4.17. All diagrams: x-axis: Δ_x^1 y-axis: Δ_x^2 "UR": Unstable region

Left: Temperature contour plot Right: Mean phonon number plot

First: familiar diagram from section 3.4 showing average temperature and phonon number in the absence of background gas. Second, Third, Fourth: Similar plots showing effect of background gas. For pressures less than 10^{-9} mbar the background gas has very little effect. At pressure above 10^{-8} mbar we start to see nearly a whole order of magnitude increasing in temperature and phonon number for every order of magnitude increase in gas pressure.

This plot and the next two Figures show cooling for P_1 = 2 mW, P_2 = 0.5 mW, $\kappa = \frac{2A}{\hbar} =$ 6 x 10^5 Hz, λ = 1064 nm, with a phase difference between the two curves of $\phi = \frac{\pi}{4}$ a bead diameter of 100 nm and a laser diameter of 25 μm.

Pressure	Temperature / K	$\bar{n}$
10^{-6} mbar 10^{-4} Pa 7.5×10^{-7} Torr	UR 3×10^{-4} 3×10^{-5}	UR 100 10 2
10^{-5} mbar 10^{-3} Pa 7.5×10^{-6} Torr	UR 3×10^{-3} 3×10^{-4}	UR 1000 100 2
10^{-4} mbar 10^{-2} Pa 7.5×10^{-5} Torr	UR 3×10^{-2} 3×10^{-3}	UR 10^4 10^3 2×10^2
10^{-3} mbar 0.1 Pa 7.5×10^{-4} Torr	UR 3×10^{-1} 3×10^{-2}	UR 10^5 10^4 2×10^3
10^{-2} mbar 1 Pa 7.5×10^{-3} Torr	HR UR 3 0.3	HR UR 10^6 10^5 2×10^3
10^{-1} mbar 10 Pa 7.5×10^{-2} Torr	HR UR 30 3	HR UR 10^7 10^6 2×10^5

Figure 4.18. All diagrams: x-axis: Δ_x^1 y-axis: Δ_x^2 other parameters as per Figure 4.16

"UR": Unstable region. "HR": Heating region where heating is containable by the background gas.

Left: Temperature contour plot Right: Mean phonon number plot

Note: the colour scheme for the right-hand plot has changed from Figure 4.17.

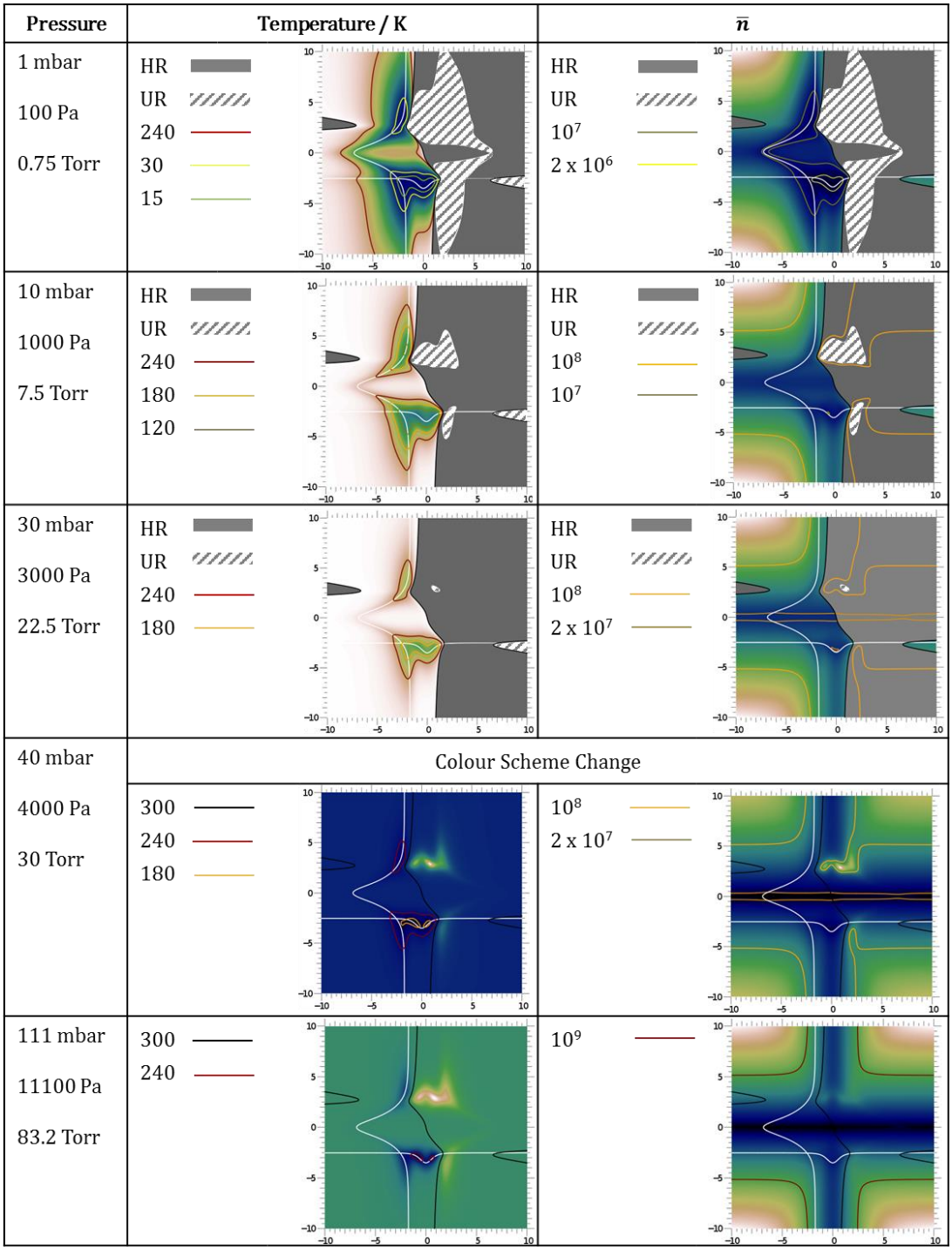

Figure 4.19. All diagrams: x-axis: Δ_x^1 y-axis: Δ_x^2 other parameters as per Figure 4.17

"UR": Unstable region. "HR": Heating region where heating is containable by the background gas.

Left: Temperature contour plot Right: Mean phonon number plot

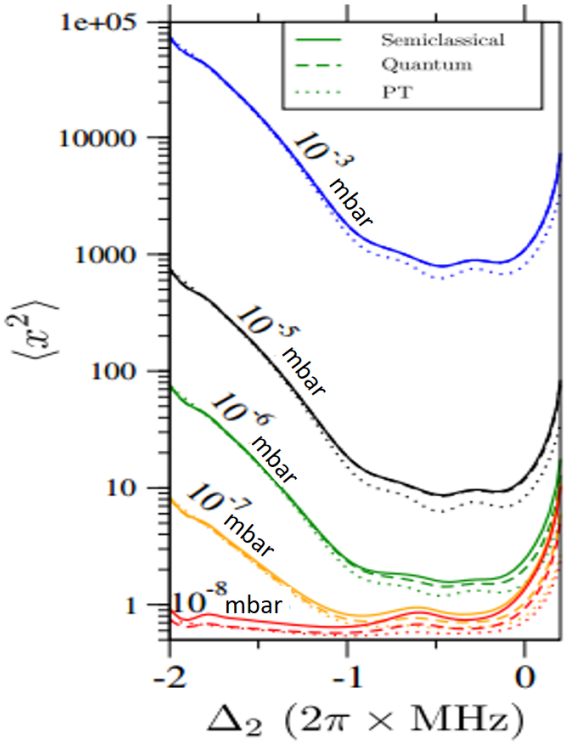

Figure 4.20. Shows equilibrium phonon number as a function of detuning for various pressures. Detuning and power of the stronger field (field 1) is -1.5 MHz and 7 mW respectively. Bead coupling parameter A = 3 x 10^5 Hz. Quantum and semi-classical results shown in dotted line and solid lines respectively. Power of field 2 = 1.75 mW.

4.5 Hollow Spheres

In certain circumstances an improvement can be made by using hollow glass spheres (*i.e.* spherical shells or bubbles) instead of solid, homogeneous spheres. The basic effect of hollowing out a sphere of a particular radius is to remove much of the mass from the sphere, while reducing the polarisability by a less significant fraction.

A reduction in mass increases the frequency of oscillation, which makes it easier to reach the ground state at higher temperatures. However, the heating powers also increase with a lower mass sphere (of the same overall size), as the recoil kicks from photons or background gas are felt more strongly.

H.C van de Hulst[138] tells us that the polarisability of a dielectric sphere (of relative refractive dielectric constant ϵ_1) covered with a concentric spherical shell of a different material (ϵ_2) is given by:

$$\alpha = 3\epsilon_0 V_{sphere} \frac{(\epsilon_2 - 1)(\epsilon_1 + 2\epsilon_2) + q^3(2\epsilon_2 + 1)(\epsilon_1 - \epsilon_2)}{(\epsilon_2 + 2)(\epsilon_1 + 2\epsilon_2) + 2q^3(\epsilon_2 - 1)(\epsilon_1 - \epsilon_2)} \tag{4.84}$$

Where q is the ratio of the small to the large radius and $V_{sphere} = \frac{4\pi R^3}{3}$ as usual.

This means that a hollow sphere with diameter R and hollow cavity diameter R' gives us a polarisability of:

$$\alpha = 3\epsilon_0 V_{sphere} \frac{(1 - q^3)(\epsilon_r - 1)(2\epsilon_r + 1)}{(1 - q^3)(\epsilon_r + 2)(2\epsilon_r + 1) + 9q^3\epsilon_r} \tag{4.85}$$

Where $q = \frac{R'}{R}$. It can be seen that the quotient in equation 4.85 reduces to the familiar $\frac{\epsilon_r - 1}{\epsilon_r + 2}$ when $q = 0$.

Equation 4.85 shows us a few things. Two things are exactly as expected.

The first is that, for low ϵ_r, the polarisability varies in proportion to the mass of glass *i.e.* $\alpha_{hollow} \to (1 - q^3)\alpha_{solid} = (1 - q^3)3\epsilon_0 V_{sphere} \frac{\epsilon_r - 1}{\epsilon_r + 2}$.

The second is that, for conductors (*i.e.* $\epsilon_r \to \infty$) the polarisability is, of course, unchanged from the $q = 0$ case, as the external electric field has no way of "knowing" what the sphere is made of at less than a few skin depths.

As can be seen from Figure 4.21 there is little gain in polarisability for an increase in bead refractive index for solid spheres. For example, with only $n = 2$ (green curve) we get to half the polarisability of an $n \to \infty$ sphere. However, for hollow spheres, we find that the higher refractive index shells have a much higher polarisability than the solid spheres. For example, while the $n = \sqrt{10}$ solid bead is only fifty percent more polarisable than the $n = 2$ bead, once you take away the middle eighty percent of the bead's mass the $n = 2$ is less than half the polarisability of the $n = \sqrt{10}$ bead.

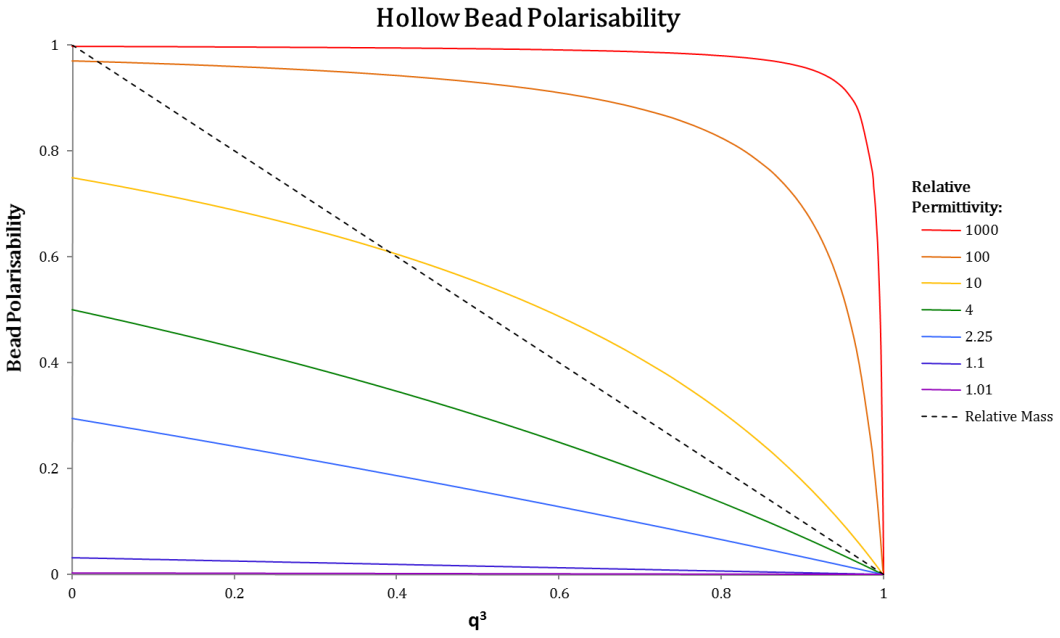

Figure 4.21. Graph showing relative polarisability of spheres as a function of q^3, and for various values of ϵ_r. q is the ratio of inner and outer radii for the shell so q^3 shows us the proportion of the mass that has been removed from the middle of a solid bead to make a hollow shell.

Figure 4.22 shows more clearly how high ϵ_r beads hold their polarisability better upon being hollowed out.

This means that for larger values of ϵ_r, the polarisability to mass ratio can be increased significantly as a result of hollowing out. This is shown in Figure 4.23.

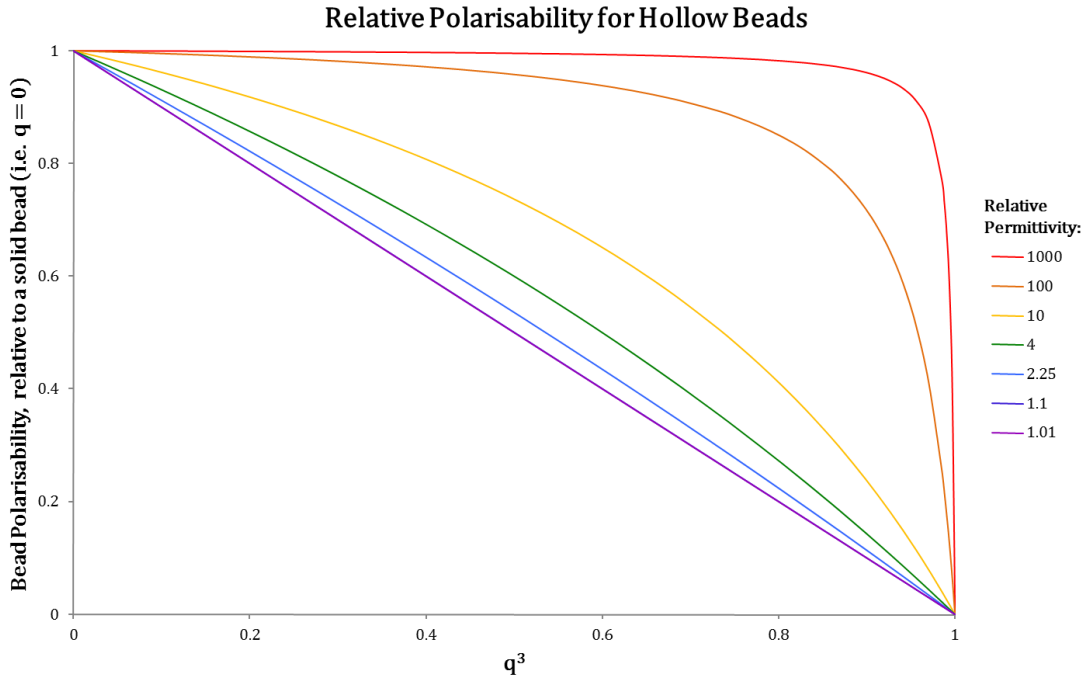

Figure 4.22. Graph showing polarisability of spheres as a function of q^3 as a proportion of solid sphere polarisability, for various values of ϵ_r.

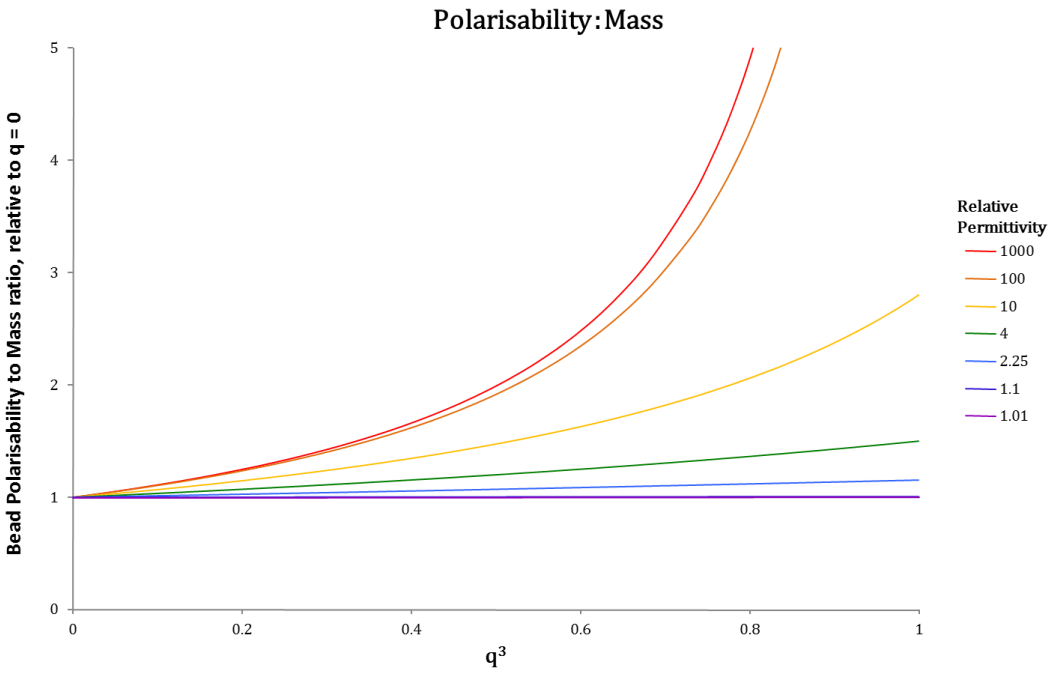

Figure 4.23. Graph showing polarisability to mass ratio as a function of q^3 as a proportion of the polarisability to mass ratio of a solid sphere, for various values of ϵ_r.

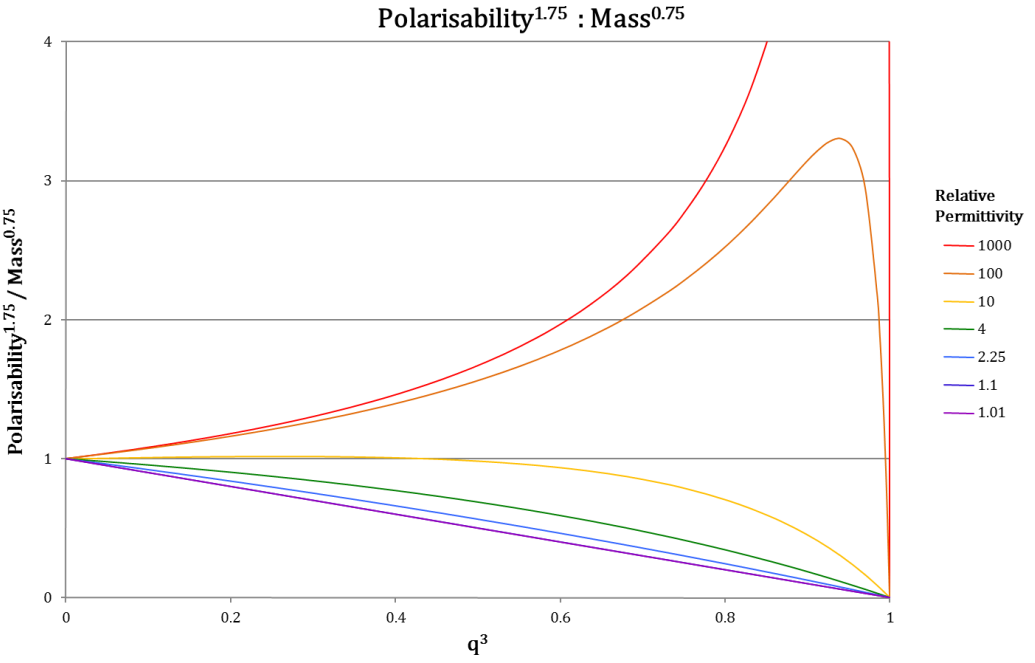

Figure 4.24. Graph showing polarisability to the power of 1.75 divided by density to the power of 0.75. Normalised to give one for solid spheres. For various values of ϵ_r.

We have studied four main heating mechanisms that may have a significant effect on our systems at, or near to, the ground state.

Table 4.2, which collates results from earlier sections, shows how the power of those heating mechanisms varies with $\frac{\epsilon_r-1}{\epsilon_r+2}$ as well as with the effective density, ρ_{Sphere}, and the sphere radius R. This is at constant laser, cavity, vacuum and thermal properties for the system.

It should be noted that this section refers to hollow spheres in a reasonably uniform electric field. It is not reasonable to use equation 4.84 for a hollowed out sphere if the radius is a significant fraction of the laser wavelength (as per section 4.1).

In order to get near to the ground state, we need to maximise the following:

$$\frac{(Cooling\ Rate)\omega_M}{Heating\ Power} \tag{4.86}$$

We know that, for hollow spheres, every time we see a $\frac{\epsilon_r-1}{\epsilon_r+2}$ we replace it with the quotient from equation 4.84:

$$\frac{\epsilon_r - 1}{\epsilon_r + 2} \rightarrow \frac{(1-q^3)(\epsilon_r - 1)(2\epsilon_r + 1)}{(1-q^3)(\epsilon_r + 2)(2\epsilon_r + 1) + 9q^3\epsilon_r} \tag{4.87}$$

It will be useful to consider these proportionalities for fixed R (as it is reasonable to insist on an upper limit of R of, perhaps, 200 nm).

It will also be useful to consider these proportionalities for fixed ρ_s (to consider the best value of R for solid spheres).

To these ends we will consider the proportionalities of expression 4.85 under various dominant heating mechanisms and cooling mechanisms (see table 4.3).

Finally, it will be useful to consider the proportionalities of the non-laser related heating mechanisms in the event of much larger values of R (but at the values of R that give local maxima for cooling).

Heating (or Cooling) mechanisms	Section	Equation	Proportionality
Brownian heating power	4.2.1	4.38	$\frac{1}{\rho_s R}$
Black-body recoil power	4.2.3	4.58	$\frac{1}{\rho_s R}$
Heating power due to stochastic variation in cavity occupancy	4.2.5	4.68, 4.67, 4.68	$\frac{R^3\left(\frac{\epsilon_r-1}{\epsilon_r+2}\right)^2}{\rho_s}$
Rayleigh Scattering Recoil heating power	4.2.6	4.74	$\frac{\left(\frac{\epsilon_r-1}{\epsilon_r+2}\right)^2}{\rho_s}$
Cooling Rate (Symmetric Double Resonance)	3.5	3.104	$R^3\left(\frac{\left(\frac{\epsilon_r-1}{\epsilon_r+2}\right)^7}{\rho_s}\right)^{\frac{1}{4}}$
Cooling Rate (Double Resonance $P_1 \gg P_2$)	3.5	3.102	$\left(\frac{\left(\frac{\epsilon_r-1}{\epsilon_r+2}\right)}{\rho_s}\right)^{\frac{5}{4}}$
Cooling Rate (Single Resonance)	3.4	3.100	$R^3\sqrt{\rho_s\left(\frac{\epsilon_r-1}{\epsilon_r+2}\right)}$
Oscillation frequency (ω_M)	3.2.4	3.64, 3.38	$\sqrt{\frac{\left(\frac{\epsilon_r-1}{\epsilon_r+2}\right)}{\rho_s}}$

Table 4.2: Table showing the proportionalities of how various heating and cooling rates depend upon the effective bead density (which changes with hollowed-out spheres), polarisability (which changes less) and R.

Cooling regime → Dominant heating mechanism	Symmetric Double Resonance	Double Resonance $P_1 \gg P_2$	Single Resonance
Brownian heating power or Black-body recoil power	$R^4\left(\rho_s\left(\frac{\epsilon_r-1}{\epsilon_r+2}\right)^7\right)^{\frac{1}{4}}$	$R\left(\frac{\left(\frac{\epsilon_r-1}{\epsilon_r+2}\right)^7}{\rho_s^3}\right)^{\frac{1}{4}}$	$R^4\rho_s\frac{\epsilon_r-1}{\epsilon_r+2}$
Heating power due to stochastic variation in cavity occupancy	$\left(\frac{\rho_s}{\left(\frac{\epsilon_r-1}{\epsilon_r+2}\right)}\right)^{\frac{1}{4}}$	$\frac{1}{R^3}\left(\frac{1}{\rho_s^3\frac{\epsilon_r-1}{\epsilon_r+2}}\right)^{\frac{1}{4}}$	$\frac{\rho_s}{\left(\frac{\epsilon_r-1}{\epsilon_r+2}\right)}$
Rayleigh Scattering Recoil	$R^3\left(\frac{\rho_s}{\left(\frac{\epsilon_r-1}{\epsilon_r+2}\right)}\right)^{\frac{1}{4}}$	$\left(\frac{1}{\rho_s^3\frac{\epsilon_r-1}{\epsilon_r+2}}\right)^{\frac{1}{4}}$	$R^3\frac{\rho_s}{\left(\frac{\epsilon_r-1}{\epsilon_r+2}\right)}$

Table 4.3: Table showing the proportionalities for $\frac{\hbar\omega_M(Cooling\ Rate)}{(Heating\ Power)}$ against dominant heating mechanism (rows) and cooling regime (columns).

From Table 4.3 we can see that there is no advantage to be had from hollowing out our sphere in the Symmetric Double Resonance or Single Resonance regimes.

In the non-symmetric, Double Resonance regime (*i.e.* where one field is much stronger than the other) we find there may be some benefit to be had from a hollow sphere.

In the case where the dominant heating is either heating from the background gas or heating from the recoil from the bead's black-body radiation we find that any advantage we gain from a hollow sphere is severely limited, and only manifests itself at all with beads of refractive index of more than 2.8. With a refractive index of 10 we find that $\frac{\hbar\omega_M(Cooling\ Rate)}{(Heating\ Power)}$ can be raised by a factor of more than three by hollowing out the middle 94 % of the bead's mass (*i.e.* by having a thickness of shell of 1 % of the bead's diameter).

However, refractive indices at this level are fairly non-physical, so there are very modest gains to be made by using hollow spheres.

Where there are considerable gains are where the dominant heating mechanism is either Rayleigh Scattering or heating from the variation in cavity occupancy. However, these will

not remain the dominant heating mechanisms in the event that the bead is overly hollowed-out. Because both these mechanisms of heating involve interaction between the bead and the trapping laser we find that, in these cases, we also get "better" heating when the bead is less refractive. But again, these mechanisms will not remain dominant in the event of drastically reduced bead permittivity.

These proportionalities do, however, show us that rather large gains can be made with respect to spheres that are simply larger.

Finally, the proportionalities in table 4.3 would imply that much larger beads would also be better in many circumstances. However, the R proportionalities are only true for $R \ll \lambda$. Table 4.4 shows the most important proportionalities for smaller R (subject to the constraint that we chose a local maximum of the effective polarisability with respect to R). Now we see that the benefits of having a much larger bead are less marked (although still present).

Cooling regime → Dominant heating mechanism	Symmetric Double Resonance	Double Resonance $P_1 \gg P_2$	Single Resonance
Brownian heating power or Black-body recoil power	$\left(R^2\rho_s\left(\frac{\epsilon_r-1}{\epsilon_r+2}\right)^7\right)^{\frac{1}{4}}$	$\left(\frac{\left(\frac{\epsilon_r-1}{\epsilon_r+2}\right)^7}{R^{10}\rho_s^3}\right)^{\frac{1}{4}}$	$R^2\rho_s\frac{\epsilon_r-1}{\epsilon_r+2}$

Table 4.4: Table showing proportionalities for $\frac{\hbar\omega_M(Cooling\ Rate)}{(Heating\ Power)}$ against dominant heating mechanism (rows) and cooling regime (columns) in the case where we have a bead that is larger than half a wavelength in diameter and at a local maximum of the effective polarisability with respect to R. In such a case the effective polarisability increases with R rather than R^3. See section 4.1 and Figure 4.2.

4.6 Sag

The bead has a mass and is pulled downwards by gravity. There is therefore a question about whether the bead sags significantly and would consequently settle further from the centreline of the cavity, changing the dynamics by, for example, showing the bead a weaker field than it might otherwise see.

The energy of a small bead ($\phi_{bead} \ll \lambda$) in the field, taking into account gravity, is given by:

$$E_{bead} = -Acos^2\ kx\ exp\left(\frac{-Ch^2}{2w^2}\right)\hat{a}^\dagger\hat{a} + m_s g h \tag{4.88}$$

To find the equilibrium position we need to find where $\frac{dE}{dh} = 0$

$$\frac{dE}{dh} = \frac{CAh}{w^2}cos^2kx\ exp\left(\frac{-Ch^2}{2w^2}\right)\hat{a}^\dagger\hat{a} + m_s g h \tag{4.89}$$

This means that so long as $\frac{m_s w g}{CA\hat{a}^\dagger\hat{a}} \ll 1$ then:

If we use the value of A from 3.38 then we get a sag of a few tenths of a micron. This is small as compared to w.

Furthermore, if we use a cavity of smaller diameter than 25 microns the sag will be fantastically smaller still (*i.e.* smaller even as a proportion of the cavity diameter). If we use a laser power of more than 4 mW of power, the sag will also be smaller.

So we have no need to worry about the bead being in a non-central radial position in the trap, due to the effects of gravity as $\frac{|h|}{w} \ll 1$.

We do not have to worry about the effects of reducing A with larger beads as per section 4.2 because the factor that reduces the radial trapping force does not go to zero like the axial force but rather it hits a floor at a value of a half.

Finally, it is worth noting that a realistic trapping set up would be likely to require cooling in three dimensions, not merely one. Conceptually the simplest way to achieve this would be to have six beams: One cooling and one trapping, in each of three mutually orthogonal directions, each using the TEM00 mode. If this was done there would be no issue with beam sag.

Yin *et al.*[139] have suggested that cooling can be achieved using the TEM00, TEM01 and TEM10 modes to cool in the three mutually orthogonal directions. In this way all trapping and cooling beams are in parallel with one another but there is stronger trapping perpendicular to the beams than in the 1D setup. And, as such, again, Sag is not important.

4.7 Chapter Conclusions

With a real bead in a real cavity we see a variety of complications which modify the idealised conditions of chapter 3. The bead being larger can help us achieve stronger cooling and a better approach to the ground state (up to a point), although beads which are larger than around a third of a wavelength are of little utility.

The effect of background gas is the most significant complication and can be overcome by using a strong vacuum with air pressure of 10^{-7} mbar or less.

We also find that there may be particular difficulties in reducing the pressure through a radiometric force threshold around 10 mbar region (where active trapping may assist us).

The issues concerned with the finite radial size of the bead, or the effects of gravity are negligible while the scattering of the trapping light (as well as Black body scattering) effectively adds to the pressure of the background gas meaning that there is little point in using vacuums much less than 10^{-9} mbar.

Some benefit can, in principle, be gained by hollowing out the nano-spheres (especially for those with very high dielectric constant where the external field hardly sees the internal bead) but for real dielectric materials this will not be a source of exceptionally great help, and the construction of hollow spheres is probably more trouble than it is worth.

5 Detection of Ground State Cooling

While previous chapters focussed on the push towards ground state cooling, this chapter focusses on the verification of this state once achieved. Direct measurement of the bead's motion cannot give a non-classical result; however, the measurement of output spectra and, in particular, a homodyne detection to show asymmetry in the x-power spectrum of the bead position is a valid way to show that near ground state cooling has occurred and, simultaneously, to use this system to verify quantum theory.

5.1 Cavity internal spectra and direct measurement of position.

We have established that it is possible to reach the ground state in certain circumstances. We now look to find a way to observe distinctly quantum phenomenon in the system, once the system is at, or near to, the ground state.

First, we will calculate the internal spectrum of the cavity, for various parameters, for both quantum and classical equations.

As well as this we present the calculated Fourier transform of the position co-ordinate.

From equations 3.64, 3.65 and 3.66 we know that:

$$\dot{\hat{b}} = \left(-i\omega_M - \frac{\Gamma}{2}\right)\hat{b} - i\left(g_1^*\hat{a}_1 \ + g_1^*\hat{a}_1^\dagger + g_2^*\hat{a}_2 \ + g_2^*\hat{a}_2^\dagger\right) + \sqrt{\Gamma}\hat{b}_{in} \tag{5.1}$$

$$\dot{\hat{a}}_1 = \left(i\Delta_1^x - \frac{\kappa}{2}\right)\hat{a}_1 - ig_1\left(\hat{b}^\dagger + \hat{b}\right) - \sqrt{\kappa}\hat{a}_{1_{in}} \tag{5.2}$$

$$\dot{\hat{a}}_2 = \left(i\Delta_2^x - \frac{\kappa}{2}\right)\hat{a}_2 - ig_2\left(\hat{b}^\dagger + \hat{b}\right) - \sqrt{\kappa}\hat{a}_{2_{in}} \tag{5.3}$$

A Fourier transform of the above gives:

$$\tilde{b} = \frac{1}{-i(\omega - \omega_M) + \frac{\Gamma}{2}}\left[-i\left(g_1^*\tilde{a}_1 + g_1\tilde{a}_1^\dagger + g_2^*\tilde{a}_2 + g_2\tilde{a}_2^\dagger\right) + \sqrt{\Gamma}\tilde{b}_{in}\right] \tag{5.4}$$

$$\tilde{a}_1 = \frac{1}{-i(\omega + \Delta_1^x) + \frac{\kappa}{2}}\left[-ig_1\left(\tilde{b}^\dagger + \tilde{b}\right) - \sqrt{\kappa}\tilde{a}_{1_{in}}\right] \tag{5.5}$$

$$\tilde{a}_2 = \frac{1}{-i(\omega + \Delta_2^x) + \frac{\kappa}{2}}\left[-ig_2\left(\tilde{b}^\dagger + \tilde{b}\right) - \sqrt{\kappa}\tilde{a}_{2_{in}}\right] \tag{5.6}$$

It will now be useful to calculate the internal field as a function of the input noise terms ($\tilde{b}_{in}$, $\tilde{a}_{1_{in}}$ and $\tilde{a}_{2_{in}}$).

The noise terms obey the usual commutation operations *e.g.* $\hat{a}_{1_{in}}(t_a)\hat{a}^{\dagger}_{1_{in}}(t_b) - \hat{a}^{\dagger}_{1_{in}}(t_a)\hat{a}_{1_{in}}(t_b) = \delta(t_a - t_b)$. It is reasonable to assume that the input laser is effectively at zero temperature (negligible entropy) while for the mechanical oscillation the temperature as calculated as per equation 4.83.

$$\hat{a}_{1_{in}}(t_a)\hat{a}^{\dagger}_{1_{in}}(t_b) = \hat{a}_{2_{in}}(t_a)\hat{a}^{\dagger}_{2_{in}}(t_b) = \delta(t_a - t_b) \tag{5.7}$$

$$\hat{a}^{\dagger}_{1_{in}}(t_a)\hat{a}_{1_{in}}(t_b) = \hat{a}^{\dagger}_{2_{in}}(t_a)\hat{a}_{2_{in}}(t_b) = 0 \tag{5.8}$$

$$b_{in}(t_a)b^{\dagger}_{in}(t_b) = \left(\frac{KT_{osc}}{\hbar\omega_M} + 1\right)\delta(t_a - t_b) \tag{5.9}$$

$$b^{\dagger}_{in}(t_a)b_{in}(t_b) = \frac{KT_{osc}}{\hbar\omega_M}\delta(t_a - t_b) \tag{5.10}$$

Where:

$$\frac{KT_{osc}}{\hbar\omega_M} = \bar{n} \tag{5.11}$$

In the Figures (below) we see the internal spectra for $\tilde{a}^{\dagger}_1\tilde{a}_1$, $\tilde{a}^{\dagger}_2\tilde{a}_2$, and $\tilde{b}^{\dagger}\,\tilde{b}$. The classically calculated spectrum is shown in green (equivalent to saying $\hat{a}_{1_{in}}(t_a)\hat{a}^{\dagger}_{1_{in}}(t_b) = \hat{a}^{\dagger}_{1_{in}}(t_a)\hat{a}_{1_{in}}(t_b) = \frac{1}{2}\delta(t_a - t_b)$) while the quantum calculated spectra is shown in blue. Where the Figure appears not to have a green line (as in the spectrum for $\tilde{a}^{\dagger}_1\tilde{a}_1$ and $\tilde{b}^{\dagger}\,\tilde{b}$) it is because there is no discernible difference between the quantum and classical calculations.

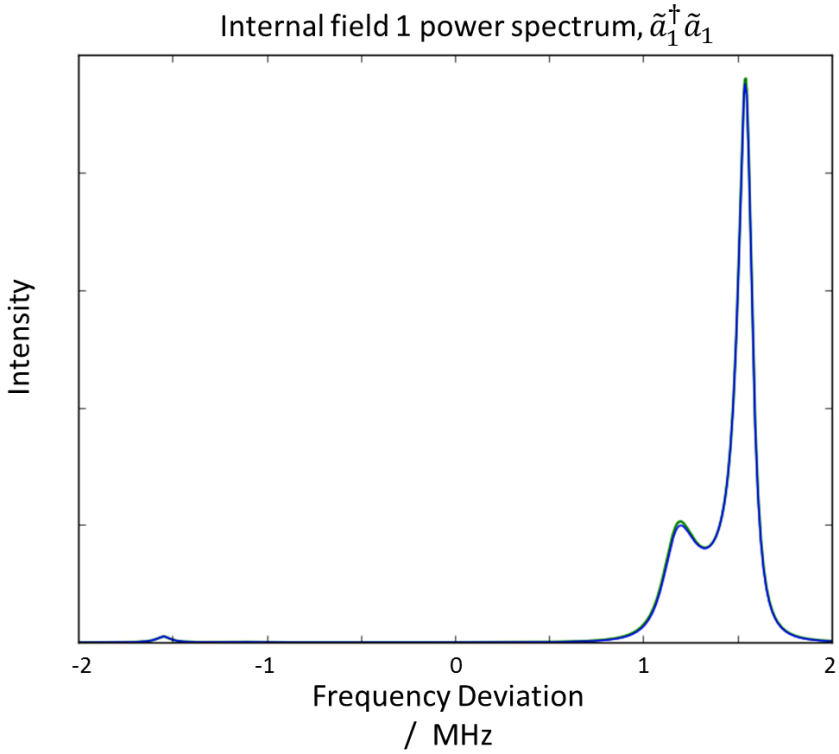

Figure 5.1. Trapping field internal spectrum, parameters as per section 3.7

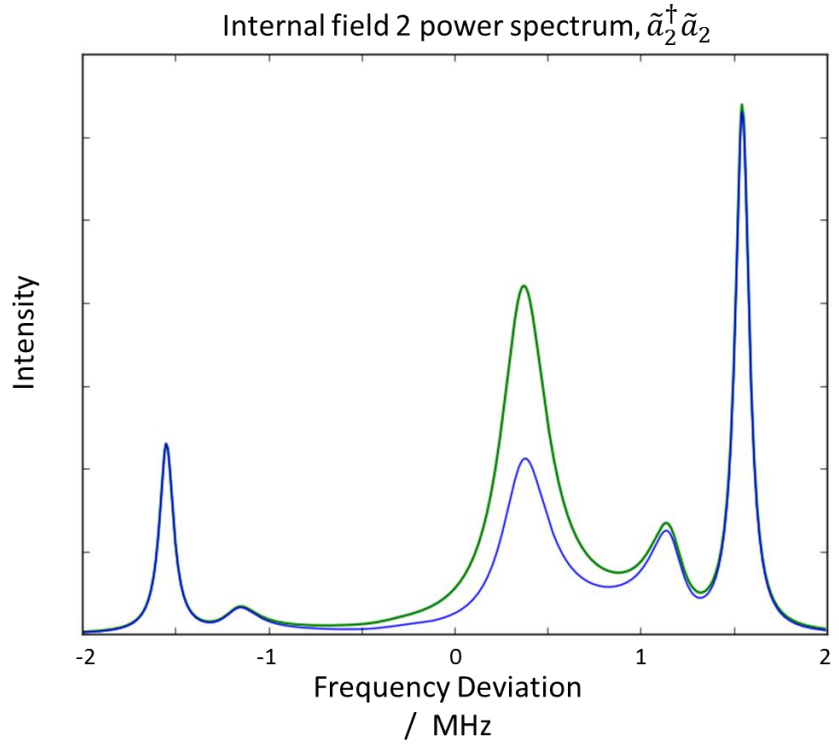

Figure 5.2. Cooling field parameters as per section 3.7. Quantum calculation in blue, Classical calculation in green.

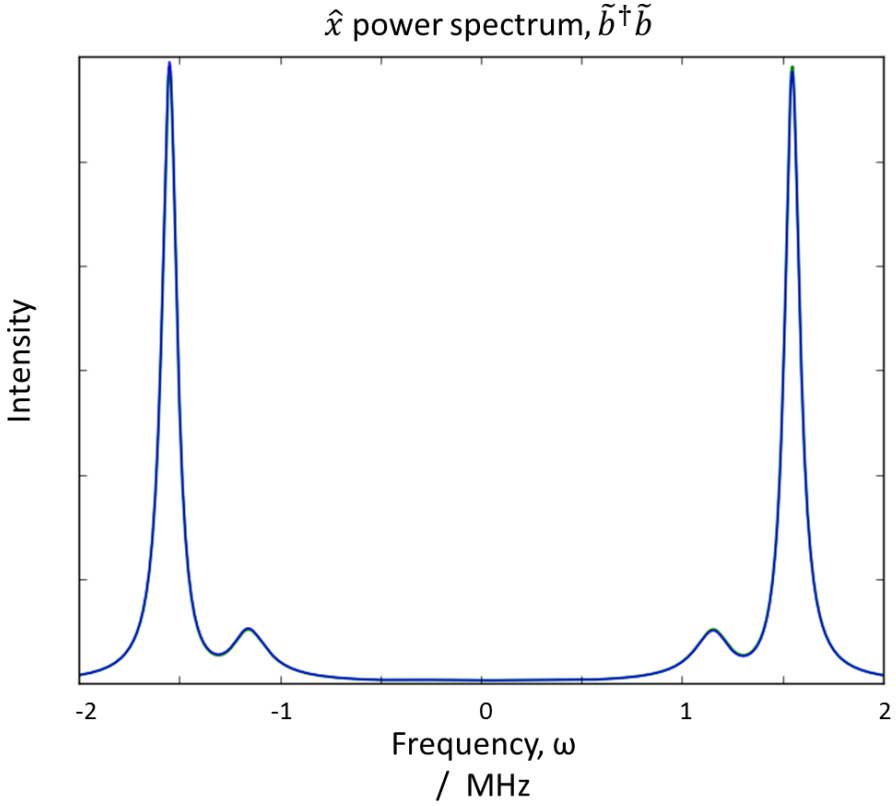

Figure 5.3. Steady state position power spectrum, parameters as per section 3.7.

Figure 5.4 shows the same plots for a range of pressures.

As we can see, when we reach near to the quantum regime, there is a marked difference in the internal spectra we calculate from quantum and classical equations in field 2. At higher phonon numbers, there is (as we would expect) little difference between the quantum and classically calculated spectra.

Obviously, we do not measure the internal spectrum directly, with a camera or similar because, while we can measure the position of the bead to some level of accuracy, the power spectrum of a position trace will always be symmetric (symmetric in the real part and anti-symmetric in any imaginary part – i.e. position is a purely real number). Consequently, the measured (as opposed to quantum) power spectrum will always be entirely symmetric.

We would also be able to measure the bead's oscillation frequency, and then by making observation of the root mean squared displacement or amplitude (say by taking multiple position measurements over time) we would be able to determine that the energy of the oscillation must be of order $\hbar\omega_M$. But that is not a direct test of quantum theory as low energies are obtainable classically.

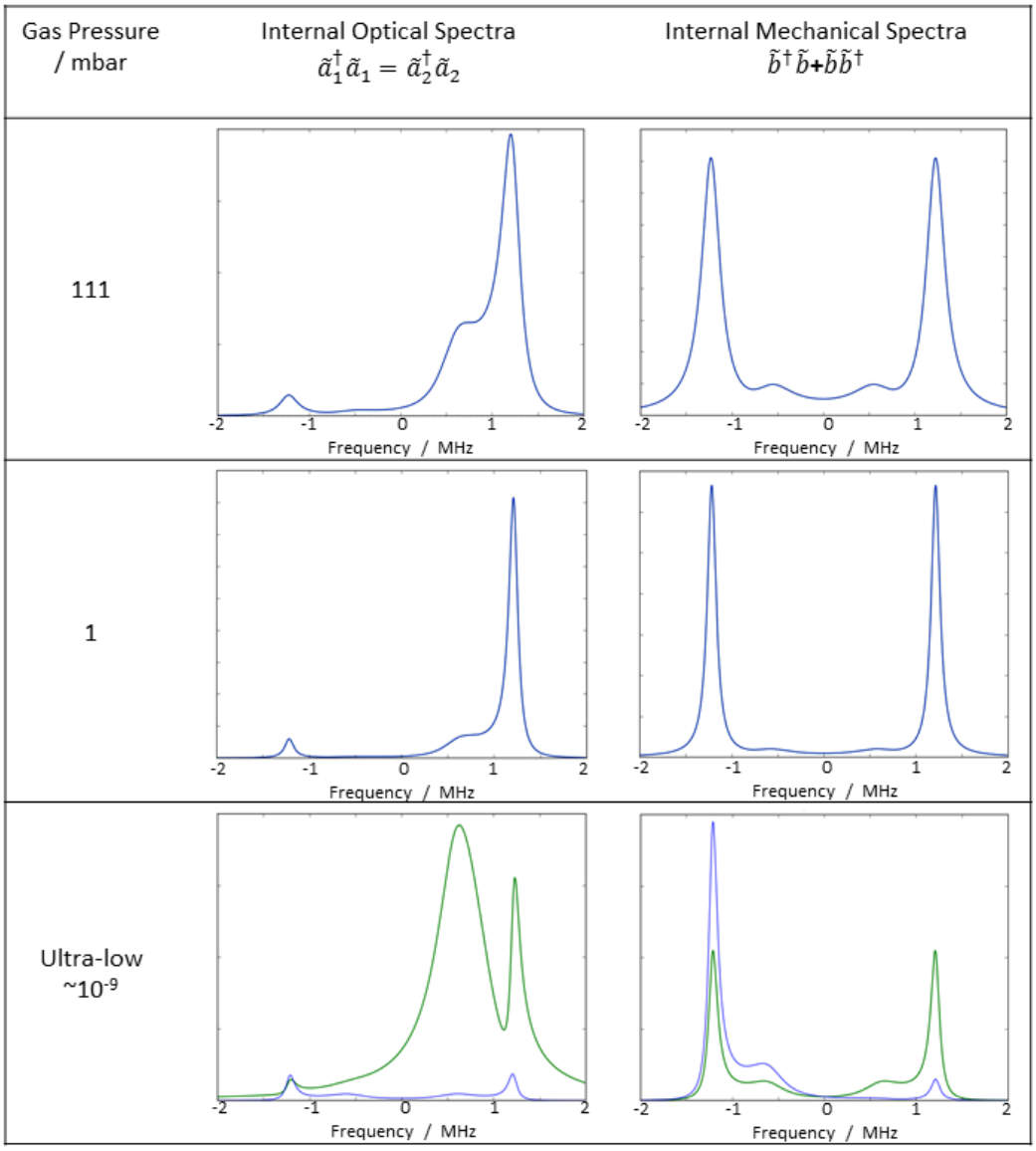

Figure 5.4. Internal optical spectra (left) and mechanical spectrum (right) for parameters shown in section 3.7. Blue is classical and (where perceptibly different) green is the quantum calculation.

5.2 Obtaining the mechanical spectrum through homodyne detection

Although it is not possible to directly observe asymmetry in the mechanical spectrum it is possible to observe this indirectly using a homodyne detection (first proposed by Yuen and Shapiro, and Walls and Zoller)[140,141] where we interfere the output spectrum with the input, it is possible to make a measurement which is proportional to this internal position spectrum.

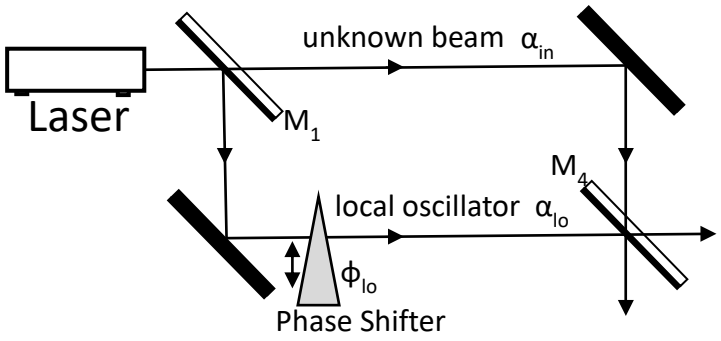

Figure 5.5. Diagram of homodyne detection from "A guide to experiments in quantum optics" by Hans A Bachor and Timothy C Ralph.[142] By interfering the cavity output (unknown beam in the above diagram) with the input we are able to observe individual quadratures of the output spectrum and also observe any quantum asymmetry in the x-power spectrum, which is classically undetectable.

It is measurements of this type which would provide the best evidence of quantum theory.

To calculate the output from such a homodyne detection we will need to make a number of different measurements at different frequencies.

We find that:

$$\tilde{a}_{homodyne} = A\tilde{a}_{out} + B\tilde{a}_{in} \tag{5.12}$$

if we have two 50:50 beam splitters then $|A| = |B|$.

Now $\hat{a}_{out} = \hat{a}_{in} + \sqrt{\kappa}\hat{a}$

So: $\tilde{a}_{homodyne} = A\tilde{a}_{in} + A\sqrt{\kappa}\hat{a} + B\tilde{a}_{in}$

$$\tilde{a}_{1_{homodyne}} = A\tilde{a}_{1_{in}} + A\sqrt{\kappa}\frac{1}{-i(\omega + \Delta_1^x) + \frac{\kappa}{2}}\left(-ig_1\left(\tilde{b}^\dagger + \tilde{b}\right) - \sqrt{\kappa}\tilde{a}_{1_{in}}\right) + B\tilde{a}_{1_{in}} \tag{5.13}$$

If we want to extract $\tilde{b}^\dagger + \tilde{b}$ we need to ensure the coefficients on the $\tilde{a}_{1_{in}}$ terms above sum to zero:

$$A - A\kappa\frac{1}{-i(\omega + \Delta_1^x) + \frac{\kappa}{2}} + B = 0 \tag{5.14}$$

So:

$$\frac{B}{A} = \left(\frac{\frac{\kappa}{2} + i(\omega + \Delta_1^x)}{\frac{\kappa}{2} - i(\omega + \Delta_1^x)}\right) \tag{5.15}$$

$$\frac{|B|^2}{|A|^2} = 1 \tag{5.16}$$

So we need a 50:50 beam splitter and we need to tune the phase difference (depending on frequency) as per Equation 5.15.

However, tuning the phase difference is a relatively simple procedure of sliding the phase plate in or out of the beam pathway, we are fortunate that we do not need to use non-50:50 beam splitters.

This allows us to extract the $\left|\tilde{b}^\dagger + \tilde{b}\right|^2$ power spectrum with a prefactor:

$$\frac{4|A|^2\kappa|g_1|^2}{4(\omega + \Delta_1^x)^2 + \kappa^2} \tag{5.17}$$

To extract the asymmetric mechanical power spectrum in the frequency we will have to make a series of measurements at each frequency (centred on the central laser frequency). For each measurement we will have to adjust the phase relationship to ensure equation 5.15 is satisfied and then, artificially, adjust our observed number to remove the frequency

dependence of expression 5.17. However, doing this, it will be possible to build up a picture of the asymmetric *x*-spectrum, thus demonstrating cooling to the quantum regime.

Figure 5.6 shows a plot of the *x*-mechanical spectrum for two different pressures. In the higher-pressure plot (upper panel) we are not in the quantum regime and no asymmetry or difference between quantum and classical spectrum appears. In the Quantum regime (at UHV pressures) we see an asymmetry in the quantum prediction and a sharp deviation from the spectrum predicted by a semiclassical theory. Here S_{xx} is a symbol for the *x*-power spectrum.

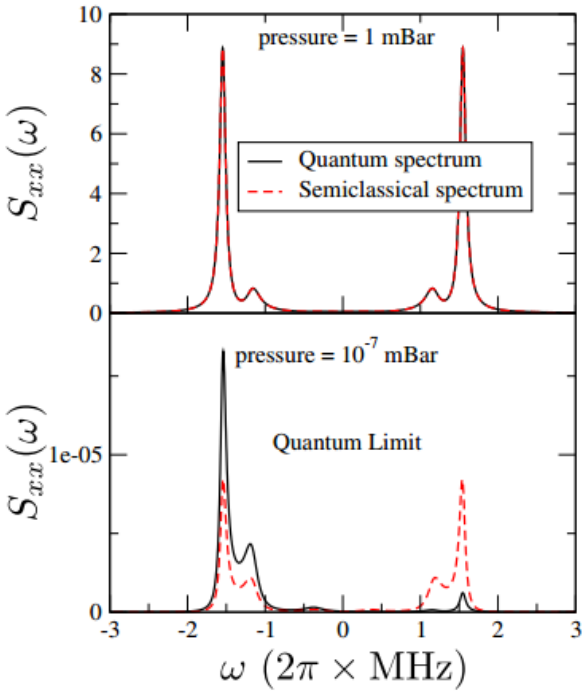

Figure 5.6. From our NJP (2012)[110] showing x-squared spectrum which can also be determined by homodyne detection. : $\Delta_1 = -1.5\ \mathrm{MHz}$, $\Delta_2 = -1.0\ \mathrm{MHz}$ and other parameters as per figure 4.20. The detection of this asymmetry is obviously not directly detectable with a camera but via a homodyne measurement it is possible to measure this asymmetry. Lower peak is associated with the gain of a phonon while the upper peak is associated with the loss of a photon. In the classical regime there is no asymmetry while asymmetry is observed as the system nears the ground state. Qualitatively this can be thought of as being associated with the fact that there is no lower state to transition to, therefore the upper peak is suppressed. This is the best way to detect quantum phenomena using this system.

Figure 5.6 shows an expanded version of 5.6, across a range of values for Δ_2. Again, clear asymmetry is seen in the quantum prediction while the classical plot is symmetric in frequency. There is also a clear avoided crossing at $\omega = \Delta_2$.

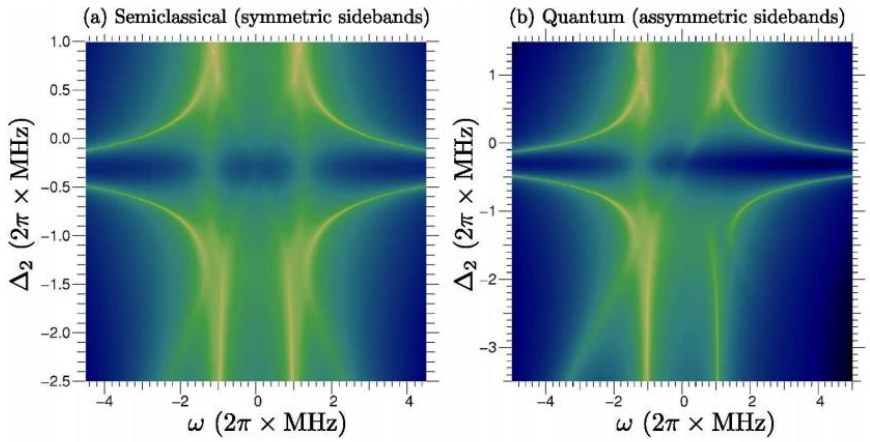

Figure 5.7. Maps of the Fourier transform of the x squared spectrum showing mode splitting / hybridisation. Fixed parameters as per Figure 5.6 (b) is quantum calculation showing asymmetry while (a) is the symmetrised approximation.

In some cooling schemes there is a slowly oscillating external force on the bead from, for example, an external Paul trap (that is, slowly oscillating compared to the mechanical frequency of vibration). This alters the equilibrium position of the bead. Figure 5.8 shows an *x* power spectrum for *x* value of 50 % and 150 % of the equilibrium, as well as the equilibrium itself and an average of the three. As we can see there is fairly little variation between these four plots meaning that the output from a homodyne detection would not be altered hugely by an external oscillating force so long as that force was not sufficient to move the bead completely out of the optical trap.

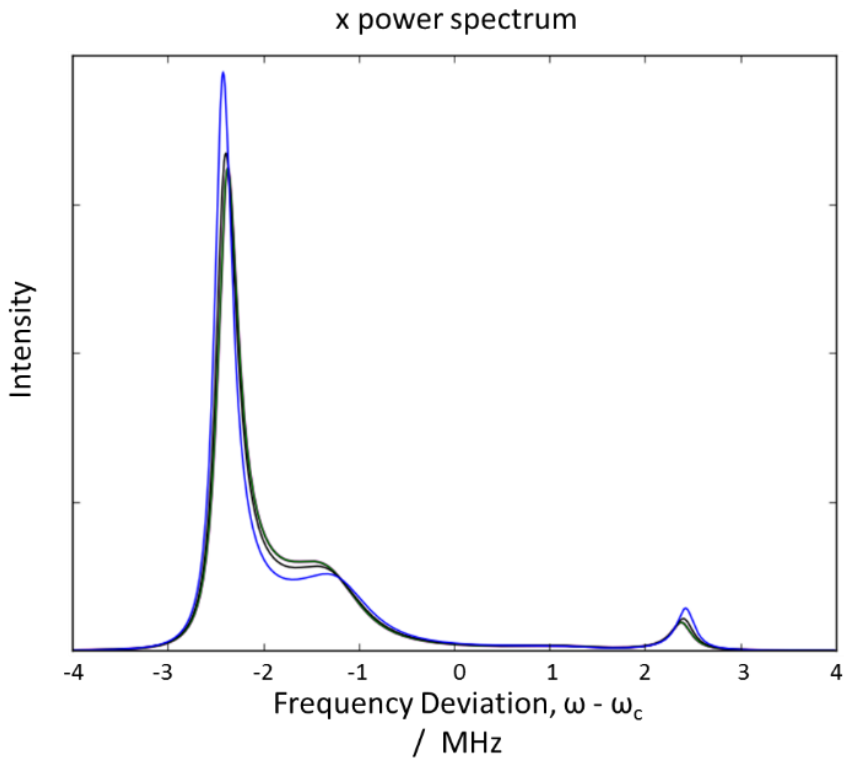

Figure 5.8. *x*-power spectrum (which can be realised with homodyne detection)[143] for 10^{-9} mbar, other parameters as per Figure 5.3. Blue line is for upshifted equilibrium, as per Figure 5.4. The green and co-incidental purple line (purple line hardly visible as green line is on top of it) are for an equilibrium *x* of 50% and 150% of this value respectively. The Black line is the average of all three. As we can see, artificial shifts in the equilibrium position of the bead do not have a substantial effect on the spectrum.

Figure 5.8 shows the internal mode 1 and mode 2 spectra for the same set of parameters as Figure 5.7, and indeed, the mode 1 and mode 2 traces show essentially the same information as Figure 5.7. This also shows the system's normal modes, and an avoided crossing.

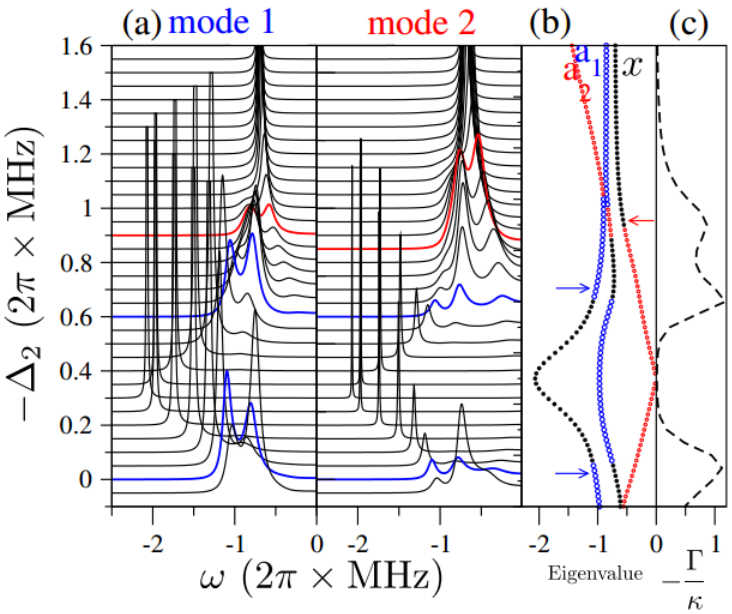

Figure 5.9. Caption: $A = 3\kappa = 6 \times 10^5\, Hz$, $\Delta_1 = -1.5$ MHz. Shows (a) Fourier Transforms of $a_1^\dagger a_1$ and $a_2^\dagger a_2$ spectra. (b) the Eigenvalues of the system which correspond to the frequencies of the system's normal modes. When unhybridised, the Eigenvalues are the two detunings and the mechanical frequency although, as can be seen, there are two avoided crossings. (c) shows the cooling rate, indicating strong cooling at each avoided crossing.

Figure 5.10 shows a noise spectrum for a lower laser power. Here we see a bi-stability whereby there is a range of field 2 detuning where two separate equilibrium positions of the bead exist. We take a series of noise spectra from a sweep of detuning and find that we see a jump, or discontinuity, when the bi-stability disappears, and the bead settles into the other equilibrium.

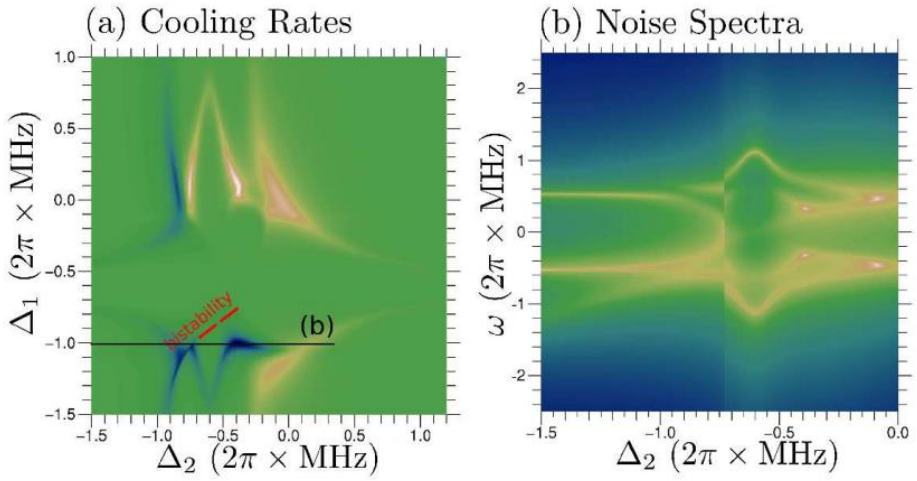

Figure 5.10. Mode mixing and bi-stability. $A = 3\kappa = 6\ \times 10^5\ Hz$. Input power (mode 1) is 0.37 mW while the second mode is a quarter of the power. (a) shows plot of cooling rate against the two detuning's while (b) shows the displacement noise spectra S_{xx} again. The vertical discontinuity of the noise spectrum is because this is the point where (for increasing Δ_2) the position of the bead jumps between the two stable states. If we had shown a plot for sweeps with Δ_2 decreasing instead of increasing, we would have seen a different position of this discontinuity (at Δ_2 = -1 MHz).

Throughout this we have made reference to the semi-classical formula for the output spectra which can be calculated according to a formula from Walls and Milburn:[144]

$$\boldsymbol{S}(\omega) = \frac{1}{2\pi}(\mathbf{A} + i\omega\mathbf{I})^{-1}\mathbf{B}\mathbf{B}^{\mathbf{T}}(\mathbf{A} - i\omega\mathbf{I})^{-1}$$

Where $\boldsymbol{BB^T}$ is the diagonal matrix: $\left(\left(n_{osc} + \frac{1}{2}\right)\Gamma_M, \left(n_{osc} + \frac{1}{2}\right)\Gamma_M, \frac{\kappa}{2}, \frac{\kappa}{2}, \frac{\kappa}{2}, \frac{\kappa}{2}\right)$ and $\boldsymbol{A}$ is the drift matrix which encompasses all the non-stochastic interactions (i.e. forces) on each system variable as a result of all the others. *i.e.* $\frac{d\boldsymbol{X}(t)}{dt} = \mathbf{A}\boldsymbol{X}(t) + \mathbf{B}\boldsymbol{E}(t)$. (The second term is the stochastic noise. $\mathbf{I}$ is the identity.) So to get the x spectrum we take the (0,0) element of **S**, while to get the field 1 internal noise spectrum we take the (1,1) element.

5.3 Direct optical output spectra.

We can also measure is the direct output spectrum of the cavity (not to be confused with the homodyne detection which effectively measures the internal x-power spectrum).

We will mainly be interested in the output frequency spectrum of the fields in steady state, rather than their time dependence (hence the need to take a Fourier transform).

It will also be useful to note that the Hermitian conjugate of the Fourier transform of an operator for a given frequency is equal to the Fourier transform of the Hermitian operator at the negative frequency. *i.e.*

$$\tilde{a}(\omega) = \int_{-\infty}^{\infty} e^{-i\omega t}\hat{a}(t)dt \tag{5.18}$$

$$[\tilde{a}(\omega)]^{\dagger} = \tilde{a}^{\dagger}(-\omega) \tag{5.19}$$

So when we take the conjugate of a Fourier transformed operator we will have to swap the sign of the frequency.

Sometimes this will not matter (*i.e.* when the spectrum is symmetric about the central frequency) but sometimes it will.

We will define

$$\chi_b(\omega) = \frac{1}{-i(\omega - \omega_M) + \frac{\Gamma}{2}} \tag{5.20}$$

$$\chi_1(\omega) = \frac{1}{-i(\omega + \Delta_1^x) + \frac{\kappa}{2}} \tag{5.21}$$

$$\chi_2(\omega) = \frac{1}{-i(\omega + \Delta_2^x) + \frac{\kappa}{2}} \tag{5.22}$$

Then:

$$\left\langle \left(\tilde{b}(-\omega) + \tilde{b}^{\dagger}(-\omega)\right)\left(\tilde{b}(\omega) + \tilde{b}^{\dagger}(\omega)\right)\right\rangle$$

$$= \frac{\kappa|\chi_b(\omega) - \chi_b^*(-\omega)|^2(|g_1|^2|\chi_1(-\omega)|^2 + |g_2|^2|\chi_2(-\omega)|^2) + \Gamma\left((\bar{n}+1)|\chi_b(\omega)|^2 + \bar{n}|\chi_b(-\omega)|^2\right)}{\left|1 + \left(\chi_b(\omega) - \chi_b^*(-\omega)\right)\left(|g_1|^2\left(\chi_1(\omega) - \chi_1^*(-\omega)\right) + |g_2|^2\left(\chi_2(\omega) - \chi_2^*(-\omega)\right)\right)\right|^2}$$

(5.23)

And:

$$\begin{aligned}
&\langle \tilde{a}_1\ (\omega)\tilde{a}_1^{\dagger}(-\omega)\rangle \\
&= |g_1|^2|\chi_1(\omega)|^2 \left\langle \left(\tilde{b}(-\omega)+\tilde{b}^{\dagger}(-\omega)\right)\left(\tilde{b}(\omega)+\tilde{b}^{\dagger}(\omega)\right)\right\rangle + \kappa|\chi_1(\omega)|^2 \\
&- \frac{\kappa|g_1|^2|\chi_1(\omega)|^2\left(\chi_b(\omega)-\chi_b^*(-\omega)\right)\chi_1(\omega)}{1+\left(\chi_b(\omega)-\chi_b^*(-\omega)\right)\left(|g_1|^2\left(\chi_1(\omega)-\chi_1^*(-\omega)\right)+|g_2|^2\left(\chi_2(\omega)-\chi_2^*(-\omega)\right)\right)} \\
&+ \frac{\kappa|g_1|^2|\chi_1(\omega)|^2\left(\chi_b(\omega)-\chi_b^*(-\omega)\right)\chi_1(\omega)}{1+\left(\chi_b(-\omega)-\chi_b^*(\omega)\right)\left(|g_1|^2\left(\chi_1(-\omega)-\chi_1^*(\omega)\right)+|g_2|^2\left(\chi_2(-\omega)-\chi_2^*(\omega)\right)\right)}
\end{aligned}$$

(5.24)

And we have a similar expression for the intensity spectrum in field 2 (with subscripts 1 and 2 switched).

In order to measure the output spectrum, we need to find the quantum calculation for the output spectrum.

Classically the rate of photon loss would be equal to kappa, κ, times the occupancy of the cavity plus a stochastic term (to take into account the Poisson noise). In a steady state, the average rate of output would equal the average rate of input and the noise statistics of the output would be equal to the noise statistics of the input. Quantum mechanically we write:

$$\hat{a}_{out} = \hat{a}_{in} + \sqrt{\kappa}\hat{a} \tag{5.25}$$

With $\hat{a}_{in}$ obeying the usual statistics (in the frequency domain):

$$\tilde{a}_{in}\tilde{a}_{in}^{\dagger} = 1 \tag{5.26}$$

$$\tilde{a}_{in}^{\dagger}\tilde{a}_{in} = 0 \tag{5.27}$$

For a zero temperature laser.

$$\tilde{b}_{in}\tilde{b}_{in}^{\dagger} = 1 + \frac{K_B T_{osc}}{\hbar\omega_M} \tag{5.28}$$

$$\tilde{b}_{in}^{\dagger}\tilde{b}_{in} = \frac{K_B T_{osc}}{\hbar\omega_M} \tag{5.29}$$

For the oscillator of temperature, T_{osc}.

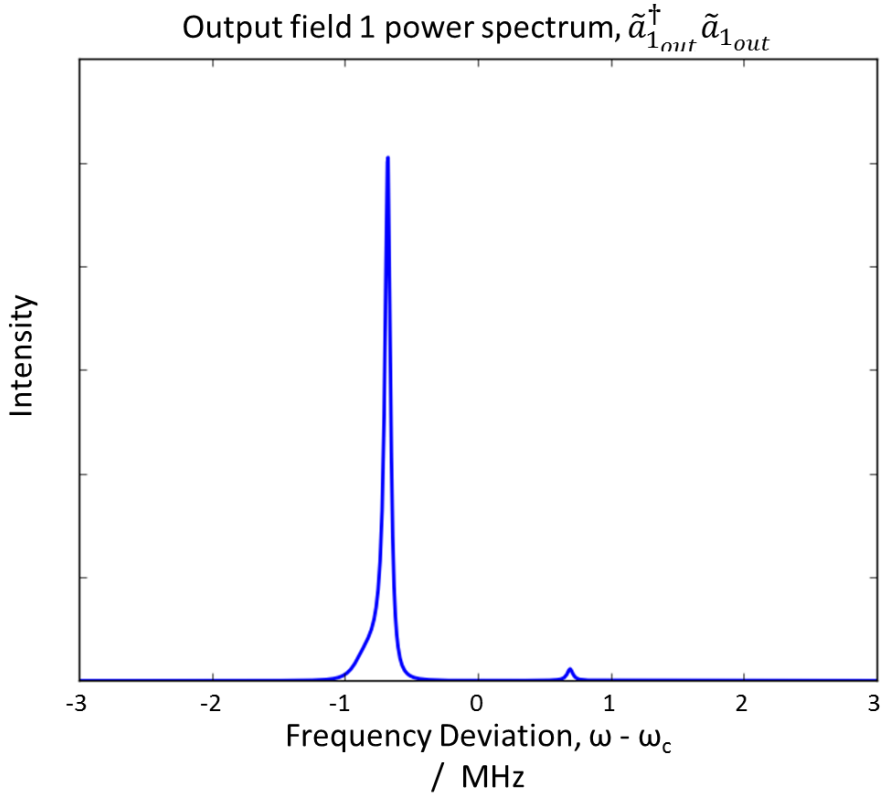

Figure 5.11. Output spectrum for trapping field (field 1) as per parameters in Figure 5.9. From the fact that more photons have been down shifted in frequency than up shifted we can see that the trapping field gives rise to net heating at equilibrium.

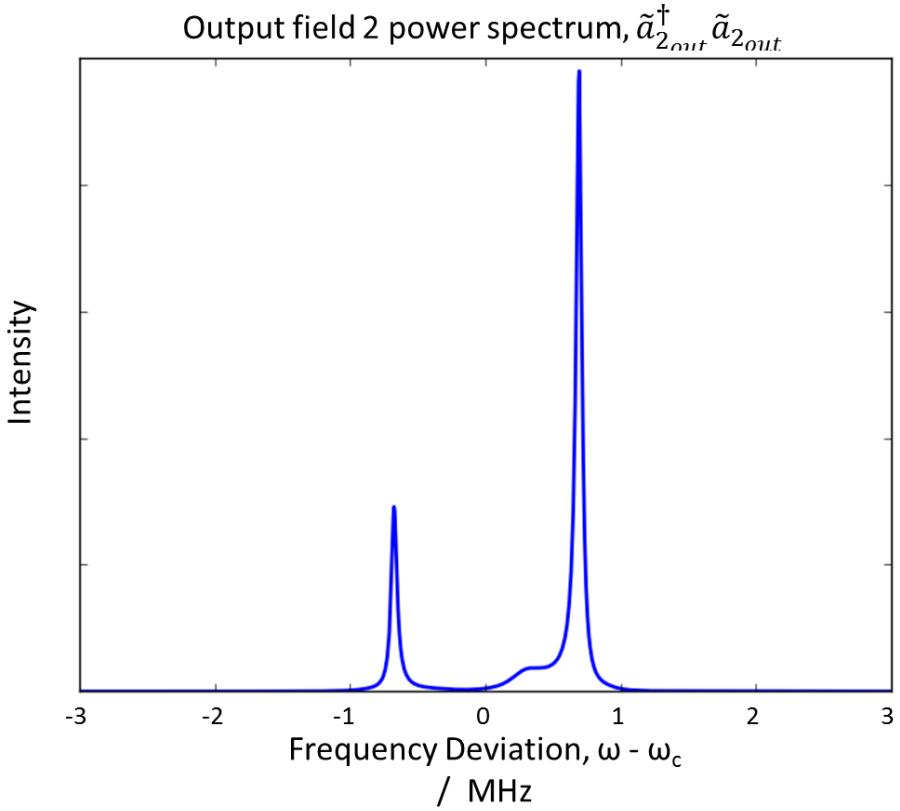

Figure 5.12. Output spectra for cooling field (field 2) as per parameters in Figure 5.9. From the asymmetry in this field we can see that, in steady state, the cooling from the cooling field compensates for the heating from the trapping field.

Again, it will be useful to present the output fields for the parameters in section 3.7, *i.e.* the symmetric trapping-cooling regime.

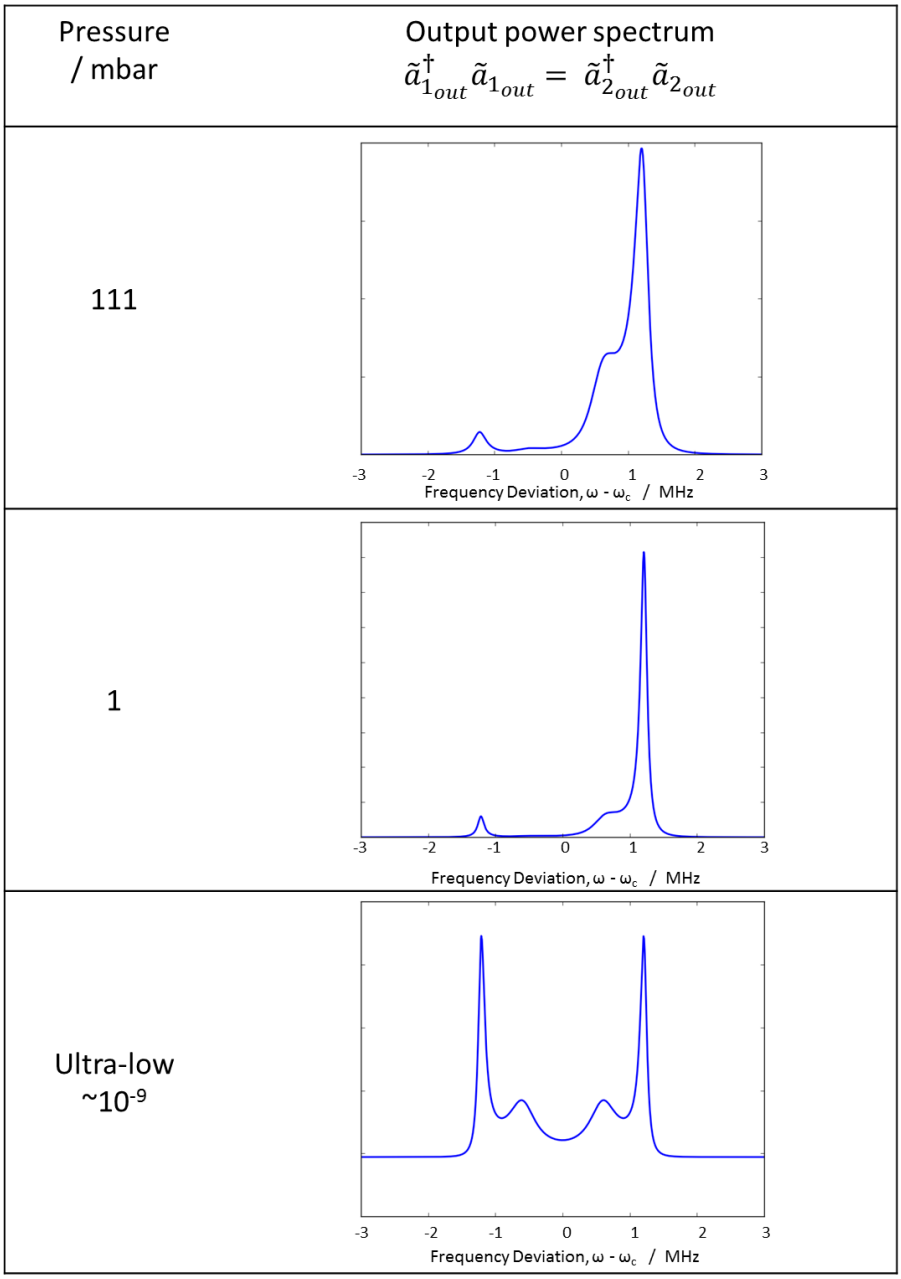

Figure 5.13. Output field spectra for various pressures and other parameters as per section 3.7. As we can see at higher pressures the steady state effect of the optical field is to cool (while the background gas heats) while at low pressures the gas is irrelevant and so, once the system reaches a low equilibrium phonon number, there is no net optical heating or cooling.

A “classical” calculation will yield a symmetric output spectrum (*i.e.* the spectrum will look like a superposition of the above spectra and their vertical axis reflection). However, the asymmetric output spectrum (though it requires the use of non-commutivity of operators in order to calculate it) is not evidence of quantum behaviour. (Again this direct output spectrum is not to be confused with a homodyne output detection.)

The asymmetric direct output spectrum can be explained via entirely classical arguments. The asymmetry in the output spectrum occurs because there is net optical cooling as the external gas heats the system. In fact, as we reach the quantum regime, where there is a big difference between the classical and quantum internal spectrum, the output spectra tend towards symmetry. Again, this can be explained entirely classically. With the background gas gone the equilibrium temperature is reached where there are as many upward optical transitions as downward optical transitions.

This means that as many photons are up-shifted by a certain amount as are downshifted by that amount. But this return to symmetry is also clearly not evidence that allows us to test quantum theory.

The classically calculated internal spectrum of the cavity is never asymmetric. At high phonon numbers, the quantum spectrum follows the classical internal spectrum and the output spectrum is, consequently, asymmetric.

At low phonon numbers, the internal quantum spectrum becomes symmetric and the output spectrum becomes symmetric in consequence. The classical output spectrum would be wrong in these circumstances, but it would be obviously wrong without any reference to quantum theory.

We cannot possibly have a net up-shift in photon energies while the internal system remains in steady state. This would violate the conservation of energy.

So while it would be an interesting experimental observation to observe the asymmetric output spectrum (a difficult experimental procedure) and then to observe an approach to symmetry as (we would assume) the internal motion reaches the quantum regime (an even more challenging experimental procedure) this could not really be considered a test of quantum theory, or rather it could not really be considered any additional falsification of classical mechanics beyond the logical falsification that classical mechanics, combined with Maxwell’s equations, can lead to a violation of the conservation of energy.

However, we already know this logical inference can be made. For example, classical mechanics would have it that a free electron moving in a magnetic field would continue making circles forever. It would also have it that it would emit electromagnetic radiation.

So here again is a (much simpler) logical conflict between electromagnetism, classical mechanics, and the conservation of energy.

But no-one would say that the observation of the slowing down and spiralling inwards of the electron in these circumstances was a test of quantum theory.

Similarly, the direct output spectrum from the double cavity, trapped dielectric sphere system cannot be considered (absent from Homodyne detection) be a test of quantum theory.

At high pressures, we don't see any asymmetry simply because of the broad Gaussian that we see (centred on the cavity frequency plus mechanical frequency). So the Gaussian is not central, but it is symmetric about its own centre.

It will be interesting and useful to find out how this output spectrum will vary if the bead is in an ion trap and, therefore, experiences an oscillatory force which is slow compared to the optical trapping frequency.

In such a case the bead, instead of always oscillating about the optical equilibrium, will oscillate about another point.

Figure 5.14 shows field 2 output power spectra for a shifted equilibria position, in this case of a displacement of 50 % and 150 % of the equilibrium displacement, the unshifted spectra and the average of these three. This gives us an idea of how much (or little) difference an ion trap could make to the output spectra.

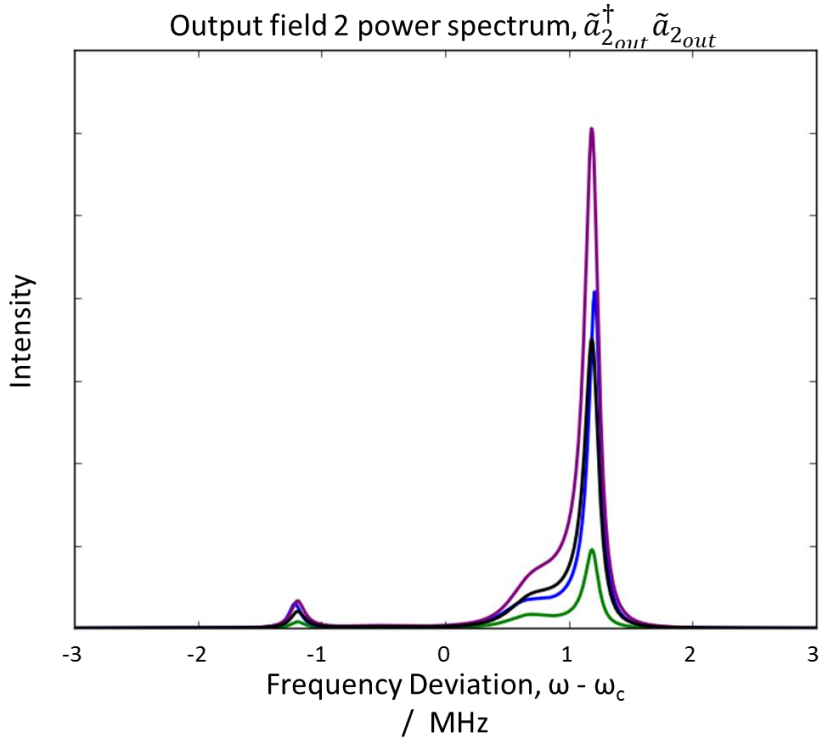

Figure 5.14. Figure showing output spectrum for field 2 blue line at the equilibrium position of kx_0. The Green line shows the field at $\frac{1}{2}kx_0$. The purple line at $\frac{3}{2}kx_0$ and the black line at the average of all three (which is approximately what would be seen if the bead experienced an external oscillatory force with frequency much slower than the essential characteristic frequencies of the system), while still being faster than the detection frequency. Overall therefore we can see that this does not make a great deal of difference.

5.4 Conclusions on measurement of quantum phenomena

The best way to measure distinctively quantum behaviour is to measure asymmetry in the homodyne detection which effectively gives the asymmetric *x*-power spectrum. It is also the case that, in practice, none of the output traces would be as clean as those shown above. They would contain a lot noise from the incoming laser beam. However, the homodyne detection allows this noise to be cancelled away.

Furthermore, while the idea of using a diffraction grating or a prism to obtain the frequency spectrum of the light is correct in principle, much more sensitive frequency detection can be obtained using an electronic spectrum analyser. In fact, frequency is one of the things that can be accurately measured with the most precision, so much so that in a number of experiments throughout experimental physics when an output would naturally present itself as a voltage, current, length, mass or temperature, many experimenters will use extra electronic apparatus to turn it into frequency first.[145]

5.5 Overall Conclusions

The previous three chapters indicate a clear a scheme by which it is possible to observe quantum phenomena in a passively cooled levitated bead system once the radiometric threshold (Section 2.4 and 4.2.2) is overcome.

Vacuum levels of at least 10^{-7} mbar are required (with full parameters shown in Section 3.7) and it may be necessary to use active cooling temporarily to get past a pressure threshold of 10 mbar, where radiometric forces are maximised (assuming background gas is 300 K). See Section 4.2 for derivation of heating rate from background gas.

Passive cooling is by using symmetric cooling and trapping which produces cooling enhanced by a factor of 20 relative to a one-field-cools-one-field-traps set up (Sections 3.2 to 3.5). This maximal cooling rate is relatively insensitive to slight failures to control the phase difference of 45 degrees (in amplitude) with a 30 % variation in phase control leading to only less than a 10 % variation in effective cooling power. The cavity properties required ($\kappa = 6 \times 10^5$ Hz, at 1064 nm, for a 10 mm cavity) are realistic.

Using a larger bead diameter (of a third of a wavelength, so ≈ 300 nm) can enhance cooling (Section 4.1), but there is little benefit to be gained from using a hollow bead (Section 4.5).

I have analysed potential sources of noise other than the background gas (e.g. laser fluctuations, Rayleigh scattering, thermal emission from bead surface). None of these are particularly relevant at the level of gas pressure required to achieve ground state cooling.

I have considered many other possible failure points and ruled them out, including some verification of my assumptions against experimental data produced by others. For example, I have successfully modelled the radial and axial trap frequencies with a simplified analytic model which, in most cases, negates the need for a more complicated (though fully accurate) computational calculation (see Figures 4.4 and 4.5)

I have made a number of predictions for the internal and output spectra of the system, under both classical and quantum assumptions. The best way to prove ground state cooling via heterodyne measurement of the asymmetric *x*-power spectrum (which is, classically, a mathematical impossibility).

In short, this thesis shows it should be possible to cool to a high ground state occupancy using this system, and to verify that this has occurred via heterodyne detection.

6 References

[1] Kepler, J. (1619). *De Cometis Libelli Tres*

[2] Harman, P. M. (1995). *The Scientific Letters and Papers of James Clerk Maxwell*, Vol. 2. Cambridge University Press, Cambridge.

[3] Lebedew, P. (1901). Untersuchungen uber die Druckkrafte des Lichtes. *Annalen der Physik,* **311**, p. 433-458

[4] Nichols, E. F., Hull, G. F. (1903). *The Astrophysical Journal*, **17** (5), p.315-351

[5] Ashkin, A. (1970). *Phys. Rev. Lett.* **24** (156)

[6] Hansch, T. W. , Schawlow, A. L. (1975). *Opt. Commun.* **13** (68)

[7] Einstein, A. (1905). Concerning an Heuristic Point of View Toward the Emission and Transformation of Light. *Annalen der Physik,* **322** (6), p.132-148

[8] Einstein, A. (1909). On the development of our understanding of the nature and composition of radiation. *Physikalische Zeitschrift* **10** (22), p.817

[9] Wineland, D., Dehmelt, H. (1975). *Bull. Am. Phys. Soc.* **20**, p.637

[10] Ashkin, A. (1997). *Proc. Natl. Acad. Sci. USA* **94**, p.4853

[11] Stenholm, S. (1986). *Rev. Mod. Phys.* **58**, p.699

[12] Savard, T. A., O'Hara, K. M., Thomas, J. E. (1997). *Phys. Rev. A* **56**, p.1095

[13] Dholakia, K, Reece, P., Gu, M. (2008). *Chem. Soc. Rev.* **37**, p.42-55

[14] Vaughan, J. M. (1989) *The Fabry-Perot Interfereometer: History, Theory, Practice and Applications*, Taylor and Francis

[15] Einstein, A. (1917). Zur Quantentheorie der Strahlung. *Physikalische Zeitschrift* **18**, p.121–128.

[16] MIT lecture, http://web.mit.edu/2.710/Fall06/2.710-wk8-a-ho.pdf [accessed on 3/4/2015]

[17] Aspelmeyer, M., Kippenberg, T., Marquardt, F. (2013). *Cavity Optomechanics*, Springer, p.1-4

[18] Schliesser, A., Riviere, O., Anetsberger, G., Kippenberg, T. J. (2010) *Nat. Phys.* **5**, p. 509-514

[19] Caltech Thesis Library, http://thesis.library.caltech.edu/2284/3/02_Ch2_Ostby.pdf [accessed on 3/4/2015]

[20] Imran Cheema, M. Mehrabani, S., Hayat, A. A., Peter, Y-A., Armani, A. M., Kirk, A. G. (2012). *Optics Express* **20** (8) p.9090-9098

[21] Li, Y. L., Millen, J., Barker, P. F. (2016). Macroscopic Centre-of-Mass Cooling using Whispering Gallery Mode Resonances. *Opt. Express,* **24**, p.1392-1401

[22] BBC, (2015) http://news.bbcimg.co.uk/media/images/77544000/jpg/_77544633_77544632.jpg [accessed on 3/4/2015]

[23] Weisberg, J. M., Taylor, J. H. (2005). The Relativistic Binary Pulsar B1913+16: Thirty Years of Observations and Analysis. *Binary Radio Pulsars ASP Conference Series*, **328**

[24] Corbitt, T., Mavalvala, N., (2004). *J. Opt B: Quantum Semi-class. Opt.* **6**, p.675

[25] Abbott, B. P., et al. (1020 other authors) (2016). Observation of Gravitational Waves from a Binary Black Hole Merger. *Phys. Rev. Lett.* **116**, 061102

[26] Hohberger-Metzger, C., Karrai, K. (2004). *Nature* **432**, p.1002

[27] Kleckner, D., Bouwmeester, D. (2006) *Nature* **444**, p.75

[28] Favero, I., Metzger, C., Camerer, S., König, D., Lorenz, H., Kotthaus, J. P., Karrai, K. (2007). Optical cooling of a micromirror of wavelength size *Appl. Phys. Lett.* **90**, 104101

[29] Regal, C., Teufel, J., Lehnert, K. W.(2008). *Nature Phys.* **4**, p.555

[30] Gigan, S., Böhm, H. R., Paternostro, M., Blaser, F., Langer, G., Hertzberg, J. B., Schwab, K. C., Bäuerle, D., Aspelmeyer, M., Zeilinger, A. (2006). Self-cooling of a micromirror by radiation pressure. *Nature* **444**, p.67.

[31] Arcizet, O., Cohadon, P. F., Briant, T., Pinard, M., Heidmann, A. (2006). Radiation-pressure cooling and optomechanical instability of a micromirror. *Nature* **444**, p.71

[32] O'Connell, A. D., Hofheinz, M., Ansmann, N., Bialczak, R. C., Lenander, M., Lucero, E., Neeley, M., Sank, D., Wang, H., Weides, M., Wenner, J., Martinis, J. M., Cleland, A. N., (2010). *Nature* **464**, p.607-703

[33] Mari, A., Eisert, J. (2009). *Phys. Rev. Lett.* **103** (21), 213603

[34] Thompson, J. D., Zwickl, B. M., Jayich, A. M., Marquardt, F., Girvin, S. M., Harris, J. G. E. (2008). *Nature* **452**, p.72
[35] Jayich, A. M., Sankey, J. C., Zwickl, B. M., Yang, C., Thompson, J. D., Girvin, S. M., Clerk, A. A., Marquardt, F., Harris, J. G. E. (2008). *New J. Phys.* **10**, 095008
[36] Brown, K. R., Britton, J., Epstein, R. J., Chiaverini, J., Leibfried, D., Wineland, D. J. (2007). *Phys. Rev. Lett.* **99**, 137205
[37] Teufel, J. D., Harlow, J. W., Regal, C. A., Lehnert, K. W. (2008). *Phys. Rev. Lett.* **101**, 197203
[38] Naik, A, Buu, O., LaHaye, M. D., Armour, A. D., Clerk, A. A., Blencowe, M. P., Schwab, K. C. (2006). Cooling a nanomechanical resonator with quantum back-action. *Nature* **443**, p.193
[39] Raman, C., Köhl, M., Onofrio, R., Durfee, D. S., Kuklewicz, C. E., Hadzibabic, Z., Ketterle, W. (1999). *Phys. Rev. Lett.* **83**, p.2502-2505
[40] Romero-Isart, O., Juan, M. L., Quidant, R., Cirac, J. I. (2010). *New J. Phys.* **12**, 033015
[41] Treutlein, P., Genes, C., Hammerer, K., Poggio, M., Rabl, P. (2014). Chapter 14 Hybrid Mechanical Systems. In: Aspelmeyer, M., Kippenberg, T. J., Marquardt, F., *Cavity Optomechanics*, Springer, Berlin, p.327-351
[42] Carmon, T., Rokhsari, H., Yang, L., Kippenberg, T. J., Vahala, K. J. (2006). *Phys. Rev. Lett.* **97**, 243905
[43] Yasir, K. A., Liu, W.-M. (2015). arXiv: 1504.06693v1 [accessed on 6/6/2015]
[44] Anderson, M. H., Ensher, J. R., Matthews, M. R., Wieman, C. E., Cornell, E. A. (1995). *Science* **269**, p.198
[45] Zwierlein, M. W., Stan, C. A., Schunck, C. H., Raupach, S. M. F., Gupta, S., Hadzibabic, Z., Ketterle, W. (2003). *Phys. Rev. Lett.* **91**, 250401
[46] Chu, S., Cohen-Tannoudji, C., Phillips, W. D. (1997). Nobel Prize Lecture
[47] Pontin, A., Rowland, L., Barker, P. (2017). Levitated Optomechanics with a fiber Fabry-Perot interferometer arXiv:1706.10227v1 [accessed on 7/8/2017]
[48] Chen, Y. (2013). *Journal of Physics B Atomic Molecular and Optical Physics* **46**, 104001
[49] Marquardt, F., Girvin, S. (2009). Trend: Optomechanics. *Physics 2*, **40**
[50] Braginsky, V. B., Manukin, A. B., Tikhonov, M. Yu. (1970). Investigation of Dissipative Ponderomotive Effects of Electromagnetic Radiation *Sov. Phys. JETP* **31** (5), p.829
[51] Braginsky, V. B., Manukin, A. B. (1967). Ponderomotive Effects of Electromagnetic Radiation. *Sov. Phys. JETP* **25** (4), p.6539
[52] Kippenberg, T., Vahala, K. J. (2009). *Science* **321**, p.1172
[53] Arndt, M., Hornberger, K. (2014). *Nature Physics* **10**, p.271
[54] Teufel, J., Donner, T., Li, D., Harlow, J., Allmann, M., Cicak, K., Sirois, A., Whittaker, J. D., Lehnert, K., Simmonds, R. W. (2011). *Nature* **475**, p.359
[55] Chan, J., Alegre, T. M., Safavi-Naeini, A. H., Hill, J. T., Krause, A., Groblacher, S., Aspelmeyer, M., Painter, O. (2011). *Nature* **478,** p.89
[56] Woolley, M. J., Doherty, A. C., Milburn, G. J., Schwab, K. C. (2008). Nanomechanical squeezing with detection via a microwave cavity. *Phys. Rev. A (Atomic, Molecular, and Optical Physics)* **78** (6), 062303
[57] Wilson-Rae, I., Nooshi, N., Zwerger, W., Kippenberg, T. J. *Phys. Rev. Lett.* **99**, 093901
[58] Marquardt, F., Chen, J. P., Clerk, A. A., Girvin, S. M . (2007). *Phys. Rev. Lett.* **99**, 093902
[59] Chang, D. E., Regal, C. A., Papp, S. B., Wilson, D. J., Ye, J., Painter, O., Kimble, H. J., Zoller, P. (2010). *PNAS* **107** (3), p.1005-1010
[60] Kiesel, N., Blaser, F., Delic, U., Grass, D., Kaltenbaek, R, Aspelmeyer, M. (2013). *PNAS USA* **110,** 14180
[61] Asenbaum, P., Kuhn, S., Nimmrichter, S., Sezer, U., Arndt, M. (2013). *Nature Commum.* **4,** p.2743
[62] Yin, Z., Geraci, A., Li, T. (2013). Optomechanics of Levitated Dielectric Particles. *J Mod. Phys. B* **27**, 1330018
[63] Metcalf, H. J., van der Straten, P. (2003). Laser Cooling and Trapping of Atoms, *Journal of The Optical Society of America B*, **20** (5), p. 887-908
[64] Bloch, I., Zwerger, W. (2008). Many-body physics with ultracold gases. *Rev. Mod. Phys.* **80**, p.885
[65] Geraci, A. A., Papp, S. B., Kitching, J. (2010). Short-range force detection using optically cooled levitated microspheres. *Phys. Rev. Lett*. **105** (10), 101101
[66] National Physics Laboratory (Kaye & Laby): http://www.kayelaby.npl.co.uk/general_physics/2_4/2_4_1.html [accessed on 3/4/2015]

[67] Rogers, B, Gullo, N. L., De Chiara, G., Palma, G. M., Paternostro, M. (2014). Hybrid optomechanics for Quantum Technologies. *Quantum Measurements and Quantum Metrology* **2** (11)
[68] Harris, S. E. (1997). Electromagnetically Induced Transparency. *Physics Today* **50** (7), p.36
[69] Weis, S., Rivière, R., Deléglise, S., Gavartin, E., Arcizet, O., Schliesser, A., Kippenberg, T. J. (2010). *Science* **330**, p.1520-1523
[70] Borkje, K., Nunnenkamp, A., Teufel, J. D., Girvin, S. M. (2013). *Phys. Rev. Lett.* **111**, 053603
[71] Kronwald, A., Marquardt, F. (2013). Optomechanically Induced Transparency in the Nonlinear Quantum Regime. *Phys. Rev. Lett.* **111**, 133601
[72] Sankey, J. C., Yang, C., Zwickl, B. M., Jayich, A. M., Harris, J. G. E. *Nature Phys.* **6**, p.707-712
[73] Dooling, C., Hauer, B. D., Kim, P. H., MacDonald, A. J. R., Ramp, H., Davis, J. P. (2014). *Phys. Rev. A* **89**, 053838
[74] Gieseler, J., Novotny, L., Quidant, R. (2013). *Nature Phys.* **9**, p.806
[75] Thompson, J. D., Zwickl, B. M., Jayich, A. M., Marquardt, F., Girvin, S. M., Harris, J. G. E. (2008). *Nature* **452**, p.72-75
[76] Safavi-Naeini, A. H., Chan, J., Hill, J. T., Mayer Alegre, T. P., Krause, A., Painter, O. (2012). *Phys. Rev. Lett.* **108**, 033602
[77] Kippenberg, T. J., Schliesser, A., Gorodetsky, M. L. (2013). *NJP* **15**, 015019
[78] Weinstein, A. J., Lei, C. U., Wollman, E. E., Suh, J., Metelmann, A., Clerk, A. A., Schwab, K. C. (2014). *Phys. Rev. X* **4**, 041003
[79] Teufel, J., Donner, T., Li, D., Harlow, J., Allmann, M., Cicak, K., Sirois, A., Whittaker, J. D., Lehnert, K. W., Simmonds, R. W. (2011). *Nature* **475**, p.359
[80] Kawakubo, T., Yamamoto, K. (2010). Optical homodyne detection in view of the joint probability distribution. *Phys. Rev. A* **82**, 032102
[81] Fabre, C., Pinard, M., Bourzeix, S., Heidmann, A., Giacobino, E., Reynaud, S. (1994). *Phys. Rev. A* **49**, p.1337
[82] Mancini, S., Tobesi, P. (1994). *Phys. Rev. A* **49**, p.4055
[83] Bose, S., Jacobs, K., Knight, P. L. (1997). *Phys. Rev. A* **82**, 013818
[84] Mancini, S., Man'ko, V. I., Tombesi, P. (1997). *Phys. Rev. A* **55**, p.559
[85] Safavi-Naeini, A. H, Painter, O. (2011). *NJP* **13**, 01301
[86] Andrews, R. W., Peterson, R. W., Purdy, T. P., Cicak, K., Simmonds, R. W., Regal, C. A., Lehnert, K. W. (2014). Bidirectional and efficient conversion between microwave and optical light. *Nature Physics* **10**, p.321–326
[87] Silanpää, M., Hakonen, P. J. (2014). Hardware for a Quantum Network. *Nature* **507**, p.45
[88] Chu, S. (1991). *Science* **253**, p.5022
[89] Ni, K.-K., Ospelkaus, S., de Miranda, M. H. G., Pe'er, A., Neyenhuis, B., Zirbel, J. J., Kotochigova, S., Julienne, P. S., Jin, D. S., Ye, J. (2008). A High Phase-Space-Density Gas of Polar Molecules. *Science* **322** (5899), p.231-235
[90] Jördens, R., Strohmaier, N., Günter, K., Moritz, H., Esslinger, T. (2008). *Nature* **455**, p.204-207
[91] Anderson, M. H., Ensher, J. R., Matthews, M. R., Wieman, C. E., Cornell, E. A. (1995). Observation of bose-einstein condensation in a dilute atomic vapor. *Science* **269** (5221) p.198-201
[92] Zwierlein, M. W., Stan, C. A., Schunck, C. H., Raupach, S. M. F., Gupta, S., Hadzibabic, Z., Ketterle, W. (2003). Observation of Bose-Einstein Condensation of Molecules. *Phys. Rev. Lett.* **91**, 250401
[93] Truscott, A. G., Strecker, K. E., McAlexander, W. I., Partridge, G. B., Hulet, R. G. (2001). Observation of Fermi Pressure in a Gas of Trapped Atoms. *Science* **291** (5513), p.2570-2572
[94] Horak, P., Hechenblaikner, G., Gheri, K. M., Stecher, H., Ritsch, H. (1997). Cavity-Induced Atom Cooling in the Strong Coupling Regime. *Phys. Rev. Lett.* **79** (25), p.4974-4977
[95] Chan, H. W., Black, A. T., Vuletic, V. (2003). *Phys. Rev. Lett.* **90**, 063003
[96] Teufel, J. D., Harlow, J.W., Regal, C. A., Lehnert, K. W. (2008). *Phys. Rev. Lett.* **101**, 197203
[97] Knobel, R. G., Cleland, A. N. (2003). *Nature* **424**, p.291
[98] Hosseini, M., Duan, Y., Beck, K. M., Chen, Y.-T., Vuleti, V. (2017) Cavity Cooling of Many Atoms. *Phys. Rev. Lett.* **118** (183601), p.1-5
[99] Barker, P. F., Shneider, M. N. (2010). Cavity cooling of an optically trapped nanoparticle. *Phys. Rev. A* **81** (2), 023826
[100] Barker, P. F., Shneider, M. N. (2010). Cavity cooling of an optically trapped nanoparticle. *Phys. Rev. A* **81** (2), 023826

[101] Singh, S., Phelps, G. A., Goldbaum, D. S., Wright, E. M., Meystre, P. (2010). *Phys. Rev. Lett.* **105**, 213602
[102] Millen, J., Deesuwan, T., Barker, P., Anders, J. (2014). *Nature Nanotech* **9**, 425
[103] Millen, J., Fonseca, P., Mavrogordatos, T., Monteiro, T. S. (2015). *Phys. Rev. Let.* **114** (12), 123602
[104] Asenbaum, P., Kuhn, S., Nimmrichter, S., Sezer, U., Arndt, M. (2013). *Nature Com.* **4**, p.2743
[105] Li, T., Kheifets, S., Raizen, M. G. (2011). Millikelvin cooling of an optically trapped microsphere in vacuum. *Nature Physics* **7**, p527-539
[106] Gieseler, J., Deutsch, B., Quidant, R., Novotny, L. (2012). *Phys. Rev. Lett.* **109**, 103603
[107] Frimmer, M., Gieseler, J., Novotny, L. (2016). Cooling Mechanical Oscillators by Coherent Control. *Phys. Rev. Lett.* **117**, 263602
[108] Bhattcharya, M., Vamivkas, A. N., Barker, P. (2017). Levitated optomechanics: Introduction. *Optical Society of America B* **34** (6), p.LO1-LO2
[109] Gieseler, J., Novotny, L., Quidant, R. (2013). *Nature Phys.* **9**, p.806
[110] Doolin, C., Hauer, B. D., Kim, P. H., MacDonald, A. J. R., Ramp, H., Davis, H. (2014). *Phys. Rev. A* **89**, 053838
[111] Fonseca, P. Z. G., Aranas, E. B., Millen, J., Monteiro, T. S., Barker, P. F. (2016). Nonlinear dynamics and millikelvin cavity-cooling of levitated nanoparticles. Phys. Rev. Lett. **117**, 173602
[112] Penrose, R. (2014). On the Gravitization of Quantum Mechanics 1: Quantum State reduction. *Foundations of Physics* **44** (5), p. 557-575
[113] Penrose, R. (1996). On gravity's role in quantum state reduction. *Gen. Relativ. Gravit.* **28**, p.581-600
[114] Chirardi, G. C., Rimini, A., Weber, T. (1986). *Phys. Rev. D* **34**, p.470
[115] Diosi, L. (1987). A universal master equation for the gravitational violation of quantum mechanics. *Phys. Lett. A* **120** (8), p.377-381
[116] Adler, S. L. (2006). *J. Phys. A* **40**, p.2935
[117] Diosi, L. (1989). Models for universal reduction of macroscopic quantum fluctuations. *Phys. Rev. A* **40**, p.1165
[118] Bassi, A., Lochan, K., Satin, S., Singh, T. P., Ulbricht, H. (2013). *Reviews of Modern Physics* **85**, p.471-527
[119] Goldwater, D., Paternostro, M., Barker, P. F. (2016). Testing Wavefunction Collapse Models using Parametric Heating of a Trapped Nanosphere Phys. Rev. A **94**, 010104
[120] Pikovski,I., Zych, M., Costa, F., Brukner, Č. (2015). *Nature Physics* **11**, p.668-672
[121] Pender, G. A. T., Barker, P. F., Marquardt, F., Millen, J., Monteiro, T. S. (2012). *Phys. Rev. A* **85**, 021802
[122] Monteiro, T. S., Millen, J., Pender, G. A. T., Marquardt, F., Chang, D., Barker, P. F. (2013) *New J. Phys.* **15**, 015001
[123] Li, T., Kheifets, S., Raizen, M. G. (2011). *Nature Phys.* **7**, p.527
[124] Gieseler, J., Deutsch, D., Quidant, R., Novotny, L. (2012). *Phys. Rev. Lett.* **109**, 103603
[125] Asenbaum, P., Kuhn, S., Nimmrichter, S., Sezer, U., Arndt, M. (2013). *Nature Commum.* **4**, p.2743
[126] Geraci, A. A., Papp, S. B., Kitching, J. (2010). *Phys. Rev. Lett*. **105**, 101101
[127] Romero-Isart, O., Pflanzer, A. C., Blaser, F., Kaltenbaek, R., Kiesel, N., Aspelmeyer, M., Cirac, J. I. (2011). *Phys. Rev. Lett.* **107**, 020405
[128] Yin, Z., Geraci, A. A., Li, T. (2013). Optomechanics of Levitated Dielectric Particles. *Int. J. Mod. Phys.* B **27**, 1330018 (2013)
[129] Nie, W., Zeng, R., Lan, Y., Zhu, S. (2013). Casimir force between topological insulator slabs. Phys. Rev. B **88**, 085421
[130] Chang, D.E., Regal, C. A., Papp, S. B., Wilson, D. J., Ye, J., Painter, O., Kimble, H. J., Zoller, P. (2013). *Proc. Natl. Acad. Sci. USA* **110** (35), p.14180-14185
[131] Barton, J. P., Alexander, D. R., Shaub, S. A. (1989) *J. Appl. Phys*. **66** (10), p.4594
[132] Encyclopaedia Britannica. (2007). Vacuum Technology. *Encyclopaedia Britannica* **12**, p.229
[133] McGraw Hill (1992). Vacuum Pumps. *Encyclopaedia of Science and Technology* **19**, p128
[134] Wilk, S. R. (2007). The Crookes' Radiometer. *Optics and Photonics News*, September 2007, p. 17-20
[135] Barker, P. F., Shneider, M. N. (2010). *Phys. Rev. A* **81**, 023826
[136] Turyshev, S. G., Toth, V. T., Kinsella, G., Lee, S.-C., Lok, S. M., Ellis, J. (2012). *Phys. Rev. Lett.* **108** (24), 241101

[137] Turyshev, S. G., Toth, V. T., Ellis, J., Markwardt, C. B. (2011). *Phys. Rev. Lett.* **107**, 081103
[138] Van de Hulst, H.C. (1957). *Light Scattering by Small Particles.* Dover Publications
[139] Yin, Z. (2009). *Phys. Rev. A* **80** (3), 033821
[140] Yuen, H. P., Shapiro, J. H. (1980). Optical communication with two-photon coherent states. Part i. Quantum-state propagation and quantum-noise reduction. *IEEE Transactions on Information Theory* **26** (1), p.78-92
[141] Walls, D. F., Zoller, P. (1981). *Phys. Rev. Lett.* **47**, p.709
[142] Bachor, H. A., Ralph, T. C. (2004). Chapter 8. In: *A guide to experiments in Quantum Optics.* Wiley-Vch, p.206
[143] Bachor, H. A., Ralph, T. C. (2004). Chapter 8. In: *A guide to experiments in Quantum Optics.* Wiley-Vch, p.200-231
[144] Walls, D. F., Milburn, G. J. (2008). *Quantum Optics*, Springer
[145] Lombardi, M. A. (1999). Chapter 19 Frequency Measurement. In: *The Measurement, Instrumentation and Sensors Handbook*, CRC Press

7 Appendix 1 – Optomechancial Appendicies

7.1 A classical, quantum and relativistic consideration of sideband cooling.

7.1.1 A classical picture

The classical explanation depends on three common sense assertions.

1) More light will circulate in a cavity when the cavity length is closer to a half-integer multiple of the driving laser's wavelength (*i.e.* when the match between the cavity's resonant frequency is closest to the laser driving frequency).
2) As the cavity length changes the amount of circulating light will change in accordance with assertion 1. However, this change will not be instantaneous but will occur with a characteristic lag time of the ring down rate (a.k.a. linewidth) of the cavity.
3) The circulating light in the cavity will push the cantilever, and the magnitude of this force will be proportional to the amount of circulating light.

If we first consider the case of red-detuned driving we see that, as the cantilever moves from its equilibrium to the right in Figure 1.9 (a.k.a. the positive *x*-direction) the cavity length increases, and so the cavity becomes more resonant with the driving laser. Therefore, the amount of circulating light begins to rise (as per principle 1 above). However, the circulating power adjusts to the length with a lag time (as per principle 2) and so by the time the cantilever travels to the extreme right and back to equilibrium (now moving to the left) there will be a greater circulating power than there was when the cantilever was in the same position traveling to the right. So the magnitude of the force is greatest when it acts to reduce the cantilever velocity. This gives rise to back-action cooling.[146]

Inversely, when the light is blue detuned and the cantilever moves to the right, the cavity becomes less resonant and so, by the time the cantilever returns to equilibrium, the circulating power has fallen. So, with blue detuned light, the moment of greatest force on the cantilever is when it is moving away from the light field.

This gives rise to a driving of the oscillation in exactly the same way an older brother wishing to drive the oscillation of a playground swing needs to push the swing most as it moves away from him (and not as it moves toward him). In general damping of a mechanical oscillation occurs when there a force opposes the velocity of system.

For an ultra-fast cavity ring down rate the circulating power will adjust almost instantaneously to the changing cavity length and so the force will be a pure function of position (not velocity). On the other hand, if the cavity ring-down rate is too slow then the circulating power will hardly change through the course of a whole cantilever oscillation cycle and a constant force in the positive *x*-direction is also no way to either heat or cool an oscillation.

So we can see, qualitatively, that these optical coolings (red-detuned) or heatings (blue-detuned) will be strongest when the cavity ring-down rate (or linewidth) is similar to the oscillation frequency.

7.1.2 A quantum picture

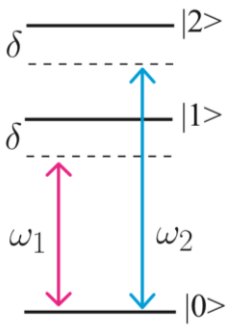

Figure 7.1. Energy level diagram for cooling. For red detuned light to excite the optical mode extra energy will be required from the mechanical mode. For blue detuned light to excite the optical mode it must give this extra energy to the mechanical mode. In principle, light that is sufficiently blue detuned will excite the next energy level. Image from P. Treutein *et al.*[147]

A self-consistent quantum mechanical approach to the mirror cavity system is provided by Paternostro *et al.*[148] and F Marquardt *et al.*[149] Their work is based on the linearised Langevin equations and is therefore quite similar to the approach taken in Chapter 3 here for the bead/cavity system. For a further discussion of the quantum Langevin equation see Genes *et al.*[150] A more generalised study is presented by Wilson-Rae *et al.*[151]

A cavity is most able to sustain a light field at its resonant frequency. So if the light is red detuned the photon may steal a small amount of energy from the cantilever oscillation in order to boost its energy to that of the cavity resonance. This will lead to cooling. Similarly, if the input laser's light is blue detuned it may give up a small amount of energy to the oscillator, heating the cantilever centre of mass motion.

It is obvious (from section 7.1.1) that there is an optimal detuning as, while we clearly need some detuning, too much will mean that the cavity is so far from resonance that the light will hardly enter at all.

Considering this problem through the lens of quantum theory immediately allows us to see the optimal detuning. The cantilever energy comes in packets (phonons) of $\hbar\omega_M$. Consequently, the optimal angular frequency of light, for cooling, is ω_M less than the cantilever energy (*i.e.* cooling is approximately optimised for $\omega_L = \omega_c - \omega_M$. Similarly, heating would be optimised for $\omega_L = \omega_c + \omega_M$).

One might think that a photon energy of two phonons less than the cavity frequency would be just as good (and we would indeed expect a subsidiary maximum in cooling rate for this detuning as predicted by Xiong *et al.*[152]). We might even expect cooling to be greater at this point (and cooling per photon-phonon interaction would indeed be better). However, the two phonon interaction is not nearly as strong an interaction as the single phonon interaction and, in any case, we are moving further out of cavity resonance, so interactions with the cavity are generally less strong for this higher level of detuning. So the global maximum in cooling will be found near to a single phonon of detuning.

Too fast a decaying cavity will lead to a small number of circulating photons, and so fewer interactions with the cantilever. Too slow a decaying cavity will mean that a laser detuned by one phonon's energy is too many line widths from the cavity resonance to interact with the cavity. So, again, we want a detuning of roughly one phonon energy and a linewidth (a.k.a. ring down rate) to roughly match this.

We can see that this qualitative quantum description therefore tells us everything that the classical description tells us but also gives us an idea of what the optimal detuning ought to be.

When we consider the photons exiting this system most will still be at the intrinsic laser frequency, while some will be at the increased, or reduced, frequency. This is directly analogous to photons scattered from an atom or molecule. When light is scattered from

an atom most of it is scattered elastically (Rayleigh scattering) while some is scattered at a shifted frequency (Raman scattering) with the energy difference either going into or coming from some internal degree of freedom of the particle (*e.g.* an molecular electron shifting energy state). Although the term Raman scattering comes from this molecular transition, the behaviour of the cavity and the atom are so similar that this photonic energy transition is often also referred to as Raman scattering.

7.1.3 A relativistic picture

We have not yet finished with the different ways to describe this phenomenon of red detuning leading to cooling. We now need to go back to Figure 1.9 and consider when the cantilever is moving to the left (*i.e.* toward the laser). The natural way of thinking of this (the way we considered in section 7.1.1) is to think of a cavity with two walls, one of which is moving to the left. However, we can also think of it as a cavity that is contracting, while bodily moving to the left (ultimately the "cavity" is nothing more than the two walls of the cavity).

If we consider the cavity as moving to the left then the driving laser will be relativistically blue-shifted, in the instantaneous rest frame of the cavity.

If the light was red-detuned to a stationary cavity, then it will now be closer to resonance for this moving cavity. This means that the force on the cantilever is greatest when "it" is moving to the left (and so we see cooling).

This basic behaviour (coupled EM and mechanical resonators – detuning leading to heating/cooling) has been observed in an almost uncountable number of systems.

7.2 The quantum limited detectable oscillating force threshold.

First consider an oscillator driven by an oscillating force $F(t)$ of amplitude, F_0, and frequency, ω.

$$F(t) = F_0 e^{-i\omega t} = m\ddot{x} + b\dot{x} + k_{sp}x \tag{7.1}$$

We will find that the amplitude of this oscillation, x_0, is given by:

$$|x_0|^2 = \frac{F_0^2}{(k_{sp} - m\omega^2) + \omega^2 b^2} \tag{7.2}$$

We also know that the thermal amplitude of an oscillator would be: $|x_0|^2 = \frac{2K_BT}{k}$.

To determine whether a signal may be detectable, it is reasonable to compare the amplitudes of signal and noise, and to assume that detection would be via a resonator resonant with that force, and with a bandwidth that covers the signal bandwidth.

This implies that it will be difficult to detect static forces above $\sqrt{2k_BTk_{sp}}$ (although this is not strictly true as one can take a time-averaged measurement to average out the thermal noise for very low frequency forces).

Similarly, with an oscillatory force, a reasonable detectability amplitude threshold would be:

$$F > \sqrt{\frac{2K_BT\omega_0^2b^2}{k_{sp}}} = \sqrt{\frac{2K_BTb^2}{m}} \tag{7.3}$$

The quality factor of an oscillator is given by the ratio of the frequency to the linewidth of the oscillator: $Q = \frac{\omega_0}{\Gamma_{osc}}$ and the linewidth is given by: $\Gamma_{osc} = \frac{b}{m}$.

Which takes our detectability threshold to:

$$F_0 > \sqrt{\frac{2K_BTk\Gamma_{osc}}{Q\omega_0}} = \sqrt{\frac{2K_BTm\omega_0\,\Gamma_{osc}}{Q}} \tag{7.4}$$

Or in terms of root-mean-squared forces:

$$F_{min-rms} = \sqrt{\frac{K_BTk\Gamma_{osc}}{Q\omega_0}} = \sqrt{K_BTm\Gamma_{osc}^2} = \sqrt{\frac{K_BTk}{Q^2}} \tag{7.5}$$

If the signal bandwidth is greater than the linewidth of the oscillator, then the signal will not be measurable in its entirety, so we need some linewidth to the oscillator, however a more quickly decaying oscillator than is necessary for this matching will make signals harder to detect.

Here we have assumed than an oscillator will have a thermal energy of K_BT and it therefore follows that a cold oscillator may be able to detect smaller oscillating forces than one at ambient temperature. However, the energy of an oscillator certainly will not fall below $\frac{1}{2}\hbar\omega_0$, which leaves us with a quantum limit on the detectability of an oscillating force of:

$$F_{min-rms\,(quantum\,limit)} \approx \sqrt{\frac{\hbar k_{sp} b_{signal}}{Q}} = \omega_0 \sqrt{\frac{\hbar m b_{signal}}{Q}} \tag{7.6}$$

This means that in order to detect low-amplitude vibrational forces one needs to have a high quality factor oscillator with a low spring constant, with the right frequency and bandwidth to match the signal. This is, therefore, a strict limit on what can be detected.

7.3 Squeezed states (particularly squeezed states of light)

Figure 7.2. In the above famous joke (image by Tomas Bzdusek[153]) Heisenberg is claiming that his car was in a position-squeezed state.

Just as one cannot simultaneously know the position and momentum of a particle one cannot simultaneously know the occupancy and phase of an oscillator, or optical field. With a mechanical oscillator this is obvious, as knowing both the total energy and the current phase of the oscillation would tell us both the centre of mass position and momentum.

It is relatively simple to show that the traditionally stated uncertainty principle implies an energy phase uncertainty principle as follows (under certain reasonable assumptions):

$$\Delta x \Delta p \geq \frac{\hbar}{2} \rightarrow \Delta E \Delta \phi \geq \frac{\hbar \omega}{2} \tag{7.7}$$

This energy phase uncertainty applies to optically excitable oscillators (*e.g.* cavity modes) just as much as mechanical oscillators.

Before we talk in terms of squeezed states we should define that a minimum uncertainty state is one where the product of the two conjugate uncertainties is minimal.

If these two uncertainties (expressed in natural units) are of similar order than this minimum uncertainty state is said to be an un-squeezed minimal uncertainty state.

However, if the uncertainty in one quadrature is significantly smaller than the Planck scale then the state is said to be squeezed (it will, of course, be the case that the uncertainty in the other quadrature will be very much larger than the Planck scale).

With mechanical states virtually all states of macroscopic size are "squeezed" in momentum-space. This is because the plank length is very small indeed at 1.6×10^{-35} m while the Planck momentum is relatively large at six and a half Newton Seconds (a momentum somewhat greater than that of any apple that ever might have fallen onto Sir. Isaac Newton's head).

The idea of a purely positionally squeezed state would, however, be remarkable (hence the joke, see Figure 7.2).

Optomechanics literature particularly talks about squeezed states of light especially of states which one would normally expect to be un-squeezed.

Another way of saying a particle is in a squeezed state is to say it has an elliptical Wigner Function while still being close to a minimal uncertainty state. Where its Wigner function is a kind of probability density in phase space. The Wigner function has the property that its value can be negative in certain places (with the stipulation that when integrated to find a measurable probability, that probability must be between zero and one.)

Rashid, Tufarelli, Bateman, Vovrosh, Hempson, Kim and Ulbricht have achieved squeezing of a thermal positional state in a levitated system and they assert that this setup would also allow them to achieve a squeezed state closer to the quantum limit.[154]

7.4 Entanglement (particularly entanglement between an optical state and a mechanical state)

Another important concept in the literature is entanglement, particularly of the optical and mechanical modes *[155,156]*.

Entanglement of states exists when there are correlations between different quantum systems, which cannot be described by purely classical probability distributions (or a local hidden variable theory).

For example, imagine two spins of two electrons in the "entangled" singlet state:

$$\frac{\uparrow\downarrow - \downarrow\uparrow}{\sqrt{2}} \tag{7.8}$$

Now let us say that we separate the spins and prepare to measure the angular momentum of each spin in one of two different directions.

Basis A = vertically up

Basis B = delta degrees away from vertically up

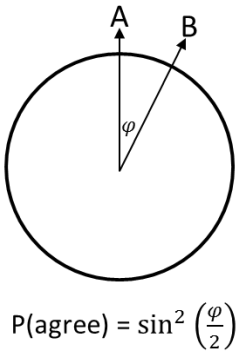

Figure 7.3. The change of two measurements of a singlet state agreeing is zero if the measurements are parallel to one another and increases with the angle of separation.

If we measure them in the same basis then we must get spins in opposite directions. If we measure them in diametrically opposite directions (*i.e.* $\varphi = \pi$), then we must get spins in the "same" direction. At $\varphi = \frac{\pi}{2}$ the measurements are totally uncorrelated with one another and at all intermediary bases we get a probability of allignment which depends upon the difference of alignment.

In fact, the chance of the spins aligning in the same direction is equal to $\sin^2 \frac{\varphi}{2}$. We can get this from considering that the expected angular momentum must be as the classical result.

Now let imagine three possible bases all in the same plane: vertical, horizontal or at 45 degrees.

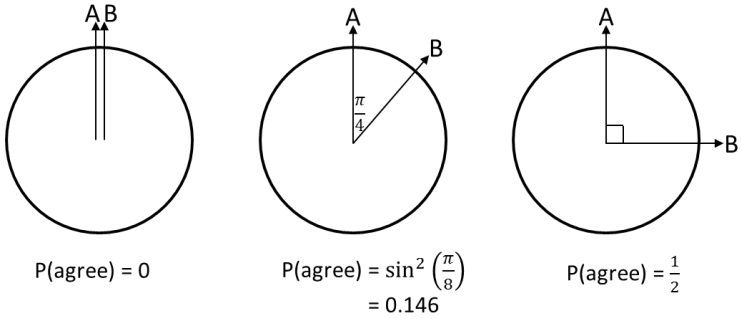

Figure 7.4. Since the measurement at 45 degrees has a 0.146 change of agreeing classically one would expect the measurement at 90 degrees to give a change of agreement in the region of 0.3. However common sense tells us that it should be exactly 50:50.

The formula from Figure 1.13 implies that if we measure one spin vertically and the other at an angle of 45 degrees then there is a 0.146 chance of alignment (and this is correct).

It also implies that if we measure the first spin at 45 degrees and the other horizontally then there is a 0.146 chance of alignment (and this is also correct).

From this we would, classically, expect that if we measure one horizontally and the other vertically then there would be a maximum of 0.292 difference probability of alignment.

This argument is incorrect but it would seem to follow logically as follows:

“We want to know the chance of alignment. Had we measured the second state at a 45-degree angle there would have been a 0.854 change of non-alignment. If the second state was non-aligned when measured at 45 degrees there would be a future 0.846 chance of alignment with this state, and therefore non-alignment with its entangled twin. So the chance of non-alignment with the entangled twin (when measured in frames of reference 90 degrees rotated from one another must be at least 0.846^2 = 0.715). “

However, we know in practice (and from symmetry) that the chance of alignment/non-alignment must be exactly 0.5 if the states are measured diametrically opposed to one another, which is a seeming contradiction.

This contradiction is due to entanglement, and to the fact that even the system does not “know” what the result of experiments would have been if they did not actually happen.

Because entanglement is a quantum phenomenon for which there is no classical analogy (and it comes from the fact that angular momentum in a particular direction is not a continuous variable) it is therefore interesting if it can be observed.

It is linked to the famous EPR paradox.

Of Particular interest is entanglement between two different characters of system, for example entanglement between light and matter q-bits[157].

Entanglement also has a number of applications in cryptography, for example entangled photons can be used to distribute a one-time pad without the existence of a secure channel, leading to un-crackable* encrypted communication over an insecure channel (so long as there are locally secure environments at either end, in which the communicators can operate).

Entanglement could also be used to factorise large numbers more quickly (using, for example, Shor's algorithm) which would render current methods of cryptography much less secure.

Happily, however, the implementation of a Random, one-time pad, is technically much easier than the implementation of Shor's algorithm, so the physical laws of the universe here are on the side of the angels.

*Of course no communication is ever totally secure when used in the real world, the secure end points need to be really secure, and this is, in practice, hard to achieve at reasonable cost. A combination of mistakes, insider treachery, and physical coercion might well render even "un-crackable" systems insecure, but this is not a matter of politics and trespass, not physics or mathematics.

7.5 Derivation of the size of the Casimir Force

7.5.1 The Casimir force between two large parallel conducting plates.

Derivation of the Casimir Force similar to that given in Dutra's "Cavity QED the strange theory of light in a box"

Consider a thin box:

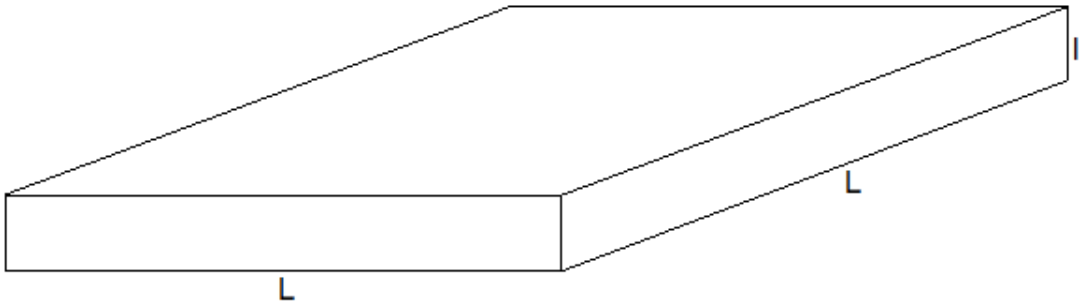

$L \times L \times l$

Figure 7.5. A thin box

The wavefunction for a massless photon in a conductive box is given by:

$$\psi = sin\left(\frac{q\pi z}{L}\right) sin\left(\frac{m\pi x}{L}\right) sin\left(\frac{n\pi y}{L}\right) sin(\omega t) \tag{7.9}$$

As this is the solutions for the wave equation, $\nabla^2\psi = \frac{1}{c^2}\frac{\partial^2\psi}{\partial t^2}$, fitting the $\phi = 0$ Dirichlet Boundary conditions.

Applying the same equation to this solution gives:

$$\omega_{qmn} = \pi c\sqrt{\frac{q^2}{l^2} + \frac{m^2}{L^2} + \frac{n^2}{L^2}} \tag{7.10}$$

If we say that the occupancy of mode q, m, n is given by N_{qmn}. Each geometric mode therefore behaves like an independent harmonic oscillator and, consequently, even at very low temperatures, each mode must contain $\frac{1}{2}\hbar\omega_{qmn}$ (or twice that if we count two linearly independent polarizations).

We therefore find that the overall zero-point energy (as a function of l and L) is given by $E(l, L)$:

$$E(l, L) = \sum_q \sum_m \sum_n \hbar\omega_{qmn} = \hbar\pi c \sum_q \sum_m \sum_n \sqrt{\frac{q^2}{l^2} + \frac{m^2}{L^2} + \frac{n^2}{L^2}} \tag{7.11}$$

In the continuous limit we can approximate sums with integrals ($\sum_m f(m) \to \int f(m)dm$). It reasonable to use the continuous limit in the x and y directions.

$k_x = \frac{\pi m}{L}$ and $k_y = \frac{\pi n}{L}$ so we find $dm = \frac{L}{\pi}dk_x$ and $dn = \frac{L}{\pi}dk_n$

$$E(l,L) = \frac{\hbar c L^2}{\pi^2} \sum_q \int\int \sqrt{\left(\frac{\pi q}{l}\right)^2 + {k_x}^2 + {k_y}^2}\, dk_x dk_y \tag{7.12}$$

By switching into cylindrical polar coordinates we find:

$$E(l,L) = \frac{\hbar c L^2}{2\pi} \sum_q \int k_r \sqrt{\left(\frac{\pi q}{l}\right)^2 + {k_r}^2}\; dk_r = \frac{\pi^2 \hbar c L^2}{4l^3} \sum_q \int_{v=0}^{\infty} \sqrt{q^2 + v}\; dv \tag{7.13}$$

It has been obvious for some time that this will give an infinite energy. It is also fair to say that the walls of the cavity may well become transparent at some high energy, and perhaps we should say that the integrand for the vacuum energy here is attenuated by $R(k)$.

$$E(l,L) = \frac{\pi^2 \hbar c L^2}{4l^3} \sum_q \int_{v=0}^{\infty} R\left(k = \frac{\pi}{l}\sqrt{q^2 + v}\right) \sqrt{q^2 + v}\; dv \tag{7.14}$$

However, we will be less interested in the absolute vacuum energy than in the difference between vacuum energy, at different values of l, and in particular the negative of its first derivative with respect to l, which will give the magnitude of the Casimir force.

Sticking with the expression for the energy, for now, we make the substitution $u = \frac{2}{3}(q^2 + v)^{\frac{3}{2}}$ so $du = \sqrt{q^2 + v}\; dv$:

$$E(l,L) = \frac{\pi^2 \hbar c L^2}{4l^3} \sum_q \int_{u=\frac{2q^3}{3}}^{\infty} R\left(k = \frac{\pi}{l}\left(\frac{3u}{2}\right)^{\frac{1}{3}}\right) du \tag{7.15}$$

The Euler-Maclaren formula states that:

$$\sum_{q=1}^{N-1} f(q) \approx \int_{q=0}^{\infty} f(q)dq - \frac{1}{2}f(0) - \frac{1}{2}f(N) + \sum_{k=1}^{\infty} \frac{B_{k+1}}{(k+1)!}\left(f^{(k)}(N) - f^{(k)}(0)\right) \tag{7.16}$$

Where B_k are the Bernoulli Numbers: $B_1 = \frac{-1}{2}, B_2 = \frac{1}{6}, B_3 = 0, B_4 = \frac{-1}{30} \ldots$

Here $f(q)$ is an integral and $N \to \infty$:

$$f(q) = \int_{u=\frac{2q^3}{3}}^{\infty} R\left(k = \frac{\pi}{l}\left(\frac{3u}{2}\right)^{\frac{1}{3}}\right) du \tag{7.17}$$

By the method of differentiation under the integral sign we can calculate the derivatives of $f(q)$, with respect to q, in the region where R remains relatively flat and equal to unity:

$$\frac{d^n f}{dq^n} = \begin{cases} -2q^2 \ , \ n = 1 \ , R \approx 1 \\ -4q \ \ , \ n = 2 \ , R \approx 1 \\ -4 \ \ \ , \ n = 3 \ , R \approx 1 \\ 0 \ \ \ \ , \ n \geq 4 \ , R \approx 1 \end{cases} \tag{7.18}$$

Meanwhile $f(\infty)$ is zero, as is every derivative of f in the region where $R \approx 0$.

This means that the only non zero terms of equation 7.16 are the first two terms (*i.e.* the terms in brown) and the term in $f'''(0)$.

This means that, by equation 7.16, $E(l, L)$ becomes:

$$E(l, L) =$$

$$\frac{\pi^2 \hbar c L^2}{4l^3}\left(\int_{q=0}^{\infty}\int_{u=\frac{2q^3}{3}}^{\infty} R\left(k = \frac{\pi}{l}\left(\frac{3u}{2}\right)^{\frac{1}{3}}\right) du\, dq - \frac{1}{2}\int_{u=0}^{\infty} R\left(k = \frac{\pi}{l}\left(\frac{3u}{2}\right)^{\frac{1}{3}}\right) du\right) - \frac{\pi^2 \hbar c L^2}{720 l^3} \tag{7.19}$$

It is quite clear that the brown terms are very large, however it will also be useful to consider how the brown terms vary with l.

First let's consider the second brown term:

$$\frac{-\pi^2 \hbar c L^2}{8l^3}\int_{u=0}^{\infty} R\left(k = \frac{\pi}{l}\left(\frac{3u}{2}\right)^{\frac{1}{3}}\right) du \tag{7.20}$$

If l were to double then the integrand in the second brown term (*i.e.* R) would drop off more slowly with increasing u, such that the integral gave exactly eight times its previous value. However, since this term is multiplied by a global prefactor $\propto l^{-3}$, we can see that this second term is not a function of l. So this second brown term (other than depending on the innate functional form of R), depends only on the area of the two plates. We can therefore call this term $-L^2 T_2$, where T_2 is a positive constant.

Secondly we can switch the order of integration in the double integral such that the remaining part of the brown integral becomes:

$$\frac{\pi^2\hbar cL^2}{4l^3}\int_{u=0}^{\infty}\int_{q=0}^{\left(\frac{3u}{2}\right)^{\frac{1}{3}}} R\left(k=\frac{\pi}{l}\left(\frac{3u}{2}\right)^{\frac{1}{3}}\right)dq\,du$$

$$=\frac{\pi^2\hbar cL^2}{4l^3}\int_{u=0}^{\infty}\left(\frac{3u}{2}\right)^{\frac{1}{3}} R\left(k=\frac{\pi}{l}\left(\frac{3u}{2}\right)^{\frac{1}{3}}\right)du \tag{7.21}$$

If we make the substitution $w=\frac{1}{2}\left(\frac{3u}{2}\right)^{\frac{4}{3}}$ this integral becomes:

$$\frac{\pi^2\hbar cL^2}{4l^3}\int_{w=0}^{\infty} R\left(k=\frac{\pi}{l}(2w)^{\frac{1}{4}}\right)dw \tag{7.22}$$

This time we can see that if l were to double R will drop off sixteen times more slowly with increasing u. Since we pre-multiply by a prefactor $\propto l^{-3}$ we see that this is energy term is proportional to only to the volume of the gap *i.e.* $\propto L^2 l$ in the same way that the first term was proportional only to the area of the plate. We can therefore call this term $L^2 l T_1$.

If we imagine two parallel metal plates, of area L^2, fixed very far apart (a separation S) and a further parallel plate, at a variable distance between them (see diagram).

We can see that the overall energy of this system is given by:

$$E(x,L)=\ L^2lT_1-L^2T_2-\frac{\pi^2\hbar cL^2}{720l^3}+\ L^2(S-l)T_1-L^2T_2-\frac{\pi^2\hbar cL^2}{720(S-l)^3} \tag{7.23}$$

$$E(l,L)=\ L^2ST_1-2L^2T_2-\frac{\pi^2\hbar cL^2}{720l^3}-\frac{\pi^2\hbar cL^2}{720(S-l)^3} \tag{7.24}$$

The first two terms do not depend on l. The first represents the general vacuum energy, in the range of frequencies for which the plates are reflective, and the second represents a reduction in that vacuum energy caused by the presence of any intermediate plate, howsoever positioned.

The only terms that do vary with l show us that that two conductive plates, a distance l apart, will experience an attractive Force given by:

$$F_{cas} = \frac{\pi^2 \hbar c L^2}{240 l^4} \tag{7.25}$$

i.e. An attractive pressure of:

$$P_{cas} = \frac{\pi^2 \hbar c}{240 l^4} \tag{7.26}$$

Finally, however, it is worth going back to look at the large constant terms.

In particular, $L^2 l T_1$ is an energy term which is simply proportional to the volume of the space. R is no longer meaningful, or at least it is no longer a function of the metal (we are talking about a property of space, the vacuum energy density). Nonetheless there is a highest meaningful energy of excitation to consider, that of The Planck energy scale, corresponding to a maximum wave vector of $k = \sqrt{\frac{c^3}{\hbar G}}$.

If we take this as a sharp cut-off we come up with a vacuum energy density of:

$$\rho_\Lambda = \frac{1}{8\pi^2} \frac{c^7}{\hbar G^2} = 5.9 \times 10^{111} \tag{7.27}$$

This corresponds to a cosmological parameter, Ω_Λ, of 7.1 x 10^{120} which is famously an estimate of energy density which is a hundred and twenty-one orders of magnitude too high, the most recent reliable experimental measurement being $\Omega_\Lambda = 0.685 \pm 0.013$. [158]

7.5.2 Unsuccessful attempt to calculate Casimir force pulling a metal bubble together.

The wave equation in a bubble is:

$$\frac{1}{c^2} \frac{\partial^2 \psi}{\partial t^2} = \nabla^2 \psi \tag{7.28}$$

$$\frac{-\omega^2}{c^2} \psi = \frac{1}{r^2} \frac{\partial}{\partial r} \left(r^2 \frac{\partial \psi}{\partial r} \right) + \frac{1}{r^2} \left(\frac{1}{\sin\theta} \frac{\partial}{\partial \theta} \left(\sin\theta \frac{\partial \psi}{\partial \theta} \right) + \frac{1}{\sin^2 \theta} \frac{\partial^2 \psi}{\partial \theta^2} \right)$$

(7.29)

With the boundary condition $\psi = 0$ when $r = R$.

The solution to this equation is:

$$\psi = N j_l\left(\frac{r\omega}{c}\right) Y_{lm}(\theta,\phi) = N\sqrt{\frac{\pi c}{2\omega r}} J_{l+\frac{1}{2}}\left(\frac{r\omega}{c}\right) Y_{lm}(\theta,\phi) \tag{7.30}$$

Where j_l are the spherical Bessel Functions, $J_{l+\frac{1}{2}}$ are the ordinary Bessel Function and $Y_{lm}(\theta,\phi)$ are the spherical Harmonic functions. $j_0 = sinc\left(\frac{r\omega}{c}\right)$ the other Spherical Bessel functions look as per figure 7.6.

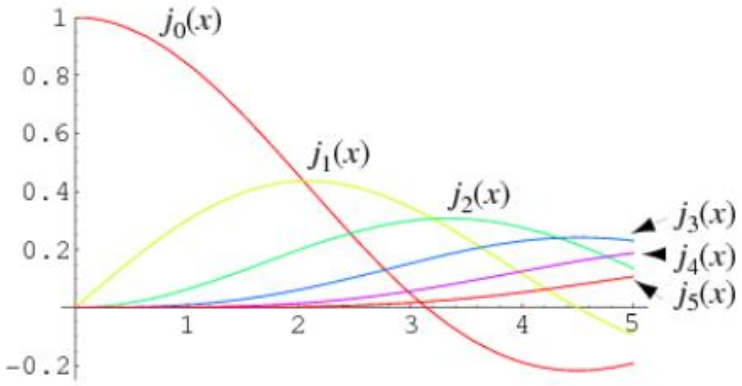

Figure 7.6. Spherical Bessel functions.

Applying the boundary conditions $\psi(R = 0) = 0$ means that each value of l gives an infinite number of solutions for ω. Furthermore, the degeneracy of each solution is equal to $2l + 1$.

The exact position of the zeros of the Spherical Bessel functions is not easy to calculate but the general pattern is quite clear. j_0, being a $sinc$ function has zeros at $\pi, 2\pi, 3\pi, 4\pi$ etc. All the other spherical Bessel functions have zeros at 0.

The zeros of j_1 are at $0, 1.43\pi, 2.46\pi$, and further zeros generally approach the **odd half-integer** multiples of π.

The zeros of j_2 are at $0, 1.83\pi, 2.90\pi$, and further zeros generally approach the **integer** multiples of π.

The zeros of j_3 are at $0, 2.22\pi, 3.32\pi, 4.36\pi$ and further zeros generally approach the **odd half- integer** multiples of π. *etc.*

This means that there is:

One mode for $\omega = \frac{c\pi}{R}$, one for $\omega = \frac{2c\pi}{R}$, one for $\omega = \frac{3c\pi}{R}$ etc.

Three modes each for $\omega = 1.43\frac{c\pi}{R}$, $\omega = 2.46\frac{c\pi}{R}$, and further frequencies just less than **odd half-integer** multiples of $\frac{c\pi}{R}$.

Five modes each for $\omega = 1.83\frac{c\pi}{R}$, $2.90\frac{c\pi}{R}$, and further frequencies just less than **integer** multiples of $\frac{c\pi}{R}$.

Seven modes each for $\omega = 2.22\frac{c\pi}{R}$, $3.32\frac{c\pi}{R}$, $4.36\frac{c\pi}{R}$, and further frequencies just less than **odd half-integer** multiples of $\frac{c\pi}{R}$

We can use the above to calculate an approximate density of states. Approximate number of states less than N_M (where $N_M = \frac{R}{c\pi}\omega_{MAX}$) is given by:

$$= N_M + \sum_{\substack{n\ even \\ from\ 2}}^{2N_M-2} \left(N_M - \frac{n}{2}\right)(2n+1) + \sum_{\substack{n\ odd \\ from\ 1}}^{2N_M-1} \left(N_M - \frac{n-1}{2}\right)(2n+1) \tag{7.31}$$

$$= \frac{N_M}{6}\left(16N_M^2 + 6N_M + 5\right) \tag{7.32}$$

$$\int_{\omega'=0}^{\omega} g(\omega')d\omega' = \frac{\omega R}{6\pi c}\left(16\left(\frac{\omega R}{\pi c}\right)^2 + 6\left(\frac{\omega R}{\pi c}\right) + 5\right) \tag{7.33}$$

The leading term tells us that:

$$\int_{\omega'=0}^{\omega} g(\omega')d\omega' = \frac{8R^3\omega^3}{3\pi^3 c^3} \tag{7.34}$$

Which is a crude approximation to the Rayleigh Jeans density of states, being an overestimate by 21%. So this approximation is simply inadequate for the purpose which we might have hoped to use it for.

8 Appendix 2 – Asymmetric Dice

This appendix details an initially unrelated vein of research which answers an interesting classical physics question which is, in its simplest form, the probability of a 4x2 piece of wood (or other rectangular cross sectioned prism) landing on the thick or narrow side. It outlines research published in 2014 ("Predicting non-square 2D dice probabilities" by G A T Pender and M Uhrin published in the European Journal of Physics 17th June 2014[159]).

Theoretical, experimental and computations results are presented to show that a k x l length of wood lands in its two possible states with a probability ratio: $\frac{\sqrt{k^2+l^2}-k}{\sqrt{k^2+l^2}-l}\frac{arctan\frac{l}{k}}{arctan\frac{k}{l}}$.

Similar theoretical and experimental results are presented for cylinders and a discussion of other geometries is pursued.

8.1 Introduction

The question of the final state probabilities of a general cuboid randomly thrown onto a surface is a problem that naturally arises in the minds of men and women familiar with regular cubic dice and the basic concepts of probability. Indeed, it was considered by Newton in 1664[160]. I have made progress on the 2D problem (which can be realised in 3D by considering a long cuboid, or alternatively a rectangular cross-sectioned dreidel).

For the two-dimensional case, I suggested that the ratio of the probabilities of landing on each of the two sides is given by $\frac{\sqrt{k^2+l^2}-k}{\sqrt{k^2+l^2}-l}\frac{\arctan\frac{l}{k}}{\arctan\frac{k}{l}}$ where k and l are the lengths of the two sides. I test this theory experimentally, and find good agreement between this theory and experiment. A fellow student, Martin Uhrin, was able to provide computational results to corroborate this with reduced random errors.

The theory is known, from its derivation, to be an approximation for particularly bouncy or "grippy" surfaces where the die rolls through many revolutions before settling. On real surfaces, we would expect (and we observe) that the true probability ratio for a 2D die is a somewhat closer to unity than predicted by this theory.

After publishing this result in the European Journal of Physics the journal drew our attention to a previous paper by Herman Bondi[161] predicting the dropping probability of a cylinder. Bondi's prediction however does not give results which agree with experiment.

Our theory for long cuboids can be extended to predict for cylinders and is found to give reasonable agreement with experiment, albeit with some systematic error.

Further subsections in this chapter extend this problem into other geometries for square based cuboids and cylinders.

8.1.1 The Problem

When a cube is thrown it bounces around and eventually has a one sixth chance of settling on any given side. A deliberately biased die is usually made by modifying the weight distribution within a cube to alter the position of the centre of mass. A die can also be biased if one of the dimensions is slightly longer or shorter than the others. For example, the biased die (net shown on the right in Figure 8.1) would have an enhanced probability of coming up with a six or a one, relative to a fair die (net on left).

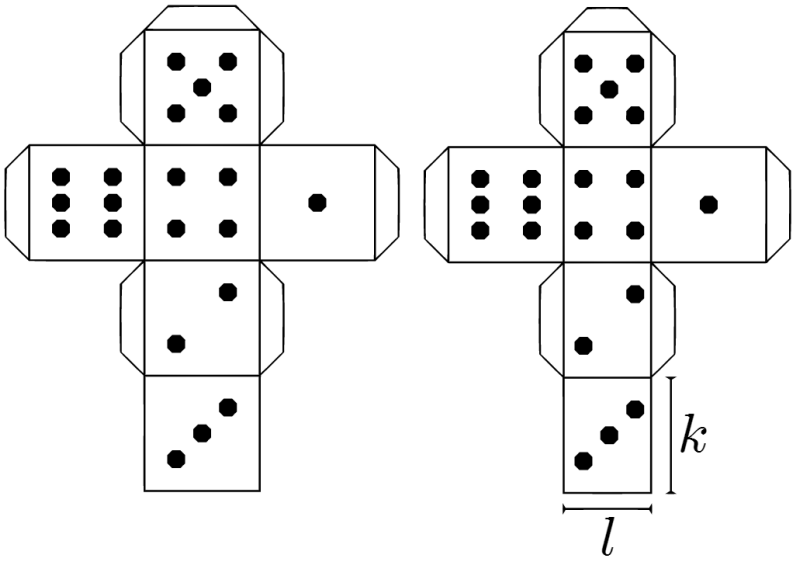

Figure 8.1. Net for a fair die (left) and a die biased to give a higher variance (right). Note that the average score for both dice would always be the same, owing to the rule that opposite sides of a die always sum to seven.

Exactly how the probability of getting a six might depend upon the ratio of k to l (or any other parameters) is a problem that would be good to solve although I have found the two-dimensional case to be far more tractable. This is equivalent to the three-dimensional case of a cuboidal "die", where the length is very much greater than the breadth (and width).

One example of a two-dimensional die is that of the dreidel (a traditional Jewish spinning toy, see Figure 8.3) which is, effectively, a four-sided, 2D die.

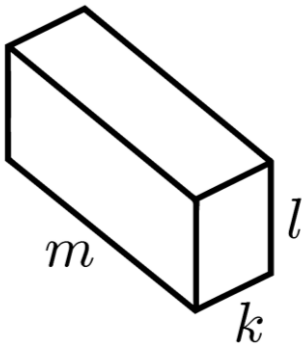

Figure 8.2. General Question: What is the probability of the cuboid eventually settling with any face uppermost if it is given a random (reasonably large) initial angular momentum and a random (reasonably large) initial collision velocity with respect to the (reasonably rough and moderately elastic) ground?

Figure 8.3. Dreidel: A two-dimensional die which forms the basis of a traditional game played by Jewish children during the festival of Hanukkah. Viewed from above, the dreidel has a square cross-section (giving a one quarter probability of landing on each side). A biased dreidel could be made by using a rectangular (non-square) cross-section. This is qualitatively understood and, for the same reason that traditional dice place the one and the six opposite each other, so too the best and worst outcomes for the dreidel ("gimel" and "shin") also tend to be placed opposite one another.

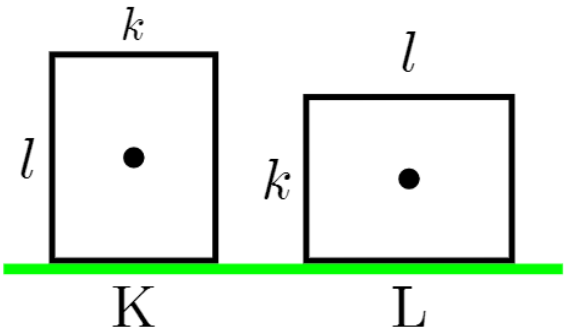

Figure 8.4. There are two possible final states labelled "K" and "L". The energy of these states are $E(K) = \frac{1}{2}mgl$ and $E(L) = \frac{1}{2}mgk$ respectively.

Newton originally considered this problem as long ago as 1664. More recently, Riemer et al.[162] considered this problem for the three-dimensional case. Riemer developed a semi-empirical method (based loosely on ideas from thermodynamics) with a free parameter (analogous to temperature) which is set empirically. This parameter allows Riemer to adjust for the fact that other variables have an impact on the final state probabilities. For example, the properties of the surface could (and our experimental results suggest, do) affect the relative probabilities of the various possible outcomes. Nonetheless, the value of Riemer's free parameter has no theoretical justification even, for example, in the limiting case of a bouncy, high friction surface: $e \to 1, \mu \to 1$ (where e and μ are the coefficients of restitution and friction). The presence of a purely empirical free parameter is clearly a drawback of Riemer's theory.

Mungan and Lipscombe[163] have proposed another semi-empirical model, mathematically different from but, in broad form, similar to that of Riemer's model (and with its own empirical free parameter) is fitted to/tested on the same historical 1980s data set[164] as that of Riemer et al. and both fit this data set to within binomial errors.

My model (which only covers the behaviour of "long" cuboids or other effectively two-dimensional dice) contains certain approximations (for example we assume the die bounces a great many times before it comes to a stop) but, within those approximations, it does not require an empirically set parameter.

8.2 2D Theory

Consider the two state, two-dimensional, model shown in Figure 8.4. First suppose that the die is dropped (in a random orientation, with zero angular momentum and from a low

height) and falls inelastically onto the floor. Under these circumstances the probability of landing on any particular side would be proportional to the angle subtended by that side.

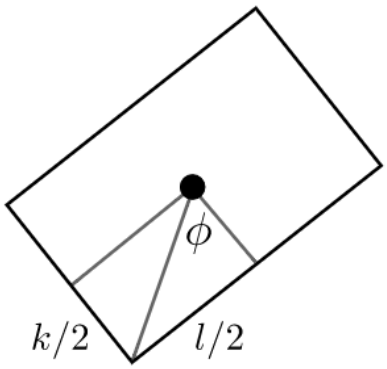

Figure 8.5. If the die were dropped inelastically then the chance of landing in any particular orientation, $P_I(K)$ and $P_I(L)$, would simply be proportional to the angle subtended by that side of the die.

For example, a die dropped from a low height in the orientation shown in Figure 8.5 would settle in state L (*i.e.* it would land on the long side). Since all initial angular orientations must be equally likely, the die, if released in a random orientation and from a low height (still with zero initial angular momentum), would exhibit the following probabilities of landing in states K and L respectively:

$$P_I(K) = \frac{\arctan\frac{k}{l}}{\frac{\pi}{2}}, \quad P_I(L) = \frac{\arctan\frac{l}{k}}{\frac{\pi}{2}} \tag{8.1}$$

These probabilities are equivalent to those predicted by a two-dimensional version of what Riemer *et al.* calls the "Simpson model",[165] named after Thomas Simpson who, in 1740, proposed that the probability of an $a \times b \times c$ cuboid landing on the $a \times b$ surface would be:

$$P_I(c-vertical)_{3D} = \frac{1}{\pi}\arctan\left(\frac{ab}{c\sqrt{a^2+b^2+c^2}}\right) \tag{8.2}$$

However, whichever way the die is dropped there is a probability of getting the other state due to the somewhat elastic nature of the collisions. Consequently, the Simpson model tends to overestimate the probability of the higher energy outcomes. To model bouncing from one state to the other, we first have to recognise (see Figure 8.6) that to make the transition the block must have a total energy of at least:

$$E_{Trans} = \frac{1}{2} mg\sqrt{l^2 + k^2} \tag{8.3}$$

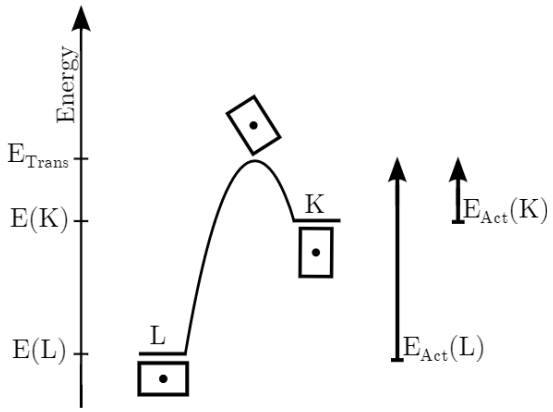

Figure 8.6. Energy Level Diagram Showing two states and transition state.

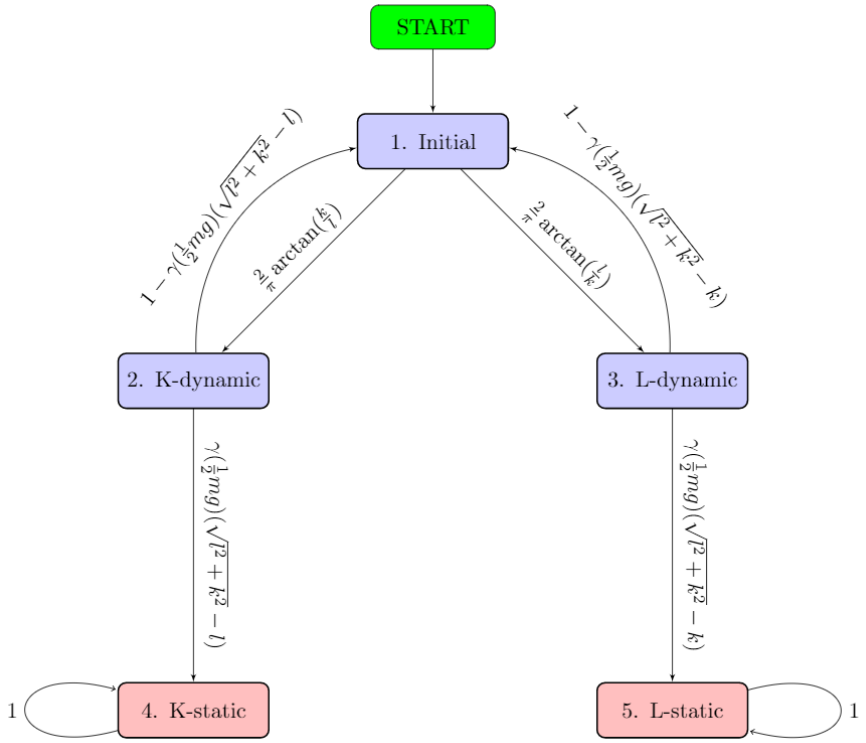

Figure 8.7. Final calculation of probability ratios for dice rolling on a reasonably elastic and reasonably grippy surface with initial angular momentum, initial height and initial velocity picked from a reasonably broad random distribution. $\gamma \to 0$ represents the case where the dice bounce or roll a large number of times before settling.

To continue the analysis of this problem we consider a five state Markov Chain (Figure 8.7), the nodes of which are as follows:

1 Top of Figure 8.7: A high-energy state (the initial state) where the die experiences a random chance of going into one or other dynamic state (states 2 and 3).

2 Middle Left of Figure 8.7: A state (K-dynamic) where the die's centre of mass is over the side of length k but it has enough energy to overcome the transition state (see Figure 8.6)

3 Middle Right of Figure 8.7: An analogous state (L-dynamic) where the centre of mass is over the side of length l but, again, with a total energy of at least E_{Trans}.

4 Bottom Left of Figure 8.7: A stable state (K-static) where the die is bound to end up in K because the die is nearly in final state K and has energy less than E_{Trans}.

5 Bottom Right of Figure 8.7: An analogous stable state, "L static". The probability arcs exiting the initial state are just the inelastic probabilities from equation 8.1.

The probabilities exiting the two dynamic states are initially unknown but we know the exiting arcs from each dynamic state must sum to unity. The chance of returning to the initial state will be higher for more elastic collisions and will tend to unity for highly elastic collisions. This chance will be higher from K-dynamic than from L-dynamic as the lower bound on the energy of K-dynamic is higher than the lower bound on the energy of L-dynamic. Once the system reaches either of the static states it remains in that state (indicated by the circular arcs found at nodes 4 and 5).

The key to solving the 2D problem lies in the assigning of the relative weights (in the limit of nearly elastic collisions) of the arcs leading from nodes 2 and 3. We will assume that the die starts with a large amount of kinetic energy (both rotational and translational) and that this energy is gradually lost until the total energy is less than $E_{Trans} = \frac{1}{2}mg\sqrt{l^2 + k^2}$, at which point the die settles. The probability of getting from L-Dynamic to L-Static is therefore proportional to the "activation energy" $E_{Act}(L)$, for this transition (see Figure 8.6).

$$E_{Act}(L) = E_{Trans} - E(L) = \frac{1}{2}mg\left(\sqrt{l^2 + k^2} - k\right) \tag{8.4}$$

So the probabilities of the two "downward" transitions (in Figure 8.7) are given by:

$$P = (L - Dynamic \rightarrow L - Static) = \gamma\left(\frac{1}{2}mg\right)\left(\sqrt{l^2 + k^2} - k\right) \tag{8.5}$$

$$P = (K - Dynamic \rightarrow K - Static) = \gamma\left(\frac{1}{2}mg\right)\left(\sqrt{l^2 + k^2} - l\right) \tag{8.6}$$

Where γ is a single (small) unknown. Numbering the five possible states as in Figure 8.7, from 1 to 5, the transpose of the transition matrix $\underline{\underline{P}}$ is therefore:

$$\underline{\underline{P}}^T = \begin{pmatrix} 0 & 1-\gamma\left(\frac{1}{2}mg\right)\left(\sqrt{l^2+k^2}-l\right) & 1-\gamma\left(\frac{1}{2}mg\right)\left(\sqrt{l^2+k^2}-l\right) & 0 & 0 \\ \frac{2}{\pi}\arctan\frac{k}{l} & 0 & 0 & 0 & 0 \\ \frac{2}{\pi}\arctan\frac{l}{k} & 0 & 0 & 0 & 0 \\ 0 & \gamma\left(\frac{1}{2}mg\right)\left(\sqrt{l^2+k^2}-k\right) & 0 & 1 & 0 \\ 0 & 0 & \gamma\left(\frac{1}{2}mg\right)\left(\sqrt{l^2+k^2}-k\right) & 0 & 1 \end{pmatrix} \tag{8.7}$$

Denoting the elements of $\underline{\underline{P}}$ by $p_{i,j}$ then, after n-steps, with an initial state vector $(1,0,0,0,0)^T$, we arrive at state $\left(\underline{\underline{P}}^T\right)^n (1,0,0,0,0)^T$. In principle, it would be possible to calculate the final state probabilities $P(K)$ and $P(L)$ by recursively applying $\underline{\underline{P}}^T$ to the initial state vector for like so,

$$\left(\underline{\underline{P}}^T\right)^\infty \begin{pmatrix} 1 \\ 0 \\ 0 \\ 0 \\ 0 \end{pmatrix} = \begin{pmatrix} 0 \\ 0 \\ 0 \\ P(K) \\ P(L) \end{pmatrix} \tag{8.8}$$

However, it will be instructive to consider the state achieved after just two iterations.

Applying $\underline{\underline{P}}^T$ to the initial state vector twice gives:

$$\left(\underline{\underline{P}}^T\right)^2 \begin{pmatrix} 1 \\ 0 \\ 0 \\ 0 \\ 0 \end{pmatrix} = \begin{pmatrix} p_{12}p_{21} + p_{13}p_{31} \\ 0 \\ 0 \\ p_{12}p_{24} \\ p_{13}p_{35} \end{pmatrix} \tag{8.9}$$

Using the exact expression for $\underline{\underline{P}}^T$, and since $\arctan(k/l) + \arctan(l/k) = \pi/2$, we get for $\gamma \ll 1$:

$$\left(\underline{\underline{P}}_{\gamma\to 0}^{T}\right)^{2}\begin{pmatrix}1\\0\\0\\0\\0\end{pmatrix}=\begin{pmatrix}\approx 1\\0\\0\\p^{(2)}(1\to 4)\\p^{(2)}(1\to 5)\end{pmatrix}=\begin{pmatrix}\approx 1\\0\\0\\\frac{\gamma mg}{\pi}\left(\sqrt{l^2+k^2}-l\right)\arctan l/k\\\frac{\gamma mg}{\pi}\left(\sqrt{l^2+k^2}-k\right)\arctan l/k\end{pmatrix} \tag{8.10}$$

Since all probability weight returned to the initial state will eventually be distributed to the final states in the same $p^{(2)}(1\to 4)$: $p^{(2)}(1\to 5)$ ratio, we find that:

$$\frac{P(L)}{P(K)}=\frac{p^{(2)}(1\to 4)}{p^{(2)}(1\to 5)}=\frac{\sqrt{l^2+k^2}-k}{\sqrt{l^2+k^2}-l}\frac{\arctan l/k}{\arctan k/l} \tag{8.11}$$

Alternatively, it may be more intuitive to think in terms of the angle between the side of the block and the block diagonal (equivalent to the angle, ϕ, in Figure 8.5).

$$\arctan\frac{l}{k}=\phi \quad , \quad \arctan\frac{k}{l}=\frac{\pi}{2}-\phi \tag{8.12}$$

In which case equation 8.11 becomes:

$$\frac{P(L)}{P(K)}=\frac{1-\cos\phi}{1-\cos\left(\frac{\pi}{2}-\phi\right)}\frac{\phi}{\frac{\pi}{2}-\phi}=\frac{sin^2\frac{\phi}{2}}{sin^2\left(\frac{\pi}{4}-\frac{\phi}{2}\right)}\frac{\phi}{\frac{\pi}{2}-\phi} \tag{8.13}$$

When analysing experimental results, it is easier to measure side length than to measure angles. So we will plot experimental results in terms of side length ratios, $R=\frac{l}{k}$:

$$\frac{P(L)}{P(K)}=\frac{\sqrt{1+R^2}-1}{\sqrt{1+R^2}-R}\frac{\arctan R}{\arctan(1/R)} \tag{8.14}$$

Clearly $P(L)+P(K)=1$ and so the raw probabilities can be extracted from the probability ratio as follows:

$$P(K)=\frac{1}{1+\frac{P(L)}{P(K)}} \tag{8.15}$$

This probability is plotted in Figure 8.8, however, generally it is better to present results in terms of probability ratios (as we will in, for example, Figure 8.10). The use of ratios has three main advantages over the use of raw probabilities: it makes the expression mathematically tidier, it will later allow us to ignore the very small number of times the block lands in the third "end-on" orientation, similarly it will allow us to more easily ignore the very small proportion of computational runs where the code yields an error of some kind.

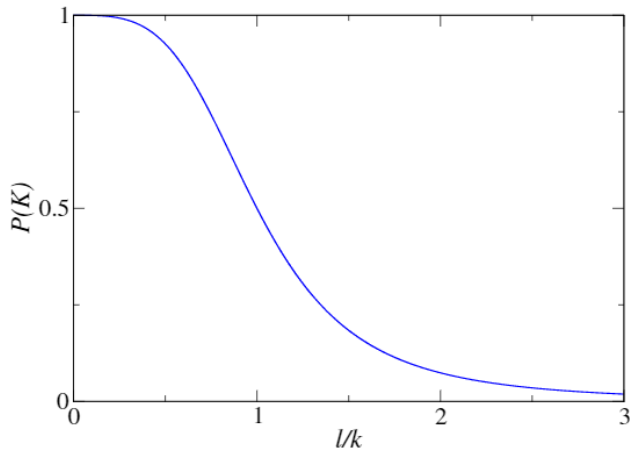

Figure 8.8. 2D-Probability: The predicted face probabilities for a two-dimensional block, although I will use probability ratios.

The above derivation has tended to assume $1 \leq R < \infty$ we can cover exactly the same parameter space by relabelling the sides to have $0 \leq R < 1$. This makes it possible to plot the whole parameter space on an axis from 0 to 1.

For more realistic surfaces (*e.g.* not highly bouncy) we would expect the frequency ratio to be closer to unity than predicted by equation 8.14, while never being as close to unity as predicted by the "no bounce" model (equation 8.1). It is useful to consider the role of γ in this new model. I initially thought of gamma as being inversely linked to the "bounciness" of the surface because decreasing it increases the probability that a die will continue to roll as opposed to settling on the current side. Clearly there is an upper bound on γ beyond which the back probabilities from the dynamic states become negative, but up to this limit, our final state probabilities are independent of its value. In fact, γ is simply a dummy variable, not linked to any physical quantity. However, physical intuition tells us that we should see probability predictions that are somewhat between our model and the "no bounce" (or Simpson) model.

8.3 Experiment – 2D

Wishing to test the derived relationship (equation 8.14), two sets of long blocks were made. First, pine blocks were rolled on either carpet or a thin layer of towelling. The second set were 3D printed from polylactide plastic using a MakerBot Replicator 2 with a quoted accuracy of 11 μm[166]. These were rolled, with initial angular momentum predominantly along the length, on a Medium Density Fibreboard (MDF) surface, as well as, separately, on tough carpet.

As this study is primarily concerned with two-dimensional blocks it is important to establish that the long side (length m) is sufficiently long that increasing it further does not affect the outcome of a roll. Verification of this can be found in Section 8.6 for several blocks.

The full set of results are plotted in results Figure 8.10. Our theory makes good predictions for both wooden and printed blocks rolled on carpet, with a spread of data consistent with ordinary binomial errors. It is noticeable that the surface on which the block rolls has a systematic effect on the probability ratios. As expected, probability ratios measured for printed blocks on MDF are invariably closer to unity than theory would predict. The same blocks rolled on carpet (a surface on which they roll, often through many revolutions, rather than "clattering") give a probability ratio closer to the theoretical prediction from section 8.2.

Table 8.1 shows the full tabulation of all experimental results including details on the total number of rolls. The probability ratio between the two outcomes, L and K (with measured frequency ratios N_L and N_K, respectively), is estimated as:

$$\frac{N_L}{N_K} \pm \sqrt{\frac{N_L N_K (N_L + N_K)}{N_K^4}} \tag{8.16}$$

i.e. the probability is estimated, with ordinary binomial errors, as:

$$\frac{N_L}{N_L + N_K} \pm \sqrt{\frac{N_L N_K}{(N_L + N_K)^3}} \tag{8.17}$$

Figure 8.9. A selection of the rectangular cross sectioned prisms used for this experiment.

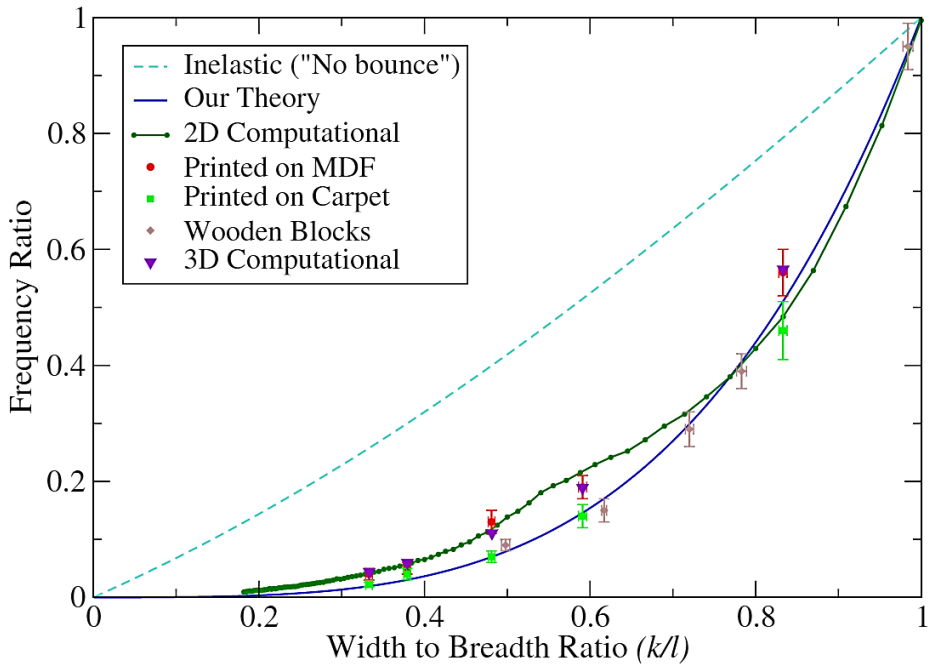

Figure 8.10. Graph comparing theory from equation 8.14 (solid dark blue line) with experimental and computational results. From theory we would expect the ratio of final state frequencies (for long cuboids) to be very slightly above the theory line with convergence for blocks which can be expected to roll many times before settling. The dashed (lighter blue) line gives a “No Bounce” prediction, the two-dimensional version of what Riemer et al [3] call the “Simpson model”. This data represents between ten to twenty thousand individual experimental rolls. Finally, the set of connected green circles and the purple triangles show results from two- and three-dimensional computational simulations.

Length (mm)	Breadth (mm)	Width (mm)	Width/ Breadth R	Predicted Probability Ratio (<1)	Block	Surface	Number of Throws	Freq. Length Vertical	Freq. Breadth Vertical	Freq. Width Vertical	Freq. Ratio <1 binomial error
782 ± 1	25.0 ± 0.1	18.0 ± 0.1	0.720 ± 0.005	0.299 ± 0.008	Pine	Carpet	800		178	622	0.29 ± 0.03
98 ± 1	"	"	"	0.299 ± 0.008	"	"	200		46	154	0.30 ± 0.06
119.3 ± 0.1	61.7 ± 0.4	48.3 ± 0.2	0.783 ± 0.006	0.406 ± 0.012	"	Thin towel	800	8	222	570	0.39 ± 0.03
360 ± 1	43.4 ± 0.2	21.6 ± 0.2	0.498 ± 0.005	0.079 ± 0.003	"	"	1000		80	920	0.09 ± 0.01
99.3 ± 0.1	43.9 ± 0.2	43.2 ± 0.2	0.984 ± 0.005	0.912 ± 0.023	"	"	2000	21	962	1014	0.95 ± 0.01
348 ± 1	70.3 ± 0.2	43.4 ± 0.2	0.617 ± 0.003	0.171 ± 0.003	"	Towel+ Rug	1000		130	870	0.15 ± 0.02
140.0 ± 0.1	24.0 ± 0.1	20.0 ± 0.1	0.833 ± 0.005	0.511 ± 0.013	Printed	MDF	1000		361	639	0.54 ± 0.04
100.0 ± 0.1	"	"	"	0.511 ± 0.013	"	"	1000		386	514	0.53 ± 0.04
80.0 ± 0.1	"	"	"	0.511 ± 0.013	"	"	1000	4	342	534	0.52 ± 0.04
140.0 ± 0.1	22.0 ± 0.1	13.0 ± 0.1	0.591 ± 0.005	0.116 ± 0.005	"	"	1000		160	810	0.19 ± 0.02
80.0 ± 0.1	"	"	"	0.146 ± 0.005	"	"	500		84	416	0.20 ± 0.03
140.0 ± 0.1	27.0 ± 0.1	13.0 ± 0.1	0.481 ± 0.004	0.070 ± 0.002	"	"	500		58	442	0.13 ± 0.02
"	29.0 ± 0.1	11.0 ± 0.1	0.379 ± 0.004	0.030 ± 0.001	"	"	500		26	474	0.05 ± 0.01
"	30.0 ± 0.1	10.0 ± 0.1	0.333 ± 0.004	0.019 ± 0.001	"	"	500		19	481	0.04 ± 0.01
140.0 ± 0.1	24.0 ± 0.1	20.0 ± 0.1	0.833 ± 0.005	0.511 ± 0.013	Printed	Tough	500		137	343	0.16 ± 0.03
"	22.0 ± 0.1	13.0 ± 0.1	0.591 ± 0.005	0.146 ± 0.005	"	Carpet	500		62	438	0.14 ± 0.02
"	27.0 ± 0.1	13.0 ± 0.1	0.481 ± 0.004	0.070 ± 0.002	"	"	300		31	469	0.07 ± 0.01
"	29.0 ± 0.1	11.0 ± 0.1	0.379 ± 0.004	0.030 ± 0.001	"	"	1000		39	961	0.04 ± 0.01
"	30.0 ± 0.1	10.0 ± 0.1	0.333 ± 0.004	0.015 ± 0.001	"	"	2000		43	1957	0.022 ± 0.004

Table 8.1. Full Experimental Data for long cuboids. (Colours as per Figure 8.10)

8.4 Computational work - 2D

Note: The Computational work outlined in this section was almost entirely conducted by Martin Uhrin, a fellow student at UCL, and this section (section 8.4) was also mostly written by him. However, it is worth including these computational results as they help to confirm the validity of the theory outlined in section 8.2.

Using a rigid body simulation, two sets of computational experiments were carried out: One constrained to two-dimensions and the other a direct analogue to our experiments, fully unconstrained in all three-dimensions, modelling the behaviour of the long cuboids thrown on MDF. Our simulation code, DicePhys, uses the Bullet physics engine[167] to provide the rigid body dynamics and integration of equations of motion.

The simulation world was configured to match the experimental conditions of the printed blocks on MDF as closely as possible. Table 8.2 shows the set of initial conditions used throughout. Where a range is shown a uniformly distributed random number spanning the interval was used. The experimental procedure used to determine the frictional coefficient, μ, is outlined in section 8.5. The coefficient of restitution, e, was estimated to be 0.5. For each set of dimensions, a minimum of 100,000 virtual rolls were performed to achieve very small random errors in outcome probabilities.

The simulation code was written using the Bullet physics engine. Bullet uses the sym-plectic Euler integration scheme[168] to integrate the equations of motions for sets of rigid bodies and impulses to resolve collisions between objects. The simulation used a fixed integration timestep. The size of this timestep was chosen such that we were confident that any further reduction in timestep would not materially affect the results. More specifically, we are confident that the outcome frequency ratio was within one percent of the frequency ratio that would be yielded by the same simulation, with timestep reduced by a further order of magnitude.

Figure 8.11 shows convergence test results for three blocks. Based on these a timestep of 0.001 s was deemed to be sufficient.

Parameter	Initial Value
Linear velocity (m/s) Angular velocity (rad/s) Drop height (m)	$-0.2 \rightarrow 0.2$ $31 \rightarrow 160$ $0.2 \rightarrow 0.4$
μ e	0.29 0.5

Table 8.2. Initial conditions used in all simulations

The results of our computational simulations can be seen in Figure 8.10. Error bars for these curves are smaller than the size of the symbols and are therefore not shown. All three-dimensional simulations (purple triangles) are in good agreement with the equivalent experimental results (red circles). Agreement between experiment and the two-dimensional simulations (green circles connected by lines) is less good with the simulation line lying outside of two of the five experimental error bars. This may be an artefact of the way the physics engine constrains the system to a plane when simulating in two dimensions as evidenced by the discrepancy between the two and three dimensional simulation results. The full simulation code is available online.[169]

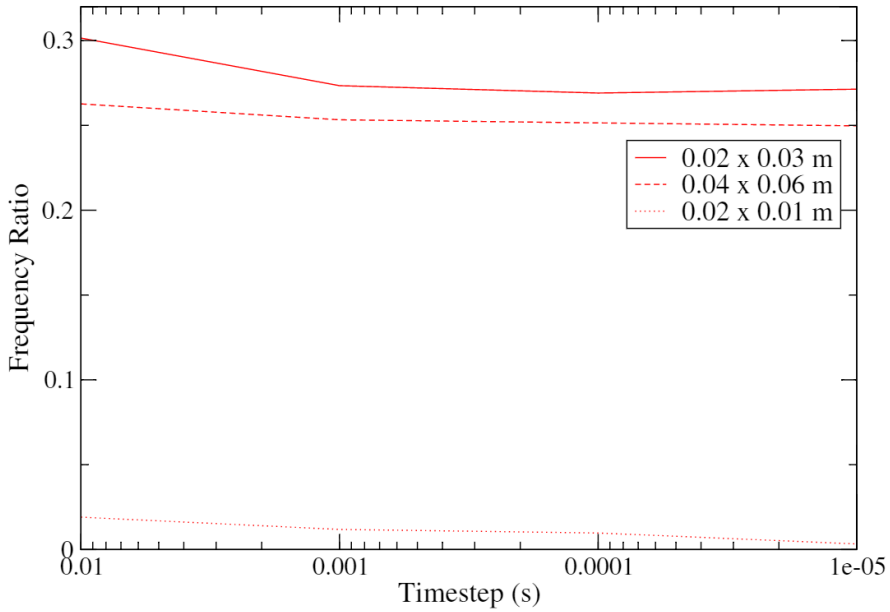

Figure 8.11. Convergence testing for three block sizes showing how the rolling outcome is changed when decreasing the computational timestep.

8.5 Determining the Coefficient of Restitution and the Frictional Coefficient

Martin's computational code required an estimate for both the coefficient of restitution and the coefficient of dynamic friction although the results were not strongly dependent on these values within quite a broad range of values (including all reasonable estimates of their true values).

The coefficient of restitution was estimated from the rebound height of blocks bouncing on MDF (which seemed, when dropped in a perpendicular fashion, to rebound to a quarter of their original height).

The coefficient of dynamic friction between the printed block material and the MDF board was determined by inclining the board at an angle and noting the behaviour of the block. The lengths of two sides of the right angled triangle were measured, as per Figure 8.12, in order to determine the angle of the slope.

The dynamic frictional coefficient is the tangent of the slope angle where a moving block has a roughly 50:50 chance of slowing to a stop. The static frictional coefficient is the tangent of the slope angle where a block placed on the slope has a roughly 50:50 chance of remaining stationary after the experimenter lets go of it. These values were found to be $\mu_{static} = 0.50 \pm 0.03$ and $\mu_{dynamic} = 0.29 \pm 0.01$ as can be seen in Table 8.3.

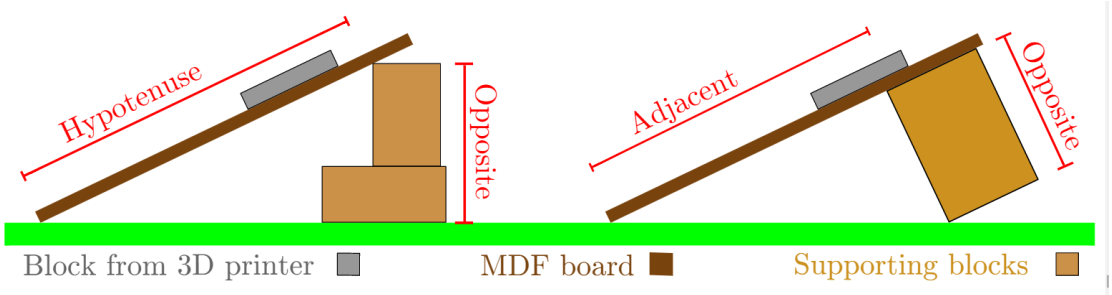

Figure 8.12. Frictional Coefficient measured by observing the behaviour of blocks on inclined surface.

Adjacent (cm)	Opposite (cm)	Hypotenuse (cm)	Slope Angle (°)	Tan(angle)	Moving (or tapped) Block Behaviour	Stationary Block Behaviour	
	16.3 ± 0.1	60.5 ± 0.2	15.6 ± 0.1	0.280 ± 0.002	Mostly stops	Sticks	
	16.3 ± 0.1	58.6 ± 0.2	16.2 ± 0.1	0.290 ± 0.002	50:50	Sticks	*
	16.3 ± 0.1	56.3 ± 0.2	16.8 ± 0.1	0.302 ± 0.002	Mostly doesn't stop	Sticks	
71.8 ± 0.1	34.8 ± 0.1		25.9 ± 0.1	0.485 ± 0.002	Doesn't stop	Sticks	
69.3 ± 0.1	34.8 ± 0.1		26.7 ± 0.1	0.502 ± 0.002	Doesn't stop	Sticks 50:50	**
65.2 ± 0.1	34.8 ± 0.1		28.1 ± 0.1	0.534 ± 0.002	Doesn't stop	Always slips	

Table 8.3. * Dynamic Friction $\mu = 0.29 \pm 0.01$ ** Static Friction $\mu = 0.50 \pm 0.03$

8.6 Invariance of Outcome When Changing Length, m

To test that experimental blocks were sufficiently long such that the outcome of a roll was unaffected by the particular length of side *m* we performed three sets of tests where m was varied but the other dimensions were fixed. Results from these tests (graphed in Figure 8.13) confirm our assertion. We can conclude that, if the length is much longer than the other two-dimensions, further increases in length do not materially affect outcome probabilities. Full data in Table 8.1, Section 8.3.

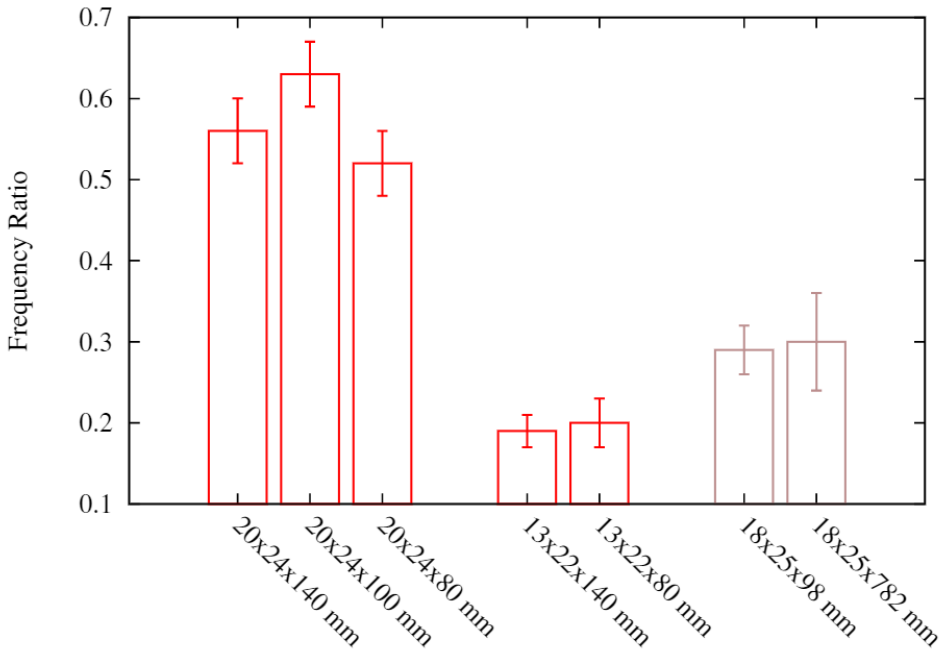

Figure 8.13. Plot of the ratio of the number of Breadth Vertical outcomes to Width Vertical outcomes for three sets of blocks. Within each set the Width and Breadth of the block was identical but the long length, m, varied. The error bar shown is binomial error.

8.7 The slightly off-square (moderately biased dreidel)

Consider the case of a deliberately biased dreidel which has one side marginally longer than the other such that $\frac{l}{k} = R = 1 + \delta$ where $\delta \ll 1$. With $\delta = 0.01$ using equation 8.13, $P(K) = 1/2.03737 \simeq 0.4908$. Hence, the probability differs from that of a fair dreidel by $1/2.03737 \simeq 0.4908$, or close to 2%. To put it another way, each of the slightly longer sides would have a 25.46 % chance of being landed on as opposed to 24.54 % for either of the shorter sides.

Expanding equation 8.14 around $R = 1$ gives a probability ratio of $\frac{P(L)}{P(K)} = 1 + \left(1 + \sqrt{2} + \frac{4}{\pi}\right)\delta + O(\delta^2)$. Combining this with equation 8.16, we see that an ordinary four sided dreidel, biased in this way, will now show side probabilities of $\frac{1}{4} \pm \frac{1+\sqrt{2}+4/\pi}{8}\delta$.

8.8 Results for a Real Biased Spinning Top

Figure 8.14. The above highly biased Dreidel was made by sanding flat an ordinary square cross sectioned Dreidel to give a rectangular cross-sectioned spinning top with side measurements 28 x 16 mm. The model set out in section 8.2 predicts that it should settle on the broad side to the narrow side in a numerical ratio of 31:4.

The above Dreidel was spun a total of 2000 times. It settled on the broader side a total of 1771 times and settled on the narrower side a total of 229 times. This is in line with the experimental results plotted for planks with side ratios of just under 0.6 in Figure 8.15.

Side Ratio (28 x 16 mm) = 1.75

Predicted Frequency Ratio	**=**	**7.7 $\pm$ 0.6**
Observed Number Flat	=	1771
Observed Number Up	=	229
Observed Frequency Ratio	**=**	**7.7 $\pm$ 0.5**

8.9 The trouble with 3D

Neither Martin nor I have managed to make any progress in predicting the final state probabilities for general cuboids and it is not at all clear how to extend our 2D model to three-dimensions. The solid angle subtended by one side of a cuboid (from the centre of mass) is given by:

$$\begin{aligned}\text{Solid Angle}\left(\underline{a \times b} \times c\right) &= \int_{x=a/2}^{a/2}\int_{y=-b/2}^{b/2} \frac{c/2}{(x^2+y^2+(c/2)^2)^{\frac{3}{2}}}dydx \\ &= 4\arctan\left(\frac{ab}{c\sqrt{a^2+b^2+c^2}}\right)\end{aligned} \tag{8.18}$$

So the probability of landing on one of the two $a \times b$ surfaces with an inelastic, randomly orientated, low drop would be:

$$P_I(c-vertical) = \frac{2}{\pi}\arctan\left(\frac{ab}{c\sqrt{a^2+b^2+c^2}}\right) \tag{8.19}$$

Riemer et al inform us that that this "inelastic" model ought to be called the "Simpson model" after Thomas Simpson who proposed an identical scheme in 1740.[147] The Simpson model should be correct for $e \to 0$. However, so far, we don't have a full, realistic, theory for 3D even in the limit of, for example ($e \to 1, \mu = 1$).

Riemer's Gibbs' model, with its free parameter, might be the best that can be obtained for three-dimensions. This would particularly be the case if, for example, the way in which the die is thrown strongly affects the final probabilities.

Riemer makes clear that (experimentally) things like rounded corners on the cuboid, or the utilisation of backgammon-style "dice cups" makes a big difference. These things will clearly effect the probabilities of getting certain outcomes, as can be seen by considering the same things in their extreme limit (*e.g.* A very thin and narrow throwing cup, such that

the cuboid fits into it in only one orientation, or cuboids with very highly rounded corners such that the smallest surface had only the most minimal flat portions). In this way it can be seen that (reasonably tall) dice cups will raise the probability of the least probable outcomes (as the sides will support the die in "end-on" positions). Conversely rounded corners will reduce the probability of these (already less probably) "end-on" outcomes.

It might be that other factors (for example the initial spin imparted to the die) will affect the outcome, or it might be that there is some true limiting behaviour (for reasonably bouncy surfaces, with a die cast from a great height) which can be modelled without the need for an empirically set parameter.

Riemer et al. have done extensive work, particularly in the 3D case with two axes of the same size (*i.e.* an xxy cuboid of the kind shown in Figure 8.1) and I have tried to adapt our model to this in section 8.11.

This Markov chain type model, is difficult to adapt to three dimensions for two reasons. Firstly, it is difficult because it would not be clear what "activation energy" to apply to each state. As a cuboid loses energy there will come a point where the highest energy state is no longer attainable but transitions between the two lower energy states are still possible.

Finally, even if it were possible to set these activation energies, we would have to predict three probability ratios which were self-consistent with one another. *i.e.* P(A):P(B) must be equal to the product of P(A):P(C) and P(C):P(B).

These extra complications are a particular feature of a three state model, and they do not arise in two state system.

Two two-state systems which our model could be adapted for would be that of a right circular cylinder thrown onto a surface (section 8.10) and an xxy cuboid – *i.e.* a cuboid with two square faces (section 8.11).

8.10 Cylinders

After the work on two-dimensional dice had been published[141] the article appeared on the European Journal of Physics website with a link to similar work, conducted in retirement, by famous cosmologist Herman Bondi.[143]

Bondi had considered the problem of the chance of a cylinder settling on its end (or circular face) as opposed to its side (*i.e.* the side on which it is able to roll).

Because a cylinder is a system with only two and not three potential final energy states the theoretical approach outlined in section 8.2 will render the problem tractable.

8.10.1 Cylinder Theory

Our predicted probability ratio for long cuboids included two terms, one was the angle ratios and the other was the ratio of "activation energies". For cylinders it seems sensible to use solid angle ratios and "activation energies" are calculated in the same way as before, as the difference in energy between the settled state and energy of the minimum energy transition state. So the analogous equation to equation 8.14 for a cylinder is:

$$\frac{P(Circular\ side)}{P(Rolling\ side)} = \frac{\sqrt{D^2+L^2}-L}{\sqrt{D^2+L^2}-D}\frac{\sqrt{D^2+L^2}-L}{L} = \frac{\left(\sqrt{D^2+L^2}-L\right)^2}{\left(\sqrt{D^2+L^2}-L\right)L} \tag{8.20}$$

Where the solid angle subtended from the centre of a cylinder (Diameter, D, Length, L) by its lateral face, is given by:

$$\Omega = \frac{4\pi L}{\sqrt{D^2+L^2}} \tag{8.21}$$

Bondi's model would just include the activation energy terms and not the solid angle consideration (*i.e.* the expression for the probability ratio would be given by the red expression from equation 8.20). Meanwhile, the Simpson model would just include the solid angle terms, and not the energy considerations (*i.e.* the green expression from equation 8.20)

8.10.2 Cylinder Experiment

By using standard British One Pound Coins and superglue I was able to make cylinders of between one and twelve pound coins in height (see Figure 8.15).

Figure 8.15. The easiest way to make good, uniform cylinders, was to glue pound coins together with superglue. The cylinders were then thrown from a reasonable height onto the two surfaces shown; Lino (white) and Laminate (wood grain surface).

These cylinders were thrown onto lino and laminate surfaces. The results were as follows:

Number of Coins	Height (cm)	*L/D*	Predicted *P(Circ)/P(Lat)*	Number Circular	Number Lateral	Observed Ratio
1	0.30 ± 0.01	0.133 ± 0.005	650 ± 70	791	9	90 ± 30
2	0.62 ± 0.01	0.276 ± 0.005	56 ± 3	375	25	15 ± 3
3	0.93 ± 0.01	0.413 ± 0.005	13.1 ± 0.6	331	69	4.8 ± 0.6
4	1.24 ± 0.01	0.551 ± 0.005	4.46 ± 0.16	265	135	1.96 ± 0.20
5	1.56 ± 0.01	0.693 ± 0.005	1.82 ± 0.06	195	205	0.95 ± 0.10
6	1.89 ± 0.01	0.840 ± 0.006	0.84 ± 0.02	145	255	0.57 ± 0.06
7	2.20 ± 0.01	0.978 ± 0.006	0.454 ± 0.012	114	286	0.40 ± 0.04
8	2.53 ± 0.01	1.124 ± 0.007	0.255 ± 0.006	80	320	0.25 ± 0.03
9	2.83 ± 0.01	1.258 ± 0.007	0.160 ± 0.003	36	364	0.099 ± 0.017
10	3.14 ± 0.01	1.396 ± 0.008	0.103 ± 0.002	28	372	0.075 ± 0.015
11	3.50 ± 0.01	1.556 ± 0.008	0.0653 ± 0.0015	19	381	0.050 ± 0.012
12	3.83 ± 0.01	1.702 ± 0.009	0.0446 ± 0.0009	16	384	0.042 ± 0.011
13	4.12 ± 0.01	1.831 ± 0.009	0.0328 ± 0.0007	13	387	0.34 ± 0.010

Table 8.4. Pound Coin Cylinders on Lino Flooring.

Diameter of all Cylinders = Diameter of a One Pound Coin = 2.25 ± 0.01 cm

Number of Coins	Height (cm)	*L/D*	Predicted *P(Circ)/P(Lat)*	Number Circular	Number Lateral	Observed Ratio

1	0.30 ± 0.01	0.133 ± 0.005	650 ± 70	1198	2	600 ± 400
2	0.62 ± 0.01	0.276 ± 0.005	56 ± 3	391	9	43 ± 15
3	0.93 ± 0.01	0.413 ± 0.005	13.1 ± 0.6	359	41	8.8 ± 1.4
4	1.24 ± 0.01	0.551 ± 0.005	4.46 ± 0.16	283	117	2.4 ± 0.3
5	1.56 ± 0.01	0.693 ± 0.005	1.82 ± 0.06	200	200	1.00 ± 0.10
6	1.89 ± 0.01	0.840 ± 0.006	0.84 ± 0.02	134	266	0.50 ± 0.05
7	2.20 ± 0.01	0.978 ± 0.006	0.454 ± 0.012	83	317	0.26 ± 0.03
8	2.53 ± 0.01	1.124 ± 0.007	0.255 ± 0.006	51	349	0.15 ± 0.02
10	3.14 ± 0.01	1.396 ± 0.008	0.103 ± 0.002	27	373	0.72 ± 0.014

Table 8.5. Pound Coin Cylinders on Laminate Flooring.

Diameter of all Cylinders = Diameter of a One Pound Coin = 2.25 ± 0.01 cm

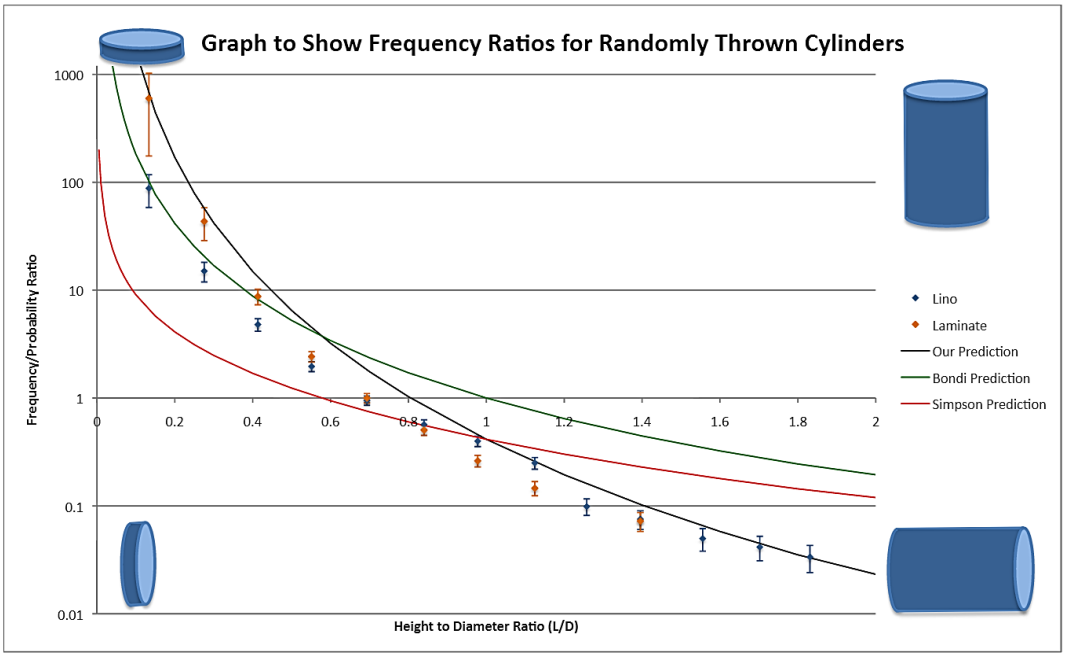

Figure 8.16. Graph comparing experimental results from tables 6.4 and 6.5 with Our Prediction, Bondi's Prediction and Simpson's Prediction.

Our prediction is a great improvement on either Bondi's or Simpson's model (although one could consider our prediction to be merely a combination of their models).

However, the true results are systematically more likely to land on the lateral face of the cylinder than our prediction would dictate. One possible explanation for this is that every tipping direction for an upright cylinder tilts it towards the other state. Contrast this with a cylinder lying on its side with its axis oriented North-South. Tipping such a cylinder to the

North or South will tip it towards the “end on” orientation, but tipping it East or West will just cause it to roll. Put another way, a cylinder on its end will not generally remain stable on its end unless it has insufficient Kinetic energy to tip over. However, a cylinder on its lateral face can remain stably on this face despite having very high energy, so long as itis rolling along the ground. This means that the rolling face is a bit more stable than our model would suggest.

8.11 xxy cuboids

Like the cylinder our model can be adapted to the x by x by y cuboid (of the kind shown in Figure 8.1). However, the model is not exact as the concept of an “activation energy” is less clear for a cuboid. For example, clearly if the cuboid is going to tip in a corner-over-corner fashion, rather than an edge-over-edge fashion, it will need a higher energy than the “activation energy” given by the energy of the minimum energy state that allows a transition. However, combining the expression for the activation energy given by equation 8.4 (effectively taking the edge over edge activation energy) with the expression for a solid angle ratio given by equation 8.19, gives an expression for the xxy cuboid probability ratio of:

$$\frac{P(Square\ sides)}{P(Rectangular\ sides)} = \frac{\sqrt{x^2+y^2}-y}{\sqrt{x^2+y^2}-x}\frac{\arctan\dfrac{x^2}{y\sqrt{2x^2+y^2}}}{2\arctan\dfrac{y}{\sqrt{2x^2+y^2}}} \tag{8.22}$$

The observed results are shown in table 8.6 and Figure 8.17.

x (cm)	y (cm)	y/x	Predicted Probability Ratio	Number settling on Square Side	Number settling on Rectangular Side	Observed Ratio
1.90 ± 0.01	0.71 ± 0.01	0.374 ± 0.006	22.0 ± 1.2	777	23	33 ± 7
1.90 ± 0.01	1.15 ± 0.01	0.605 ± 0.006	3.65 ± 0.14	170	30	5.6 ± 1.1
1.90 ± 0.01	1.46 ± 0.01	0.768 ± 0.007	1.44 ± 0.05	133	67	2.0 ± 0.3
1.90 ± 0.01	2.30 ± 0.01	1.211 ± 0.008	0.228 ± 0.006	137	613	0.22 ± 0.02
1.90 ± 0.01	3.00 ± 0.01	1.579 ± 0.010	0.076 ± 0.002	26	574	0.045 ± 0.009

Table 8.6. x by x by y cuboids, thrown on laminate floor

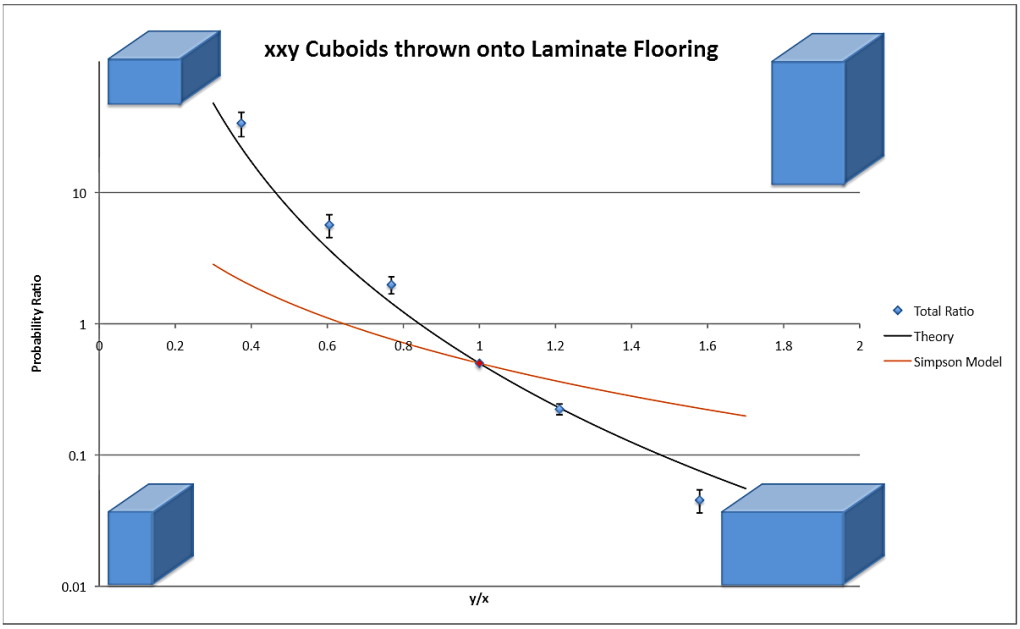

Figure 8.17. Graph showing experimental results from tables5.6 alongside prediction using an extension to our Markov Chain Model and a Simpson's model prediction. The red point in the middle of the Graph shows a probability ratio of 1:2 for a perfect cube, as demanded by symmetry. Real data seems to give a systematically more extreme probability ratio than the model predicts

It is noticeable that the corners of the pine blocks that I am using do get slightly rounded off after a hundred or so throws (and this would lead to a systematic offset in exactly the direction observed.

However, I am stretching the bounds of our new model by trying to fit it to this scenario so there may be other contributions to this offset.

8.12 Overall Conclusions about dropping experiments

We have developed and tested (both experimentally and computationally) a model for the landing probabilities of two-dimensional dice (or long 3D cuboid, or biased dreidel). We have found that, as suggested theoretically, the ratio or the probabilities of landing in each of the two potential orientations (when the plank is thrown onto a reasonably bouncy surface) is given by $\frac{\sqrt{l^2+k^2}-k}{\sqrt{l^2+k^2}-l}\frac{\arctan\frac{l}{k}}{\arctan\frac{k}{l}}$ where k and l are the lengths of the two sides.

We hope that this result might be used in order to assist in the teaching of Markov Chain analysis for young undergraduate students.

Unfortunately, I have only made limited progress towards adapting this theoretical approach to the three-dimensional problem.

It may be that the theory can be extended generally into three dimensions. Alternatively, it may be that, in three dimensions, the final state probabilities are dependent, in some complicated way, on the way in which the dice are thrown (for example, the outcome probabilities may be dependent on the typical magnitude and direction of the initial spin imparted to the die). Although other work has been done which predicts three-dimensional, cuboidal dice probabilities, [161,145] these models contain one or more free parameters which must be set experimentally (even in the limit of, for example, $e \to 1, \mu = 1$).

Finally, it has been possible to make good predictions for certain three-dimensional shapes, in particular that of a cuboid with two equal sides and a cylinder.

9 References to Appendices

[146] Clerk, A. A., Marquardt, F., Jacobs, K. (2008). *New J. Phys.* **10**, 095010, p.20

[147] Treutlein, P., Genes, C., Hammerer, K., Poggio, M., Rabl, P. (2014). Chapter 14 Hybrid Mechanical Systems. In: Aspelmeyer, M., Kippenberg, T. J., Marquardt, F., *Cavity Optomechanics*, Springer, Berlin, p.327-351

[148] Paternostro, M., Gigan, S., Kim, M. S., Blaser, F., Böhm, H. R., Aspelmeyer, M. *New J. Phys* **8**, 107 (2006).

[149] Marquardt, F., Chen, J. P., Clerk, A. A., Girvin, S. M . (2007). *Phys. Rev. Lett.* **99**, 093902

[150] Genes, C., Vitali, D., Tombesi, P., Gigan, S., Aspelmeyer, M. (2008). *Phy. Rev. A* **77**, 033804

[151] Wilson-Rae, I., Nooshi, N., Zwerger, W., Kippenberg, T. J. *Phys. Rev. Lett.* **99**, 093901

[152] Xiong, H., Si, L-G., Zheng, A-S. (2012). *Phys. Rev. A* **86** (1), 013815

[153] The Gates of the Wonder World, (2014). Available at: https://tomasbzdusek.files.wordpress.com/2014/05/joke1.jpg [Accessed (20/4/15)]

[154] Rashid, M., Tufarelli, T., Bateman, J., Vovrosh, J., Hempston, D., Kim, M. S., Ulbricht, H. (2016). Experimental realization of a thermal squeezed state of levitated optomechanics. *Phys. Rev. Lett.* **117** (27)

[155] Bose, S., Jacobs, K., Knight, P. L. (1997). *Phys. Rev. A* **82**, 013818

[156] Mancini, S., Man'ko, V. I., Tombesi, P. (1997). *Phys. Rev. A* **55**, p.559

[157] Ristè, D., Dukalski, M., Watson, C. A., de Lange, G., Tiggelman, M. J., Blanter, Y. M., Lehnert, K. W., Schouten, R. N., DiCarlo, L. (2013). Deterministic entanglement of superconducting qubits by parity measurement and feedback. *Nature* **502**, p.350-354

[158] Ade, P. A. R., Aghanim, N., Arnaud, M. *et al.* (257 other authors not shown) (2015). Planck 2015 results. XIII. Cosmological parameters (Feb 2015) *Astronomy & Astrophysics* **594,** A13

[159] Pender, G. A. T., Uhrin, M. (2014). Predicting non-square 2D dice probabilities. *Eur. J. Phys.* **35** (4), 045028

[160] Newton, I. *The Mathematical Papers of Isaac Newton*, Volume I, p.60-61. Cambridge University Press, 1967

[161] Bondi, H. (1993). *Eur. J. Phys.* **14**, 136

[162] Riemer, W., Stoyan, D., Obreschkow, D. (1967). Cuboidal Dice and Gibbs' Distributions. *Metrika* **77** (2), p. 247-256, 2014 ISSN 0026-1335. URL: http://dx/doi.org/10.1007/s00184-013-0435-y. Volume I, pages 60-61, Cambridge University Press, 1967

[163] Mungan, C., Lipscombe, T. (2013). *The Mathematical Gazette*, **97** (538), p.163

[164] Budden, F. (1980). Throwing non-cuboidal dice. *The Mathematical Gazette* **64** (429), p.190-198

[165] Simpson, T. (1740). *The nature and laws of chance.* Edward Cave, London

[166] Maker Bot: http://store.makerbot.com/replicator2.html [accessed 3/4/2013]

[167] Bullet Physics: http://bulletphysics.org/wordpress/ [accessed 3/4/2013]

[168] Giordano, N. J., Nakanishi, H. (2005). *Computational Physics*, Addison-Wesley

[169] Uhrin, M. (2014): https://github.com/muhrin/DicePhys [accessed and last updated 30/9/2013]